ABSTRACT

Title of Document: PLD GROWTH OF HIGH QUALITY ZINC OXIDE THIN FILMS ON SI SUBSTRATES AND DEVICE DEVELOPMENT.

Saeed Esmaili Sardari, PhD , 2012

Directed By: Professor Agis. A. Iliadis
Department of Electrical and Computer Engineering and Computer

Growth of high quality zinc oxide thin films on silicon substrates is particularly important because it combines the unique features of zinc oxide (ZnO) with mature CMOS technology and paves the way for device developments. However, this is a challenging task due to several technical and material-related fundamental issues which exist with the growth of this highly sought after compound semiconductor. In general, metal-oxide semiconductors suffer from non-stoichiometric growth which leads to unipolar doping properties, such as ZnO grows nominally n-type while NiO grows p-type. Thus, these materials can be doped easily either n or p-type while the other polarity is hard to achieve, if not impossible. Although methods for the growth of p-type films, using extrinsic doping or exotic precursors with post growth treatments have been reported on different substrates, the problem of controlled and stable extrinsic p-type doping of ZnO films remains an open subject for research.

In the present work, we have achieved the growth of undoped p-type ZnO films on Si (100) substrates by pulsed laser deposition through the optimization of growth conditions and adjustments of growth dynamics. Currently no other reports of undoped p-type ZnO on Si substrates by PLD growth exist, showing stable p-type conductivity in a repeatable process. The structural, optical, and electrical properties of the grown films were examined using techniques such as X-ray photoelectron spectroscopy (XPS), X-ray diffraction spectroscopy (XRD), Photoluminescence spectroscopy (PL), Hall Effect four-point probe Van Der Pauw measurements, and Current-Voltage (I-V) measurements for the p-n heterojunctions. Electrical behavior of ZnO is generally attributed to intrinsic defects which include vacancies, interstitials, and anti-sites of Zn and O in addition to external contamination related defects such as hydrogen complexes. The effects of growth conditions and intrinsic defects including hydrogen contamination on the properties of the grown layers are studied. Moreover, the growth dynamics of ZnO polar planes, i.e. the stacking of O^{-2} and Zn^{+2} planes, on n and p-type Si substrates are discussed.

Once material studies and growth optimizations are completed, high quality ZnO films are used in device fabrication. Two types of optoelectronic devices, a photoresistor and a Schottky diode are fabricated on Si substrates, and the electrical behavior of the devices are investigated. The high quality ZnO films also contributed to the development of a surface acoustic wave (SAW) biosensor.

PLD GROWTH OF HIGH QUALITY ZINC OXIDE THIN FILMS ON SI SUBSTRATES AND DEVICE DEVELOPMENT

By

Saeed Esmaili Sardari

Dissertation submitted to the Faculty of the Graduate School of the
University of Maryland, College Park, in partial fulfillment
of the requirements for the degree of
Doctor of Philosophy
2012

Advisory Committee:
Professor Agis A. Iliadis, Chair
Professor Neil Goldsman
Professor Martin Peckerar
Professor Robert Newcomb
Professor Lourdes Salamanca-Riba

©Copyright by

Saeed Esmaili Sardari

2012

Dedication

I am dedicating this work to my parents; not because it is of a value, but this is the least I can do to show my gratitude for their unconditional love and support.

To my parents,

Zarrin Taj and Abbas

Acknowledgments

First and foremost, I would like to express my sincere appreciations to *Dr. Agis Iliadis* for his intellectual stimulation, mentorship, guidance, support, and most importantly his thoughtfulness throughout the course of this study. Indeed, his expertise on the subject along with his ideas created this opportunity for me, and I am appreciating all his supports sincerely.

I did not have the opportunity of being his student as an undergraduate here at the university of Maryland, but I was lucky to have Dr. Iliadis in my PhD qualifying examination where I was challenged by his deeply-thought questions regarding semiconductors "band bending," and the subject became my passion for the next five years then after. During this period, Dr. Iliadis has generously shared his knowledge and expertise as well as his novel ideas and intuitions with me to create the frame work of my research. In addition to his superb theoretical and technical knowledge, professional attitude, patience, and humbleness, Dr. Iliadis is an extremely meticulous technical writer and editor. Even though this gave me hard times to present documents or publish papers with him, but I truly enjoyed his critical reviews, and I learned a lot about professional and ethical reporting; I am sure I will enjoy this more in future though. I truly appreciate all his hard work, comments, and corrections to my never-ending revisions!

I would like to extend my gratitude to the faculty of the Electrical Engineering Department at the University of Maryland in College Park who provided me with so many opportunities to study, learn, discuss, and teach in this amazing university. In particular, I would like to thank *Dr. Neil Goldsman, Dr. Martin Peckerar, Dr. Robert Newcomb,* and *Dr. Lourdes*

Salamanca-Riba for their constructive discussions throughout this work as well as their teachings for the past several years which I have had the privilege of being their student both as an undergrad and a grad student.

I should also thank *Dr. Thomas E. Murphy* and *Dr. Romel Gomez* for the opportunities they provided for me in the first couple of years of my studies at the University of Maryland. Dr. Murphy provided me with an Undergraduate Teaching Fellowship in my second semester here at Maryland, and it became a gateway for further chances. Dr. Gomez also provided me with my first research opportunity when he accepted me in his excellent research group; it sure built the foundation for my research later.

I am also grateful to *Dr. Peter Zavalij* of the Chemistry Department for his helps with the crystallographic experiments and his discussions during this work. Also, I would like to thank *Dr. Unchul Lee* of the Army Research Lab (ARL) for XPS measurements.

The success of this work relies heavily on the experiments and fabrications performed in the fabrication laboratory facility at the University of Maryland, and I would like to express gratitude to FabLab staff, and in particular, *Mr. Thomas C. Loughran* who was a significant help throughout this study.

The smooth operation of our machines was made possible with the help of all the people in the ECE technical operations office, and most importantly *Mr. Bryan Quinn* the director of the technical operations. I would like to sincerely thank him and his staff.

At the beginning of my research, I enjoyed the helps of our previous group member, *Dr. Hasina Ali*, and in final months of this research, a young and energetic graduate student who has recently joined our group, *Mr. Andrew Berkovich*; I truly appreciate their work.

I should also thank *Dr. Pamela Abshire* and *Dr. Marc Dandin* for their helps with the light-dark electrical measurements of my fabricated devices. Their helps and supports are gratefully acknowledged.

Finally, I want to express my sincere gratitude to all the people who made it possible for me to pursue my studies and focus on my research care freely; departmental and the university staff, my fellow classmates, my friends, and most importantly my family.

I am grateful for the supports of all my family members here in the United States and especially those back in Iran. I am sincerely thanking my mother and my father, Zarrin Taj and Abbas, who have selflessly provided me with all one can wish for; not only for the past ten years or so, but throughout my whole life. They sacrificed their youth to provide the best education and services for their children, and I can never be thankful enough.

I am thankful to my sister Foroozandeh and my brother Hamid who have always supported me with all their love and compassion. They have filled in for all my family responsibilities since I moved to the States more than ten years ago, and I truly appreciate it; without them none of this was possible.

Last and definitely not least, I want to thank my friend, my partner in life, my wife Mariam and her family for the love and supports during this period. They have been a great help for the past several years.

Saeed Esmaili Sardari

Table of Contents

Acknowledgments ... iii

List of Figures ... xii

List of Tables ... xxiii

Chapter One: Introduction and Contributions ... 1

- **1.1 Motivations and Contributions** ... 1
  - **1.1.1 Contributions** ... 1
  - **1.1.2 Practical Motivation** ... 3
- **1.2 Transparent Conductive Oxides** ... 3
- **1.3 ZnO Properties and Applications** ... 4
  - **1.3.1 Zinc Oxide Structure and Properties** ... 5
  - **1.3.2 Metal-oxide Semiconductors Applications** ... 10
  - **1.3.3 ZnO Applications** ... 11
  - **1.3.4 Future Applications** ... 11
- **1.4 Growth Techniques** ... 12

Chapter Two: ZnO Growth and Challenges ... 13

- **2.1 Growth Challenges** ... 13
- **2.2 Possible Explanations** ... 13
  - **2.2.1 Native Defects** ... 13
  - **2.2.1.1 Oxygen Vacancy, V_O** ... 14
  - **2.2.1.2 Zinc Vacancy, V_{Zn}** ... 15
  - **2.2.1.3 Oxygen and Zinc Interstitial, O_i and Zn_i** ... 15
  - **2.2.1.4 Oxygen and Zinc Antisites, O_{Zn} and Zn_O** ... 16
  - **2.2.2 Hydrogen Contamination** ... 16
- **2.3 Extrinsic doping of ZnO thin films** ... 19
  - **2.3.1 Extrinsic Single Dopants** ... 19
  - **2.3.2 Extrinsic Co-doping** ... 19
  - **2.3.3 Growth of Undoped Intrinsic ZnO thin films** ... 20

Chapter Three: PLD Growth ... 21

- **3.1 PLD Parameters** ... 21
- **3.2 PLD System** ... 22

3.2.1 PLD Dynamics 26
3.2.2 Energy of the Particles 27
3.3 Sample Preparation for Growth and Fabrication 30
Chapter Four: Equipments and Measurements 31
4.1 Measurements 31
4.1.1 X-ray Photoelectron Spectroscopy, XPS 31
4.1.2 X-ray Diffraction Spectroscopy, XRD 31
4.1.3 X-ray Powder Diffraction Spectroscopy, XRD 32
4.1.4 Photo Luminescence Electron Spectroscopy, PL 32
4.1.5 Electrical Measurements 33
Chapter Five: Structural Evaluation Results of the ZnO Films 34
5.1 XPS Results 34
5.1.1 Stoichiometric Deviations of the Films 35
5.2 XRD Results 41
5.2.1 GADDS Frames 41
5.2.2 GADDS Frames and XRD Plots 43
5.2.3 XRD of the PLD Target 45
5.2.4 ZnO XRD Spectrum 46
5.2.5 ZnO Crystal Parameters 48
5.3 PL Results 50
5.3.1 PLD Target 50
5.3.2 Optimization, Alignment, and Early Results 52
5.3.3 ZnO Peak Detection 53
5.3.4 Si Substrate Background PL 57
5.3.5 The Effects of Substrates Types on PL Emission Results 57
5.3.6 Low Oxygen Overpressure Growth Regime 57
5.3.7 High Oxygen Overpressure Growth Regime 58
5.3.8 PL Spectra of the Grown Films vs. the Target and the Reference ZnO Wafer 59
5.3.9 The Effects of Growth Temperature on PL Emission Results 60
Chapter Six: Hall Effect Measurements 65

6.1 Principles of Hall Effect 65
6.1.1 Theory and Derivations 65
6.1.2 Other Induced Voltages in Hall Effect 67
6.1.3 Multi-layer Hall Effect 69
6.1.4 Contact Size and Shape 70
6.1.5 Reading Error 71
6.1.6 Contact Material 72
6.2 Hall Effect Measurement System 80
6.3 Hall Mobility 81
6.3.1 Scattering Mechanism 81
6.4 Grain Size 100
6.5 Electrical Studies of n and ZnO/p-Si Devices 102
6.5.1 Results 102
6.6 Discussion 109
6.6.1 Electronic Surface Structure of Si Substrates 110
6.6.2 Morphologic Surface Structure of Si Substrates 111
Chapter Seven: Device Development 113
7.1 Vertical Transport Devices 113
7.1.1 ZnO/n-Si Devices 113
7.1.2 ZnO/p-Si Devices 114
7.1.3 Transport Mechanism 116
7.1.4 Ideality factor 118
7.1.5 Derivation of Junction Parameters 121
7.2 Bacterial Biofilm Growth Monitoring SAW Sensor 123
7.3 Photoresistors and Schottky Diodes 124
7.3.1 Device Structures 124
7.3.2 Contact Material Optimization and Metallization Process 124
7.3.3 Results 128
Chapter Eight: Conclusions and Future Work 136
Bibliography 140

List of Figures

Figure 1.1. The 3D ball-stick representation of ZnO unit cell (left) and its primitive unit cell (right).

Figure 1.2. Zn-terminated (left) and O-terminated configurations of [0001] wurtzite ZnO. O-terminated and Zn-terminated ZnO films show different electrical, mechanical, and chemical properties.

Figure 1.3. Surface configuration of O-terminated ZnO films. Smooth terraces separated by two double-layer ZnO heights are expected.

Figure 1.4. Surface configuration of Zn-terminated ZnO films. Many islands and pits of one double-layer ZnO height are expected.

Figure 1.5. The 3D ball-stick representation of zinc oxide crystal. Left is the perfect crystal without any defects. In the middle, zinc vacancy created positive holes, and right is the charged oxygen interstitial with created positive holes.

Figure 1.6. The 3D ball-stick representation of zinc oxide crystal. Left is the depiction of oxygen vacancy created free electrons. To the right, zinc interstitial introduces electron carriers.

Figure 2.1. Formation energy of oxygen vacancy as a function of the Fermi level for oxygen poor (left) and oxygen rich (right) growth conditions.

Figure 2.2. Formation energy of oxygen vacancy along with other native defects in ZnO as a function of the Fermi level for oxygen poor (left) and oxygen rich (right) growth conditions. The circles show the transition points between different charged states.

Figure 2.3. The formation energy of various intrinsic defects in ZnO over the working Fermi energy levels. Two ambient conditions are shown; zinc rich (left), and oxygen rich (right) condition.

Figure 2.4. Schematic representation of hydrogen incorporation in ZnO crystal at the interstitial bond-center site (left), the interstitial antibonding site (center), and the substitutional oxygen site (right).

Figure 2.5. Formation energy of hydrogen related defects along with oxygen vacancy as a function of the Fermi level. Hydrogen defects are stable at +1 charge state and oxygen vacancy is stable as a neutral or doubly charge defect.

Figure 2.6. Formation energies of interstitial hydrogen in ZnO as a function of the Fermi level.

Figure 3.1. PLD deposition chamber. Left is the schematic of the chamber showing various parts: 1 is the incident laser beam, 2 is the optics, 3 is the laser port, 4s are the glass view ports, 5 is the controlled target holder, 6 is the controlled sample holder, and 7 is the ejected plume from the PLD target. Right is the top view of the actual growth chamber.

Figure 3.2. Schematics of laser profile at different positions in our PLD system.

Figure 3.3. Experimental laser profiles at different positions in our PLD systems. Laser profile at the PLD target becomes more uniform and confined with the optical diaphragm.

Figure 3.4. PLD grown ZnO films on Si substrates. The non-uniform nature of PLD growth (left) is significantly improved by appropriate optical treatment and laser optimization (right).

Figure 3.5. Schematic of equipotential surfaces of PLD plume evolving pattern (left). The actual PLD plume inside the growth chamber (right).

Figure 3.6. Various interactions in PLD growth technique. 1 is laser-gas interaction, 2 is laser-matter interaction, 3 is laser-plume interaction, 4 is plume-gas interaction, and 5 is plume-matter interaction.

Figure 3.7. Regardless of the incident angle θ_i which is the same as the reflection angle θ_r, the ejected plume is traveling forward with high directional preference perpendicular to the target.

Figure 5.1. Full spectrum normalized intensity vs. binding energy plot for ZnO thin films. The peaks are as the followings: 1. Zn3d, 2. Zn3p, 3. Zn3s, 4. Auger Zn LMM, 5. Auger Zn LMM, 6. C1s, 7. Auger Zn LMM, 8. Auger Zn LMM, 9. Auger Zn LMM, 10. O1s in ZnO, 11. Auger O KLL, 12. Zn2p3/2, 13. Zn2p1/2.

Figure 5.2. Normalized intensity of O1s peak vs. binding energy for p-ZnO/Si device grown at high oxygen overpressure. O1s peak is observed at 530.63 eV

Figure 5.3. Normalized intensity of Zn2p3/2 peak vs. binding energy for p-ZnO/Si device grown at high oxygen overpressure. Zn2p3/2 peak is observed at 1021.63 eV.

Figure 5.4. Normalized intensity of O1s peak vs. binding energy for n-ZnO/Si device grown at high oxygen overpressure. O1s peak is observed at 530.70 eV.

Figure 5.5. Normalized intensity of Zn2p3/2 peak vs. binding energy for n-ZnO/Si device grown at high oxygen overpressure. Zn2p3/2 peak is observed at 1021.83 eV.

Figure 5.6. Normalized intensity of O1s peak vs. binding energy for p-ZnO/Si device grown at low oxygen overpressure. O1s peak is observed at 530.89 eV.

Figure 5.7. Normalized intensity of Zn2p3/2 peak vs. binding energy for p-ZnO/Si device grown at low oxygen overpressure. Zn2p3/2 peak is observed at 1021.65 eV.

Figure 5.8. Normalized intensity of O1s peak vs. binding energy for n-ZnO/Si device grown at low oxygen overpressure. O1s peak is observed at 530.85 eV.

Figure 5.9. Normalized intensity of Zn2p3/2 peak vs. binding energy for n-ZnO/Si device grown at low oxygen overpressure. Zn2p3/2 peak is observed at 1021.72 eV.

Figure 5.10. Typical normalized intensity of Zn2P3/2 and Zn2p1/2 peaks vs. binding energy observed for our devices.

Figure 5.11. Two-dimensional GADDS frames showing the whole diffraction range of θ=8o to θ=45o. The confinement of the diffraction patterns to line segments show the high alignment of ZnO textured structure.

Figure 5.12. GADDS frames for two samples grown on Si (bottom) and Si/SiO_2 (top) substrates. ZnO's (0002) peaks (left) and (0004) peaks (right) are shown. The confinement of the reflection pattern for ZnO/Si sample suggests a perfectly aligned textured structure for the grown layer. On the other hand, the extended reflection pattern for the film grown on Si/SiO_2 substrate indicates the textured structure of the ZnO film with random alignment. The diffused spot to the left of the (0004) diffraction is due to background diffraction from the Si substrate.

Figure 5.13. GADDS frames of (0002) ZnO peaks for samples grown at 2.0×10^{-6} (left), 6.5×10^{-6} (middle) and 1.0×10^{-4} Torr (right) oxygen overpressures. It is evident that the confinement of the diffraction pattern is increased as the oxygen pressure increases.

Figure 5.14. The bright region in the GADDS frame (top) corresponds to the (0002) ZnO peak at 34.05^{o} in the XRD plot (bottom).

Figure 5.15. The bright region in the GADDS frame (top) corresponds to the (0004) ZnO peak at 71.7^{o} in the XRD plot (bottom) and the diffused region to the left of this region is the substrate's diffraction.

Figure 5.16. XRD spectrum of ZnO shows ZnO (0002) peak at 33.85^{o} and ZnO (0004) peak at 71.4^{o}. In addition to ZnO peaks, Si (400) peak at 69.2^{o} is observed.

Figure 5.17. ZnO XRD spectrum shows the large main ZnO (0002) peak at 34° and small secondary ZnO (0004) peak at 71.7^{o}. No other peaks are detected.

Figure 5.18. Room temperature PL spectrum of ZnO wafer. The ZnO bandgap peak at 376 nm (3.29 eV) along with a broad peak centered at 541 nm (2.28 eV) is observed.

Figure 5.19. Room temperature PL spectrum of ZnO sputtering target. The ZnO bandgap peak at 387 nm (3.20 eV) along with a broad peak centered at 500 nm (2.47 eV) is observed.

Figure 5.20. The schematics of our PL setup. The sample location is optimized to ensure maximum PL emission detection.

Figure 5.21. PL spectra of the ZnO film grown on p-Si substrate and high pressure using different excitation wavelengths. The results are derived for 250, 260, 270, 280, and 290 nm excitations. ZnO NBE UV emission peak at 380 nm is observed for all excitation energies.

Figure 5.22. PL spectra of the ZnO film grown on p-Si substrate and high pressure using different excitation wavelengths. The results are derived for 250, 260, 270, 280, and 290 nm excitations. ZnO NBE UV emission peak at 380 nm is observed for all excitation energies. Another non-ZnO-related peak which shifts with the changes in the excitation energy is observed at lower wavelengths.

Figure 5.23. PL spectra of the ZnO film grown on p-Si substrate and low pressure using different excitation wavelengths. The results are derived for 250, 260, 270, 280, and 290 nm excitations. ZnO NBE UV emission peak at 378 nm is observed for all excitation energies.

Figure 5.24. PL spectra of the ZnO film grown on p-Si substrate and low pressure using different excitation wavelengths. The results are derived for 250, 260, 270, 280, and 290 nm excitations. ZnO NBE UV emission peak at 378 nm is observed for all excitation energies.

Figure 5.25. PL spectra of the ZnO film grown on p-Si substrate and low pressure using different excitation wavelengths. The results are derived for 250, 260, 270, 280, and 290 nm excitations. ZnO visible defect related broad band at 450—550 nm is observed for all excitation energies.

Figure 5.26. The average PL spectrum of Si substrates. It is evident that the intensity of the background emission is extremely low, and there are no peaks observed at 350—400 nm and 450—550 nm regions.

Figure 5.27. Room temperature PL spectra for ZnO films grown on p-Si (red) and n-Si (blue) substrates at 300 ^{o}C and low oxygen overpressure. Both spectra are very similar showing a high intensity near band-edge peak at 377 nm (3.28 eV) and a substantially suppressed defect related broad peak at 450-550 nm with the maximums at 485 nm for sample grown on n-Si and 493 nm for sample grown on p-Si.

Figure 5.28. Room temperature PL spectra for ZnO films grown on p-Si (red) and n-Si (blue) substrates at 300 ^{o}C and high oxygen overpressure. Both spectra are very similar showing a high intensity near band-edge peak at 379 nm (3.27 eV) for n-Si and 380 nm (3.26 eV) for p-Si. The defect related broad band emission is strongly suppressed.

Figure 5.29. The normalized PL spectra of the target, the ZnO wafer, and ZnO films grown at high and low oxygen overpressures.

Figure 5.30. PL spectra of n-ZnO/Si samples grown at low oxygen overpressure and different growth temperatures of 100, 200, 250, 300, and 350 ^{o}C.

Figure 5.31 PL spectra of p-ZnO/Si samples grown at low oxygen overpressure and different growth temperatures of 100, 200, 250, 300, and 350 ^{o}C.

Figure 6.1. Hall Effect structure and the related coordination. The grown layer is etched out to a clover leaf pattern.

Figure 6.2. Schematic of the Hall Effect setup. Left is the square patters and right is the clover-leaf pattern.

Figure 6.3. Experimental setup for Hall Effect measurements. A sample placed on the sample holder of Ecopia® Hall Effect Measurement system HMS-5000 is shown.

Figure 6.4. Lithography mask design for ZnO etching with detailed information.

Figure 6.5. The clover-leaf photolithography mask used for device fabrication in this study. The pattern provides a larger peripheral length which reduces the finite contact size induced error.

Figure 6.6. Electronic bands alignment for Ohmic contacts on an n-type (left) and a p-type (right) semiconductor. To have an Ohmic contact on an n-type material the work function of the metal should be less than the electron affinity of the semiconductor, and for a p-type material, the work function of the contact metal should be larger than the summation of the electron affinity and the band gap of the semiconductor.

Figure 6.7. Electronic bands alignment for Schottky contacts on an n-type (left) and a p-type (right) semiconductor.

Figure 6.8. Band bending in MS junction when $\Phi_M < \chi_e$. Bands always bend downward to accumulate electrons and deplete holes at the junction.

Figure 6.9. Band bending in MS junction when $\Phi_M > E_G/q + \chi_e$. Bands always bend upwards to accumulate holes and deplete electrons at the junction.

Figure 6.10. Schottky MS junction for n-type semiconductor when $\Phi_M > \chi_e$ with a potential barrier height of $\Phi_M - \chi_e$.

Figure 6.11. Schottky MS junction for p-type semiconductor when $\Phi_M < E_G/q + \chi_e$ with a potential barrier height of $\Phi_S - \Phi_M$. Note that $\Phi_S = E_G/q + \chi_e$.

Figure 6.12. The boundary conditions for Ohmic and Schottky contacts to n-type and p-type ZnO.

Figure 6.13. Selected materials for device analysis and fabrication. The Ohmic-Schottky boundary for both n-type and p-type cases are presented. Selected materials are examined and optimized through the optimization process.

Figure 6.14. Ecopia® Hall Effect Measurement System, HMS-5000 . The controller system (left) along with the temperature controlled sample holder and the magnets system (right) are shown. LN2 is introduced to the holder cavity for low temperature readings.

Figure 6.15. Hall mobility vs. Hall temperature for n-ZnO/Si device grown at 150 ^{o}C.

Figure 6.16. Hall mobility vs. Hall temperature for n-ZnO/Si device grown at 200 ^{o}C.

Figure 6.17. Hall mobility vs. Hall temperature for n-ZnO/Si device grown at 250 ^{o}C.

Figure 6.18. Hall mobility vs. Hall temperature for n-ZnO/Si device grown at 300 ^{o}C.

Figure 6.19. Hall mobility vs. Hall temperature for n-ZnO/Si device grown at 350 ^{o}C.

Figure 6.20. Hall mobility vs. Hall temperature plots for n-ZnO/Si samples grown at different growth temperatures.

Figure 6.21. Hall mobility vs. Hall temperature for p-ZnO/Si device grown at 150 ^{o}C.

Figure 6.22. Hall mobility vs. Hall temperature for p-ZnO/Si device grown at 200 ^{o}C.

Figure 6.23. Hall mobility vs. Hall temperature for p-ZnO/Si device grown at 250 ^{o}C.

Figure 6.24. Hall mobility vs. Hall temperature for p-ZnO/Si device grown at 300 ^{o}C.

Figure 6.25. Hall mobility vs. Hall temperature for p-ZnO/Si device grown at 350 ^{o}C.

Figure 6.26. Hall mobility vs. Hall temperature plots for p-ZnO/Si samples grown at different growth temperatures.

Figure 6.27. Hall mobility vs. Hall temperature for n-ZnO/Si device grown at 150 ^{o}C.

Figure 6.28. Hall mobility vs. Hall temperature for n-ZnO/Si device grown at 200 ^{o}C.

Figure 6.29. Hall mobility vs. Hall temperature for n-ZnO/Si device grown at 250 ^{o}C.

Figure 6.30. Hall mobility vs. Hall temperature for n-ZnO/Si device grown at 300 ^{o}C.

Figure 6.31. Hall mobility vs. Hall temperature for n-ZnO/Si device grown at 350 ^{o}C.

Figure 6.32. Hall mobility vs. Hall temperature plots for n-ZnO/Si samples grown at different growth temperatures.

Figure 6.33. Hall mobility vs. Hall temperature for p-ZnO/Si device grown at 150 ^{o}C.

Figure 6.34. Hall mobility vs. Hall temperature for p-ZnO/Si device grown at 200 ^{o}C.

Figure 6.35. Hall mobility vs. Hall temperature for p-ZnO/Si device grown at 250 ^{o}C.

Figure 6.36. Hall mobility vs. Hall temperature for p-ZnO/Si device grown at 300 ^{o}C.

Figure 6.37. Hall mobility vs. Hall temperature for p-ZnO/Si device grown at 350 ^{o}C.

Figure 6.38. Hall mobility vs. Hall temperature plots for p-ZnO/Si samples grown at different growth temperatures.

Figure 6.39. Maximum Hall mobility vs. growth temperature for n-ZnO/Si devices grown at low and high oxygen overpressures. The mobility is maximized at 300 ^{o}C and high oxygen overpressure.

Figure 6.40. Maximum Hall mobility vs. growth temperature for p-ZnO/Si devices grown at low and high oxygen overpressures. The mobility is higher for samples grown at high oxygen overpressure.

Figure 6.41. Electrical resistivity vs. Hall temperature for p-ZnO/Si devices grown at different growth temperatures of 150, 250, and 350 ^{o}C and low growth pressure. Three regions of resistivity (an almost constant region for low temperatures, a fast-reduction region for middle range temperatures, and an increasing region for high temperatures) are observed.

Figure 6.42. Electrical resistivity vs. Hall temperature for p-ZnO/Si devices grown at different growth temperatures of 150, 250, and 350 ^{o}C and high growth pressure. Three regions of resistivity (an almost constant region for low temperatures, a fast-reduction region for middle range temperatures, and an increasing region for high temperatures) are observed.

Figure 6.43. Electrical conductivity vs. Hall temperature for p-ZnO/Si devices grown at different growth temperatures of 150, 250, and 350 ^{o}C and low growth pressure.

Figure 6.44. Electrical conductivity vs. Hall temperature for p-ZnO/Si devices grown at different growth temperatures of 150, 250, and 350 ^{o}C and high growth pressure.

Figure 6.45. Carrier concentration vs. Hall temperature for samples grown on n-Si substrates under high oxygen overpressure. Different plots are for different growth temperatures.

Figure 6.46. Carrier concentration vs. Hall temperature for samples grown on n-Si substrates under low oxygen overpressure. Different plots are for different growth temperatures.

Figure 6.47. Carrier concentration vs. Hall temperature for samples grown on p-Si substrates and high oxygen overpressure. Different plots are for different growth temperatures.

Figure 6.48. Carrier concentration vs. Hall temperature for samples grown on p-Si substrates and low oxygen overpressure. Different plots are for different growth temperatures.

Figure 6.49. Hall Coefficient vs. growth temperature for films grown on p-type Si (100) substrates at high oxygen overpressure. All samples show n-type behavior at low measuring

temperatures while p-type behavior is observed for higher Hall Effect measurement temperatures. As compared with the low oxygen regime p-type conductivity at high oxygen overpressure is more dominant due to the further reduction in donor-like oxygen vacancy defects.

Figure 6.50. Hall Coefficient vs. growth temperature films grown on p-type Si (100) substrates at low oxygen pressure. All samples show n-type behavior at low measuring temperatures while p-type behavior is observed for higher Hall Effect measurement temperatures.

Figure 6.51. Hall Coefficient vs. Hall measuring temperature for ZnO films grown on p-type Si (100) substrates and high oxygen overpressure. Different plots are for different growth temperatures.

Figure 6.52. Hall Coefficient vs. Hall measuring temperature for ZnO films grown on p-type Si (100) substrates and low oxygen overpressure. Different plots are for different growth temperatures.

Figure 53. Hall Coefficient vs. Hall measuring temperature for ZnO films grown on p-type Si (100) substrates and low oxygen overpressure and 300 ^{o}C. This is the extended plot of the sample shown in figure 52.

Figure 6.54. Conductivity conversion temperature vs. growth temperature for the samples grown at low (top plot) and high (bottom plot) oxygen overpressure.

Figure 6.55. A comparison between the transition points vs. growth temperature for samples grown at high and low oxygen overpressures.

Figure 6.56. Schematics of silicon crystal. Boron tends to substitute for sub-surface bulk Si atoms whereas phosphorus appear in (100) Si surface. The existence of donor atoms in n-type Si surface and the lack of acceptor atoms in p-type Si surface change the growth dynamics of ZnO and affect the electrical behavior of the thin-film.

Figure 6.57. Atomic scale schematics of ZnO growth process on O-terminated surface. The ejected material (top) travels toward the substrate. The arriving ZnO on smooth surface (left) makes a single bond with the substrate which does not stick to the substrate. On the other hand, when the arriving ZnO is at the step of the substrate (right) it connects to the surface with double bonds.

Figure 6.58. Atomic scale schematics of ZnO growth process on Zn-terminated surface. The ejected material (top) travels toward the substrate. The arriving ZnO on smooth surface (left) makes a single bond with the substrate which does not stick to the substrate. On the other hand, when the arriving ZnO is at the step of the substrate (right) it connects to the surface with double bonds.

Figure 7.1 IV characteristics of n-ZnO/Si system for the film grown at 300 ^{o}C and low oxygen pressure. High electron concentration makes the film heavily doped with respect to the lightly doped substrate. The rectification is observed for the "p-n junction" device.

Figure 7.2. IV characteristics of n-ZnO/Si system for the film grown at 300 ^{o}C and high oxygen pressure. High oxygen overpressure makes the film lightly doped with respect to the substrate. The current is allowed for both polarities.

Figure 7.3. I-V characteristics of ZnO/p-Si system for the film grown at 300 ^{o}C and high oxygen pressure. High carrier concentration makes the film heavily doped with respect to the lightly doped substrate. The rectification is observed for the "p-n junction" device.

Figure 7.4. I-V characteristics of ZnO/p-Si system for the film grown at 300 ^{o}C and low oxygen pressure. Low oxygen overpressure makes the film lightly doped with respect to the substrate, and the reverse current is significantly increases with respect to fig. 3.

Figure 7.5. Coordinates used for the discussion.

Figure 7.6. The IV characteristics for n++ZnO/n-Si devices grown at low (blue) and high (red) oxygen overpressure and 300 oC. We observed a reverse saturation current of 3.0×10-6 A for the sample grown at low pressure and 5.5×10-6 A for the sample grown at high oxygen overpressure at +1 V.

Figure 7.7. The IV characteristics for p++ZnO/p-Si devices grown at low (red) and high (blue) oxygen overpressure and 300 oC. We observed a reverse saturation current of 8.5×10-5 A for the sample grown at low pressure and 6.0×10-6 A for the sample grown at high oxygen overpressure at -1 V.

Figure 7.8. Device fabrication process. The process can be summarized as the followings: A: Silicon substrate is cleaned for growth, B: ZnO thin film is grown, C: Sample is coated with photoresist, D: Photoresist is removed from the periphery of the sample using the clover leaf mask, E: Exposed ZnO is etched, F. Photoresist is removed from the sample, G: Sample is coated with photoresist, H: Photoresist is removed from the corners of the ZnO layer to open contact windows, I: Metal contacts are deposited, J: Lift-off.

Figure 7.9. Device fabrication process. Both Ohmic and Schottky contacts are deposited on the sample.

Figure 10. The IV characteristics of 200 nm circular Al contacts on n-ZnO/n-Si. The linear characteristics confirm the Ohmic properties of the contacts.

Figure 7.11. The IV characteristics of 200 nm circular Au contacts on p-ZnO/p-Si. The linear characteristics confirm the Ohmic properties of the contacts.

Figure 7.12. The IV characteristics of Al/p-ZnO/p-Si Schottky diode.

Figure 7.13. Semi logarithmic plot of the IV characteristics of Al/p-ZnO/p-Si Schottky diode. The inset shows the linear region between 1 and 2 volts.

Figure 7.14. The IV characteristics of Au/n-ZnO/n-Si Schottky diode.

Figure 7.15. Semi logarithmic plot of the IV characteristics of Au/n-ZnO/n-Si Schottky diode. The inset shows the linear region between 1 and 4 volts.

Figure 7.16. The IV characteristics of Al/n-ZnO/n-Si photoresistor grown at low oxygen overpressure and 300 oC. The response of the device is derived at 365 nm.

Figure 7.17. UV sensitivity mechanism for our Al-n-ZnO/n-Si photoconductor. Top left (1) shows the film's band-gap along with the defects traps band. When UV is illuminated (top right) electon-hole pairs are generated and electrons are trapped by defects traps activating defects (shown in 3). Excess holes then reduce the majority carrier concentration, i.e. electrons. Thus, UV illumination activates acceptor-like defects and generates holes in the valance band (shown in 4).

Figure 7.18. The IV characteristics of our Al/p-ZnO/p-Si Schottky diode grown at high oxygen overpressure. The differences between dark and light (λ=320, 345, and 365 nm) responses of this device are evident.

Figure 7.19. Sensitivity of Al/p-ZnO/p-Si Schottky diode is calculated by I"/I' using polynomial fit.

List of Tables

Table 1.1. Summary of properties of ZnO.

Table 2.1. PLD growth parameters and their effects.

Table 5.1. The crystallographic properties of our ZnO PLD target.

Table 6.1. The dependence of the induced voltages to the direction of the current and the polarity of the magnetic field in Hall Effect measurement. It is observed that only the Seebeck voltage, V_S, is not affected by the changes in magnetic polarity or current direction; however, adding up all the four readings allows for the calculation of V_S.

Table 6.2. ZnO parameters along with work functions of some relevant metals.

Table 6.3. The linear I-V characteristics of the contacts are verified prior to Hall effect measurements.

Table 6.4. Carrier concentration and Hall coefficients for n and ZnO/p-Si devices grown at low oxygen overpressure of ~5.0×10^{-6} Torr and various temperatures. A 500 nm oxide layer is grown by PECVD prior to ZnO growth. All the Hall readings are performed for a wide range of Hall temperatures (80K to 350K) and the average values are reported here.

Table 6.5. Carrier concentration and Hall coefficients for n and ZnO/p-Si devices grown at oxygen overpressure of 1.0×10^{-4} Torr and 250 ^{o}C.

Table 7.1. A summary of the studied devices, growth conditions and IV characteristics results for n and ZnO/p-Si device grown at 300 ^{o}C.

Table 7.2. A summary of the studied devices, growth conditions and calculated barrier heights and ideality factors for the given linear intervals.

Chapter One: Introduction and Contributions

Zinc oxide is a group II-VI wide band-gap compound semiconductor with unique electrical, chemical, and mechanical properties and potential in device applications. Bulk growth of ZnO and epitaxial growth on various substrates including Sapphire and GaN have been studied; however, it is important to develop and understand ZnO growth on Si substrates to improve the functionality of this technologically important substrate as well as the integration with the mature CMOS technology. In this chapter, a comprehensive study of ZnO, its properties, merits, along with applications are studied.

1.1 Motivations and Contributions

This work was proposed and carried out to understand ZnO growth mechanism, growth parameters, and device development. Scientific contributions of this research along with its practical motivations are discussed.

1.1.1 Contributions

The contributions of this work are as the followings:

- Achieved the highest quality ZnO thin films on Si (100) substrates grown by PLD.
- Demonstrated the growth of undoped p-type ZnO for the first time and clarified the mechanism and conditions for p-type growth.
- Demonstrated conductivity type conversion in ZnO films for the first time based on the thermal competition between acceptor and donor-like native defects.
- Demonstrated ZnO/Si heterojunction devices.
- Demonstrated ZnO optoelectronic devices.

Growth of high quality ZnO films on technologically important Si substrates and development of ZnO based devices as well as understanding the effects of native defects and growth parameters on electrical behavior of undoped ZnO films is a challenging task. This, however, improves the functionality of Si for optoelectronic applications and paves the way for monolithic integration of ZnO films with advanced CMOS technology. This work demonstrates a thorough investigation of high quality thin ZnO films growth on Si substrates.

The work of this dissertation has been presented partially in the following publications and conferences:

- *"Observation of conductivity type conversion in undoped ZnO films grown by pulsed laser deposition on silicon (100) substrates,"* Saeed Esmaili-Sardari, Andrew Berkovich, and Agis A. Iliadis. Applied Physics Letters, Device Physics, Vol. 100, Issue 5, 2012.

- *"An ALD aluminum oxide passivated Surface Acoustic Wave sensor for early biofilm detection,"* Young Wook Kim, Saeed Esmaili Sardari, Mariana T. Meyer, Agis A. Iliadis, Hsuan Chen Wu, William E. Bentley, Reza Ghodssi, Sensors and Actuators B: Chemical, Vol. 163, Issue 1, 2012.

- *"Crystal quality and conductivity type of (002) ZnO films on (100) Si substrates for device applications,"* Saeed Esmaili Sardari, Agis A. Iliadis, M. Stamataki, D. Tsamakis, and N. Konofaos. Solid-State Electronics, Vol. 54, Issue 10, October 2010.

- *"Study of Conductivity Type of Undoped ZnO films Grown on n and p-type (100) Si Substrates under Low and High Oxygen Pressure by Pulsed Laser Deposition,"* S. Esmaili-Sardari, Andrew Berkovich, and Agis A. Iliadis. International Semiconductor Device Research Symposium (ISDRS) 2009, University of Maryland, College Park, December 7-9, 2011.

- *"Atomic Layer Deposition of Aluminum Oxide for Effective Surface Passivation of a MEMS Biosensor,"* Young Wook Kim, Saeed E. Sardari, Agis A. Iliadis, and Reza Ghodssi. The 11th International Conference on Atomic Layer Deposition, Cambridge, Massachusetts, June 26-29, 2011.

- *"A Bacterial Biofilm Surface Acoustic Wave Sensor For Real Time Biofilm Growth Monitoring,"* Young Wook Kim, Saeed Esmaili Sardari, Agis Iliadis, and Reza Ghodssi. The 9th Annual IEEE Conference on Sensors, IEEE Sensors 2010 Conference, November 2-4, 2010.

- *"Development of Lab on a Chip Platforms for Bacterial Biofilm Monitoring and Detection,"* Mariana T. Meyer, Young Wook Kim, Varnika Roy, Saeed E. Sardari, Agis Iliadis, William E. Bentley, and Reza Ghodssi. 2010 International Biofabrication Conference, Philadelphia, PA, October 4-6, 2010.

- *"Growth of High Quality (002) ZnO Thin Films on (100) Si by Pulsed Laser Deposition,"* American Conference on Crystal Growth and Epitaxy ACCGE-17, Lake Geneva, Wisconsin, August 9-14, 2009.

- *"The p-n Conduction Character of High Quality (002) ZnO Thin Films Grown on (100) Si Substrates by Pulsed Laser Deposition,"* International Semiconductor Device Research Symposium (ISDRS) 2009, University of Maryland, College Park, December 9-11, 2009.

1.1.2 Practical Motivation

With the current pace of innovative designs and miniaturizations in semiconductor devices introducing a new species which is relatively cheap and easy to fabricate packed with a set of mechanical, chemical, and electrical merits has significant impacts on device fabrication. For instance, full color displays and high capacity storage devices are extremely popular. If we just consider the market size of only group II-VI metal oxide compound semiconductors for various applications ranging from flat panel displays to various sensors, the importance of this research becomes evident(Thomas Pearsall, 2008).

All ZnO p-n junctions, diodes, UV LEDs, LDs, UV sensors, and gas sensors are the major applications of this work, and there are numerous potentials for this research. Thus, there is a huge practical motivation behind this work.

1.2 Transparent Conductive Oxides

Zinc oxide is a metal oxide compound semiconductor which along with some other materials such as tin oxide and indium oxide falls into transparent conductive oxides, also known as TCOs. Typically, TCOs are insulators because of their large bandgaps (Hiroshi Kawazoe, 1997); however, there are exceptions, and oxides of zinc, tin, and indium can have carrier concentrations of up to 2×10^{21} cm^{-3}(Hiroshi Kawazoe, 1997)(Atsushi Kudo, 1 NOVEMBER 1999). The combination of high electric conductivity and optical transparency has created many applications in optoelectronics for TCOs; solar cells electrodes, flat panel displays, and smart windows[*] are just a few examples. Another major application of these oxides is in solid state gas sensing, and the field is dominated by SnO_2 and ZnO. Finally, the catalytic behavior of oxides is employed in chemical applications(Matthias Batzill).

Nevertheless, for most TCOs electrons are the majority carriers and they exhibit n-type behavior (Hiroshi Yanagi, 2002). This limits their application in device fabrication significantly(Atsushi Kudo, 1 NOVEMBER 1999). It is assumed that intrinsic defects are the reason behind this behavior. Three scenarios are suggested; one, intrinsic defects readily donate electrons to the

[*] Smart windows are a type of energy-conserving windows which change their coloring and their transparency with respect to the environmental exposures. TCOs are used for contacts of electrochromic films which are responsible for optimizing the window's color and transparency. Aside from the smart windows, tin oxide coated architectural windows are also a type of energy-conserving windows which allow visible light but filter out the infrared region of the spectrum for better thermal isolation (Matthias Batzill).

conduction band of the host lattice. Two, localized impurity bands show up just below the conduction band, and three, the donor bands merge with the conduction band and essentially become the conduction band (Matthias Batzill).

In general, despite all the potential of II-VI semiconductors, a major achievement in device applications has not been reported yet(R. Krause-Rehberg, 1998). The problem lies in the very structure of these materials; they cannot be doped both n and p-type. Elemental semiconductors like silicon and germanium can be doped either n or p-type by introduction of foreign atoms into their structures, but it is very difficult, if not impossible, to dope a compound semiconductor both n and p-type. As we will see, several explanations are provided for this issue, but it is not fully understood yet (R. Krause-Rehberg, 1998)(Desnica, 1998 Published by Elsevier Ltd).

Native point defects are the most favorable candidates for intrinsic concentrations. For example, in the case of ZnO, zinc vacancy leaves holes behind and oxygen interstitial draws electrons to form oxygen ion; holes are then created.

On the other hand, donor-like defects including oxygen vacancies and zinc interstitials create free electrons. These donor-like defects have lower formation energies at certain growth conditions which dominate the electrical behavior of the material and create the high electron concentration.

.

1.3 ZnO Properties and Applications

Group II-VI semiconductors are especially interesting due to their wide range of band-gaps and lattice constants. These compound semiconductors are particularly useful for fast particle detectors and emitter-detector devices due to their transport properties and optical features (R. Krause-Rehberg, 1998). Structurally, group II-VI compound semiconductors are binary compounds of zinc, cadmium, mercury with oxygen, sulfur, selenium, and tellurium and their ternary or quaternary alloys(Klingshirn, 2007). Zinc oxide, in particular, has dual semiconducting and piezoelectric properties which along with several physical, mechanical, and electrical features have made it the material of interest for many research groups(Janotti, et al., 2009)(Ü. Özgür, 2005)(Wang, 2004) . Moreover, the ever increasing interest on nanotechnology has drawn attentions to zinc oxide since it has probably the richest family of nanostructures of all materials; structures such as nanowires, nanotubes, nanobelts, nanorods, nanosprings, and nanocombs (Wang, 2004). Zinc oxide has a high resistance to electric degradation in high temperature operation, and among the family of group II-VI semiconductors it is the hardest member(Shubra Singh, J. Phys. D: Appl. Phys. 40 (2007) 6312–6327).

1.3.1 Zinc Oxide Structure and Properties

ZnO has a direct bandgap of 3.37 eV (at room temperature) with large exciton binding energy of 60 meV which makes it a potential material for low threshold lasing (Gyu-Chul Yi, 2005). Its exciton binding energy is almost 2.4 times larger than that of its main rival GaN with 25 meV (Janotti, et al., 2009). In fact, among all classical compound semiconductors of group II-VI and III-V, zinc oxide has the largest exciton binding energy; this allows high temperature excitonic emission of up to 550K(R. Triboulet, 47 (2003) 65-138).

Under normal pressure, ZnO crystallizes in hexagonal wurtzite structure where each Zn ion is tetrahedrally bounded to four O ions and vice versa. ZnO can also form into zinc-blend and rock salt configurations, but the two are stable at high pressures. ZnO has a preferred growth direction along the *z* axis, called the *c*-axis, which O^{-2} and Zn^{+2} polar planes are stacked along this axis; therefore ZnO can be either O-terminated or Zn-terminated (Klingshirn, 2007).

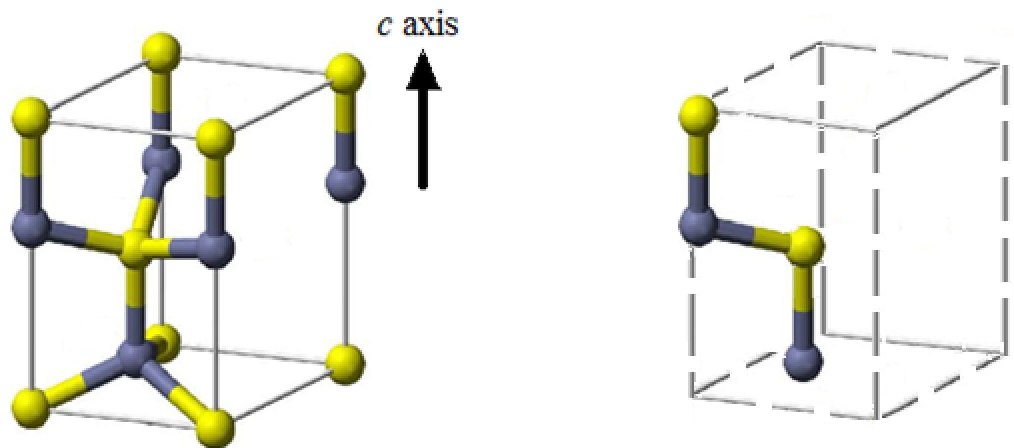

Figure 1. The 3D ball-stick representation of ZnO unit cell (left) and its primitive unit cell (right).

The two terminating configurations can be shown schematically as the following:

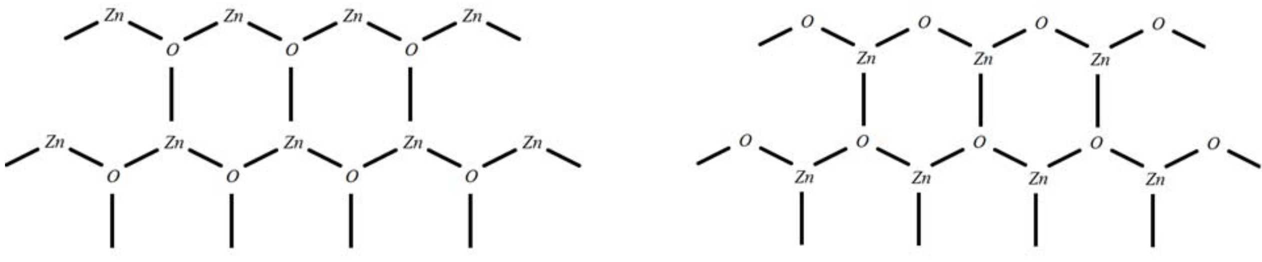

Figure 2. Zn-terminated (left) and O-terminated configurations of [0001] wurtzite ZnO. O-terminated and Zn-terminated ZnO films show different electrical, mechanical, and chemical properties.

Scanning tunneling microscopy studies have shown that the surface of the two ZnO terminating polar planes, i.e. O-terminated plane and Zn-terminated plane, have different structures. For the Zn-terminated plane, many small islands and pits of one double-layer ZnO height are observed and for the O-terminated plane, smooth terraces separated by two double-layer ZnO heights are expected(Meyer, et al., 2003). Schematically, we can show the differences as the followings:

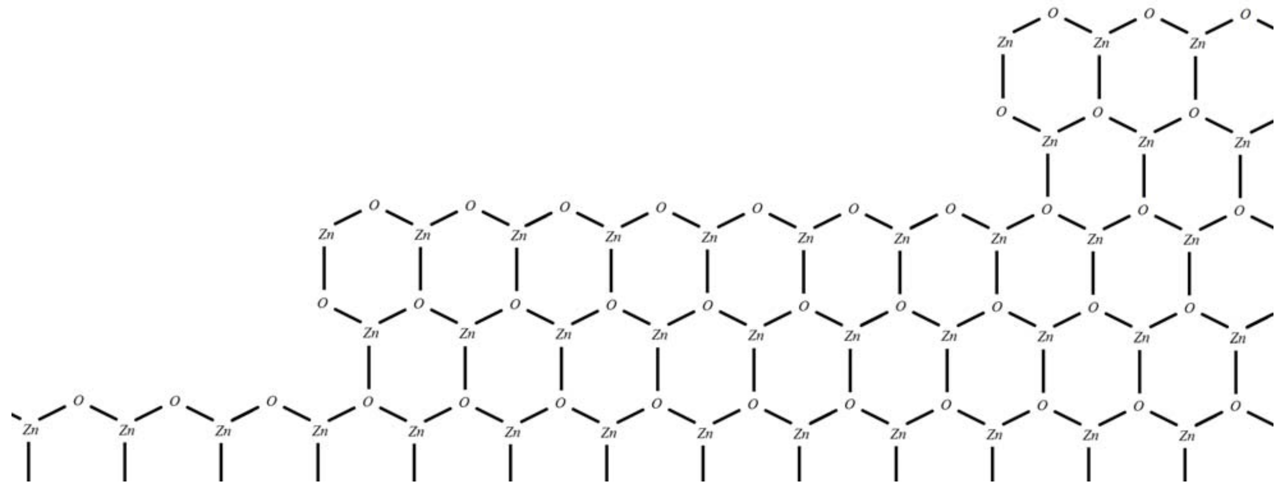

Figure 3. Surface configuration of O-terminated ZnO films. Smooth terraces separated by two double-layer ZnO heights are expected.

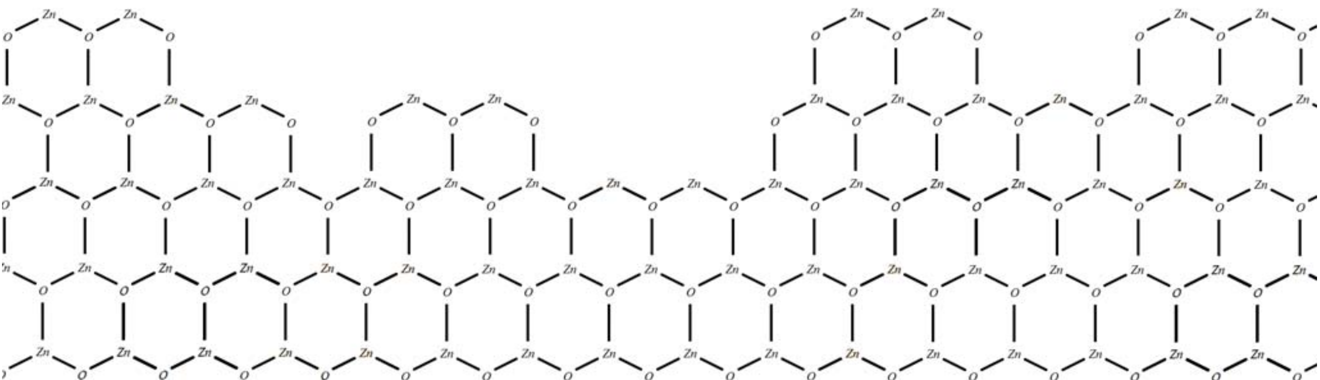

Figure 4. Surface configuration of Zn-terminated ZnO films. Many islands and pits of one double-layer ZnO height are expected.

There are also electrical, mechanical, and chemical differences between Zn-terminated and O-terminated films which will be discussed in chapter 6.

As mentioned before, native defects which play an important role in the electrical properties of ZnO can be shown schematically in the followings. Figure 5 shows the structure of zinc oxide crystal and p-type defects, and figure 6 shows native donor-like defects.

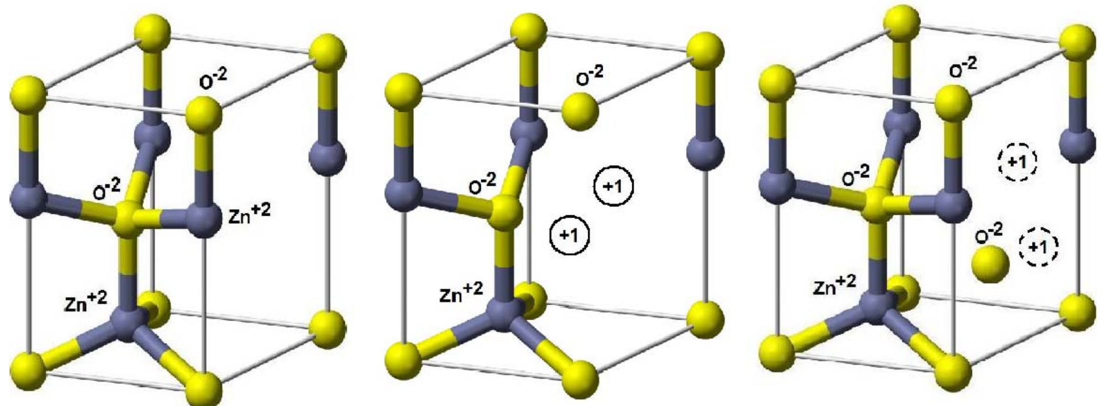

Figure 5. The 3D ball-stick representation of zinc oxide crystal. Left is the perfect crystal without any defects. In the middle, zinc vacancy created positive holes, and right is the charged oxygen interstitial with created positive holes.

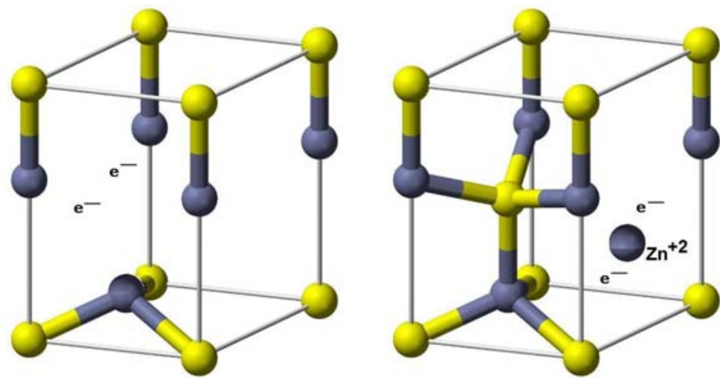

Figure 6. The 3D ball-stick representation of zinc oxide crystal. Left is the depiction of oxygen vacancy created free electrons. To the right, zinc interstitial introduces electron carriers

Despite other II-VI semiconductors, ZnO has a hexagonal closet packing (hcp) value of 1.6 which deviates slightly from the ideal value of *c*/a = 1.633; this explains the formation of ZnO in wurtzite structure as opposed to zinc-blend and rock salt configurations(Klingshirn, 2007).

ZnO crystal structure has a hexagonal unit cell which belongs to $P6_3mc$ or C_{6v}^4 space group using Hermann-Mauguin or Schoenflies notation, respectively(Morkoç, et al., 2009). $P6_3mc$ refers to primitive hexagonal crystal system with 6 fold rotation symmetry along the [0001] axis, *c*-axis, with a $\frac{1}{3}$ of lattice vector translation along this axis. It also shows that there are mirror planes ($P6_3$**m**c) perpendicular to the rotation axis as well as a glide translation plane ($P6_3$m**c**) along the lattice vector. Similarly, C_{6v}^4 shows the cyclic space group with 60° rotation symmetry and mirror planes(Vainshtein, 1994)(Sands, 1993).

Despite group IV elemental semiconductors like Si and Ge which have covalent bonding, ZnO has a mixture of covalent and ionic bonding. In fact, from completely covalent for group IV semiconductors to completely ionic for II-VI and I-VII insulators, ZnO with substantial ionic bonding resides at the center of this spectrum (Klingshirn, 2007).

Because of the low symmetry in wurtzite crystal structure and high electromechanical coupling, ZnO has high piezoelectric constants which make it a material of choice for sensory applications such as force and mass sensors (Janotti, et al., 2009).

It is worth noting that for many device applications band-gap engineering is necessary, and ZnO's band-gap can be tuned with proper doping of Mg, Be, or Cd. Magnesium and beryllium doping leads to an increase in the band-gap and cadmium reduces the gap. For a ternary compound $A_xZn_{1-x}O$ with 'A' of the dopants mentioned earlier, the energy gap $E_G(x)$ can be calculated as the following(N. Izyumskaya, 2007):

$$\mathrm{EG(x) = (1 - x)EZnO + xEAO - bx(1 - x)} \qquad \text{eq.1}$$

Where

$EZnO$ is the band-gap energy of ZnO
EAO is the band-gap energy of the AO compound
b is the bowing factor(J. A. Van Vechten, 1970)

It is reported that the band-gap of zinc oxide can be tuned from 2.99 eV to 7.7 eV (N. Izyumskaya, 2007)(Johnson, 94, 845 (1954))(Walker, 1967)(Koffyberg, 1976) depending on the dopant and mole fraction x. On the other hand, zinc oxide has a direct band-gap which makes it useful for optoelectronics. In this field, light emission and detection are of extreme importance. The light emission is due to the radiative recombination of excess carriers. Generally, excess carriers can recombine thru either radiative or non radiative paths. Radiative paths include intrinsic band-to-band transitions, free exciton annihilation, band fluctuations localized excitons recombination, and impurity levels transitions. Radiative recombination is governed by the conservation of energy and momentum. The wavelength or the energy of the emitted photon is fixed by the energy conservation and for intrinsic band-to-band transitions the mean energy of the photons is close to the energy gap; for all other radiative paths including the excitons and the impurity level transitions, the mean energy is somewhat lower than the distance between the

involving energy levels. In addition to the wavelength, the emission line width is determined by the energy conservation and it is typically $1.8k_BT$ where k_BT is the thermal energy of the carriers. On the other hand, the conservation of momentum ensures a proper transition in crystal lattice space. Since the wave number of a phonon, $k_{ph}= 2\pi\gamma/c$, is much smaller than that of electrons and holes with $k \sim h^{-1}(2m^* kT)^{1/2}$ where h is the Plank's constant and m^* is the effective mass for electrons and/or holes; thus, the band-to-band transition or the photon emission is vertical in energy vs. crystal momentum graphs. This means that direct gap semiconductors have higher radiative recombination rates than indirect ones. If the gap is not direct, then a third particle such as a phonon or a plasmon takes care of the momentum change; the probability of such a three-particle process is low. Thus, direct band gap materials are particularly interesting in optoelectronic applications(Arturas Zukauskas, 2002).

Recently a lot of attention is paid to bioengineering and bioelectronics. Biosensors and biogadgets are getting more and more popularity among the scientists, and having a biocompatible material for device fabrication is essential; zinc oxide is a biosafe and biocompatible material (Gyu-Chul Yi, 2005). It can be used in biosensors without any additional coatings which would potentially increase the sensitivity and the versatility of ZnO base sensors.

Zinc oxide is highly stable both chemically and thermally (M. Rusop). It also has a high resistance to electric degradation in high temperature operation, and among the family of group II-VI semiconductors it is the hardest member with the largest bulk and Young's modulus values(Shubra Singh, J. Phys. D: Appl. Phys. 40 (2007) 6312–6327). In addition to the mechanical hardness, it has high radiation hardness. Finally, zinc oxide is available in large area substrates with relatively low cost (Dae-Kue Hwang). Whereas GaN is not available in high quality substrates, ZnO substrates are now produced; therefore, homoepitaxy is now feasible(R. Triboulet, 47 (2003) 65-138).

Table 1 summarizes the properties discussed earlier.

Property	Features
Band-gap	Direct wide band-gap of 3.44 eV at low temperature and 3.37 eV at room temperature
Exciton binding energy	Large excition binding energy of 60 meV compared to 25 meV for GaN
Piezoelectric and pyroelectric properties	Large piezoelectric constants in the piezoelectric tensor, and strong pyroelectric properties
Strong luminescence	Broad peak in the blue-green (450 nm to 550 nm) region of the electromagnetic wave spectrum
Highly sensitive surface	Strong surface sensitivity to adsorbed species

Non-linear resistance and optical coefficients	Non-linearity of textured ZnO can be employed in varistors and optical non-linearity in integrated non-linear optical applications
High thermal conductivity	Appropriate for device application
Bulk single crystals available	Epitaxial growth of high quality thin-films with reduced extended defects (stress/strain) is possible
Chemical and mechanical stability	Allows for wet chemical etching which is extensively used in fabrication process, and it has a Mohs hardness of 4
Radiation hardness	Excellent radiation hardness makes ZnO useful for space applications
Abundant and cheap	ZnO is found at 132 ppm in the earth's crust

Table1. Summary of properties of ZnO (Matthias Batzill) (Janotti, et al., 2009).

1.3.2 Metal-oxide Semiconductors Applications

Metal-oxide semiconductors have been extensively studied and used for gas sensing devices, and the current trend of miniaturization drives the research for smaller, more sensitive, and more power efficient gas sensors. Due to their wide range of detection species and selective sensitivities, solid state sensors are preferred over other options. These sensors cover a broad spectrum of materials including carbon monoxide, carbon dioxide, methane, methanol, ethanol, propane, hydrogen, hydrogen sulfide, ammonia, nitrogen monoxide, nitrogen dioxide, oxygen, ozone, oxides of sulfur, acetone, dimethylamine, petrol, liquid petroleum gas, trimethylamine, smoke, and humidity. The choice of the active layer, i.e. the metal-oxide layer, depends on several parameters which include operating temperatures and target gases.

Metal-oxides that have been used in gas sensors include the oxides of aluminum, bismuth, cadmium, cerium, chromium, cobalt, copper, gallium, indium, iron, manganese, molybdenum, nickel, niobium, ruthenium, tantalum, tin, titanium, tungsten, vanadium, zinc, and zirconium; mixed or multi component metal oxides are also employed in gas sensors (G.Eranna).

Moreover, employing metal-oxide semiconductors in the form of field effect devices makes it possible to achieve higher sensitivities at lower temperatures. Lowering the operating temperature reduces the power consumption of the device which is extremely important for wireless sensor networks (F. V. Farmakis, 2008). Moreover, gas sensors can be used in

hazardous regions with explosive gases where elevated temperatures are dangerous[†], it also reduces the expensive and complicated circuitry needed for temperature control(Isolde Simon).

1.3.3 ZnO Applications

The applications are derived from the properties discussed earlier. For example, high exciton binding energy has made zinc oxide ideal for low threshold lasing devices. Similarly, its 3.37 eV band-gap which lies in the UV region of the electromagnetic spectrum creates an ideal material for photovoltaic applications. Zinc oxide has applications in light emitting diodes, transparent contacts, ferromagnetic semiconductors, short wavelength optoelectronics, various nano sensors[‡], nano actuators, MEMS cantilevers, ultra violet LEDs, and laser diodes(Ü. Özgür, 2005). It has also applications in various gas sensors(X. Cheng), UV sensors(Junya Suehiro), secure communications, and mass storage devices (M. Rusop). Aside from its conventional applications, several futuristic applications for zinc oxide have been reported; some novel applications of ZnO with enormous market demands are quantum computers and high capacity storage devices.

Among all the materials mentioned earlier, ZnO based devices show sensitivity to various targets, chemical stability, along with no toxicity and low cost. Moreover, low temperature growth techniques enable us to grow high quality ZnO on virtually all types of substrates. Finally, ZnO growth can be integrated with silicon process for mass production (S. Christoulakis, 2006). Zinc oxide has been used in ethanol, Dimethyl methylphosphonate (DMMP), hydrogen, nitrogen dioxide, ammonia, carbon monoxide, carbon dioxide, chlorine, gasoline, sulfur dioxide, liquefied petroleum gas (LPG), oxygen ,ozone, and many more gas sensors.

1.3.4 Future Applications

Aside from conventional applications of metal-oxide semiconductors, there have been some reports on future applications of such materials. I will conclude this section by brushing over two interesting, yet relevant, ideas: digital audio and video disks and drivers using UV laser, and spintronic applications.

1.3.4.1 Digital Audio and Video Disks and Drivers

Since the introduction of portable storage devices, there has been an evolution towards more compact yet higher capacity devices. Currently blue ray seems to be the ultimate storage device for multimedia applications like music, movies, and gaming software. If we compare compact

[†] On the other hand, it has been also reported that metal-oxide semiconductors can be used in high temperature hostile industrial environments(M.F. Al-Kuhaili, 2008).

[‡] Biological, chemical, thermal, mass, pressure, and force sensors.

discs, digital versatile discs (DVDs), and blue ray discs, we can see that the trick to increase the capacity is to decrease the laser's beam spot size(October 2006). UV laser has an even smaller wavelength and, thus, smaller beam spot which leads to higher information density.

1.3.4.2Spintronic Devices

Doping of transition metals such as Cu, Mn or Co can lead to a ferromagnetic phase transition near room temperature in ZnO (R. Triboulet, 47 (2003) 65-138). This shows the potential application of zinc oxide in spintronic devices like quantum computers(R. Triboulet, 47 (2003) 65-138).

1.4 Growth Techniques

Various growth techniques including magnetron sputtering, chemical vapor deposition, RF magnetron sputtering, molecular beam epitaxy, pulse laser deposition, metal organic chemical vapor deposition, and halide vapor phase epitaxy have been reported (Ü. Özgür, 2005). But the most popular techniques are sputtering, MBE, PLD, and MOCVD (R. Triboulet, 47 (2003) 65-138).

Among all the growth techniques, pulsed laser deposition (PLD) is the most attractive one because of its unique features:

- Low growth temperature, 200 ^{o}C to 800 ^{o}C
- Fast growth rate, 0.033 nm/pulse to 0.066 nm/pulse
- Simple technique
- Low cost

Various flavors of PLD have also been reported. For instance, to grow ZnO layers, UV assisted PLD, radical assisted PLD, electron cyclotron resonance assisted PLD, and nano or femtosecond PLD techniques have been employed. PLD is the best choice to grow high quality zinc oxide layers at low temperatures. Chemical vapor deposition, spray pyrolysis, reactive evaporation, and DC/RF sputtering require high temperatures which might not be compatible with fabrication process(F. V. Farmakis, 2008). Furthermore, PLD is considered an easy method which is widely used in laboratories and research facilities. This technique will be discussed in more details later in this work.

Chapter Two: ZnO Growth and Challenges

It is shown that among group II-VI semiconductors ZnSe, ZnO, ZnS, CdSe, and CdS are n-type. CdTe is the only compound with amphoterical properties and ZnTe appears to be p-type (R. Krause-Rehberg, 1998). Even though the difficulties of ambipolar doping for group II-VI elements, and generally for wide band-gap compound semiconductors, is not fully understood yet, internal and external defects as well as compensating complexes are considered the primary source of the issue(R. Krause-Rehberg, 1998). In this chapter, the growth challenges and their theoretical explanations are presented in details.

2.1 Growth Challenges

To fully utilize the potentials of a semiconductor in device fabrication, we should have both polarities available, i.e. n and p-type materials are necessary for most device applications, but a repeatable and reliable p-type growth technique for ZnO is not developed yet. Currently, most ZnO based devices use heterojunction structures due to the growth difficulties of p-type zinc oxide. Since GaN and ZnO have several similarities in their crystal structure, lattice constants, and band-gaps (Dae-Kue Hwang, 2005) most of the heterojunctions are ZnO-GaN junctions. However, lattice mismatches and thermal coefficients' inconsistency affect the efficiency of the device. Introduction of interface states and dislocations creates undesired electrical properties; thus, a homojunction device is more efficient. Moreover, the fabrication process would be simplified greatly if we can have both n and p-type films available.

2.2 Possible Explanations

Growth difficulty of metal-oxides including group II-VI semiconductors is attributed to several compensating mechanisms including(Desnica):

- Native defects
- Ambipolar behavior of dopants
- Lattice relaxation around dopants
- Low solubility of dopants
- Lattice softness of the group II-VI semiconductors

2.2.1 Native Defects

Native defects in ZnO are zinc and oxygen vacancies, interstitials, and antisites. These defects and more specifically V_O, Zn_i, and Zn_O are generally considered as the source of shallow donors and compensating centers for acceptors. Various techniques including local density approximation (LDA) and generalized gradient approximation (GGA) in conjunction with density functional theory (DFT) have been employed to study the formation energies and

electrical structure of these defects (Oba, et al., 2011). The results, however, depend on the approximation schema and model parameters used in the method.

2.2.1.1 Oxygen Vacancy, V_O

V_O can be found in three charge states of neutral, single charged and doubly charged defects. However, thermodynamically, only the neutral and doubly charged states are stable. More importantly, the formation energy of this defect is the lowest among all native point defects. It is worth noting that the formation energy of defects depends on the Fermi level, and as the concentrations of electrons and holes change the formation energies of native defects change as well. Figure 1 shows the formation energy of V_O as a function of the Fermi level at oxygen poor (left) and oxygen rich (right) growth conditions. Note that the slopes of the lines show the charge state of the defect(Oba, et al., 2011).

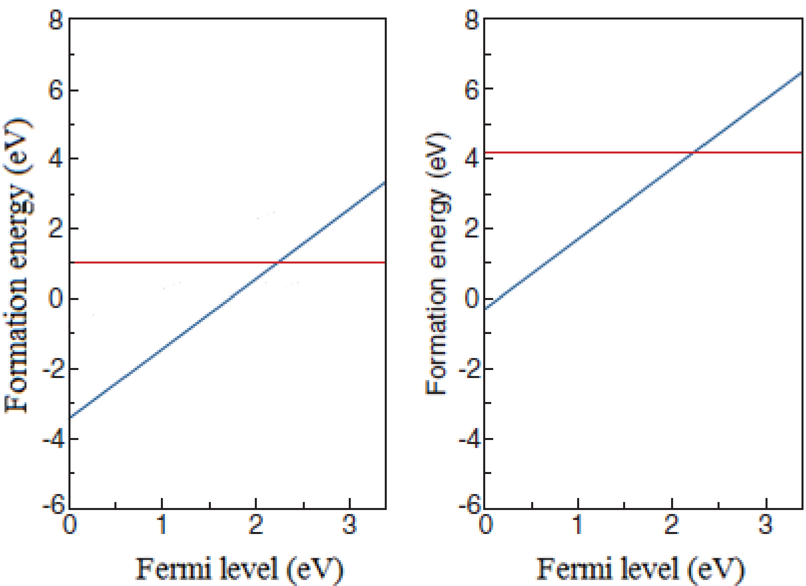

Figure 1. Formation energy of oxygen vacancy as a function of the Fermi level for oxygen poor (left) and oxygen rich (right) growth conditions(Oba, et al., 2011).

From figure 1, it is obvious that at low Fermi levels, i.e. p-type material, the formation energy of V_O^{++} is close to zero for O-rich growth condition. For the other extreme growth condition, i.e. O-poor situation, it is even negative. This shows that oxygen vacancies are already formed at high concentrations and act as compensating centers which hammer p-type growth efforts(Oba, et al., 2011).

As mentioned before, V_O^{++} has the lowest formation energy among all the native defects for the most positions of the Fermi level, and figure 2 shows the formation energy of oxygen vacancies with respect to the other defects as a function of the Fermi level.

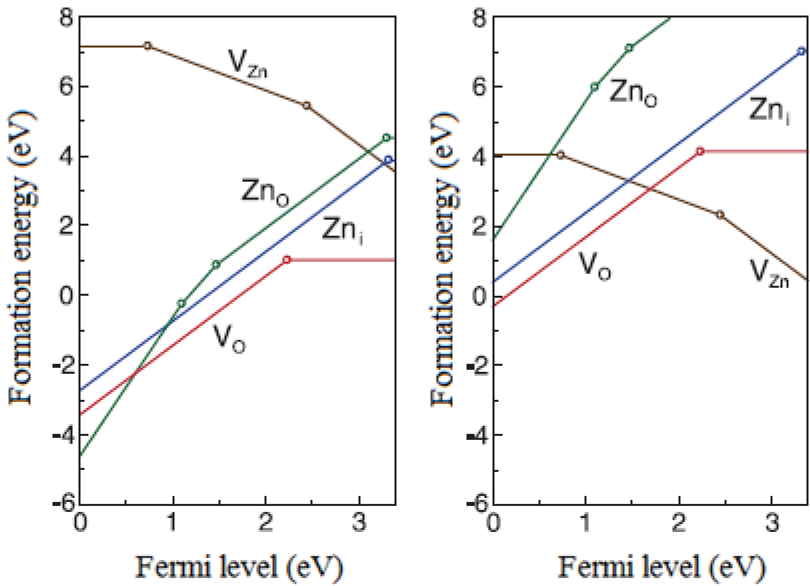

Figure 2. Formation energy of oxygen vacancy along with other native defects in ZnO as a function of the Fermi level for oxygen poor (left) and oxygen rich (right) growth conditions. The circles show the transition points between different charged states (Oba, et al., 2011).

2.2.1.2 Zinc Vacancy, V_{Zn}

V_{Zn} is an acceptor-like defect with two charge states of V_{Zn}^{-} and V_{Zn}^{-2} as shown in figure 2. The formation energy of this defect is generally higher than native donor-like defects especially under O-poor growth conditions. Therefore, V_{Zn} is a deep acceptor which is not a significant source of holes under various growth conditions (Oba, et al., 2011).

2.2.1.3 Oxygen and Zinc Interstitial, O_i and Zn_i

Zn_i is a shallow donor and its formation energy is low, especially for p-type conditions. For low Fermi levels, as seen in figure 2, Zn_i^{+2} forms at high concentrations which compensate holes. Zn_i has two stable charged states of Zn_i^{+2} and Zn_i^{+} which the thermodynamic transition point is very close to the conduction band minimum. This means that at high Fermi positions, not only the formation energy is high, but also the charge contribution of this defect is minimal. Under this condition, no significant concentration of Zn_i is expected(Oba, et al., 2011).

On the other hand, O_i occurs in different configurations, but regardless of its structure and crystallographic position, the charged state has high formation energy. Oxygen interstitial with low formation energy is the neutral state across the whole Fermi positions; thus, they are not that much of an interest to study.

2.2.1.4 Oxygen and Zinc Antisites, O_{Zn} and Zn_O

O_{Zn} has a high formation energy; even higher than O_i, so we are not interested in this defect. Zn_O, on the other hand, has low formation energy especially at low Fermi positions. This defect has four charged states of Zn_O^{+}, Zn_O^{+2}, Zn_O^{+3}, and Zn_O^{+4}. The relative formation energy of this defect along with its variations along the Fermi level can be observed in figure 2. This defect is not a major electron source for n-type material, but it is present in high concentration for p-type material and compensates holes(Oba, et al., 2011).

As mentioned before, the calculations of defects' properties are carried out by different methods and the results can vary for different approximations and different conditions. For example, using the first principles pseudo potential calculations, the formation energies of intrinsic defects for nitrogen doped ZnO have been calculated (Eun-Cheol Lee). As before, it is shown that depending on the growth ambient various defects form and affect the electric characteristics of the grown film. Figure 3 shows the calculated formation energy for various defects in nitrogen doped ZnO. The high formation energy of O_{Zn} and the relative positions of O_i defects discussed before can be seen in figure 3.

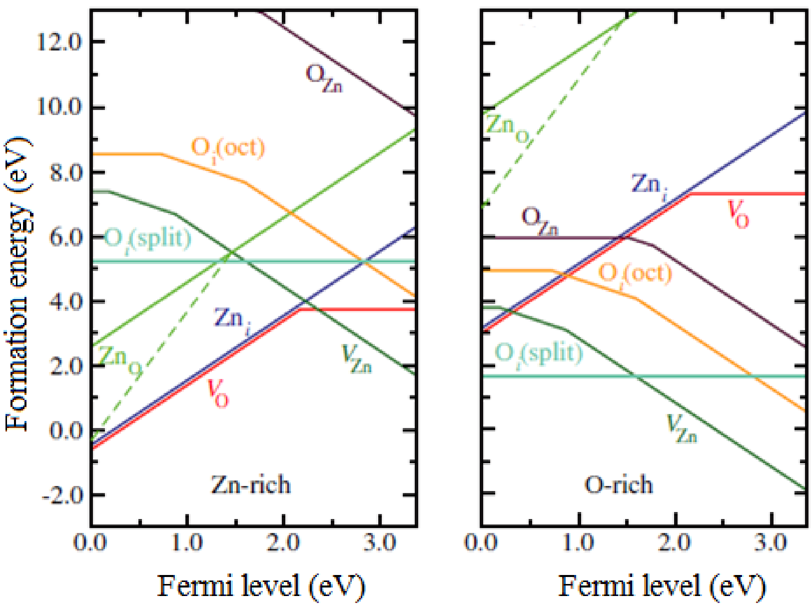

Figure 3. The formation energy of various intrinsic defects in ZnO over the working Fermi energy levels. Two ambient conditions are shown; zinc rich (left), and oxygen rich (right) condition (Eun-Cheol Lee).

2.2.2 Hydrogen Contamination

It was shown recently that hydrogen has a peculiar behavior in ZnO semiconductor which should be considered for p-type growth. In almost all semiconductors hydrogen incorporates as either H^{+} or H^{-} depending on the majority carriers. For p-type semiconductors with holes as the majority carriers, hydrogen acts as a donor and incorporates as H^{+}; it donates an electron to form the ion. For n-type materials, on the other hand, it behaves as an acceptor and fits in as H^{-}.

Therefore, hydrogen always counteracts with the majority carriers, but in ZnO hydrogen always shows up as a donor(Janotti, et al., 2009)(Van de Walle).

First principle calculations have shown that only interstitial and substitutive H^+ are thermodynamically stable with low formation energies (Janotti, et al., 2009). Interstitial hydrogen, H_i^+, occurs at the bond-center site parallel to the terminating plane of ZnO crystal structure, or at the antibonding site perpendicular to the terminating plane. In both cases, hydrogen binds to an oxygen atom to create a strong O—H bond. Lattice relaxations of 40% and 11% of the bond length occur around H_i^+ for the bond-center and the antibonding sites, respectively(Janotti, et al., 2009). Hydrogen can also substitute oxygen, H_O, in ZnO structure to form equal bondings with its four nearest neighbor zinc atoms(Janotti, et al., 2009). Figure 4 shows the schematic representation of hydrogen incorporation in ZnO crystal structure.

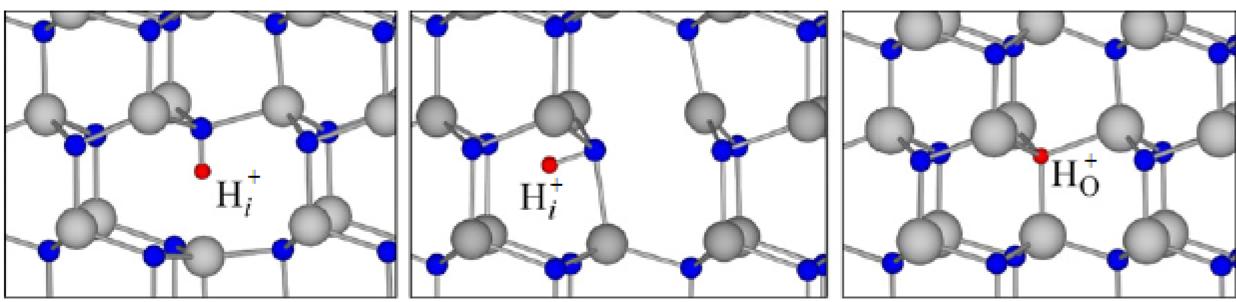

Figure 4. Schematic representation of hydrogen incorporation in ZnO crystal at the interstitial bond-center site (left), the interstitial antibonding site (center), and the substitutional oxygen site (right) (Janotti, et al., 2009).

For the two interstitial states an electron can bind to the H_i^+ in an extended state and acts as a shallow donor. Oxygen substitutive site is a shallow donor too and occurs only as H_O^+. Since, hydrogen is an always present contamination in any growth process, growth atmosphere is extremely important(Janotti, et al., 2009) (Van de Walle). As mentioned before H_i and H_O have low formation energies which translate to high concentrations. Figure 5 shows the formation energy of the two species along with the oxygen vacancy defect which is the dominant intrinsic defect in ZnO structure. The slope of the lines represents the stable charge state of the defect (Janotti, et al., 2009).

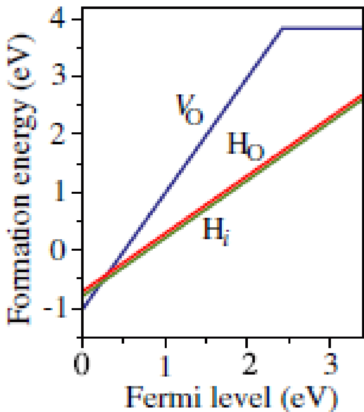

Figure 5. Formation energy of hydrogen related defects along with oxygen vacancy as a function of the Fermi level. Hydrogen defects are stable at +1 charge state and oxygen vacancy is stable as a neutral or doubly charge defect (Janotti, et al., 2009).

Other calculations based on DFT density functional theory within the local density approximation (Van de Walle) have shown similar properties for hydrogen-related defects. Figure 6 shows the formation energy of interstitial hydrogen in ZnO as a function of the Fermi level. Again, the slope of the line shows the stable charge state of the defect.

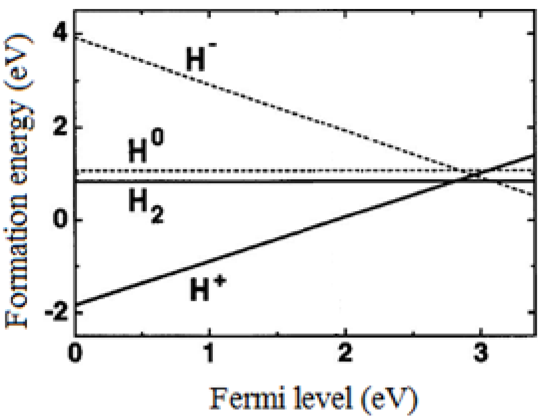

Figure 6. Formation energies of interstitial hydrogen in ZnO as a function of the Fermi level (Van de Walle).

Therefore, there are a lot of donor-like and acceptor-like intrinsic defects that affect the electrical properties of the films. These defects are usually at high concentrations and a survey of the literature shows that as grown undoped intrinsic ZnO films are nominally n-type with high free electron concentrations in the order of 10^{18}—10^{20} cm^{-3} range which results in severe problems for extrinsic doping to overcome such high levels of intrinsic defect concentrations. Indeed

extrinsic doping with single dopants as well as co-doping result in not stable and controllable doping sufficient for device work.

2.3 Extrinsic doping of ZnO thin films

To overcome the compensating mechanisms and grow p-type ZnO, doping and co-doping of ZnO have been employed.

2.3.1 Extrinsic Single Dopants

Among various acceptor dopants including Li, Na, K, Cu, N_2, P, As and Sb only a few are considered as potential candidates for p-type doping(Janotti, et al., 2009). Formation of interstitial compensating centers, low solubility of the dopants, and introduction of deep acceptor levels have made only N_2, arsenic, and antimony as the candidates for acceptor dopants. Even though N_2 introduces shallow acceptor level and is considered as the best candidate for p-type growth, it does not easily incorporate in ZnO crystal, and even atomic nitrogen resulting from plasma cannot create p-type conductivity(R. Triboulet). Post growth treatment, and specially annealing, is necessary to activate the acceptor dopants(Janotti, et al., 2009)(R. Triboulet).

Phosphorous doped ZnO shows n-type conductivity since P introduces deep acceptor levels which cannot overcome the intrinsic concentration of electrons and therefore it is not a good candidate for p-type doping. Arsenic and antimony, on the other hand, proved to be good acceptors for ZnO; however, special treatments are required (Janotti, et al., 2009) (R. Triboulet).

2.3.2 Extrinsic Co-doping

The idea of co-doping is to agitate the holes, or to populate desired carriers. One of the problems with p-type doping is that high hole concentration shows low Hall mobility, and any attempt to increase the mobility, lowers the carrier concentration. Co-doping was suggested to have a balance on high concentration of holes with high mobility. In this method, both donor and acceptor atoms are doped to achieve the desired characteristics. Doping with acceptors and donors at the same time may seem to be a redundant task, but in fact the compensation helps p-type growth by moving the Fermi level away from the valance band maximum to increase the formation energy of native donor-like defects, and at the same time, the solubility of the acceptor is increased. The introduced donor will reside in the grown ZnO and if it does not bound strongly, it can be removed by out diffusion(Janotti, et al., 2009)(R. Triboulet). For example, H_2 doped along with N_2, or N_2 along with Ga, improves the solubility of the acceptors to provide p-type ZnO (Janotti, et al., 2009).

2.3.3 Growth of Undoped Intrinsic ZnO thin films

Since extrinsic doping results in unstable and uncontrollable p-type conductivity, it is important to understand the effects of the aforementioned intrinsic defects on the electrical conductivity of the films through the development of growth protocols and optimization of growth conditions including laser's pulse energy, pulse frequency, growth base vacuum pressure, oxygen overpressure, substrate choice, growth temperature and the target. In this work, growth parameters are optimized to obtain high quality material. Moreover, ZnO growth dynamic is manipulated to obtain p-type conductivity in thin films grown on Si substrates.

Table 1, below, summarizes growth parameters and their effects on the PLD technique.

Growth Parameter	Effects on Growth
Laser Pulse Energy	High energy introduces chaotic plume pattern which leads to non uniform and low quality films. Very low energy does not provide enough plume fluence for deposition
Laser Pulse Frequency	High frequency does not allow particle to follow the crystal pattern and introduces dislocations in the films. Very low frequency increases the risk of contaminations and defects
Base Vacuum Pressure	The better the vacuum, the longer the mean-free-path of plume particles and less collision
Precursors' Partial Pressures	High pressures introduce particle collisions and lower the quality of the films. A minimum pressure is required to provide the crystal with enough resources to grow
Substrate's Choice	Various substrates introduce stress or strain to the grown films due to crystal mismatches. N and p-type (100) Si substrates show different electrical behavior due to their morphological and electrical surface differences
PLD Target	PLD grown films follow the stoichiometry of PLD target, and it is important to have a high quality target

Table 1. PLD growth parameters and their effects.

Chapter Three: PLD Growth

PLD technique has several advantages over other growth methods which allow for high quality growth of ZnO thin films. Moreover, it is a relatively straight forward technique, and it has been employed by many research groups. The details of our PLD system are discussed in this chapter.

3.1 PLD Parameters

PLD has been used primarily because of its high quality outputs, simplicity of use, and promising results for fabrication of ambipolar metal oxides(R. Triboulet, 2003). Aside from sample preparation, sample placement, and the standard operational procedure, PLD can be divided into four steps(R. Triboulet, 2003):

- Laser-matter interaction
- Plume[§] ejection and propagation
- Ambient gas interaction
- Film growth on the substrate

Growth parameters are then simply all the variables that affect the steps above. Major growth parameters are the substrate temperature, growth pressure and choice of the substrate. There are, however, other parameters including laser power, laser frequency, and target-substrate distance. The target-substrate distance is pretty much fixed by our device. We can change this distance by dismantling the sample holder and re-assemble it in a different position; however, changing the laser power is more practical. It is worth noticing that there is a relationship between the laser power, P, and the target-sample distance, d, which states that any change in distance can be compensated by a change in power. In other words, by keeping the distance constant, growth optimization can be done by changing the laser power(R. Triboulet, 2003). Experimentally, laser specifications are optimized to produce an energetic plume with enough time for particles to settle on the substrate(Krishnamoorthy, 2007).

High energy pulses create energetic particles which might re-sputter the substrate and effectively lower the film quality. On the other hand, very weak pulses cannot ablate the target. Similarly, very low and very high frequency pulses adversely affect the grown layer. Throughout this work laser pulse energy level of 200~250 mJ with 10 Hz pulses have been employed.

Once laser parameters are optimized, growth pressure is the most important parameter which affects films' quality and their electrical properties. Oxygen is needed for the growth, and the quality and the stoichiometry of the films depend on the oxygen pressure. Lack of ambient oxygen leads to off stoichiometric and poorly crystallized ZnO films. It has been studied that the

[§] Plume is defined as the jet of supersonic particles ejecting from PLD target(Morkoç, et al., 2009).

oxygen present in the metal oxide film is mainly provided by the ambient gas and the target material only contributes 1% of the oxygen. Therefore, low oxygen growth leads to oxygen vacancies and stimulating the n-type conductivity. An increase in the oxygen pressure increases the collisions of the plume energetic particles with gas molecules(R. Triboulet, 2003). This may improve the film quality by decreasing the defects, but it can have adverse effects too. Thus, there is a growth window for the oxygen pressure which assures high quality film deposition.

Alternatively, there is a three-step view of PLD mechanism. In this model PLD process is divided to three domains of target conduction, target evaporation, and high temperature plume expansion(Zhang, et al., 2001). Similarly, PLD parameters are all parameters affecting each of these three domains. Since the two models are merely two views of the same process, the parameters are the same as before.

3.2 PLD System

Our PLD system employs krypton fluoride (KrF) excimer laser which runs at 248 nm (near UV) with 25 ns pulse duration. Other lasers including ArF running at 193 nm, Nd:YAG running at 355 nm, and Cu-vapor laser running at 510-578 nm are also used for ZnO PLD growth(Morkoç, et al., 2009). A high voltage power source charges internal capacitors of the system which then discharge up to 24 kV across the laser tube. The radiation from the excited gas is amplified inside the tube and finally beams out of the semi-reflective laser window of our Lambda-Physik LASERTECHNIK LPX-200 laser system.

The laser passes through a clipping shutter and a converging lens to form an approximately 1×4 mm spot on the target as it's shown in figure 2 and figure 3. Since ceramic targets produce higher quality films(Wei, et al., 2009), we have employed a high purity (99.99%) ZnO ceramic PLD target purchased from MTI[**] Corporation. Material analysis of the sputtering target shows high purity ZnO with typical contaminations.

The growth is carried out inside a stainless steel growth chamber shown in figure 1. The details of the growth chamber, figure 1 (left), are as the followings:

1. **Incident laser beam** escapes the laser system and travels to the deposition chamber.
2. **The optics** which includes a shutter and a converging lens focus the incident laser on the PLD target. The shutter is applied to reduce laser diffraction. The out coming laser has a rectangular shape which then creates a distorted laser spot on the target; applying the shutter reduces this distortion which in turn improves the uniformity and the quality of the grown films. Figure 2 shows the schematics of the laser profiles at different positions in our PLD systems, and figure 3 shows the experimental laser profiles at the same points.

[**] www.mtixtl.com

3. Focused laser enters the deposition chamber through this **quartz laser port**.
4. Glass **view ports** around the chamber allow for growth observation.
5. PLD target is attached to a controlled **target holder**. The holder rotates the target so the laser does not strike the same point.
6. Samples are attached to a **temperature controlled holder** inside the deposition chamber.
7. Laser ablates the PLD target to create the **laser plume** which consists of high temperature and high energy particle.

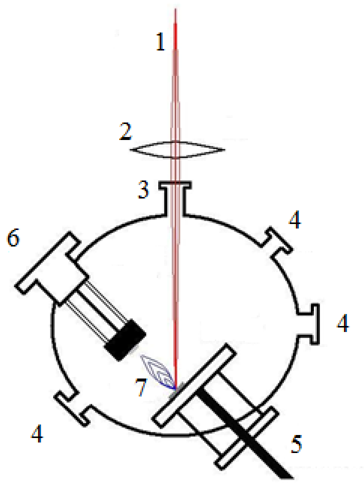

Figure 1. PLD deposition chamber. Left is the schematic of the chamber showing various parts: 1 is the incident laser beam, 2 is the optics, 3 is the laser port, 4s are the glass view ports, 5 is the controlled target holder, 6 is the controlled sample holder, and 7 is the ejected plume from the PLD target. Right is the top view of the actual growth chamber.

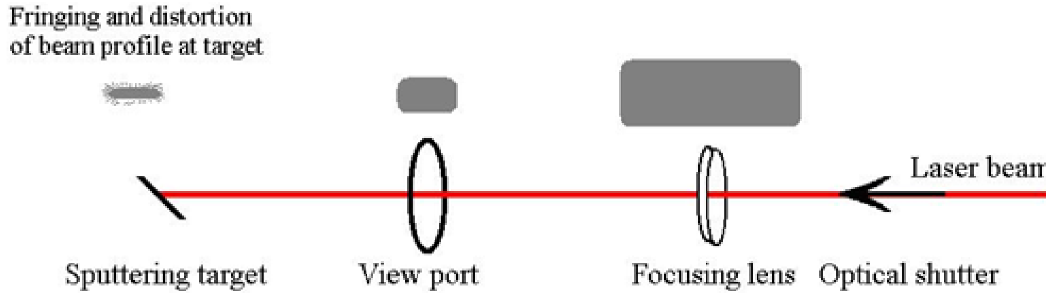

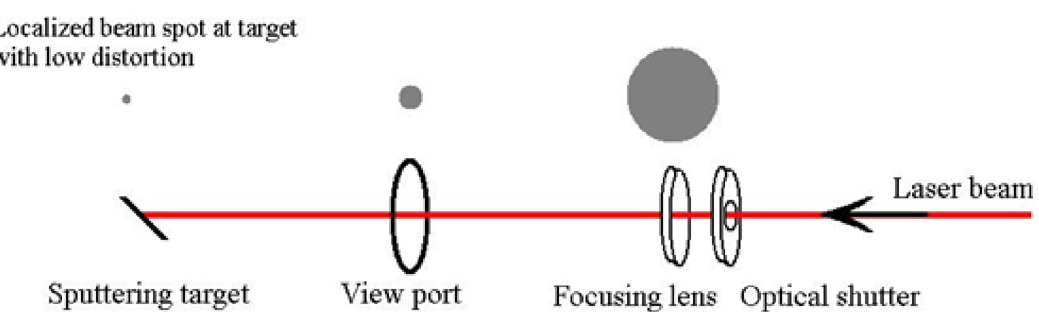

Figure 2. Schematics of laser profile at different positions in our PLD system.

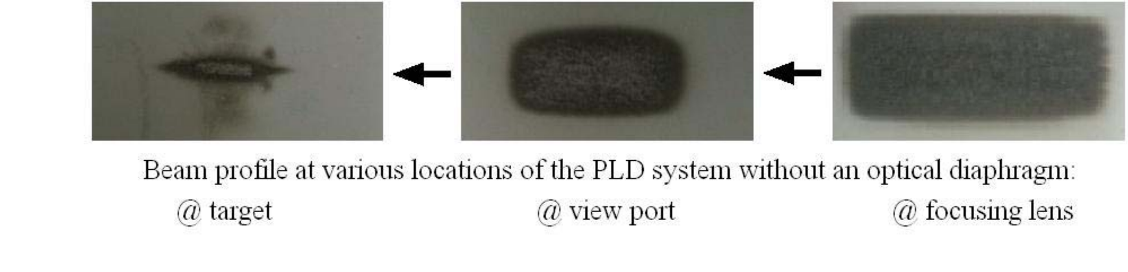

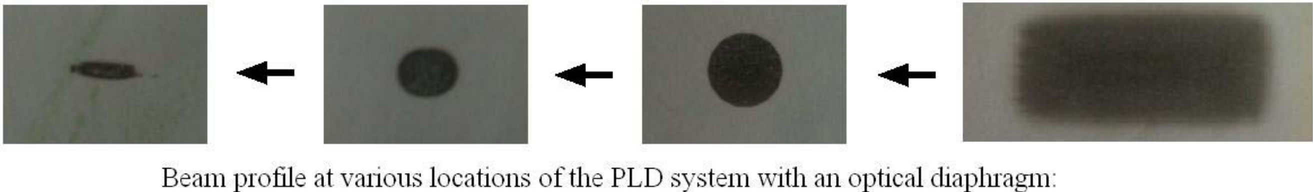

Figure 3. Experimental laser profiles at different positions in our PLD systems. Laser profile at the PLD target becomes more uniform and confined with the optical diaphragm.

As we will discuss it later in the results chapter, laser optimizations and optical treatments significantly improved the quality of the grown films. The uniformity of the grown layers, for example, is an issue with PLD growth, and it takes a lot of careful alignments and optimizations to grow a relatively large uniform film. Figure 4 shows two of our PLD grown samples; left is one of our early samples grown without the clipping shutter. The colorful rings of ZnO on the sample clearly show the non-uniformity of the grown layer. On the other hand, figure 4 right shows a more uniform sample grown after all the optimizations are carried out. The effects of the laser parameters, optical treatments, and proper alignments are observed.

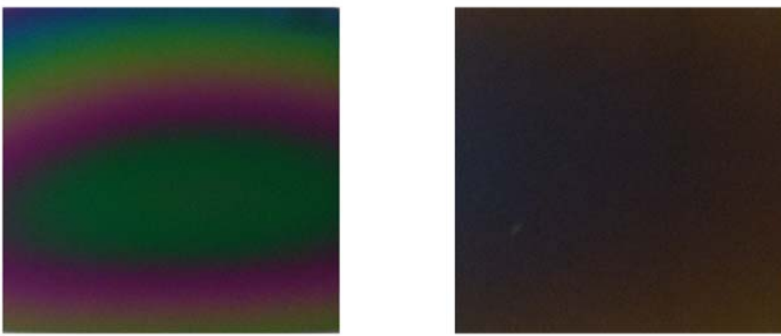

Figure 4. PLD grown ZnO films on Si substrates. The non-uniform nature of PLD growth (left) is significantly improved by appropriate optical treatment and laser optimization (right).

The non-uniform nature of PLD is due to the fact that the ejected plume from the target has a spherical or elliptical evolving pattern, and the flat surface of the sample cuts through these equipotential surfaces; thus the plume hits the sample at different distances and various energies. Figure 5 shows the schematic of the ejected plume with the equipotential surfaces along with the actual plume inside the growth chamber.

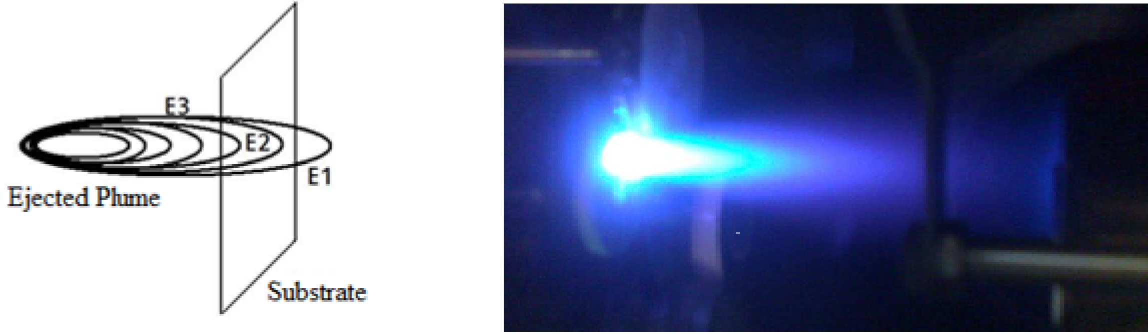

Figure 5. Schematic of equipotential surfaces of PLD plume evolving pattern (left). The actual PLD plume inside the growth chamber (right).

3.2.1 PLD Dynamics

The dynamics of the laser ejected plume and calculation of the vapor/plume materials are not trivial. Various models and different techniques have been proposed for modeling the plume dynamics of the laser ablated targets(Zhang, et al., 2001)(Wen, et al., 2007)(Shan, et al., 2007). However, the details of the laser-material interactions and the effects of background pressure and laser specifications on the energy of the plume particles are still not clearly understood. Therefore, despite its simple setup and straight-forward operation, PLD is a quite complex method in terms of the details of the plume kinetics and growth dynamics. Several interactions between laser, target, plume, and substrate occur in the process which are broadly discussed and modeled and sometimes ignored. For instance, the interaction of the incident laser beam and the background gas molecules are generally ignored. Figure 7 indicates each interaction by number in the PLD(Wen, et al., 2007) process. The interactions are as the followings:

1. The incoming incident beam interacts with the background gas molecules, and the gas pressure affects the laser beam by reducing its energy. Depending on type of background gas, its temperature and overpressure the energy of the laser at the target is affected. The energy of the laser transferred to the ambient gas, O_2 in our case, is inversely proportional to the atomic mass of the background gas, and it is directly proportional to the O_2 pressure.

2. Once the laser hits the target, its energy is transferred to the surface atoms on the target material increasing lattice vibrations substantially within a very short period of time to result in breaking the bonds and ablating the target atoms. More specifically, energy is transferred from laser photons to the target's lattice in a few tens of picoseconds time interval. Typical lattice temperatures reach several thousand—to a few tens of thousands, degrees locally (Shan, et al., 2007). It is worth noting that not all of the laser's energy is transferred to the target. In fact, reflection from target reduces laser penetration flux and wastes some energy(Zhang, et al., 2001).

If the laser energy is high enough, the evaporation which is not desired due to deposition of macroscopic particles and droplets is reduced and ablation occurs. It is shown that the surface temperature of the target increases logarithmically with the increase of the laser intensity, but the ablation rate of the target increases linearly due to thermal losses, heat diffusion, and laser reflection(Zhang, et al., 2001).

3. The ejected plume then travels towards the sample holder and interacts with the background gas as well as the incident laser. The interaction of the ejected plume and the incident laser is negligible since the pulse duration and the plum's absorption coefficient for KrF laser are both small.

4. For plume-O_2 interaction, increasing the pressure increases the collisions between plume particles and gas molecules and leads to a decrease in the energy of the particles arriving at the sample surface. For example, the velocity of the ejected particles can reach up to 23000 ms^{-1} at

high vacuum levels while at atmospheric pressures it is reported as slow as 2000 to 8000 ms^{-1}(Shan, et al., 2007).

5. Once the particles arrive at the surface of the sample, they stick to the surface and they have limited mobility to find an appropriate site and initiate the growth of the thin-film, or they can re-evaporate from the surface depending on growth temperature and plume energy. If they have high enough energy they can even sputter the substrate. The energy of the particles on the surface of the substrate increases with the growth temperature and we have shown that too low and too high growth temperatures degrade the quality of the grown films(Esmaili Sardari, et al., 2010). Low growth temperatures reduce surface mobility of the arriving species failing to find appropriate lattice sites for incorporation and high growth temperatures favor the re-evaporation of the arriving species.

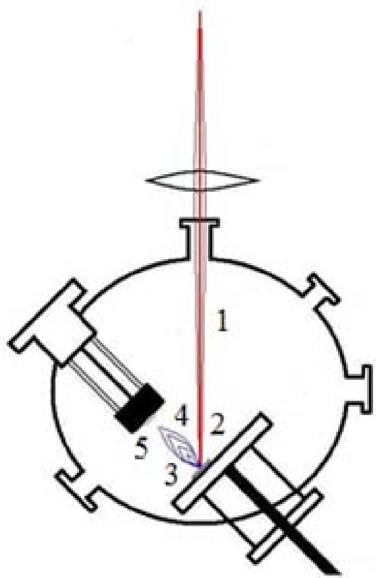

Figure 6. Various interactions in PLD growth technique. 1 is laser-gas interaction, 2 is laser-matter interaction, 3 is laser-plume interaction, 4 is plume-gas interaction, and 5 is plume-matter interaction.

3.2.2 Energy of the Particles

The energy of the particles arriving at the surface of the substrate is a function of the laser energy, pulse duration, growth pressure which is a combination of background vacuum pressure and oxygen overpressure, distance of the sample to the target and the target material. We can define this energy as the following:

$$E_a = f_m(E_l, \tau_P, P_g, d) \qquad \text{eq.1}$$

Where

E_a is the energy of the arriving particles at the surface
E_l is the laser energy
τ_P is the pulse duration
P_g is the growth pressure
d is the target-substrate distance
f_m is the material dependent function

On the other hand, the energy of the particles on the surface of the substrate is a function of the energy of the arriving particles E_a and the growth temperature (the substrate's temperature). We can define this energy as the following:

$$E_s = f(E_a, T) \qquad \text{eq.2}$$

Where
E_s is the energy of the particles on the surface of the substrate
E_a is the energy of the arriving particles at the surface
T is the growth temperature

So:

$$E_s = f_m(E_l, \tau_P, P_g, d, T) \qquad \text{eq.3}$$

Calculation of the energy of the plume particles, therefore, depends on several parameters where their contributions are not fully known or modeled; however, the effecting parameters are expressed by eq.3, and their contributions are discussed previously. If we assume ideal gas dynamics for the laser plume, then its energy can be evaluated by the average energy of an ideal gas at temperature T by the following:

$$E_k = \frac{3}{2} k_B T \qquad \text{eq.4}$$

Where
k_B is the Boltzmann's constant of 1.38×10^{-23} JK^{-1}

In the working temperature range of 473 to 673K the average energy of the plume using the ideal gas model is in the order of 10^4-10^5 $Jmol^{-1}$ ($k_B T.N_A$). The actual temperature and the number of molecules in the plume is of extreme complexity where one can solve several thermodynamic differential equations with given initial and boundary conditions to obtain a more precise temperature and molecular density functions. This initial and boundary conditions are as the followings:

- The molecular density of the plume particles is zero before the ablation
- The temperature of the target and the growth chamber are at room temperature before the ablation
- The temperature of the sample which faces the ablation target is fixed at a high growth temperature

- All laser parameters which effectively change the molecular number density of the particles and the growth temperatures including the chamber's body and sample's temperature remain constant throughout the whole process

We ignore the very details of f_m in this work, but the effects of the above parameters and overall behavior of f_m is studied.
Finally, because of the beam reflection from the surface of the target, laser penetration flux into the sputtering target is reduced. Laser penetration flux is expressed by the following equation(Zhang, et al., 2001):

$$Q = (1- R)\, Q_s\, e^{-k[z - s(r,t)]} \qquad \text{eq. 5}$$

Where

Q is the penetration flux
R is the reflection coefficient of the target
Q_s is the laser flux at the surface of the target
s(r,t) is the surface equation as a function of time and position

The ablation rate is proportional to the vapor pressure at the surface of the target, target material density, target surface temperature, and mass of the evaporating molecules (Zhang, et al., 2001). The evaporating particles, i.e. the plume, escape the target with a high perpendicular directional preference as shown in figure 8. In other words, the plume propagates in a forward direction normal to the surface of the target, and regardless of the incident angle, the ejected plume creates a cone shaped distribution; a $\cos\theta$ forward distribution dependence where θ is measured from the normal direction(Singh, et al., 1990).

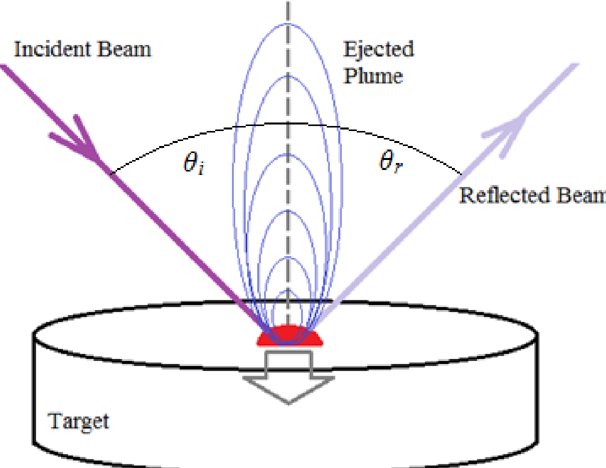

Figure 7. Regardless of the incident angle θ_i which is the same as the reflection angle θ_r, the ejected plume is traveling forward with high directional preference perpendicular to the target.

The two most important growth parameters determining the energy of the particles on the surface of the substrate and ultimately growth kinetics are growth temperature and growth oxygen pressure. As discussed before, there is an optimum growth temperature window which allows for the growth process. Similarly, for the oxygen overpressure there is an optimum pressure window which ensures ample oxygen atoms for high quality growth of ZnO.

The oxygen required for the growth is mainly provided by the ambient oxygen overpressure and a small fraction is supplied by the PLD target. Therefore, oxygen is required for high quality growth of ZnO thin film. However, too high pressure reduces the energy of the particles due to increased laser-gas and plume-gas interactions which adversely affect the quality of the film. The optimum growth pressure of 10^{-5}-10^{-4} Torr is systematically derived based on our experimental results.

3.3 Sample Preparation for Growth and Fabrication

Si substrates are cleaned prior to each growth. First, substrates are cleaned off of particulate debris and greasy contaminations by a three-stage methanol-acetone-methanol process for 15 minutes. In this process, samples are bathed orderly in methanol, acetone, and methanol for 5 minutes at each step. Samples are washed off with deionized water (DIW) between the steps. Second, oxide layer is etched by 10% diluted hydrofluoric acid (BHF) or buffered oxide etchant (BOE) for 3 minutes. The samples are then washed off by DIW and blow dried by N2.

After the growth, samples are patterned and etched using conventional photolithography process.

Chapter Four: Equipments and Measurements

4.1 Measurements

4.1.1 X-ray Photoelectron Spectroscopy, XPS

XPS is used to examine surface materials as well as their concentrations. In this technique, the samples are irradiated with X-rays which ionize the atoms. The ionized atoms release core level photoelectrons that are collected by the instrument's detector to create the emission intensity vs. electron binding energy spectrum. Each element has a unique set of binding energies which can be used to identify the material. Moreover, the emission intensity is used to evaluate the concentration of the elemental constituents. XPS is a surface study technique, because the kinetic energy of the escaping photoelectrons limits the depth of this technique to a few nanometers. A high sensitivity Kratos AXIS 165 spectrometer has been employed for XPS analysis. This high performance spectrometer has the following key features:

- "165 mm radius hemispherical analyzer and eight channeltron detection system for excellent energy resolution and sensitivity for small areas
- Magnetic immersion lens for superior sensitivity for small area analysis and imaging
- Charge neutralization system for insulating samples
- Variable temperature sample stage (150-750 K) for temperature controlled measurements
- Capable of XPS imaging and multipoint spectroscopy
- Depth profiling with argon ion bombardment
- Automated sample stage and XYZ manipulator for angle resolved measurements
- Two x-ray sources: Monochromatic Al and Dual anode (Mg/Al)
- Fully computer controlled system with windows based Vision software"[††]

4.1.2 X-ray Diffraction Spectroscopy, XRD

Similar to XPS, XRD technique employs X-rays for crystallographic study of the grown films. X-rays are irradiated to a horizontally placed sample at different incident angles θ. The reflections are detected by a general area diffraction detector system (GADDS) to form the reflection intensity vs. 2θ angles spectrum. According to the Bragg's law, the reflection peaks are detected at specific angles for a known material which in turn defines the crystal structure of the material. For instance, comparing the resulted spectrum with the reference values of the XRD peaks for ZnO defines the crystal structure of ZnO. Moreover, the peak positions are used to calculate crystal parameters and the stress on the films if there are any deviations from bulk reference values(Pecharsky, et al., 2009). For XRD measurements, we have used the Bruker C2 Discover Powder Diffractometer. The specifications of the device are as the followings:

- "CuK_α sealed X-ray tube with Göbbel mirror
- HiStar (GADDS) detector for real-time data collection, 2D diffractometry and quality patterns from small samples

[††] http://www.chem.umd.edu

- Parallel beam geometry to probe small areas or regular or irregularly shaped sample
- XYZ stage for combinatorial screening; it also allows measuring samples of practically any size
- Video microscope with laser alignment for precise sample positioning
- Hot stage providing high temperature up to 900 ^{o}C”[‡‡]

4.1.3 X-ray Powder Diffraction Spectroscopy, XRD

The diffraction pattern of our PLD target was derived by a D8 Advance powder diffraction system with LynxEye and SolX detectors. The specifications of the device are as the followings:

- “Choice of MoKα, CuKα or even single wavelength CuKβ radiation
- SolX and LynxEye (insert) detectors for fast and/or high resolution measurements
- 9 positions sample changer
- ICDD powder diffraction database and search/match software
- Advanced TOPAS software for structure refinement”

4.1.4 Photo Luminescence Electron Spectroscopy, PL

Optical properties of the grown films are studied by room temperature photoluminescence (PL) electron spectroscopy. In this technique a monochromic light source irradiates the sample and excites the electrons. Excited electrons then return to the ground state through radiative and non-radiative paths. Most importantly band-to-band transitions (CB to VB), excitonic emissions, and radiative trap assisted transitions are detected and recorded by the device’s detector. Since the signals are fairly weak, a photon multiplier tube (PMT) with variable voltage control is used for signal amplification.

PL measurements are performed with a Cary 50 Eclipse Fluorescence Spectrometer from Varian Inc. Some of the features—that are relevant to our work, include:

- Wavelength sweep for the excitations beam; this is particularly used to distinguish between material related peaks or real peaks and invalid noise peaks which shift by changing the excitation wavelength.
- Multiple internal filters both for excitation and emission; we use this feature to narrow down the wide bandwidth of the nominal[§§] excitation, and filter out the noise in the emission.
- Variable slut widths for excitation and emission windows
- Variable photomultiplier tube, PMT, voltage to increase the resolution.

[‡‡] http://www.chem.umd.edu

[§§] Even though the emission wavelength can be fixed to a specific value, the Xenon flash lamp which is the light source in this machine has a wide bandwidth which should be filtered.

4.1.5 Electrical Measurements

Electrical measurements including the characteristic study of the devices, I-V studies, as well as the Hall Effect measurements are performed by an Ecopia® Hall Effect Measurement System, HMS-5000 with fixed magneto flux density of 0.53-0.57 Tesla. The magnetic flux is set to 0.55 T, but the air gap difference makes it different for each system. In our experimental setup, the magnetic flux is 0.51 T. The injected current can be controlled between 1 nA to 20 mA. The system allows for variable temperature readings from 77K to 350K.

Chapter Five: Structural Evaluation Results of the ZnO Films

5.1 XPS Results

Full spectrum XRD pattern of our ZnO thin films is shown in figure 1 where the peaks are observed at 10, 89, 139, 241, 264, 284, 328, 352, 430, 530, 742, 1021, and 1044 eV for Zn3d, Zn3p, Zn3s, Auger Zn LMM, Auger Zn LMM, C1s, Auger Zn LMM, Auger Zn LMM, Auger Zn LMM, O1s in ZnO, Auger O KLL, $Zn2p_{3/2}$, and $Zn2p_{1/2}$, respectively.

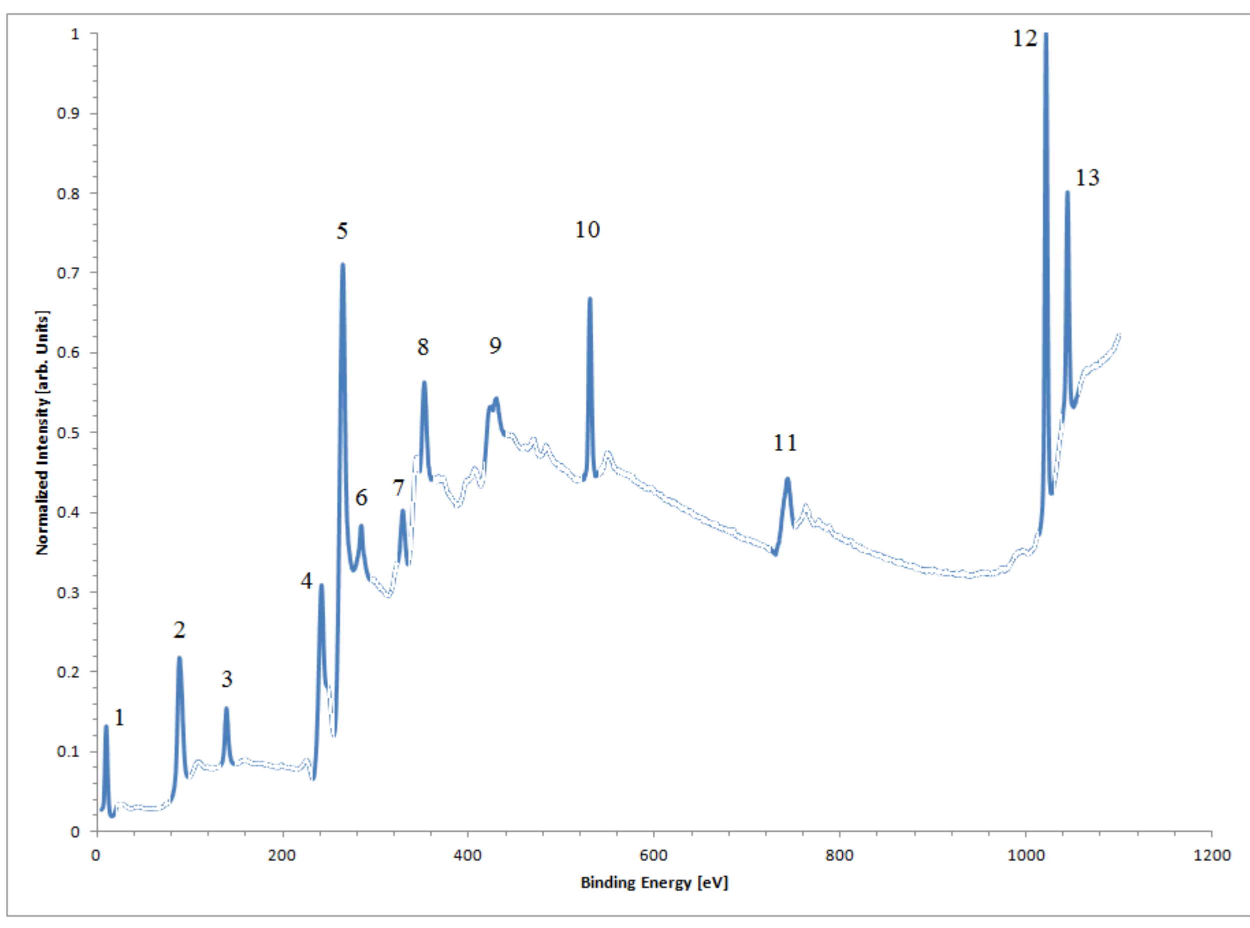

Figure 1. Full spectrum normalized intensity vs. binding energy plot for ZnO thin films. The peaks are as the followings: 1. Zn3d, 2. Zn3p, 3. Zn3s, 4. Auger Zn LMM, 5. Auger Zn LMM, 6. C1s, 7. Auger Zn LMM, 8. Auger Zn LMM, 9. Auger Zn LMM, 10. O1s in ZnO, 11. Auger O KLL, 12. $Zn2p_{3/2}$, 13. $Zn2p_{1/2}$.

Using the NIST's X-ray photoelectron spectroscopy database*** we confirmed that all of our samples show the formation of ZnO with differences in the intensity of the peaks, i.e. the zinc-to-oxygen (Zn/O) ratio or the stoichiometry of the films.

5.1.1 Stoichiometric Deviations of the Films

The stoichiometry of ZnO thin films are calculated from our XPS results using the normalized O1 s and $Zn2P_{3/2}$ peaks with C1s peak.

In other words, the observed intensity of O1s and $Zn2P_{3/2}$ XPS peaks for various devices are normalized to C1s peak, and the results are presented in the followings.

5.1.1.1High Oxygen Overpressure Growth

ZnO/p-Si Device

Figure 2 shows the normalized intensity of O1s peak versus the binding energy for ZnO/p-Si device grown at high oxygen overpressure. The peak is observed at 530.63 eV.

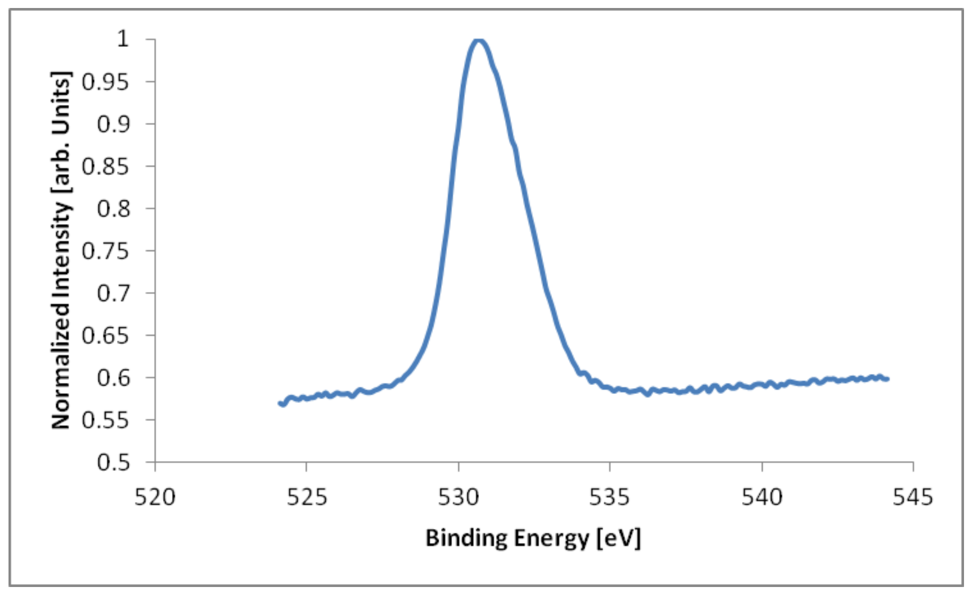

Figure 2. Normalized intensity of O1s peak vs. binding energy for ZnO/p-Si device grown at high oxygen overpressure. O1s peak is observed at 530.63 eV.

Figure 3 shows the normalized intensity of $Zn2p_{3/2}$ peak versus the binding energy for ZnO/p-Si device grown at high oxygen overpressure. The peak is observed at 1021.63 eV.

*** http://srdata.nist.gov/xps/Default.aspx

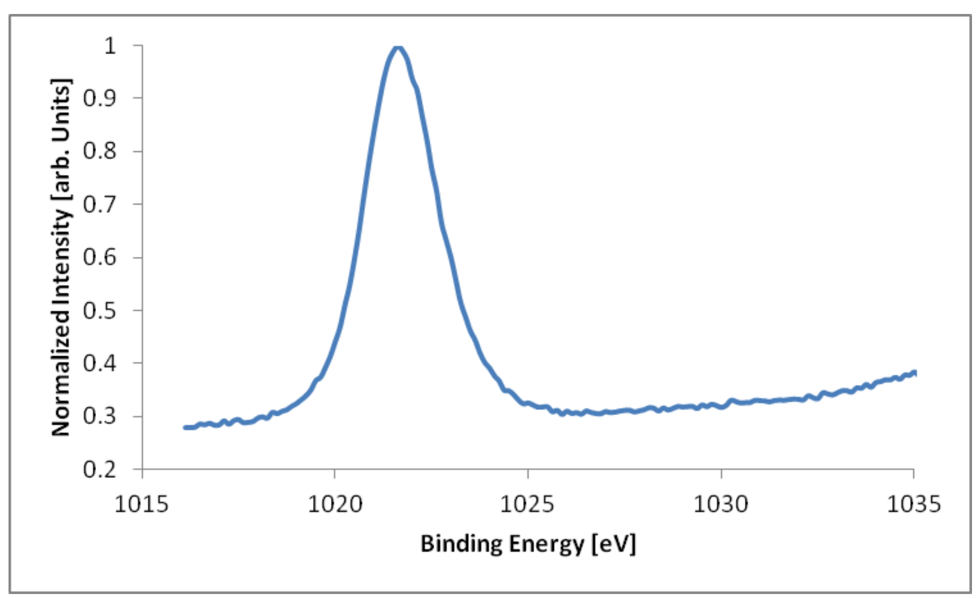

Figure 3. Normalized intensity of $Zn2p_{3/2}$ peak vs. binding energy for ZnO/p-Si device grown at high oxygen overpressure. $Zn2p_{3/2}$ peak is observed at 1021.63 eV.

For this device, the calculated Zn/O ratio is 1.85.

ZnO/n-Si Device

Figure 4 shows the normalized intensity of O1s peak versus the binding energy for ZnO/n-Si device grown at high oxygen overpressure. The peak is observed at 530.70 eV.

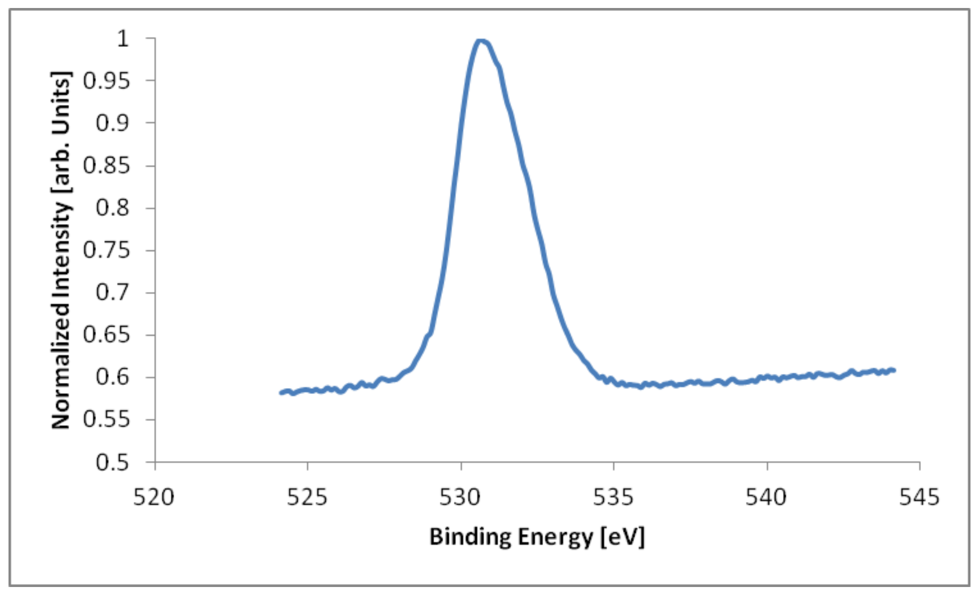

Figure 4. Normalized intensity of O1s peak vs. binding energy for ZnO/n-Si device grown at high oxygen overpressure. O1s peak is observed at 530.70 eV.

Figure 5 shows the normalized intensity of $Zn2p_{3/2}$ peak versus the binding energy for ZnO/n-Si device grown at high oxygen overpressure. The peak is observed at 1021.83 eV.

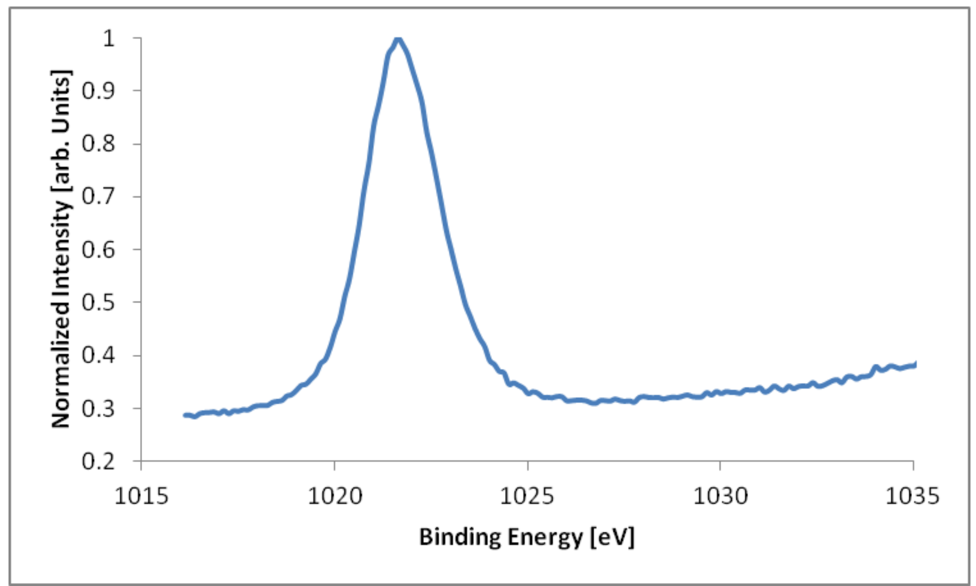

Figure 5. Normalized intensity of $Zn2p_{3/2}$ peak vs. binding energy for ZnO/n-Si device grown at high oxygen overpressure. $Zn2p_{3/2}$ peak is observed at 1021.83 eV.

For this device, the calculated Zn/O ratio is 1.83

5.1.1.2 Low Oxygen Overpressure Growth

ZnO/p-Si Device

Figure 6 shows the normalized intensity of O1s peak versus the binding energy for ZnO/p-Si device grown at low oxygen overpressure. The peak is observed at 530.89 eV.

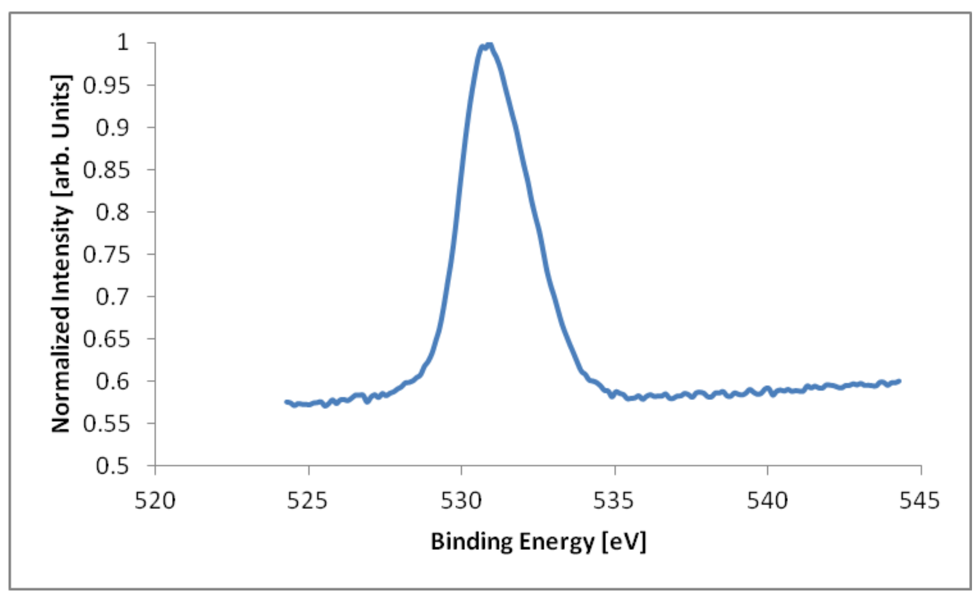

Figure 6. Normalized intensity of O1s peak vs. binding energy for ZnO/p-Si device grown at low oxygen overpressure. O1s peak is observed at 530.89 eV.

Figure 7 shows the normalized intensity of $Zn2p_{3/2}$ peak versus the binding energy for ZnO/p-Si device grown at low oxygen overpressure. The peak is observed at 1021.65 eV.

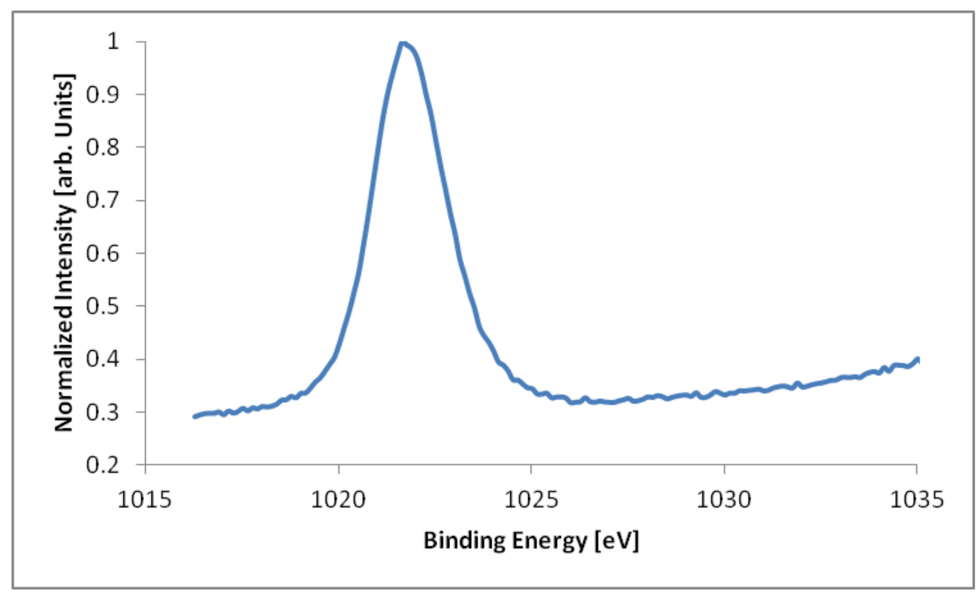

Figure 7. Normalized intensity of $Zn2p_{3/2}$ peak vs. binding energy for ZnO/p-Si device grown at low oxygen overpressure. $Zn2p_{3/2}$ peak is observed at 1021.65 eV.

For this device, the calculated Zn/O ratio is 1.72.

ZnO/n-Si Device

Figure 8 shows the normalized intensity of O1s peak versus the binding energy for ZnO/n-Si device grown at low oxygen overpressure. The peak is observed at 530.85 eV.

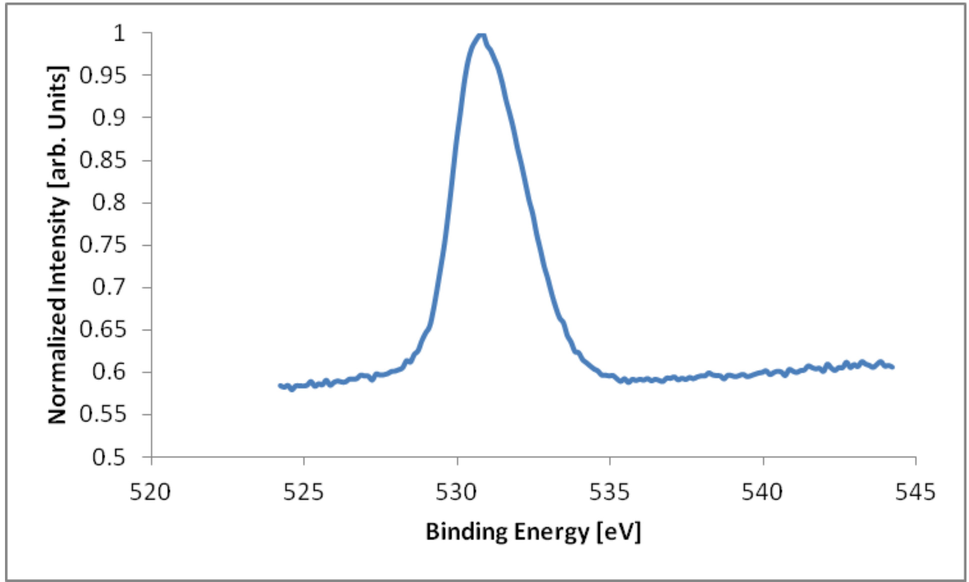

Figure 8. Normalized intensity of O1s peak vs. binding energy for ZnO/n-Si device grown at low oxygen overpressure. O1s peak is observed at 530.85 eV.

Figure 9 shows the normalized intensity of $Zn2p_{3/2}$ peak versus the binding energy for ZnO/n-Si device grown at low oxygen overpressure. The peak is observed at 1021.72 eV.

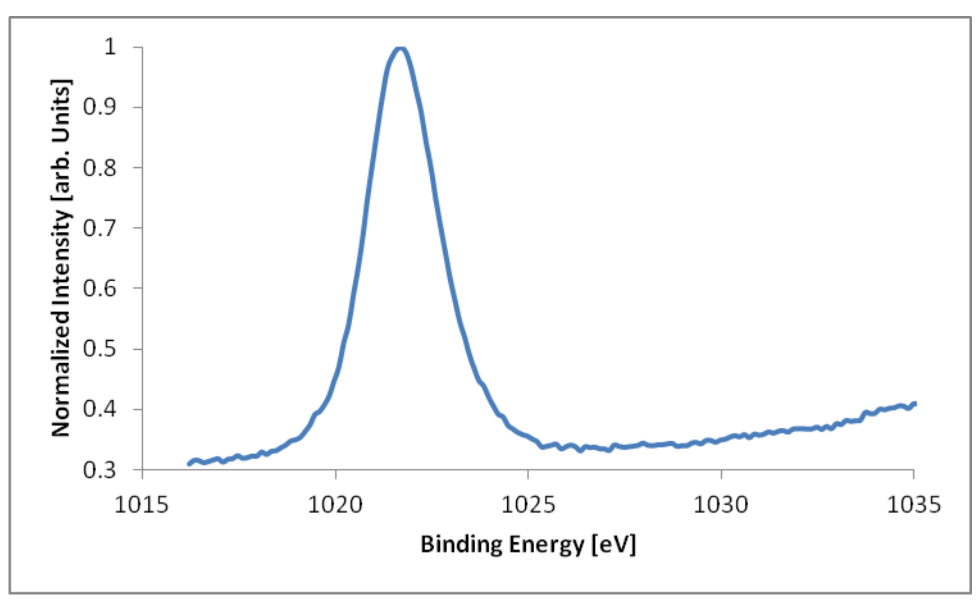

Figure 9. Normalized intensity of $Zn2p_{3/2}$ peak vs. binding energy for ZnO/n-Si device grown at low oxygen overpressure. $Zn2p_{3/2}$ peak is observed at 1021.72 eV.

For this device, the calculated Zn/O ratio is 1.66.

$Zn2p_{1/2}$ Peak

In addition to $Zn2p_{3/2}$ peak, we also observed the $Zn2p_{1/2}$ for all samples at ~1044 eV. Figure 10 shows the XPS spectrum of the two Zn peaks.

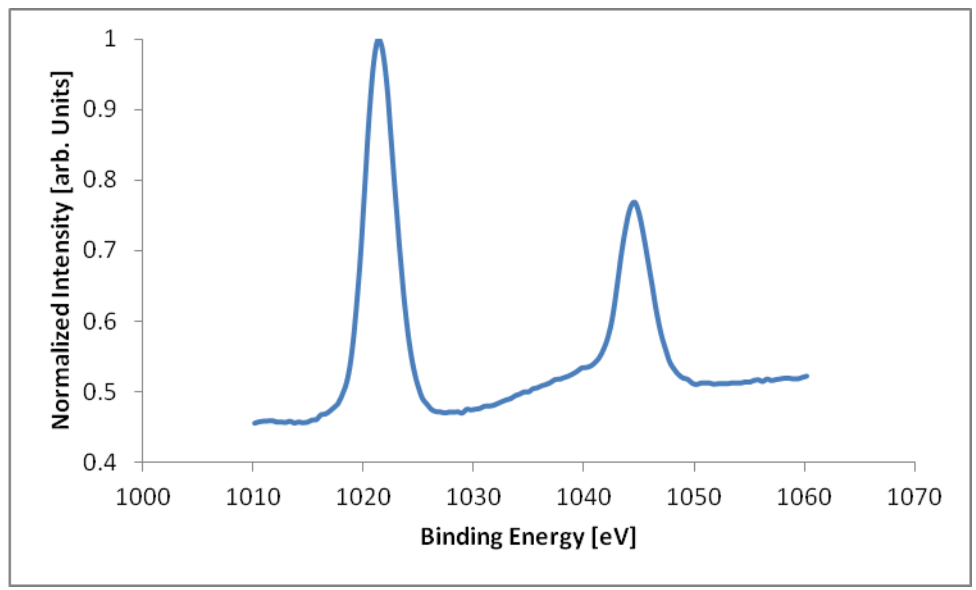

Figure 10. Typical normalized intensity of $Zn2P_{3/2}$ and $Zn2p_{1/2}$ peaks vs. binding energy observed for our devices.

Our results are in perfect agreement with the reference values of 1021.4, 1044, and 529.4 eV for $Zn2p_{3/2}$, $Zn2p_{1/2}$, and O1s binding energy peaks for ZnO crystal lattice, respectively (Karamat, et al., 2010)(Saravanakumar, et al., 2011). The slight shifts to higher energies can be attributed to the surface species such as H_2O and CO_2 due to air contamination(Saravanakumar, et al., 2011). The observation of O1s peak at higher energies than 530 eV (for ZnO/SiO_2) suggests no significant oxide layer formation at the interface; this result along with the 2-D General Area Diffraction Detector System (GADDS) frames implies the lack of any significant oxide layer, except the native oxide, at the interface.

5.2 XRD Results

The structural characteristics of the films were studied by a Cu Kα XRD system. The details of the Bruker C2 Discover XRD with HiStar general area diffraction detector system (GADDS) are presented in the equipment chapter. In this section, we have used the results for crystallographic analysis of our samples.

5.2.1 GADDS Frames

The observed diffraction patterns in the two-dimensional GADDS frames show highly aligned textured structure for our ZnO thin films. It has been shown that the diffraction patterns of single crystal structures appear as singular points (diffraction spot) while for textured structures, the diffractions appear as lines or line segments (for well-aligned structure)(Pecharsky, et al., 2009)(West, 1999).

Figure 11 shows the typical diffraction pattern of our ZnO thin films. The bright line segments in this figure correspond to the diffraction peaks (2θ angles), and the confinement of the diffraction patterns to line-segments show the high in-plane alignment of our ZnO textured domains.

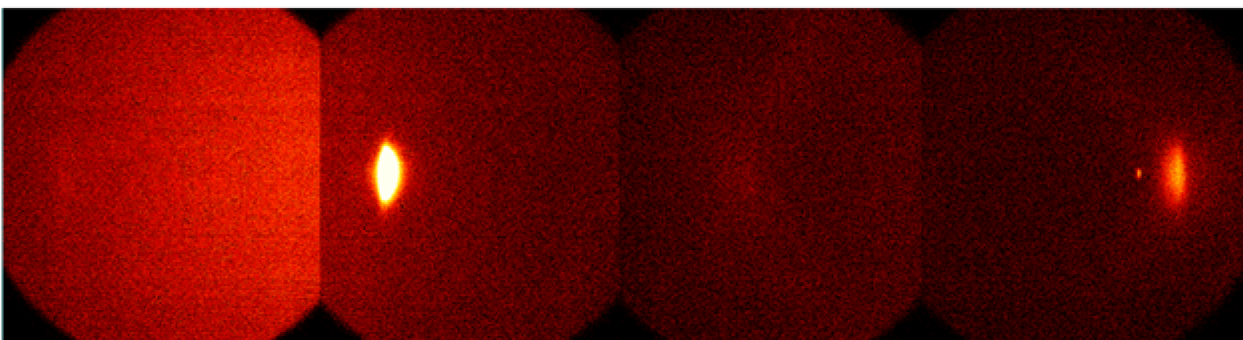

Figure 11. Two-dimensional GADDS frames showing the whole diffraction range of $\theta=8^o$ to $\theta=45^o$. The confinement of the diffraction patterns to line segments show the high alignment of ZnO textured structure.

5.2.1.1 The Effects of Oxide Layer

The XRD frames also confirm the lack of significant oxide layer at the Si-ZnO interface for all of our samples. To observe the difference, we grew ZnO thin films on oxide removed Si and Si/SiO_2 substrates. The comparison of the XRD frames show that films grown on substrates without an oxide layer have more diffraction confinement which confirms the higher alignment. Figure 12 compares the GADDS frames for the two films; one grown on an oxide removed Si substrate and the other is grown on a substrate with a 60 nm thermally grown oxide layer. It is evident that the oxide layer distorts the alignment of ZnO textured domains.

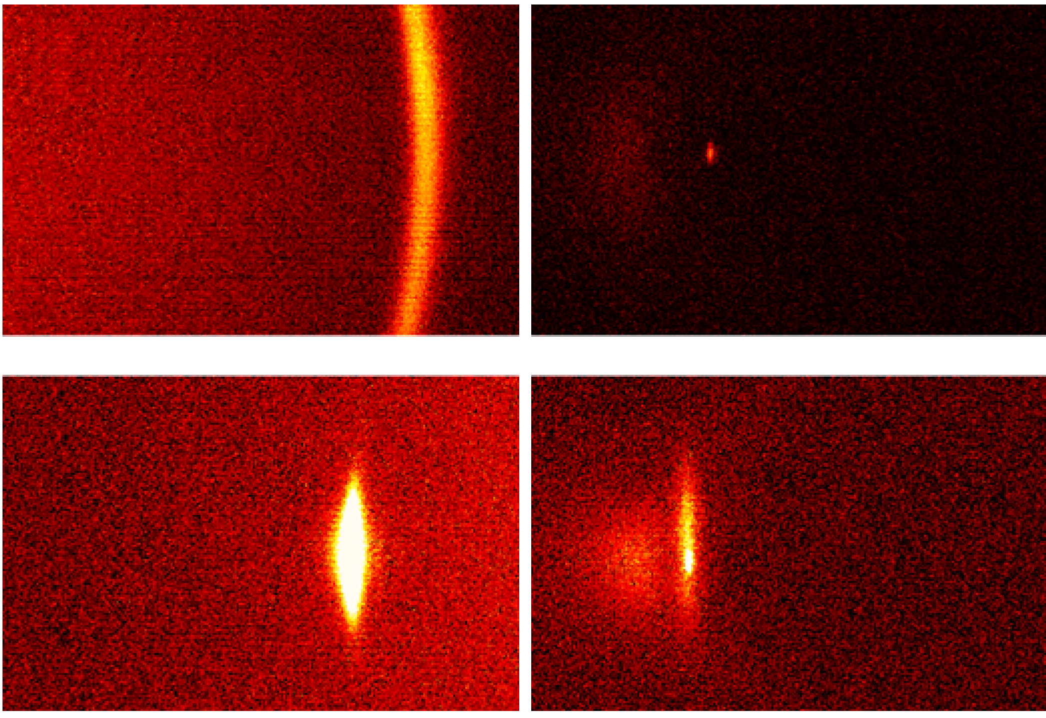

Figure 12. GADDS frames for two samples grown on Si (bottom) and Si/SiO_2 (top) substrates. ZnO's (0002) peaks (left) and (0004) peaks (right) are shown. The confinement of the reflection pattern for ZnO/Si sample suggests a perfectly aligned textured structure for the grown layer. On the other hand, the extended reflection pattern for the film grown on Si/SiO_2 substrate indicates the textured structure of the ZnO film with random alignment. The diffused spot to the left of the (0004) diffraction is due to background diffraction from the Si substrate.

5.2.1.2 The Effects of Growth Conditions

Growth conditions including growth temperature and oxygen overpressure also affect the collected GADDS data. While the effects of the growth temperature are studied later in this chapter, our results show that increasing oxygen overpressure improves the alignment as shown in figure 3. Three samples were prepared at three oxygen overpressures of 2.0×10^{-6}, 6.5×10^{-6}, and 1.0×10^{-4} Torr. Our results show that the film grown at the lowest oxygen overpressure has

the least confined XRD pattern which shows the minimum alignment of ZnO domains. Increasing the oxygen pressure improves the quality of the grown layer and reduces the diffraction line. Figure 13 shows the GADDS frames of (0002) ZnO peak for the three samples.

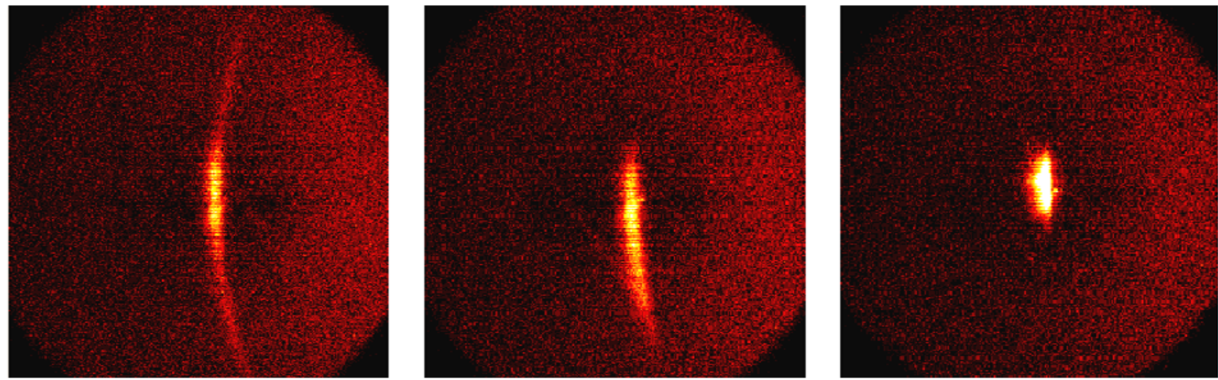

Figure 13. GADDS frames of (0002) ZnO peaks for samples grown at 2.0×10^{-6} (left), 6.5×10^{-6} (middle) and 1.0×10^{-4} Torr (right) oxygen overpressures. It is evident that the confinement of the diffraction pattern is increased as the oxygen pressure increases.

5.2.2 GADDS Frames and XRD Plots

The XRD plot is derived based on the GADDS data. Figure 14 and figure 15 show the relation between the XRD plots and the GADDS frames. Figure 15 shows the (0002) ZnO peak detected at 34.05^{o}, and figure 16 shows the (0004) ZnO peak detected at 71.7^{o} along with the substrate's fuzzy diffraction.

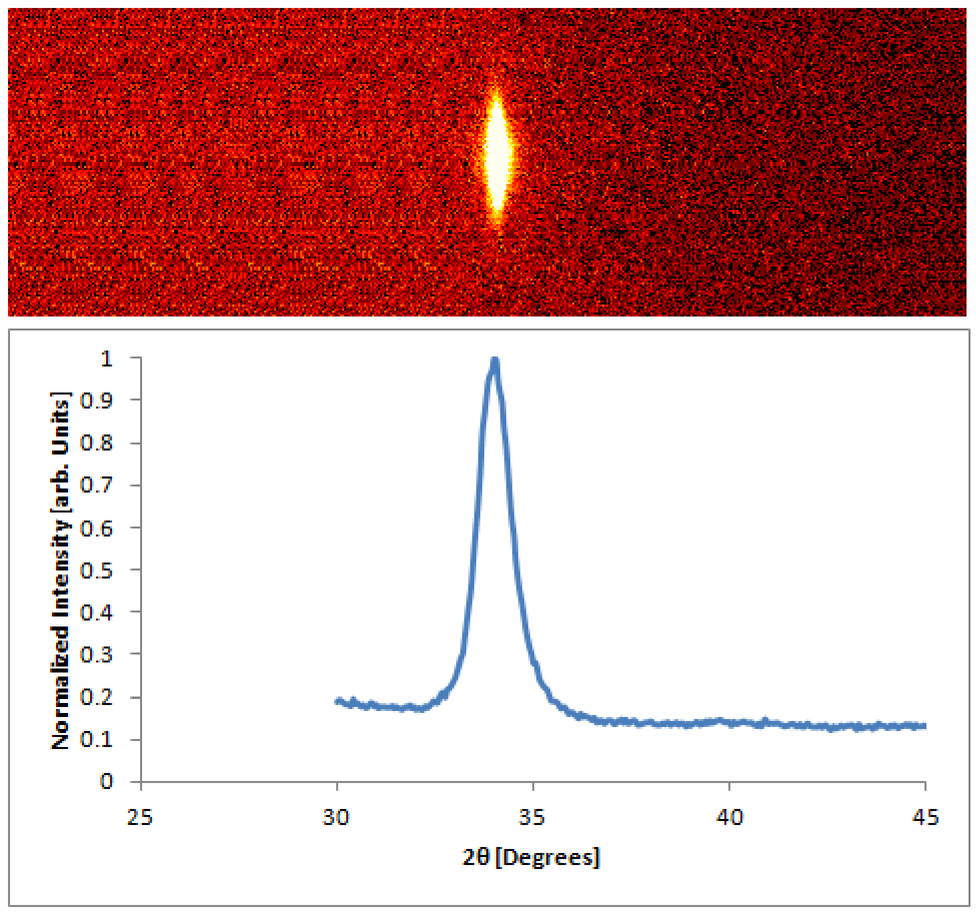

Figure 14. The bright region in the GADDS frame (top) corresponds to the (0002) ZnO peak at 34.05° in the XRD plot (bottom).

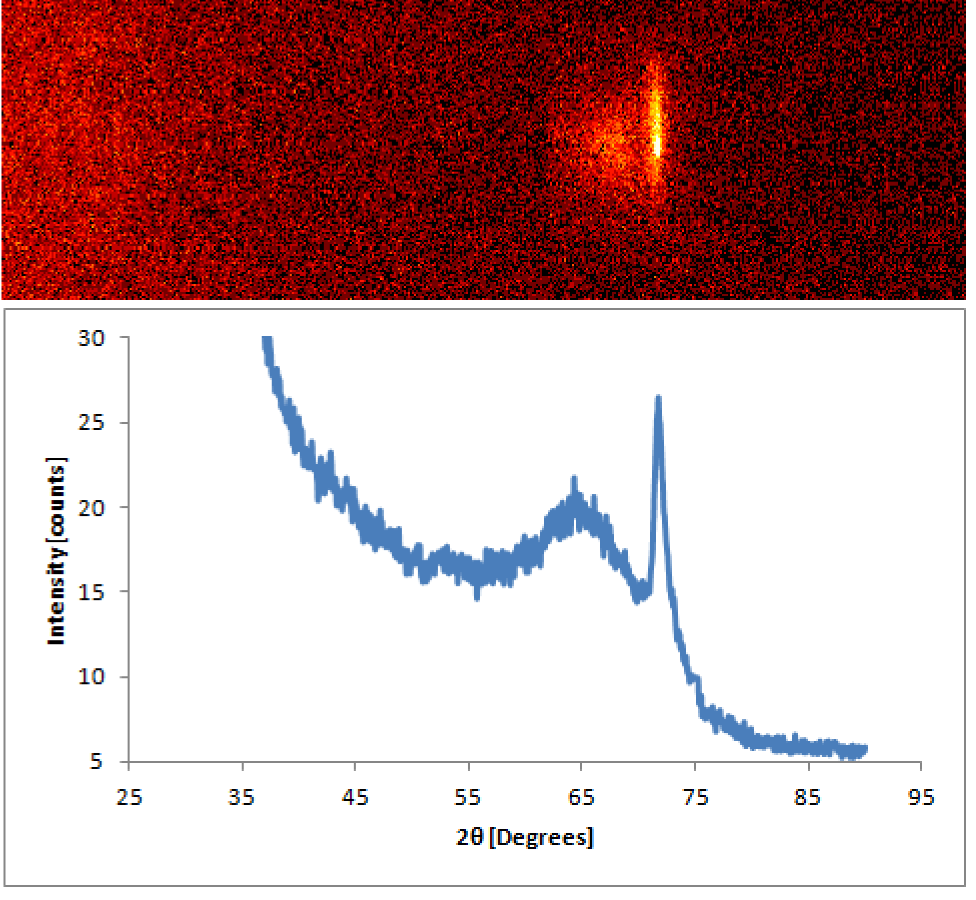

Figure 15. The bright region in the GADDS frame (top) corresponds to the (0004) ZnO peak at 71.7° in the XRD plot (bottom) and the diffused region to the left of this region is the substrate's diffraction.

5.2.3 XRD of the PLD Target

The powder diffraction of our ZnO PLD target is obtained by a D8 Advanced Bruker XRD system. Our results confirm the high purity of the target. The crystallographic properties of our ZnO PLD target and the instrumental setup are show in table 1 below. R values, also called structural reliability factors, represent the reliability of observed data points with calculated peaks(Song, et al., 2012).

<table>
<tr><td colspan="6">R-Values [%]
GOF (Goodness of fit) = 3.26
DW (Debye-Waller factor) = 0.28</td></tr>
<tr><td colspan="2">R_{exp} = 2.2</td><td colspan="2">R_{wp} = 7.47</td><td colspan="2">R_{p} = 5.67</td></tr>
<tr><td colspan="2">$R_{exp'}$ = 2.89</td><td colspan="2">$R_{wp'}$ = 9.72</td><td colspan="2">$R_{p'}$ = 8.33</td></tr>
<tr><td colspan="6">Instrument Setup</td></tr>
<tr><td colspan="3">Primary Radius = 217.5 mm</td><td colspan="3">Secondary Radius = 217.5 mm</td></tr>
</table>

Specimen Displacement = -0.0065±0.0006	
Structural Properties of ZnO target	
R-Bragg	0.680
Space Group	$P6_3mc$
Cell Volume	47.6147±0.0008 Å^3
Crystallite Size	192±5 nm (Lorentzian)
Crystallite Size	122±2 nm (k: 1 LVol-IB) (Length Diffraction column volume Integral Breadth)
Crystallite Size	171±4 nm (k: 0.89 Lvol FWHM) (Volume-weighted Full Width at Half-Maximum)
Strain L	0.120±0.003
Crystal Linear Absorption Coeff.	277.661±0.005 cm^{-1}
Crystal Density	5.67679±0.00009
Lattice Parameters	
a	3.250046±0.000023 Å
c	5.205128±0.000045 Å

Table 1. The crystallographic properties of our ZnO PLD target.

5.2.4 ZnO XRD Spectrum

XRD spectra of our ZnO thin films confirm the wurtzite structure with (001) growth direction for all of our samples(Esmaili Sardari, et al., 2010). Early in our studies, the XRD system was not fixed to pre-set angles; therefore, we were able to detect all the diffraction peaks including the ones of the substrates. Figure 16 shows the XRD spectrum of ZnO thin film on Si substrate. The large peaks at 34 and the small peak at 71° correspond to (002) and (004) ZnO peaks respectively while the large peak at 69° is (004) peak of the Si substrate(Esmaili Sardari, et al., 2010)(Park, et al., 2009). A small peak at 63° for (103) ZnO is also observed(Chen, et al., 2010). In general higher angle peaks show lower intensities due to several parameters including scattering and thermal factors.

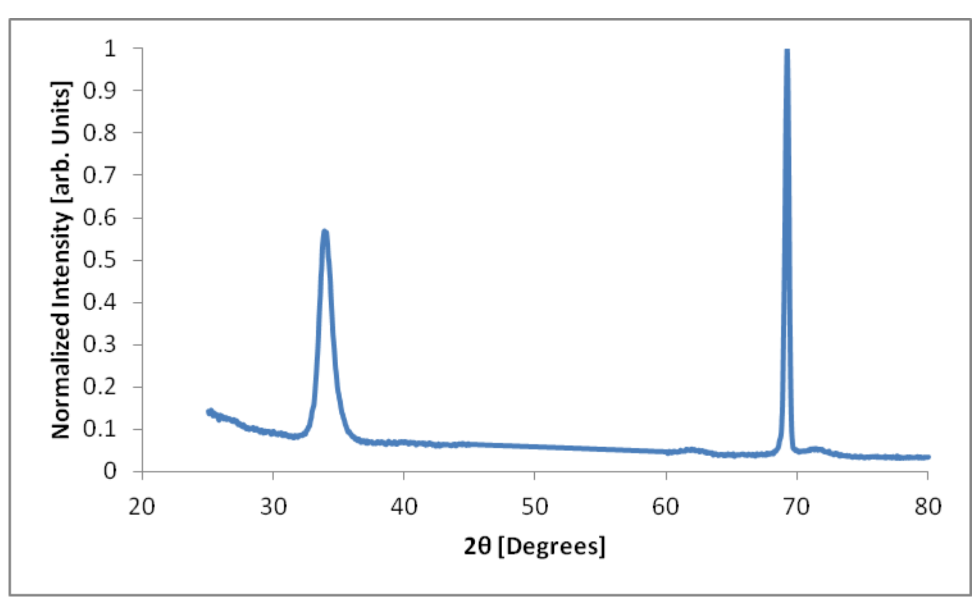

Figure 16. XRD spectrum of ZnO shows ZnO (0002) peak at 33.85° and ZnO (0004) peak at 71.4°. In addition to ZnO peaks, Si (400) peak at 69.2° is observed.

Then the XRD system was fixed at pre-set angles of 34 and 71° to only detect the films diffraction as shown in figure 17.

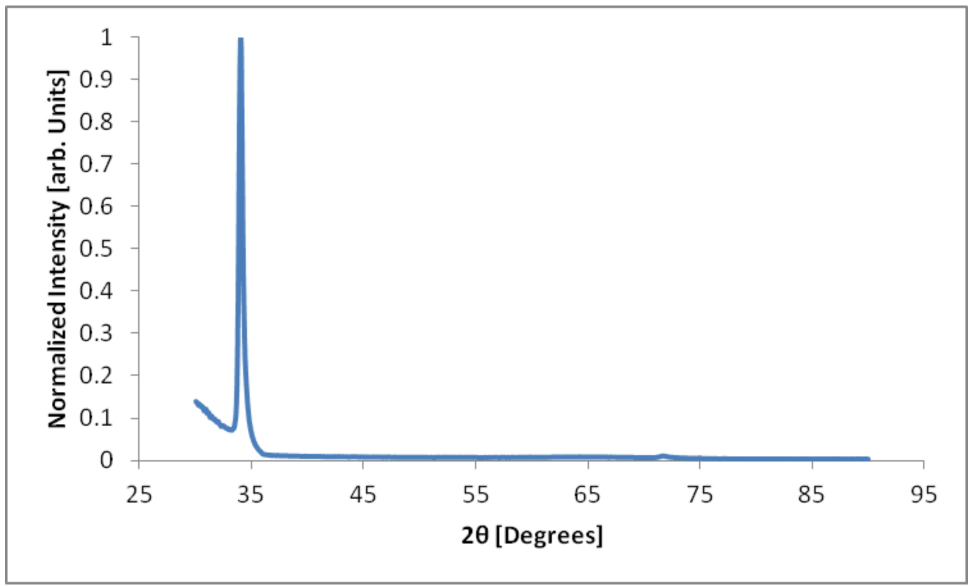

Figure 17. ZnO XRD spectrum shows the large main ZnO (0002) peak at 34° and small secondary ZnO (0004) peak at 71.7°. No other peaks are detected.

ZnO crystal parameters including the lattice constant *c*, grain sizes, and the stress along the *c*-axis are calculated based on our results.

5.2.5 ZnO Crystal Parameters

5.2.5.1 Derivation of the Lattice Constant c

We have used our XRD results to calculate the lattice parameter along the *c*-axis. As we will see in the followings, we can only derive the *c* parameter of our samples since our films only showed (000L) diffraction peaks.

To calculate the lattice constant we begin by finding the d-spacing of the crystal structure. The d-spacing of our samples is calculated using the Bragg's equation(Esmaili Sardari, et al., 2010):

$$2d \sin\theta = n\lambda \qquad \text{eq. 1}$$

Where

d is the d-spacing
θ is the diffraction angle in degrees
λ is the X-ray wavelength
n is an integer

Our system employs Kα X-ray of 1.54 Å (λ= 0.154 nm), and for lattice parameters we set n=1; thus, the d-spacing of our samples (in nm) are derived using the following equation:

$$d = 0.077/\sin\theta \qquad \text{eq. 2}$$

On the other hand, the d-spacing of the hexagonal crystal structure is related to the lattice parameters and Miller indices through the following(West, 1999):

$$d^{-1/2} = \frac{4}{3}(h^2+hk+k^2)\, a^{-2} + l^2 c^{-2} \qquad \text{eq.3}$$

Where

h,k,and l are Miller indices
a and c are lattice parameters

Since we have observed only (002) and (004) peaks, then we can find lattice parameter *c* by substituting for *h*=0, k=0*,* and *l*= 2 for (002) peak or *l*= 4 for (004) peak.

Thus, the lattice constant can be calculated by the following equations:

$$c = 2d \text{ for (002) peak} \qquad \text{eq. 4}$$
$$c = 4d \text{ for (004) peak} \qquad \text{eq. 5}$$

Substituting for d from eq.2, the lattice constant is related to the diffraction angle as the followings:

$c = 0.154/\sin\theta$ for (002) peak   eq. 6

$c = 0.308/\sin\theta$ for (004) peak   eq. 7

We studied the XRD spectra of several samples grown at different conditions, and an average lattice constant of 0.522 nm was derived. In particular, we studied three samples grown at 200, 250, and 300 ^{o}C. Based on our results samples grown at 200 and 250 ^{o}C both have a lattice constant of $c = 0.523$ nm, and the sample grown at 300 ^{o}C has $c = 0.519$ nm.

5.2.5.2Stress/Strain Evaluation

The stress in the grown ZnO thin films is due to several parameters including the differences between the lattice parameters and thermal expansion coefficients of ZnO and Si substrates(Lee, et al., 2009)(Jin, et al., 2002) as well as the intrinsic crystal defects introduced during the growth process(Lee, et al., 2009). Lattice misfit, *f*, for an epilayer with a lattice constant of *b* grown on a substrate with a lattice constant of *a* is defined as the following(Jin, et al., 2002):

$$f = 2 \times \frac{(b-a)}{(b+a)} \qquad \text{eq. 8}$$

For ZnO thin films grown on Si substrates, the lattice misfit turns out to be:

$$f = 2 \times \frac{(3.24-3.82)}{(3.24+3.82)} = -16.43 \qquad \text{eq. 9}$$

In addition to this large lattice mismatch between Si and ZnO, the thermal expansion coefficient of ZnO (6.05×10^{-6} C^{-1}) is bigger than that of Si (2.50×10^{-6} C^{-1}); therefore, once the growth process is finished and the sample is cooled down, the substrate exerts a tensile stress to the ZnO layer. On the other hand, intrinsic defects introduced during the growth, create a compressive stress in the ZnO thin film(Lee, et al., 2009). Using our XRD results, we can find the net stress as the followings.

The strain along the *c*-axis is expressed as the following(Esmaili Sardari, et al., 2010):

$$e_z = [(c - c_o)/ c_o]\times100 \qquad \text{eq. 10}$$

Where

c is the lattice constant
c_o is the stress-free bulk lattice constant

The stress-free bulk ZnO has a lattice constant value of 0.5205 nm(Esmaili Sardari, et al., 2010); thus, for the three samples grown at 200, 250, and 300 ^{o}C, samples grown at lower temperatures show tensile stress ($c> c_o$), while the sample grown at high temperature has compressive stress ($c< c_o$). Therefore, for the samples grown at low temperature the effects of substrates lattice

mismatch and thermal expansion differences are dominant while for the sample grown at 300 ^{o}C, the intrinsic defects are the dominant stress inducing factor.

Based on our results, the film grown at 300 ^{o}C has lower strain ($e_z = 0.28\%$) than the other films ($e_z = 0.48\%$).

Alternatively, the strain along the *c*-axis (for ZnO thin films) can be evaluated by(Ghosh, et al., 2004):

$$E_G = 3.3285 - 0.0177\ e_z \qquad \text{eq. 11}$$

Where

E_G is the energy gap in eV

5.2.5.3 Grain Size Derivation

The average grain size of our ZnO samples is calculated by Scherrer formula(Esmaili Sardari, et al., 2010):

$$D = (0.89\ \lambda)/\ (B\ \cos\theta) \qquad \text{eq. 12}$$

Where

D is the average grain size
λ is the X-ray wavelength
B is the FWHM in radians
θ is the diffraction angle

Based on our results, our samples have an average grain size of 26 nm with the smallest grain size of 22 nm.

5.3 PL Results

5.3.1 PLD Target

Prior to study the optical properties of the grown species, room temperature PL spectra of the PLD target along with a ZnO wafer provided by the MTI Corporation are studied. The wafer was used as a reference for the quality of the provided material.

Figure 18 shows the PL spectra of the polished ZnO wafer. A sharp and relatively low intensity peak at 376 nm along with an intense broad peak centered at 541 nm is observed. The 376 nm peak is the near-band-edge (NBE) UV emission peak for ZnO (E_G=3.29 eV). This NBE peak is

related to the direct free exciton recombination. While donor or acceptor bound exciton recombination may be present, their emissions could not be resolved at room temperature(Esmaili Sardari, et al., 2012). The full width at half maximum (FWHM) value of this peak is 15 nm (0.13 eV).

The broad peak, on the other hand, known as the visible defect related PL band is due to various intrinsic and extrinsic defects in crystal structure. This broad emission band is believed to be due to defects including oxygen vacancies, hydrogen complexes, zinc interstitials, and impurity contamination usually present in ZnO films(Esmaili Sardari, et al., 2012). The FWHM value of this peak for our reference material is 126 nm (0.54 eV).

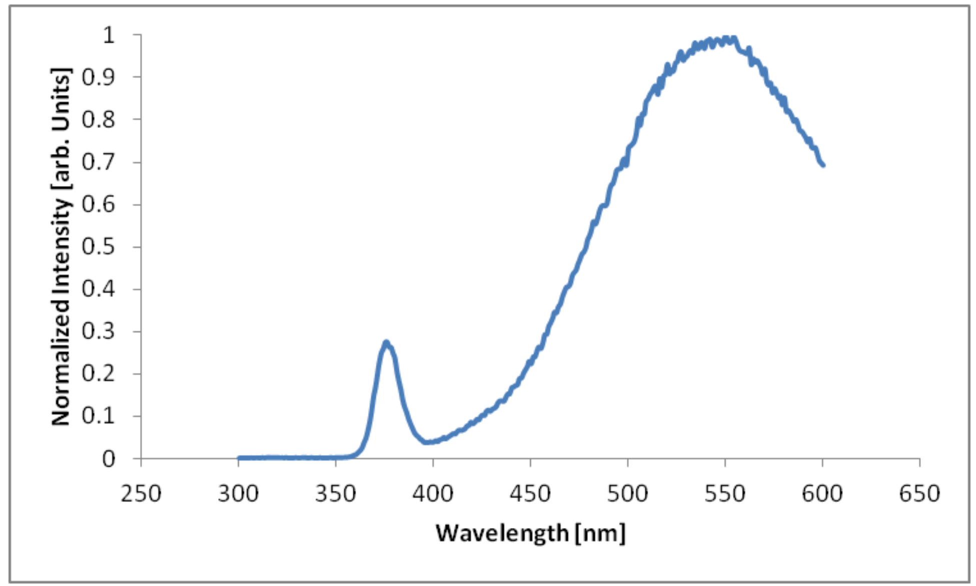

Figure 18. Room temperature PL spectrum of ZnO wafer. The ZnO bandgap peak at 376 nm (3.29 eV) along with a broad peak centered at 541 nm (2.28 eV) is observed.

Figure 19 shows the room temperature PL spectrum of the ceramic target. The typical ZnO PL spectrum with the NBE UV peak at 387 nm (3.20 eV) and the visible defect related band at 450-550 nm is observed. The FWHM of the NBE peak is 40 nm (0.33 eV) and that of the defect related broad peak is 92 nm (0.45 eV).

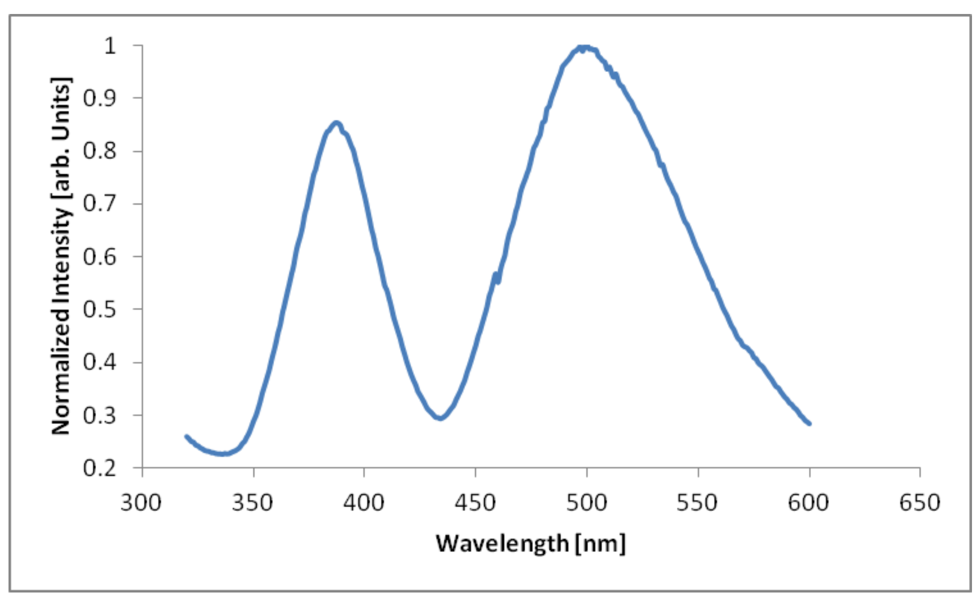

Figure 19. Room temperature PL spectrum of ZnO sputtering target. The ZnO bandgap peak at 387 nm (3.20 eV) along with a broad peak centered at 500 nm (2.47 eV) is observed.

5.3.2 Optimization, Alignment, and Early Results

Our early results showed an immediate improvement in the optical properties of the grown films. Specifically, the visible defect related PL band was suppressed significantly, and the NBE UV emission peak was substantially enhanced. The results were achieved after methodical optimization and alignment procedures. Prior to PL measurements, the position of the sample inside the PL chamber should be optimized, and we performed numerous measurements to find the optimum position of the sample holder. Moreover, the angular direction of the holder should be aligned with respect to the excitation source and emission detector to ensure maximum detection and minimum distortion. Once the alignment is performed, the position of the sample holder is fixed, and all measurements are performed with the optimized set up.

Figure 20 shows the relative position of the monochromatic excitation source, the sample, and the detector schematically. Since the location of the source and the detector are fixed, then the angular direction of the sample should be aligned to reduce the detection of the reflection and increase the PL emission capture.

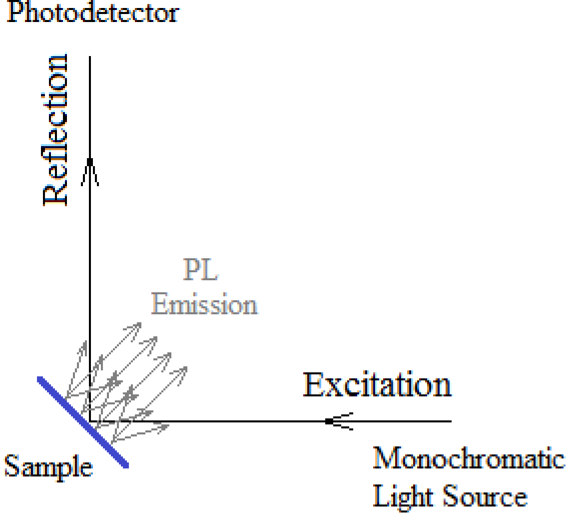

Figure 20. The schematics of our PL setup. The sample location is optimized to ensure maximum PL emission detection.

In addition to the typical ZnO peaks discussed earlier, our early results showed several artificial peaks, and we managed to resolve these peaks by proper alignment of the samples and application of excitation and emission filters.

5.3.3 ZnO Peak Detection

It is important to verify that the observed peaks are material-related emission peaks, and the results are due to the radiative decay of excited electrons of the material. To this end, we have excited our samples with different excitation wavelengths. ZnO peaks do not shift with the change in the excitation energy, and they always peak at the same energy level.

We have excited our samples with different excitation energies and verified that our results are indeed ZnO PL emission peaks. Figure 21 shows the PL spectra of a single sample excited with 250, 260, 270, 280, and 290 nm. It is evident that the peak at 380 nm does not shift with the changes in the excitation source.

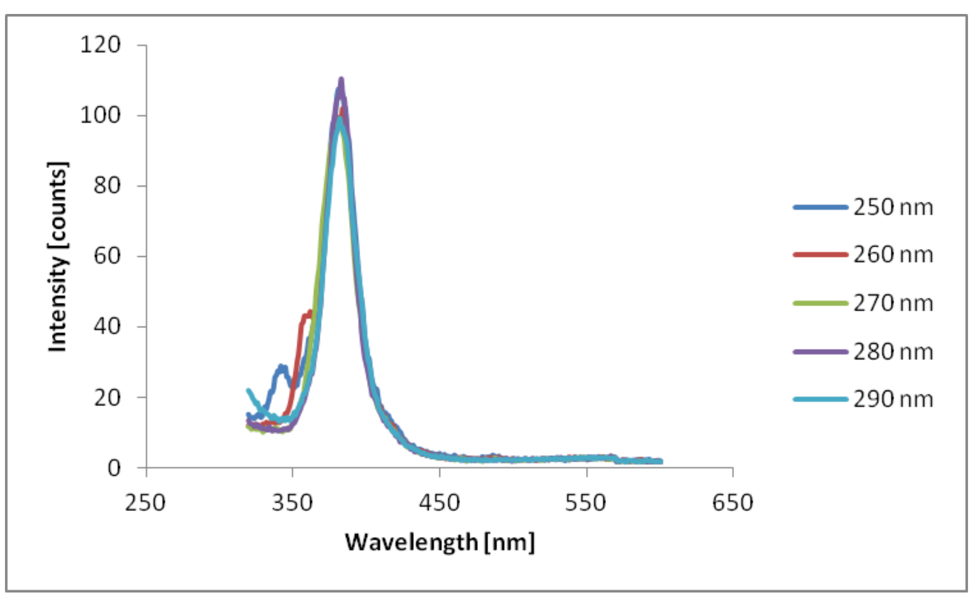

Figure 21. PL spectra of the ZnO film grown on p-Si substrate and high pressure using different excitation wavelengths. The results are derived for 250, 260, 270, 280, and 290 nm excitations. ZnO NBE UV emission peak at 380 nm is observed for all excitation energies.

On the other hand, a moving peak at 340—360 nm is observed which is not due to ZnO PL emission. Figure 22 shows the 330—430 nm region of our previous result in more details. ZnO's NBE UV emission peak at 380 nm is observed (overlapping for all excitation wavelengths).

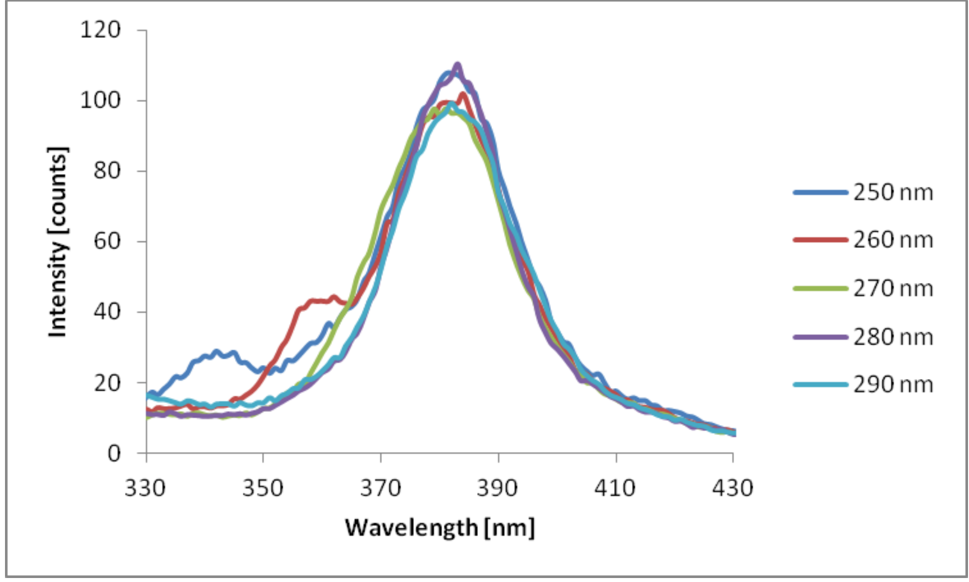

Figure 22. PL spectra of the ZnO film grown on p-Si substrate and high pressure using different excitation wavelengths. The results are derived for 250, 260, 270, 280, and 290 nm excitations. ZnO NBE UV emission peak at 380 nm is observed for all excitation energies. Another non-ZnO-related peak which shifts with the changes in the excitation energy is observed at lower wavelengths.

We further confirmed our result for the films grown at high oxygen overpressure. Figure 23 shows the PL spectra of a single sample excited with 250, 260, 270, 280, and 290 nm. It is evident that the peak at 380 nm does not shift with the changes in the excitation source; thus, this is a true material related ZnO peak

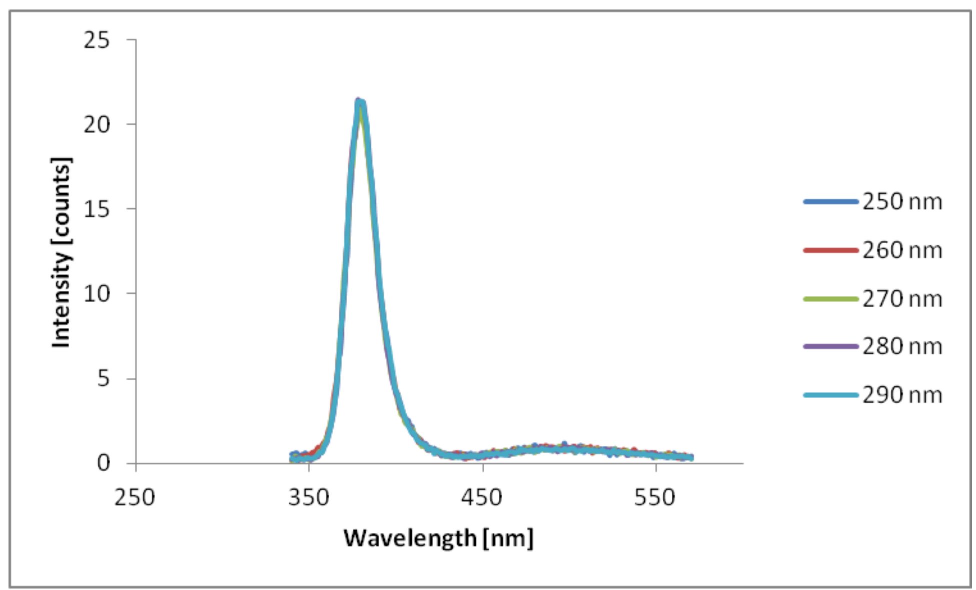

Figure 23. PL spectra of the ZnO film grown on p-Si substrate and low pressure using different excitation wavelengths. The results are derived for 250, 260, 270, 280, and 290 nm excitations. ZnO NBE UV emission peak at 378 nm is observed for all excitation energies.

Figure 24 shows the 330—430 nm region of our previous result in more details. The NBE UV emission peak at 378 nm is observed (overlapping for all excitation wavelengths).

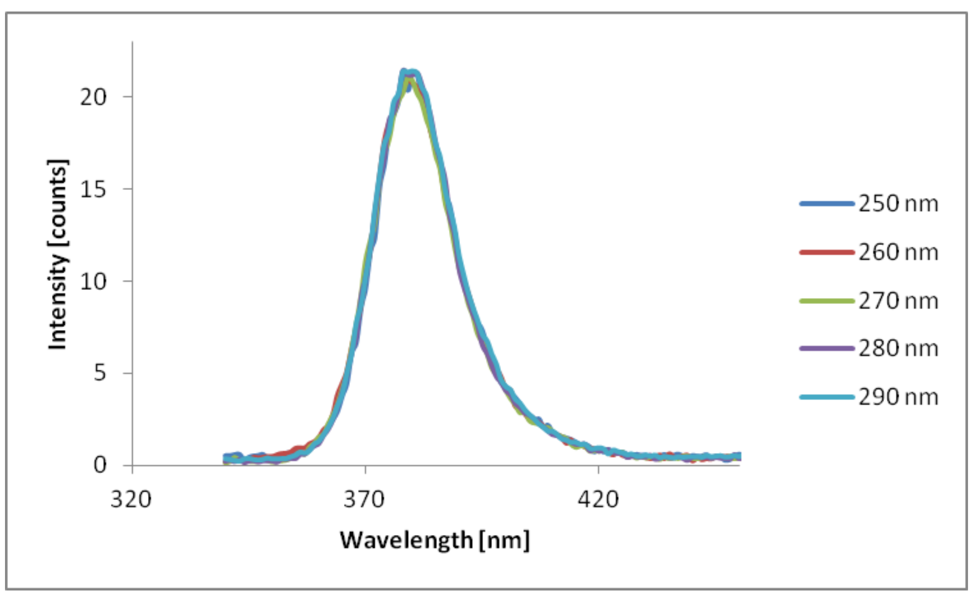

Figure 24. PL spectra of the ZnO film grown on p-Si substrate and low pressure using different excitation wavelengths. The results are derived for 250, 260, 270, 280, and 290 nm excitations. ZnO NBE UV emission peak at 378 nm is observed for all excitation energies.

For this sample (grown at low oxygen overpressure) the visible defect related broad band at 450—550 nm is also observed. This band, like the NBE UV emission peak, is a material emission peak and does not shift with the changes in the excitation energy. Figure 25 shows the PL spectra of the defect related broad band for 250, 260, 270, 280, and 290 nm excitation wavelengths. It is evident that all spectra overlap.

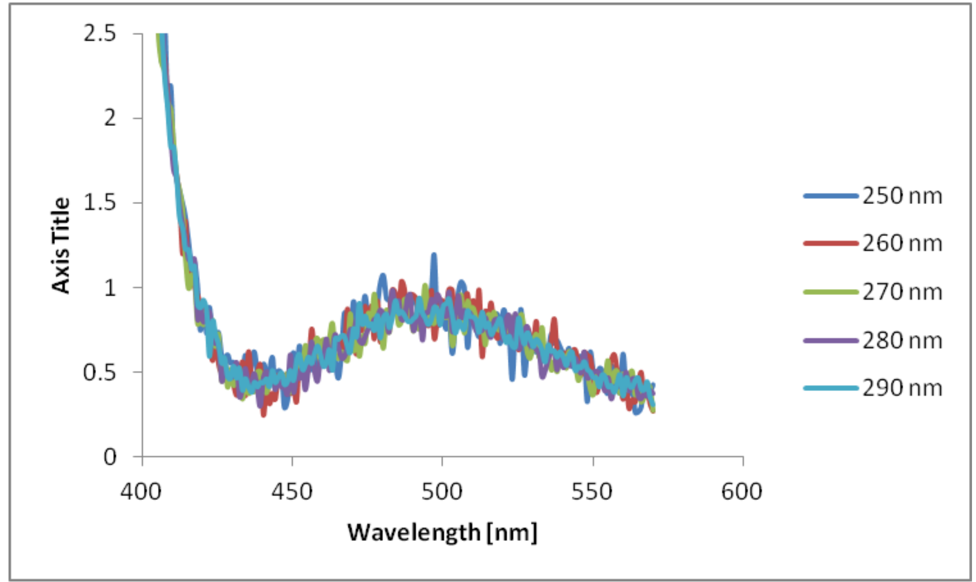

Figure 25. PL spectra of the ZnO film grown on p-Si substrate and low pressure using different excitation wavelengths. The results are derived for 250, 260, 270, 280, and 290 nm excitations. ZnO visible defect related broad band at 450—550 nm is observed for all excitation energies.

5.3.4 Si Substrate Background PL

Since ZnO is transparent to excitation energies >3.3 eV at room temperature (wavelengths >375 nm), then it is important to confirm that Si substrates do not contribute to the observed PL spectra of our samples.

We have calculated the average PL spectrum for our Si substrates, and it is shown that the intensity of this background PL emission is extremely low. Moreover, no peaks are observed at the ZnO's regions of interests, i.e. 350—400 nm and 450—550 nm. Figure 26 shows the average PL spectrum of Si substrates used in our work.

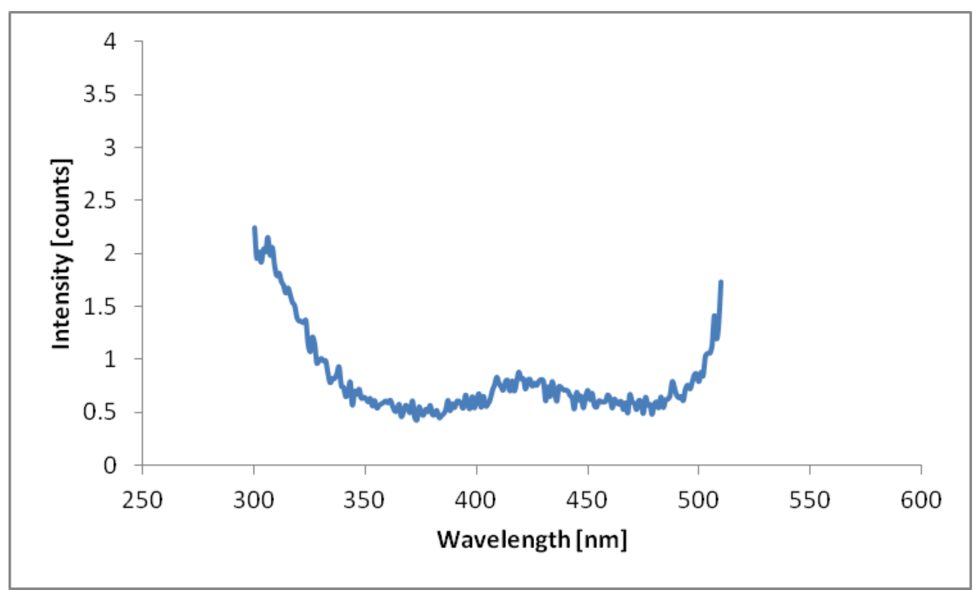

Figure 26.The average PL spectrum of Si substrates. It is evident that the intensity of the background emission is extremely low, and there are no peaks observed at 350—400 nm and 450—550 nm regions.

Therefore, the effects of Si substrates on PL emission results are ignored.

5.3.5 The Effects of Substrates Types on PL Emission Results

The photoluminescence spectra of the films grown on n and p-type Si substrates are studied, and the results are evaluated for films grown at different conditions. Our results indicate that the PL emissions of the films grown on n and p-Si substrates are practically indistinguishable.

5.3.6 Low Oxygen Overpressure Growth Regime

PL spectra of both ZnO/n-Si and ZnO/p-Si devices show a high intensity NBE UV emission peak and a substantially suppressed broad band defect related emission peak (relative to the target) as shown in figure 27 for the films grown at 300 ^{o}C and low oxygen overpressure.

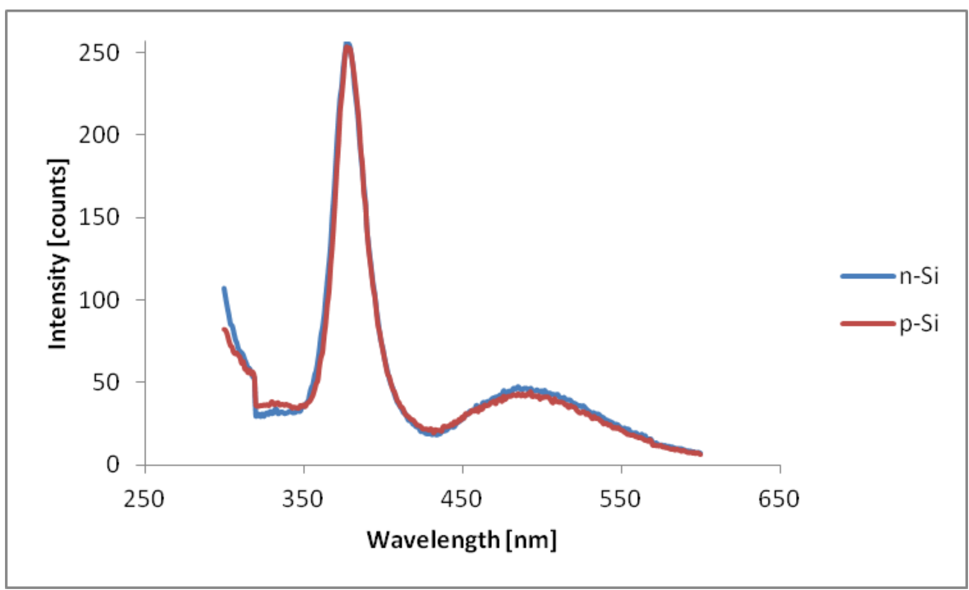

Figure 27. Room temperature PL spectra for ZnO films grown on p-Si (red) and n-Si (blue) substrates at 300 ^{o}C and low oxygen overpressure. Both spectra are very similar showing a high intensity near band-edge peak at 377 nm (3.28 eV) and a substantially suppressed defect related broad peak at 450-550 nm with the maximums at 485 nm for sample grown on n-Si and 493 nm for sample grown on p-Si.

Both samples have FWHM values of 21 nm (0.18 eV) for the NBE UV emission peak.

5.3.7 High Oxygen Overpressure Growth Regime

Similar to low oxygen overpressure regime, PL spectra of both ZnO/n-Si and ZnO/p-Si devices show the high intensity NBE UV peak. However, the visible defect related broad band emission is further suppressed (relative to the low oxygen overpressure growth regime) and essentially eliminated. Figure 28 shows the PL spectra for n and ZnO/p-Si devices grown at 300 ^{o}C and high oxygen pressure.

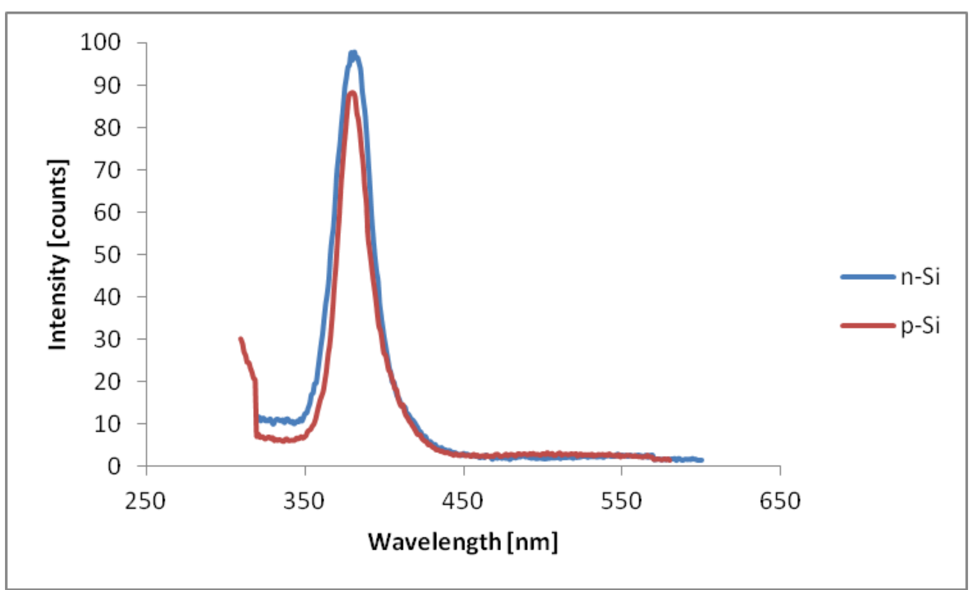

Figure 28. Room temperature PL spectra for ZnO films grown on p-Si (red) and n-Si (blue) substrates at 300 ^{o}C and high oxygen overpressure. Both spectra are very similar showing a high intensity near band-edge peak at 379 nm (3.27 eV) for n-Si and 380 nm (3.26 eV) for p-Si. The defect related broad band emission is strongly suppressed.

The NBE UV emission peak of the ZnO/n-Si sample has a FWHM value of 23 nm (0.20 eV), and the FWHM value of this peak for the ZnO/p-Si sample is 22 nm (0.18 nm).

Our results show that the PL properties of the films grown on n and p-Si substrates are the same. Moreover, regardless of the growth substrate and oxygen overpressure, the NBE UV emission peak is a high intensity sharp peak (FWHM= 0.18 eV) at about 379.5 nm (3.26 eV). The slight shifts in the positions of the peaks are due to the different stress/strain on the films.

5.3.8 PL Spectra of the Grown Films vs. the Target and the Reference ZnO Wafer

We have compared the emission properties of the grown ZnO thin films with the PL spectra of the target along with the ZnO wafer. This gives us an indication of our growth quality. Since the emission spectra are derived with different settings (of the PL measurement system) first we have normalized each spectrum using its maximum peak value. Figure 29 shows the normalized PL spectra of the target, the ZnO wafer, and ZnO films grown at high and low oxygen overpressures.

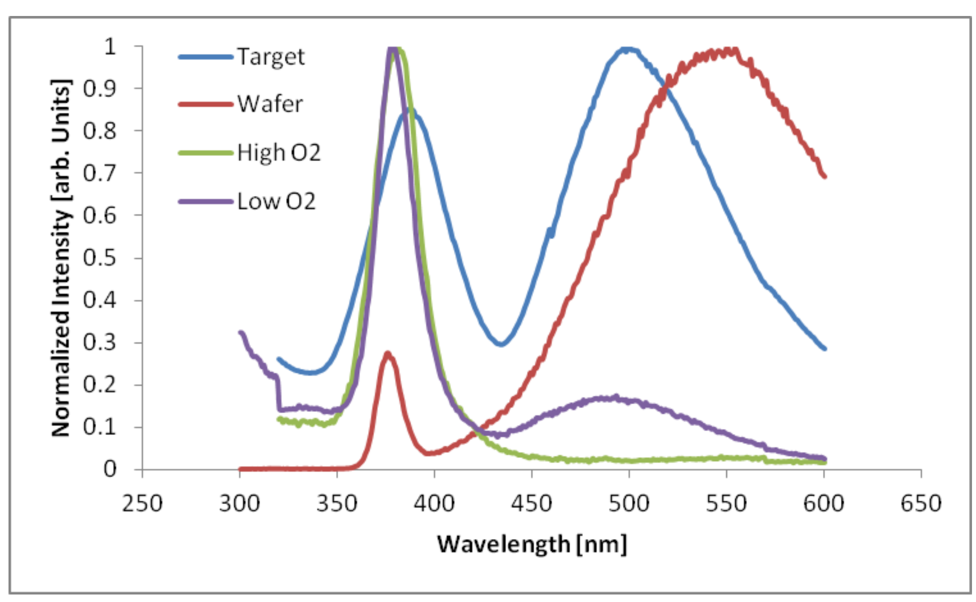

Figure 29. The normalized PL spectra of the target, the ZnO wafer, and ZnO films grown at high and low oxygen overpressures.

Our results indicate that the intensity of the NBE UV emission peak is strongly improved with respect to the target and the ZnO wafer. The visible defect related broad band, on the other hand, is suppressed for our grown thin films. More specifically, the NBE emission peak is improved by 66% with respect to the target and 270% with respect to the ZnO wafer sample, and the defect related broad band is suppressed down to 4800% for the films grown at high oxygen pressure regime.

The FWHM value of the grown films (22 nm) is also improved by 50% with respect to the target (FWHM= 40 nm) and approaches to that of our ZnO reference value (15 nm).

5.3.9 The Effects of Growth Temperature on PL Emission Results

The intensity of the defect related broad emission band is substantially suppressed for the samples grown at moderate temperatures (below 350 ^{o}C). Specifically, the defect induced peak is reduced for samples grown at or about 300 ^{o}C, indicating the minimum defect density for this condition of growth. Such suppression in the visible luminescence of ZnO thin films has not been reported earlier for films grown directly on Si and at these low temperatures. Similar results, however, have been observed for films grown with buffer layers at elevated growth temperatures(Esmaili Sardari, et al., 2010). This suppression is particularly important because not only it indicates the low defect density, but also enables us to fabricate high quality solar-blind optical devices.

On the other hand, increasing the growth temperature beyond 350 ^{o}C degrades the quality of the grown films. Figure 30 and figure 31 show the PL spectra of samples grown at low oxygen pressure (thus the observation of visible defect related broad emission band) and different growth temperatures of 100, 200, 250, 300, and 350 ^{o}C. The adverse effects of high growth temperatures is observed for samples grown on both n and p-Si substrates.

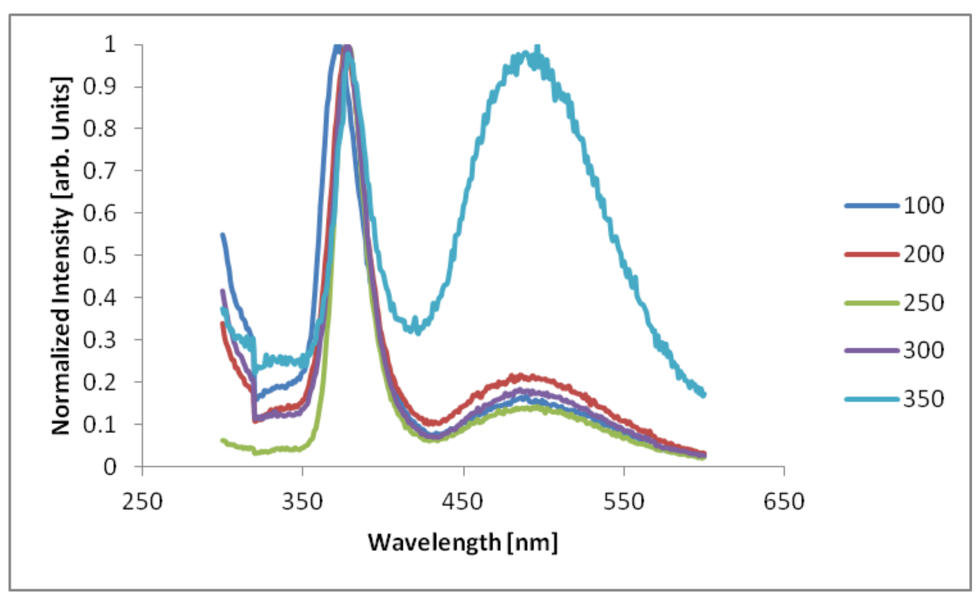

Figure 30. PL spectra of ZnO/n-Si samples grown at low oxygen overpressure and different growth temperatures of 100, 200, 250, 300, and 350 ^{o}C.

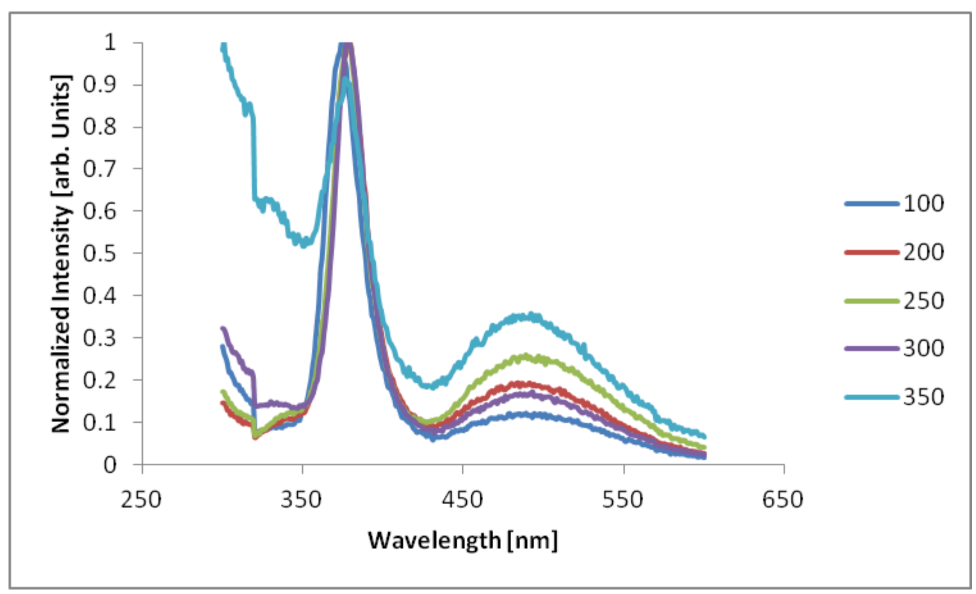

Figure 31. PL spectra of ZnO/p-Si samples grown at low oxygen overpressure and different growth temperatures of 100, 200, 250, 300, and 350 ^{o}C.

These results along with structural and electrical results suggest that at extremely low growth temperatures the arriving atoms do not have enough surface mobility to fill the appropriate lattice sites, while at high temperatures they are probably too mobile to stay in their lattice sites, degrading the crystal structure and optical properties of the films(Esmaili Sardari, et al., 2010).

As seen before, PL spectrum of ZnO has two differentiable bands: an ultra violet emission band and a visible one(Wang, et al., 2009)(Yu, et al., 2005)(Vanheusden, et al., 1996)(Pal, et al., 2006). The UV emission band is due to the annihilation of excitons(Wang, et al., 2009) which is the near band edge excitonic emission for ZnO and has been confirmed by several groups (Yu, et al., 2005)(Pal, et al., 2006)(Zhang, et al., 2009). The origins of the visible emission band, however, are more complicated, and there are several explanations for the exact mechanisms of this deep-level emission (DLE) band(Wang, et al., 2009)(Zhao, et al., 2007).

The visible defect related PL band, or the DLE band, of ZnO PL spectrum can be divided into the following sub-bands(Yu, et al., 2005)(Pal, et al., 2006)(Zhang, et al., 2009):

- The blue emission band near 440 nm
- The green emission band near 520 nm
- The yellow emission band near 580 nm
- The orange emission band near 626 nm
- The red emission band centered near 676 nm

Generally speaking, intrinsic defects including zinc vacancy (V_{Zn}), oxygen vacancy (V_o), zinc interstitial (Zn_i), oxygen interstitial (O_i), and oxygen antisite (O_{Zn}) along with extrinsic growth contaminations including hydrogen, Li, and Cu are discussed as the origins of the impurity levels introduced to the band gap of ZnO.

The origin of the blue emission line which is also reported for ZnO nano-crystals and ZnO nano-rod arrays is related to the radiative defects at the interface of the grain boundaries(Yu, et al., 2005).

Oxygen vacancies have been widely discussed as the origins of the green emission band(Wang, et al., 2009)(Vanheusden, et al., 1996)(Pal, et al., 2006)(Zhang, et al., 2009). In addition to oxygen vacancies, O_{Zn} and O_i have also been considered as the origins of the green emission of PL spectrum(Fan, et al., 2007). Oxygen vacancies occur in three various charge states; the neutral vacancy (V_o^0), the singly ionized vacancy (V_o^+) and the doubly ionized vacancy (V_o^{+2})(Wang, et al., 2009)(Vanheusden, et al., 1996)(Pal, et al., 2006)(Zhang, et al., 2009). Only the singly ionized oxygen vacancy (V_o^+) can act as a luminescence center(Wang, et al., 2009)(Zhang, et al., 2009). Therefore, the green emission is due to the recombination of V_o^+ and electrons(Vanheusden, et al., 1996). Moreover, at the depletion region of the grain surface, the recombination of the V_o^{+2} and a photo-excited electron from near conduction band gives rise to a green emission with lower energy(Wang, et al., 2009).

Thus, the intensity of the green emission band in the PL spectrum of ZnO is closely related to oxygen vacancies. As we saw in our results earlier, samples with extremely low visible emission bands, i.e. low defects, have been fabricated successfully.

The yellow emission is attributed to the radiative recombination of a delocalized electron near the conduction band with a hole in O_i center(Pal, et al., 2006). For ZnO films prepared by chemical methods the presence of hydroxide group, OH^-, has also been reported as the origin of the yellow-green emission band(Zhang, et al., 2009). Thus, having hydrogen contamination can lead to the presence of OH^- groups and, thus, visible emission.

Orange emission could be achieved by Li or other impurity doping(Zhang, et al., 2009). Interstitial oxygen has also been suggested as an origin of orange luminescence, but it cannot be accompanied with green luminescence which is due to oxygen vacancies. Thus, if green and orange bands are both present in PL spectrum another explanation is needed to justify the peaks, and it might be the surface states that create the orange emission band. Similar to the orange emission, there are various explanations for red luminescence. This band always appears in iron or rare earth doped ZnO, and there are few reports on red emission for undoped ZnO as well. It has been ascribed to the excess oxygen defects, V_{Zn} related complexes and other types of defect complexes including surface or grain boundary defects. Zhang et al. attributed the orange and red emissions to the surface states, since annealing increased the crystal quality and lowered the surface states as well as the orange and red emissions(Zhang, et al., 2009).

Finally, a shoulder peak along with the NBE emission was observed for some of our early samples. This low energy peak is assigned to the donor-acceptor pair (DAP) transitions(Zhao, et al., 2007) for intrinsic acceptor-like defects, i.e. zinc V_{Zn}, O_i, and O_{Zn}. Moreover, hydrogen can create complex defects with oxygen vacancies in the form of HV_o^+ or $H_2V_o^{2+}$ that can shift the UV emission to slightly lower energies. Our results are in good agreement with the very same behavior reported earlier but for the low temperature (80K) measurements(Choopun, et al., 1999). The high energy peak is due to the free excitons radiative annihilation and the low energy peak is attributed to the bound excitons or shallow acceptor level defects. In low temperatures, however, the two peaks are observed at ~367 nm and 369.5 nm which indicates that while the (free) excitonic emission stays at 367 nm for low temperature (and room temperature readings), the DAP transition is at lower energies for higher temperatures(Choopun, et al., 1999). In other words, increasing the temperature activates more acceptor sites (V_{Zn}, O_i, Zn_i) near the valance band which ultimately shift the bound exciton peak to the lower energies inside the band-gap.

Chapter Six: Hall Effect Measurements

Quantitative study of the electrical properties of the grown layers has been performed by Hall Effect measurements. This technique is widely used in semiconductor studies for evaluation of electrical properties including the conductivity type, carrier concentration and mobility(Arnaudov, et al., 2003)(Rhoderick, 2000).

6.1 Principles of Hall Effect

6.1.1 Theory and Derivations

Hall Effect is due to the Lorentz force applied to the moving charges in a magnetic field. This force bends the trajectories of the carriers, and; thus, changes the concentration of carriers inside the ZnO layer. An electric filed—called *Hall field*—is created as the result of this charge concentration which at steady state is balanced with the Lorentz force.

$$\mathbf{F_M} = q(\mathbf{V} \times \mathbf{B}) \qquad \text{eq. 1}$$
$$\mathbf{F_E} = \mathbf{E}.q \qquad \text{eq. 2}$$

Where

$\boldsymbol{F_M}$ is the Lorentz force due to the magnetic field
$\boldsymbol{V}$ is the velocity of the moving charged-particle
q is the charge of the moving particle
$\boldsymbol{F_E}$ is the force due to the Hall field
$\boldsymbol{E}$ is the Hall filed

To make our discussion more specific, let's assume the following structure:

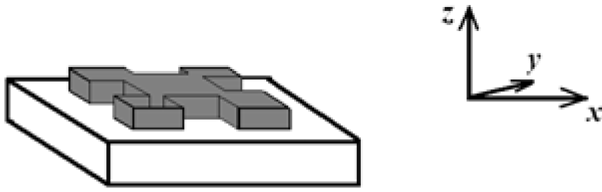

Figure 1. Hall Effect structure and the related coordination. The grown layer is etched out to a clover leaf pattern.

A fixed dc-current is applied in the $+x$ direction along with a magnetic field in the $+z$ direction. The Lorentz force, $\mathbf{F_M}$, would be in $+y$ direction:

$$F_{My} = qV_x B_z \qquad \text{eq. 3}$$

The Hall filed force, $\mathbf{F_E}$, would be in $-y$ direction:

$$F_{Ey} = E_y.q \qquad \text{eq. 4}$$

At the steady-state situation we have:

$$E_y = V_x B_z \qquad \text{eq. 5}$$

This field creates a potential difference V_H, called *the Hall Potential*, which is detected.

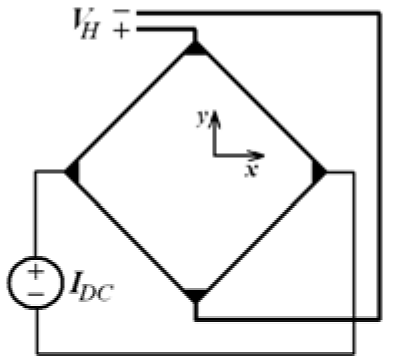

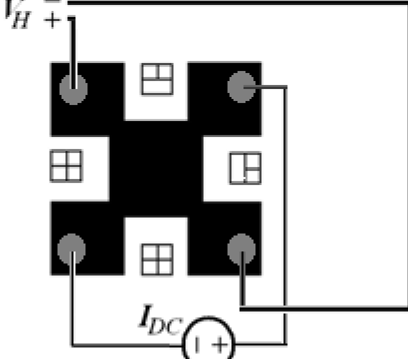

Figure 2. Schematic of the Hall Effect setup. Left is the square patters and right is the clover-leaf pattern.

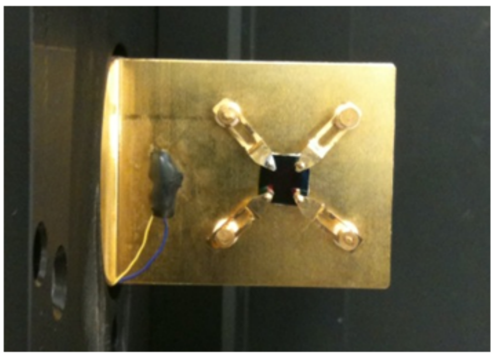

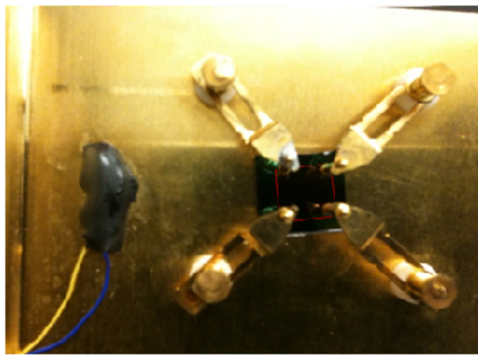

Figure 3. Experimental setup for Hall Effect measurements. A sample placed on the sample holder of Ecopia® Hall Effect Measurement system HMS-5000 is shown.

Hall coefficient which is a measure of the conductivity type of a semiconductor is defined as the following:

$$R_H = E_y / (J_x.B_z) \qquad \text{eq. 6}$$

If we make an assumption on the homogeneity of the electrical properties of the ZnO layer and ignore the random motion of the electrons due to thermal agitation (Arnaudov, et al., 2003)(Rhoderick, 2000), we can assume a uniform velocity equal to the drift velocity for V_x. Having said that, the current density, J_x, can be written as the following for an n-type semiconductor:

$$J_x = q.n.V_x \qquad \text{eq. 7}$$

Then:

$$R_H = E_y / (J_x.B_z) = (V_x\ B_z) / (J_x.B_z) = V_x / q.n.V_x \qquad \text{eq. 8}$$

Thus,

$$R_H = 1/ q.n \qquad \text{eq. 9}$$

Similarly, for a p-type material we have the following:

$$R_H = 1/ q.p \qquad \text{eq. 10}$$

The Hall mobility is derived from the conductivity of the films. Once the conductivity of the ZnO layer, σ, is calculated, we can then calculate carrier mobility as the following:

$$\sigma = J_x / E_x = (q.n.V_x) / E_x = q.n.\mu_x \qquad \text{eq. 11}$$

Or:

$$\sigma = \mu_x / R_H \qquad \text{eq. 12}$$

6.1.2 Other Induced Voltages in Hall Effect

6.1.2.1 Contact Voltage Drop, V_C

The measured voltage in the van der Pauw configuration is the summation of Hall voltage and contact voltage drop. Therefore, to evaluate and eliminate contact voltage drop, positive and negative magnetic fields are applied. The direction of the Hall voltage changes with the change of the magnetic field polarity. On the other hand, the Ohmic voltage drop at the contacts remains the same for two situations, therefore:

$$V^* = V_H + V_C \qquad \text{eq. 13}$$

Where

V^* is the measured voltage
V_H is the Hall voltage
V_C is the contact voltage drop

The Hall voltage can be evaluated by averaging over the positive and negative field values:

$$V^{*N} = -V_H + V_C \qquad \text{eq. 14}$$
$$V^{*P} = +V_H + V_C \qquad \text{eq. 15}$$

So

$$V_H = \tfrac{1}{2}\,(V^{*P} - V^{*N}) \qquad \text{eq. 16}$$

6.1.2.2 V_M, V_S, V_E, V_N and V_R

The Hall Effect voltage is calculated by averaging over all the possible current directions and magnetic field polarities; there are namely four possible combinations for the magnetic field polarity along with the current direction—we can inject a current into the contact or draw the current out for positive and negative magnetic fields.

This averaging process is necessary to eliminate the undesired induced electro-magnetic fields. There are several false voltages, or induced fields, which can appear in Hall measurements(Nalwa, 2002)(Jagadish, et al., 2006):

- First, if the contacts are not perfectly aligned and there are geometrical deviations in the contact patterns, then a voltage is created due to this misalignment which is more pronounced for high current densities. This misalignment voltage or V_M reverses with current which can be eliminated by the averaging process.
- Second, if there is an external temperature gradient along the length of the sample due to the mounting surface for instance, then the contacts create a thermocouple which leads to an undesired induced field. Because of the Seebeck effect, this filed is designated as V_S. Unfortunately, this voltage remains unaffected by changing the polarity of the current or the magnetic field. However, we will see that Seebeck voltage, V_S, can be determined by adding the four measured voltages. Moreover, this voltage can be ignored if the temperature gradient is negligible.
- Third, if the temperature gradient transverse to the current direction is due to the sample itself, then an internal Seebeck effect is generated—since *hot* and *cold* electrons have different velocities, then they will experience different Lorentz forces (eq. 1) and will arrive to the side electrodes in different numbers. This effect is known as Ettingshausen effect, and the voltage induced is designated by V_E. In contrast to V_S, V_E is proportional to both current and magnetic field.
- Longitudinal temperature gradient can also affect the Hall readings. Electrons diffuse from the hot side of the sample to the cold side, and this diffusion current experiences the Hall Effect as well. This phenomenon is known as the Nernst or Nernst-Ettingshausen effect and the induced voltage due to this effect is V_N. This voltage is independent of the external current, but it is proportional to the magnetic field.

- Finally, Nernst electrons, discussed before, experience the Ettingshausen effect as well. This phenomenon is referred to as the Righi-Leduc effect and the Righi-Leduc voltage, V_R, similar to the Nernst voltage is just proportional to the magnetic field.

Measured Hall voltage is the summation of all these values:

$$V^* = V_H + V_C + V_M + V_S + V_E + V_N + V_R \qquad \text{eq. 17}$$

The dependence of the undesired voltages to the current direction and magnetic field polarity can be summarized as the following:

Current Polarity	Magnetic field Polarity	V_H	V_M	V_S	V_E	V_N	V_R
+	+	+	+	+	+	+	+
+	-	-	+	+	-	-	-
-	+	-	-	+	-	+	+
-	-	+	-	+	+	-	-

Table 1. The dependence of the induced voltages to the direction of the current and the polarity of the magnetic field in Hall Effect measurement. It is observed that only the Seebeck voltage, V_S, is not affected by the changes in magnetic polarity or current direction; however, adding up all the four readings allows for the calculation of V_S.

In our experiments, the Hall Effect measurement system[†††] switches the magnetic polarity as well as the direction of the injected currents automatically and reports the average Hall coefficient.

6.1.3 Multi-layer Hall Effect

Since our thin films are deposited on yet another semiconducting substrate, it is important to fully understand the Hall Effect in a multi-layer system, and more specifically in a two layer system. The contribution of the underlying substrate in Hall readings should be taken into account to make sure that the measured values represent the electrical properties of the deposited layer.

The issues with thin-film measurements are generally due the substrate's conduction, the interface depletion between the thin film and the substrate, depth non-homogeneity of the layer, and the electron transfer in hetero-structures(Look, 1989). Comprehensive study of two-layer Hall measurements and the details of a more general case, including the multi-layer system with different contacts configurations are reported elsewhere(Look, 1989)(Arnaudov, et al., 2003).

6.1.3.1 The effect of substrates conductivity on Hall

If the substrate is an insulator or a semi-insulating material, then there is no significant current through the substrate and the Hall readings are insured to quantitatively evaluate the thin-layer's electrical properties, but this is not always the case. The current ratio between layer's current, I_2, and substrate's current, I_1, is inversely proportional to the resistances:

[†††] Ecopia® Hall Effect Measurement System HMS-5000.

$$I_2/ I_1 = R_1/ R_2 \qquad \text{eq. 18}$$

Where

I_1 is substrate's current
I_2 is thin film's current
R_1 is substrate's sheet resistance
R_2 is thin film's sheet resistance

Our results show much higher carrier concentrations for the grown layers than the substrates. Therefore, $R_1/ R_2 >> 1$ and from eq. 18 we have $I_2/ I_1 >> 1$ which means that the current is limited mainly to the thin layer.

Moreover, since the film's concentration is higher, the interface depletion is mostly inside the substrate which in turn isolates the substrate and with non-alloyed surface deposited contacts, the current is thru the thin film(Look, 1989). For instance, the carrier concentrations of ZnO films deposited on p-Si substrates are found to be in the order of 10^{19} cm^{-3} while the concentration of substrates are in 10^{14} cm^{-3} range. Assuming a large built in potential to maximize depletion with we have:

$$x_{p+} = [(2\varepsilon_{ZnO} V_b)(Na/(Na^+(Na^++Na)))]^{1/2} = 0.03 \text{ nm} \qquad \text{eq. 19}$$
$$x_p = [(2\varepsilon_{Si} V_b)(Na+/(Na(Na^++Na)))]^{1/2} = 3 \text{ um} \qquad \text{eq. 20}$$

Where

x_{p+} is the depletion width inside the ZnO film
x_p is the depletion with inside the Si substrate
V_b is the built in potential of 1 eV
ε_{ZnO} and ε_{Si} are the relative electron permeability of ZnO (8.5) and Si (11.8)

Thus the depletion region is mainly inside the Si substrate ($x_p = 10^5\ x_{p+}$) which prevents the injection of carriers from the substrate to the grown ZnO layer.

6.1.4 Contact Size and Shape

The size and the shape of the contacts are important in resistivity measurements and Hall Effect readings using van der Pauw method. In his method, van der Pauw assumed infinitesimal contacts to the sample which is indeed a non-practical assumption, and therefore, correction factors and error estimation techniques have been used to account for the adverse effects of finite size contacts in van der Pauw method(Chwang, et al., 1974).

Circular contacts on the corners of clover-leaf pattern etched ZnO are deposited.

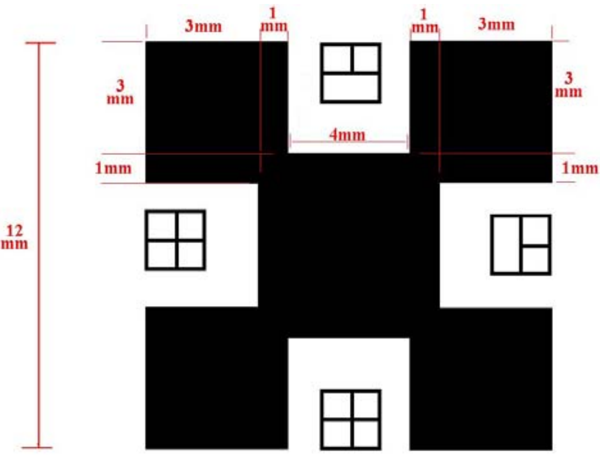

Figure 4. Lithography mask design for ZnO etching with detailed information.

6.1.5 Reading Error

Finite contacts introduce errors due to the shortening of the Hall field by the current contacts and current shunting of Hall electrodes which causes current loss at the edge of the contacts. It is shown that if the contact size is much smaller than the sample itself, the measurement error can be significantly reduced. For instance, for relatively large contacts of $\frac{Hall\ probe\ width}{sample\ length} = \frac{1}{8}$, then the error is less than 10% for Hall measurements and it is even less (0.25%) for resistivity measurements(Chwang, et al., 1974). In this work, to reduce the ratio of the contact width to the sample length, ZnO films are etched to create a clover-leaf pattern(Rhoderick, 2000) which reduces the ratio to $\frac{1}{20}$. Figure 4 and figure 5 show the clover leaf pattern photolithography mask uses in this study. The pattern increases the sample effective periphery (length) by 66% from 48 mm to 80 mm.

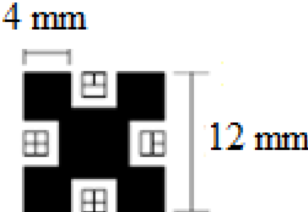

Figure 5. The clover-leaf photolithography mask used for device fabrication in this study. The pattern provides a larger peripheral length which reduces the finite contact size induced error.

Assuming a linear relation for the correction factor with respect to the $\frac{Hall\ probe\ width}{sample\ length}$ ratio, with this configuration, the error introduced due to the finite contact size is less than 4%.

6.1.6 Contact Material

6.1.6.1 Metal-Semiconductor Junctions

Metal-semiconductor (MS) junction has been studied in details(Look, 1989), and the properties of these junctions are discussed here briefly. More specifically, Ohmic and Schottky contacts for various materials as well as ZnO films on Si substrates are studies and discussed.

When a metal contact is deposited on a semiconductor material, a potential barrier due to the discontinuity of the electronic bands of the two forms at the interface, and depending on the relative location of energy levels, i.e. electron affinity and energy gap of the semiconductor on one hand, and work function of the metal on the other hand, two types of contacts can occur:

- An Ohmic contact is formed when the junction shows a voltage-indifferent behavior, and for various biasing conditions metal-semiconductor junction conduction remains the same. In this case, the *I-V* characteristic of the junction is linear and the variation of voltage with respect to the current shows the contact resistance.
- On the other hand, if the biasing of the MS junction increases or decreases the barrier voltage, then the electrical characteristics of the junction are not linear, and for different polarities it shows rectifying behavior. This type of non-linear and non-Ohmic, i.e. does not follow the linear Ohm's law, junction is called Schottky.

Ohmic Contact

Generally speaking, an Ohmic contact is a perfect source and sink of both electrons and holes which does not collect or inject carriers(Look, 1989). This definition, however, is merely an academic definition with no practical meaning since any contact will have a non-zero internal resistance. Therefore in reality, an Ohmic contact either has a negligible resistance compared to the semiconductor's resistance, or as it mentioned before, its resistance follows Ohm's law(Look, 1989).

Schottky Contact

A Schottky contact is a non-linear rectifying MS junction where a potential barrier is formed for electrons and/or holes due to the discontinuity of the semiconductor's Fermi level and the work function of the metal. The barrier height and different situations will be discussed and examined in more details next.

Schottky devices are interesting because some properties of p-n junctions, and most importantly the rectifying property, can be realized simply by making a MS Schottky contact. These junctions are simpler to fabricate, and in multilayer fabrication processes they are more attractive

than conventional p-n junctions; the lithography processes required for Schottky contacts are less. In terms of their performance, the delay time in p-n junctions which is due to the minority carriers in the depletion region, or in the insulator layer of p-i-n junctions, is eliminated; thus, the Schottky contacts can perform faster than p-n or p-i-n junctions. On the other, since the current in Schottky contacts is essentially due to the majority carriers—electrons if the semiconductor is n-type and holes if the semiconductor is p-type, the leakage current is suppressed; therefore, the power loss in Schottky contacts is less than p-n junctions.

6.1.6.2 Metal-Semiconductor Junction Analysis Using Surface Potential

Let's consider a MS junction and carefully examine the metallurgical junction. Suppose than the metal has a work function of Φ_M and the semiconductor has an electron affinity of χ_e with a band-gap of E_G and surface potential or work function (Fermi level) of Φ_S. Let V_{VAC}, E_C, and E_V be the vacuum level, conduction band, and the valance band of the semiconductor respectively.

The alignment of the bands and the potential barrier at the junction depend on the values of these parameters. Most generally, based on the value of the metal's work function and the type of the semiconductor we can have four possibilities:

- Case 1: $\Phi_M < \Phi_S$, and n-type semiconductor
- Case 2: $\Phi_M < \Phi_S$, and p-type semiconductor
- Case 3: $\Phi_M > \Phi_S$, and n-type semiconductor
- Case 4: $\Phi_M > \Phi_S$, and p-type semiconductor

Cases 1 and 4 lead to Ohmic contacts, and cases 2 and 3 lead to Schottky contacts.

Ohmic Contact Analysis

The easiest case would be the Ohmic contact where there is no potential barrier at the MS junction. For a non-degenerate n-type semiconductor, the work function or the Fermi level is close to the conduction band within the energy gap of the semiconductor. Thus, the work function of the semiconductor Φ_S is always greater than its electron affinity χ_e. This means that if $\Phi_M < \chi_e$ then $\Phi_M < \Phi_S$.

It is important because prior to Hall readings we have no information on the concentration of the carriers and thus the value of Φ_S; however, electron affinity of the semiconductor is independent of the concentration. In a similar fashion, for a non-degenerate p-type semiconductor, the work function or the Fermi level is close to the valance band within the energy gap; therefore, Φ_S is always smaller than ($\chi_e + \frac{EG}{q}$); thus, for an Ohmic contact it suffices that $\Phi_M > \chi_e + \frac{EG}{q}$.

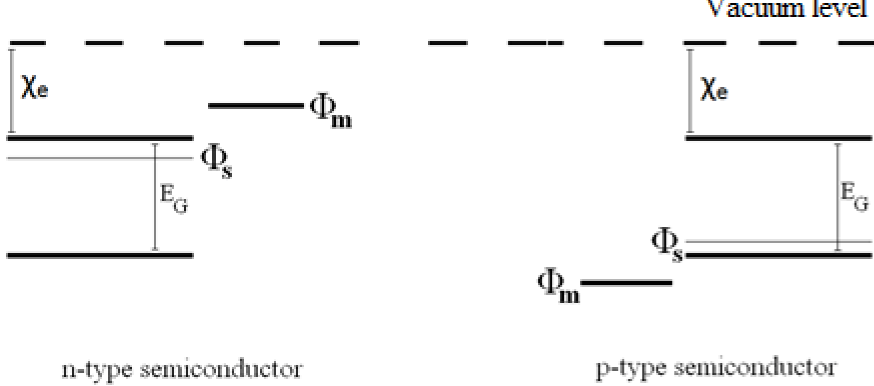

Figure 6. Electronic bands alignment for Ohmic contacts on an n-type (left) and a p-type (right) semiconductor. To have an Ohmic contact on an n-type material the work function of the metal should be less than the electron affinity of the semiconductor, and for a p-type material, the work function of the contact metal should be larger than the summation of the electron affinity and the band gap of the semiconductor.

Schottky Contact Analysis

Having examined the Ohmic conditions, if $\Phi_M > \Phi_S$ for an n-type semiconductor (and $\Phi_M < \Phi_S$ for a p-type semiconductor), then there will be a potential barrier for electrons (and holes) at the MS junction. The barrier height is equal to the band discontinuities.

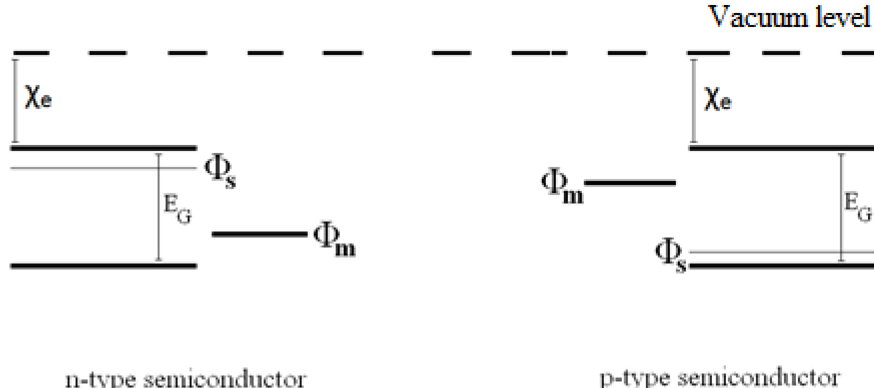

Figure 7. Electronic bands alignment for Schottky contacts on an n-type (left) and a p-type (right) semiconductor.

6.1.6.3 Metal-Semiconductor Junction Analysis Using Electron Affinity

Another approach to explain the MS junction behavior is to consider three cases based on the value of Φ_M, χ_e and E_G. If Φ_M is less than χ_e then at the junction, semiconductor bands always bend downwards, i.e. conduction band bends toward the midgap and the valance band bends away from the midgap level. This is due to the fact that when the work function and the Fermi level align at a same level (at equilibrium), the vacuum level is closer to Φ_M and it is further away from E_C.

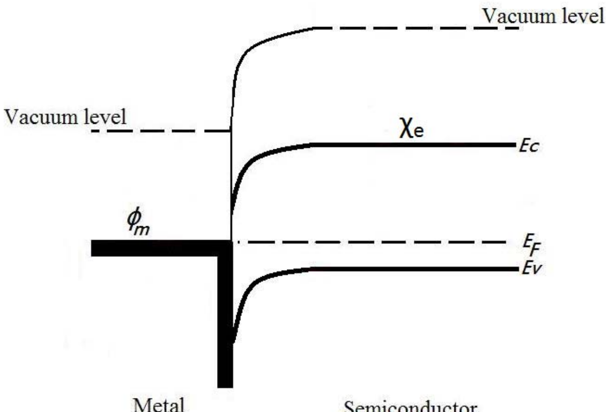

Figure 8. Band bending in MS junction when $\Phi_M < \chi_e$. Bands always bend downward to accumulate electrons and deplete holes at the junction.

On the other hand, if Φ_M is greater than $\chi_e + \frac{EG}{q}$ then semiconductor bands always bend upwards, i.e. conduction band bends away from the midgap and the valance band bends towards the midgap level.

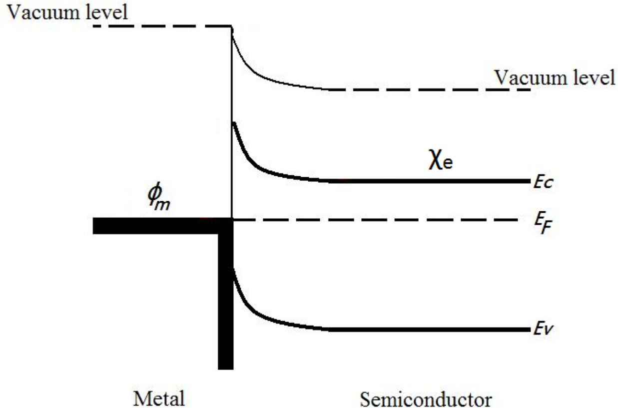

Figure 9. Band bending in MS junction when $\Phi_M > \frac{Eg}{q} + \chi_e$. Bands always bend upwards to accumulate holes and deplete electrons at the junction.

Finally, if $\chi_e < \Phi_M < \chi_e + \frac{EG}{q}$, then depending on the doping type and doping level, the bands will bend upward or downward. These cases are examined more carefully next.

Case 1: $\Phi_M < \chi_e$

In this case the downward bending of the conduction band at the junction increases the local concentration of electrons which is in favor of majority carriers for an n-type semiconductor. Therefore the MS contact becomes an Ohmic contact without a potential barrier.

For a p-type semiconductor, on the other hand, the downward bending of valance band decreases the local concentration of holes, i.e. majority carriers. Thus, a potential barrier is formed at MS junction. The barrier height is equal to the difference in the work function of the metal and the Fermi level of the p-type semiconductor.

Case 2: $\Phi_M > \chi_e + \frac{EG}{q}$

In this case the upward bending of the conduction and valance band decrease the local concentration of electrons and increase the concentration of holes. Therefore, while a potential barrier forms at MS junction for n-type semiconductor, the MS contact will be Ohmic for p-type semiconductors. The barrier height is equal to the difference in the work function of the metal and the Fermi level of the n-type semiconductor.

Case 3: Case 2: $\chi_e < \Phi_M < \chi_e + \frac{EG}{q}$

If the work function of the metal contact and the Fermi level of the semiconductor do not align, then depending on the relative position of the two energy levels and the majority carrier types, there might be a potential barrier for electrons and holes in n-type and p-type semiconductors respectively. Note that the Fermi level of an n-type semiconductor can be anywhere between the midgap energy level, $E_i = \frac{EG}{2}$, and the conduction band E_C. Similarly, the Fermi level of a p-type semiconductor can be anywhere between he midgap energy level and the valance band E_V.

MS Junction Approximate Analysis

Another approach to study the band alignment of MS junctions would be similar to our previous approach with somewhat relaxed conditions, or some approximations. In our relaxed conditions regime we consider the conduction and valance band edges, i.e. conduction band minimum (CBM) and valance band maximum (VBM) as the potential levels of electrons and holes for n and p-type semiconductors, respectively. This significantly simplifies the MS junction analysis, especially when $\chi_e < \Phi_M < \chi_e + \frac{EG}{q}$.

In this approach for an n-type semiconductor, the MS junction has no barrier if $\Phi_M < \chi_e$ and there will be a potential barrier if $\Phi_M > \chi_e$ with a barrier height of $\Phi_M - \chi_e$. This can be explained by the conduction band bending and the change in local electron concentration at the junction similar to our previous approach.

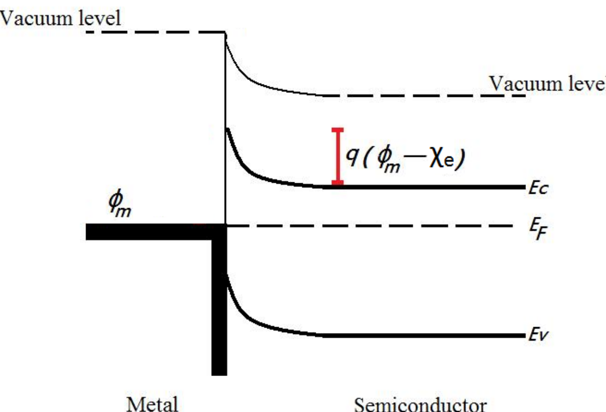

Figure 10. Schottky MS junction for n-type semiconductor when $\Phi_M > \chi_e$ with a potential barrier height of Φ_M - χ_e.

For p-type semiconductors, the MS junction would be Ohmic, i.e. no potential barrier, if $\Phi_M > \chi_e + \frac{EG}{q}$ and there will be a barrier otherwise. In this case the barrier height is equal to $\chi_e + \frac{EG}{q} - \Phi_M$.

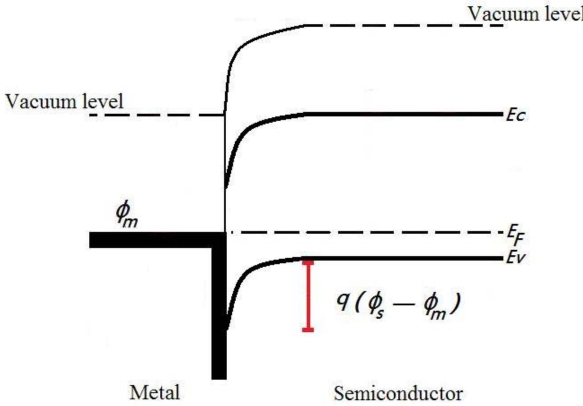

Figure 11. Schottky MS junction for p-type semiconductor when $\Phi_M < \frac{EG}{q} + \chi_e$ with a potential barrier height of $\Phi_S - \Phi_M$. Note that $\Phi_S = \frac{EG}{q} + \chi_e$.

The analysis of MS junction, therefore, is reduced to the comparative study of electron affinity and band-gap of the semiconductor with the work function of the metal contact. Table 2 shows ZnO parameters along with work functions of some relevant metals.

	χ_e , E_G/q, Φ_M
ZnO	χ_e= 4.5 eV E_G= 3.3 eV
Silver (Ag)	Φ_M= 4.52 — 4.74 eV
Aluminum (Al)	Φ_M= 4.06 — 4.26 eV
Lithium (Li)	Φ_M= 2.93 eV
Gold (Au)	Φ_M= 5.31 — 5.47 eV
Nickel (Ni)	Φ_M= 5.22 — 5.35 eV
Palladium (Pd)	Φ_M= 5.22 eV
Platinum (Pt)	Φ_M= 5.64 — 5.93 eV

Table 2. ZnO parameters along with work functions of some relevant metals(Wang, et al., 2006)(Lide, et al., 2010).

In this study we have employed the relaxed approximation model, and based on this model, for an n-type ZnO, metals with work functions of less than 4.5 eV (the electron affinity of ZnO) will form Ohmic contacts while metals with $\Phi_M > 4.5$ eV will be Schottky contacts. For p-type ZnO, metals with $\Phi_M < 7.8$ eV (the electron affinity plus the energy gap for ZnO) will form Schottky contacts while metals with $\Phi_M > 7.8$ eV will be Ohmic contacts. It is worth noting that this, however, is not an absolute boundary since there are several values reported for work function of metals as well as the electron affinity of ZnO. Figure 12 below shows the boundary conditions for Ohmic and Schottky contacts to n and p-type ZnO.

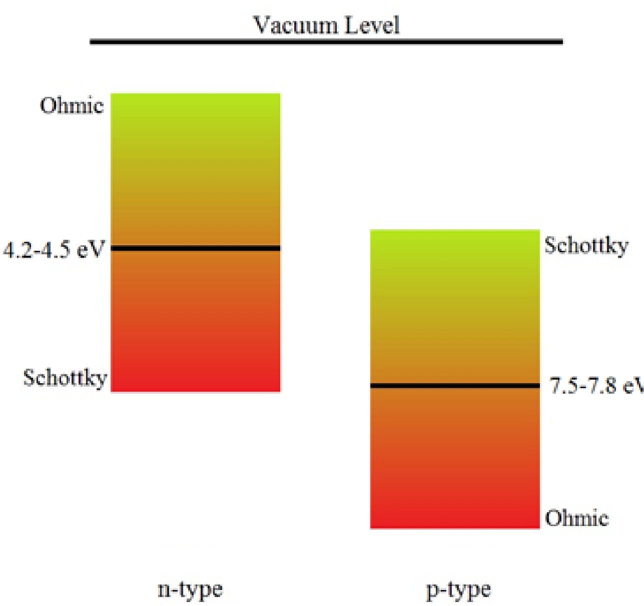

Figure 12. The boundary conditions for Ohmic and Schottky contacts to n-type and p-type ZnO.

Based on the work function of several metals and the electron affinity and bandgap of ZnO, we have selected Al and Au for our devices. Figure below shows the relative position of the materials with respect to the boundary conditions for n and p-type ZnO.

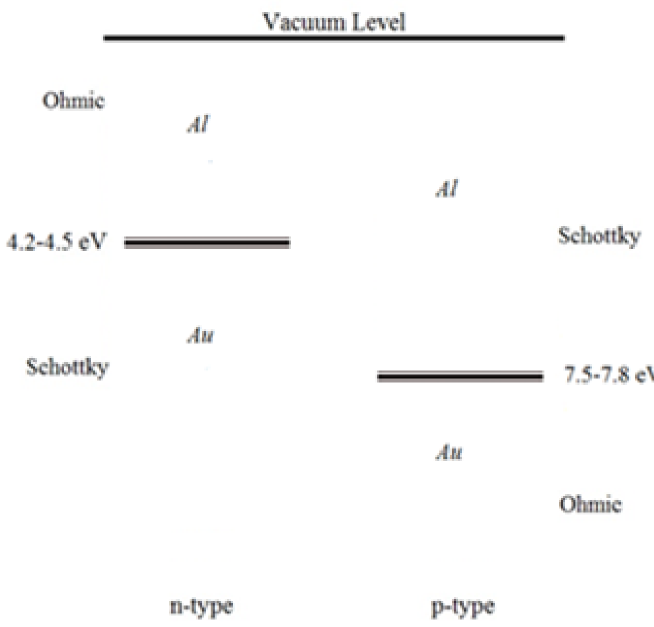

Figure 13. Selected materials for device analysis and fabrication. The Ohmic-Schottky boundary for both n-type and p-type cases are presented. Selected materials are examined and optimized through the optimization process.

6.2 Hall Effect Measurement System

Our Hall measurements were performed by an Ecopia® Hall Effect Measurement System, HMS-5000[‡‡‡]with fixed magneto flux density of 0.53-0.57 Tesla. The magnetic flux is set to 0.55 T, but the air gap difference makes it different for each system. In our experimental setup, the magnetic flux is 0.51 T. The injected current can be controlled between 1 nA to 20 mA. The system allows for variable temperature readings from 77K to 350K. Liquid nitrogen is employed to allow for varying temperature measurements[§§§].

Figure 14. Ecopia® Hall Effect Measurement System, HMS-5000[****]. The controller system (left) along with the temperature controlled sample holder and the magnets system (right) are shown. LN2 is introduced to the holder cavity for low temperature readings.

Prior to run Hall measurements, each sample is attached to the sample holder with four probe clips. The sample is then placed into the test chamber. The connection of contacts and probes are tested and validated automatically and characteristic *I-V* curves for the contacts are obtained. One of the assumptions of Hall Effect measurements is the linearity of the *I-V* characteristics for the contacts. In our work, the linearity is tested automatically by the HMS-5000. Table 3 shows typical readings for the verification of the contacts. The contacts are labeled clockwise as A for the top left corner of the sample to D for the bottom left corner; thus, AB, BC, CD, and DA are adjacent contacts, and AC and BD are cross contacts.

[‡‡‡] http://ecopia21.co.kr

[§§§] LN2 is necessary for low temperature readings (below room-temperature), but for high temperature readings (above room-temperature) it speeds the cooling process. It takes 35 to 45 minutes for the sample holder to reach 300K from 350K in air (the clean-room temperature of about 19 ^{o}C)

[****] http://ecopia21.co.kr

Trial	Current	Voltage	Contacts
1	1 mA	-1.67×10^2 mV	AB
2	1 mA	-1.59×10^2 mV	AB
1	1 mA	$+1.67\times10^2$ mV	-AB
2	1 mA	$+1.59\times10^2$ mV	-AB
1	1 mA	-1.64×10^2 mV	BC
2	1 mA	-1.56×10^2 mV	BC
1	1 mA	$+1.64\times10^2$ mV	-BC
2	1 mA	$+1.56\times10^2$ mV	-BC
1	1 mA	-2.96 mV	AC
2	1 mA	-2.43 mV	AC
1	1 mA	+3.03 mV	-AC
2	1 mA	+2.49 mV	-AC
1	1 mA	-1.66×10^2 mV	CD
2	1 mA	-1.59×10^2 mV	CD
1	1 mA	$+1.67\times10^2$ mV	-CD
2	1 mA	$+1.59\times10^2$ mV	-CD
1	1 mA	-1.63×10^2 mV	DA
2	1 mA	-1.56×10^2 mV	DA
1	1 mA	$+1.63\times10^2$ mV	-DA
2	1 mA	$+1.56\times10^2$ mV	-DA
1	1 mA	-3.06 mV	BD
2	1 mA	-2.53 mV	BD
1	1 mA	+3.16 mV	-BD
2	1 mA	+2.61 mV	-BD

Table 3. The linear *I-V* characteristics of the contacts are verified prior to Hall effect measurements.

If the contacts are not properly connected or if there is a short, the system does not allow for further readings. Sheet resistance and electrical conductivity of the samples are determined first and then magnets are brought close to the test chamber automatically. Once the positive field readings are performed, the polarity is reversed by bringing another pair of magnets. As mentioned before, this polarity change is applied to remove the undesired induced emfs.

6.3 Hall Mobility

6.3.1 Scattering Mechanism

The mobility of carriers in a semiconductor is affected by several scattering mechanisms. Most significantly, ionized impurities and acoustic phonons are responsible for carriers' scatterings. Other mechanisms include intra-valley scattering where an electron is scattered within an energy

valley along with long wavelength phonons, inter-valley scattering where an electron is scattered from one energy minimum to another along with an energetic optical phonon, and polar-optical-phonon scattering(Sze, et al., 2007).

The mobility of carriers from interactions with acoustic phonons of the lattice is related to the temperature and is proportional to $T^{-3/2}$. On the other hand, the mobility from ionized impurities is proportional to $T^{3/2}$(Sze, et al., 2007). Therefore, by studying the mobility behavior with respect to Hall temperature, we can suggest the dominant scattering mechanism. It is worth noting that there will be deviations from the theoretical values of ±3/2 which show that other scattering mechanisms are present as well, and the general trend, i.e. positive or negative slope, shows the dominance of ionized impurities or acoustic phonons scattering respectively.

In all of our Hall experiments, we observed that ZnO/n-Si devices show a relatively consistent Hall mobility throughout the wide range of Hall temperatures. The positive slope of the Mobility vs. Hall temperature plot confirms that ionized impurity scattering is the main scattering mechanism for these devices. More specifically, ZnO films grown at different growth temperatures of 150, 200, 250, 300, and 350 ^{o}C were studies and the results are as the followings:

6.3.1.1Mobility vs. Hall Effect Temperature Plots; Low Oxygen Overpressure Growth

ZnO/n-Si Devices

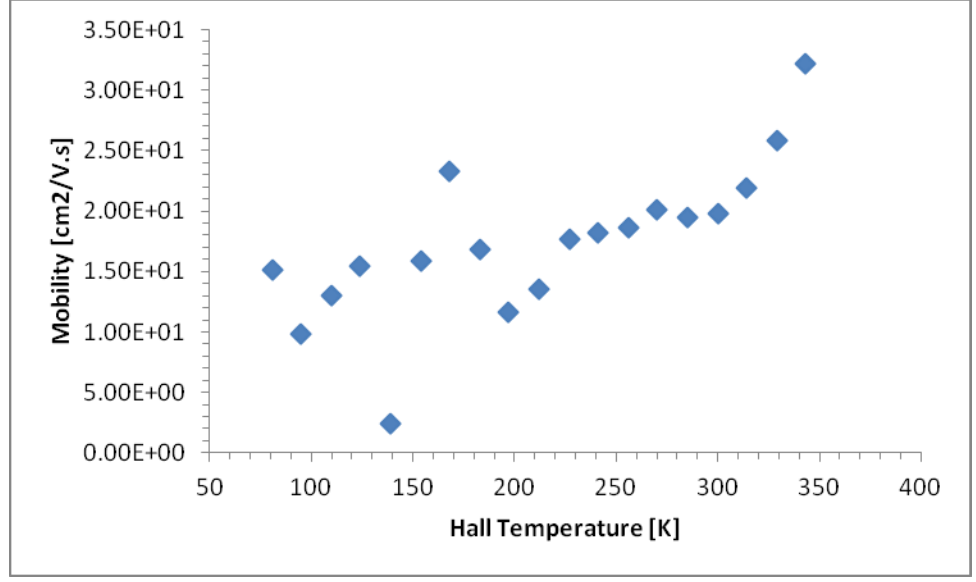

Figure 15. Hall mobility vs. Hall temperature for ZnO/n-Si device grown at 150 ^{o}C.

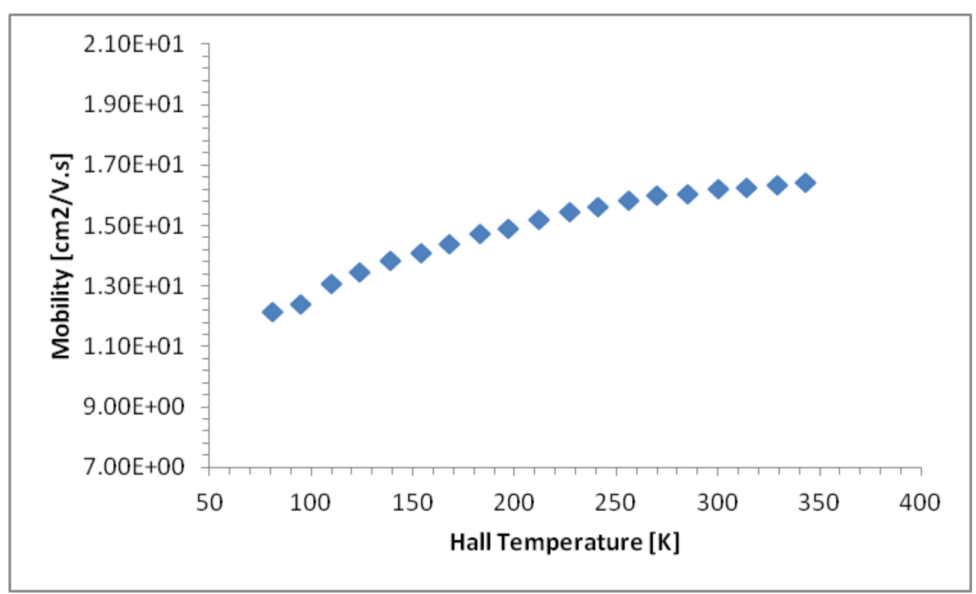

Figure 16. Hall mobility vs. Hall temperature for ZnO/n-Si device grown at 200 ^{o}C.

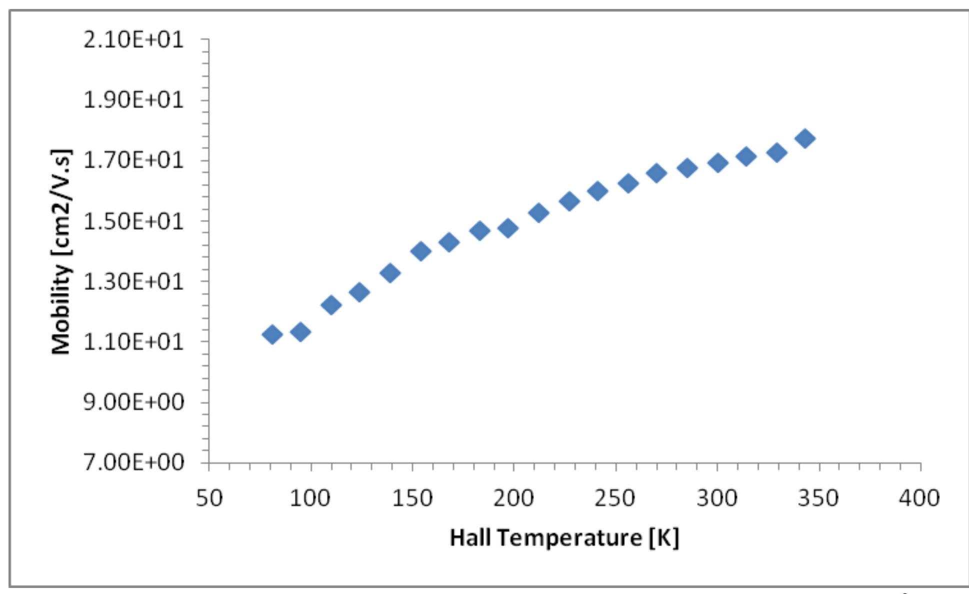

Figure 17. Hall mobility vs. Hall temperature for ZnO/n-Si device grown at 250 ^{o}C.

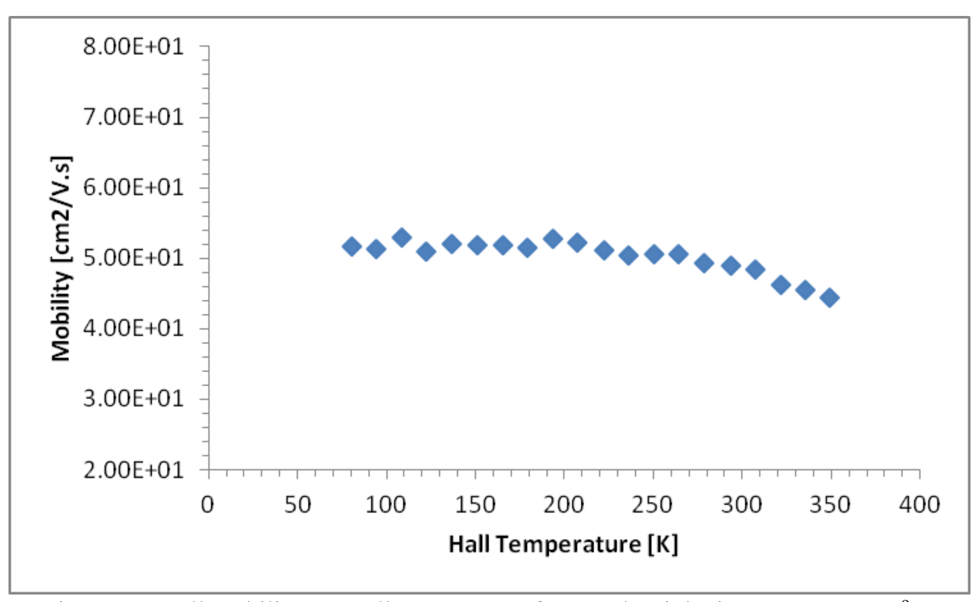

Figure 18. Hall mobility vs. Hall temperature for ZnO/n-Si device grown at 300 ^{o}C.

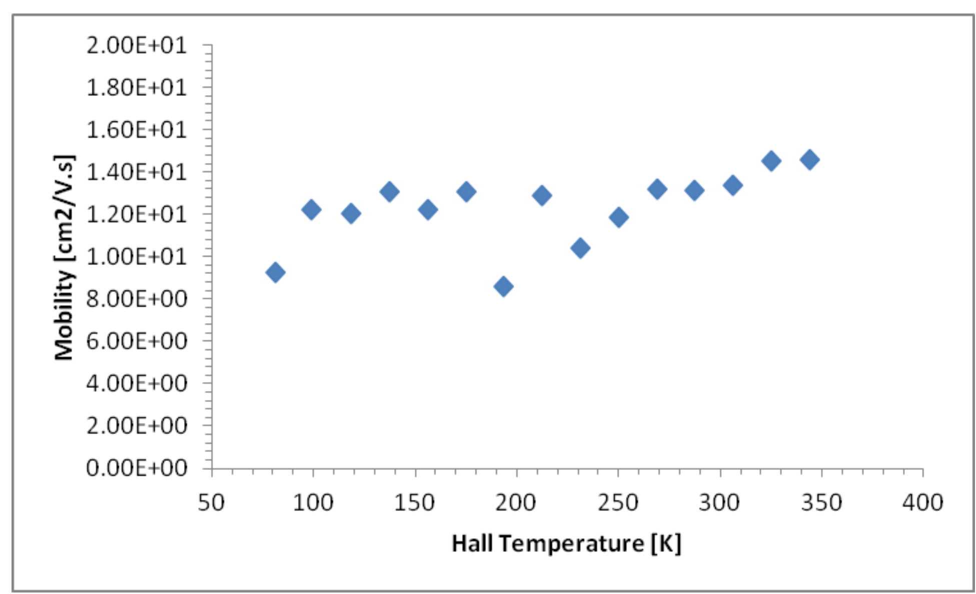

Figure 19. Hall mobility vs. Hall temperature for ZnO/n-Si device grown at 350 ^{o}C.

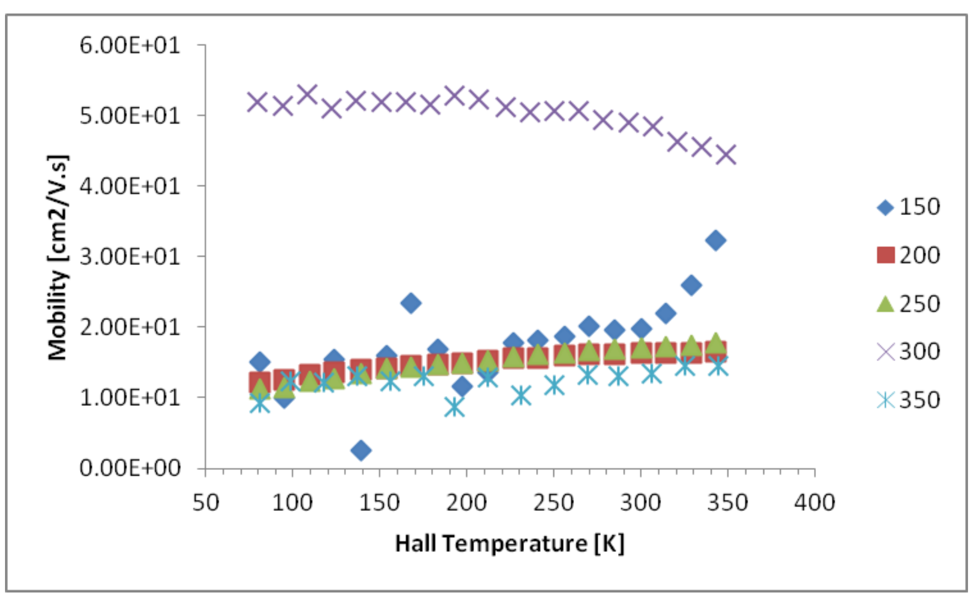

Figure 20. Hall mobility vs. Hall temperature plots for ZnO/n-Si samples grown at different growth temperatures.

Our results show that the Hall mobility for these devices are relatively constant for each growth temperature, and the positive slope shows the dominance of ionized impurity scattering for ZnO/n-Si systems throughout the whole Hall temper range.

The maximum Hall mobility for each growth condition is derived and the result which is consistent with the carrier concentrations results show that at 300 ^{o}C the scattering centers, i.e. ionized impurities and defects, are at their lowest concentration; hence, the maximum Hall mobility of 52.8 cm^2/Vs is achieved.

ZnO/p-Si Devices

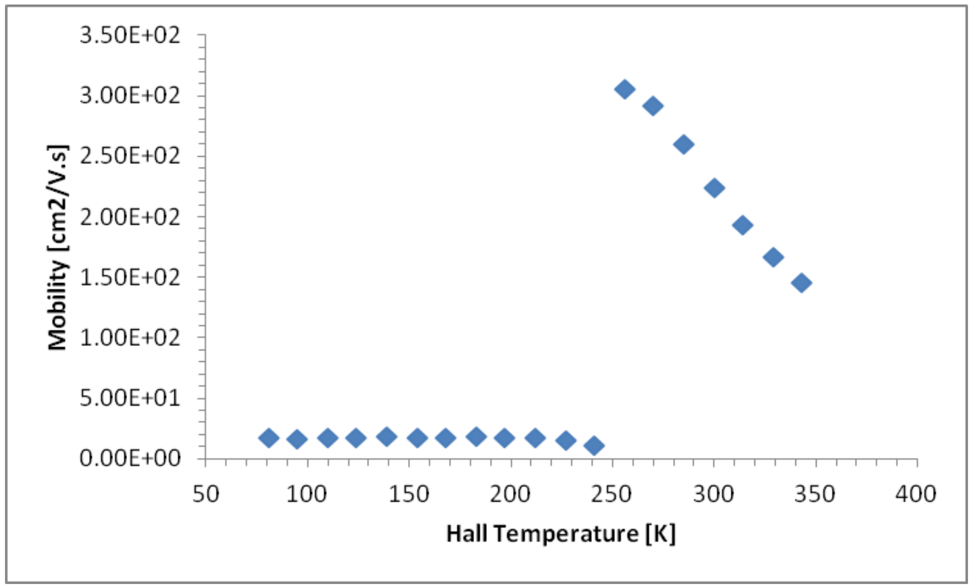

Figure 21. Hall mobility vs. Hall temperature for ZnO/p-Si device grown at 150 ^{o}C.

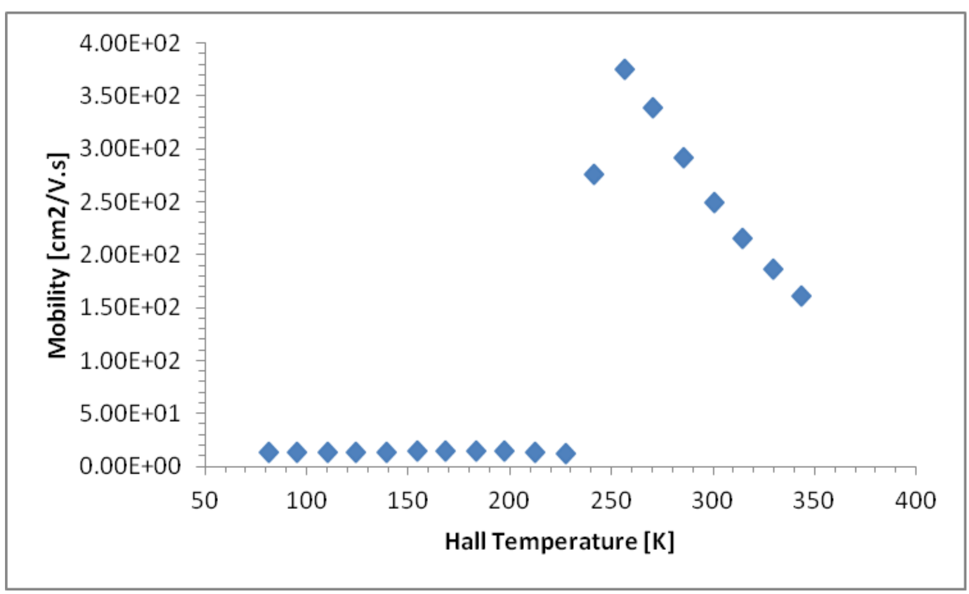

Figure 22. Hall mobility vs. Hall temperature for ZnO/p-Si device grown at 200 ^{o}C.

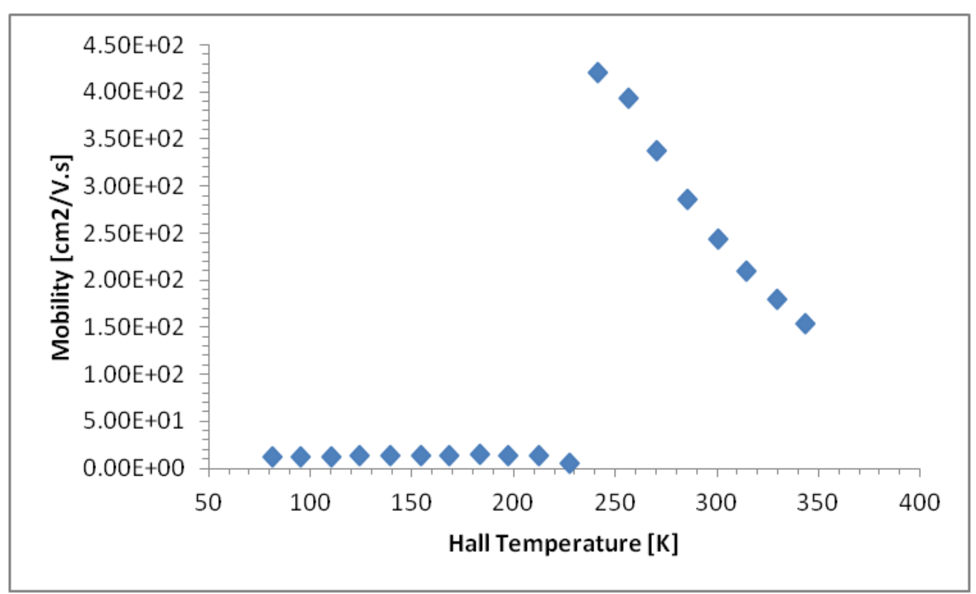

Figure 23. Hall mobility vs. Hall temperature for ZnO/p-Si device grown at 250 ^{o}C.

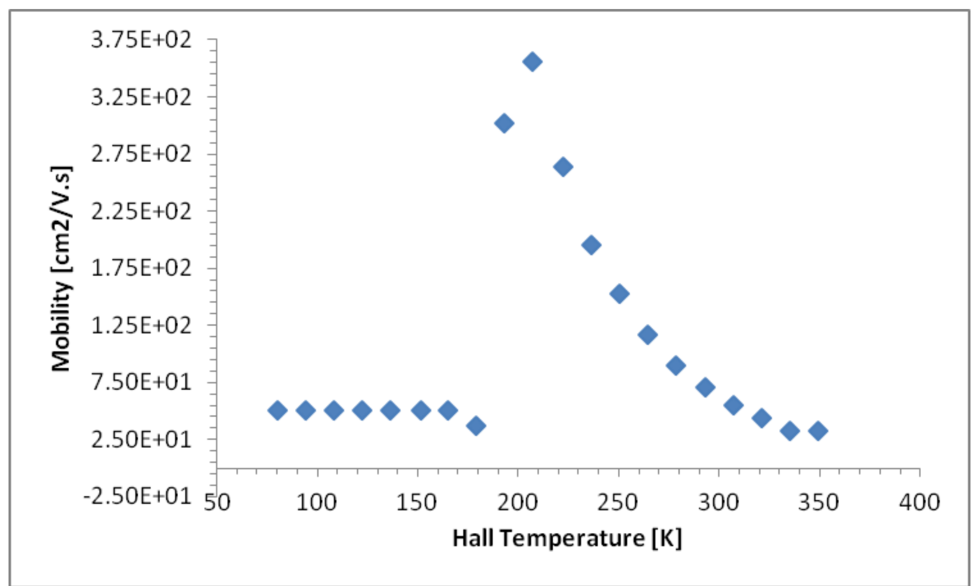

Figure 24. Hall mobility vs. Hall temperature for ZnO/p-Si device grown at 300 ^{o}C.

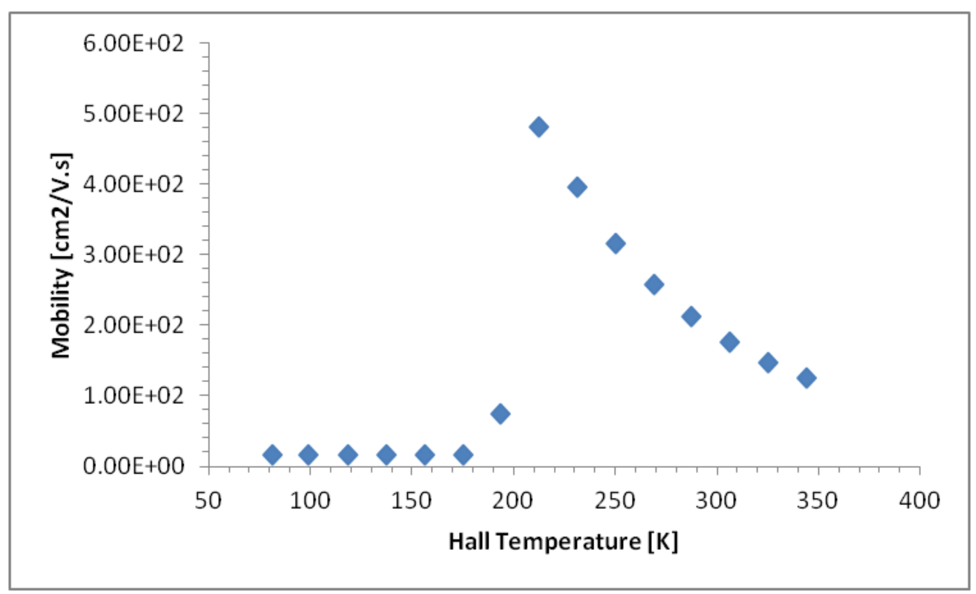

Figure 25. Hall mobility vs. Hall temperature for ZnO/p-Si device grown at 350 ^{o}C.

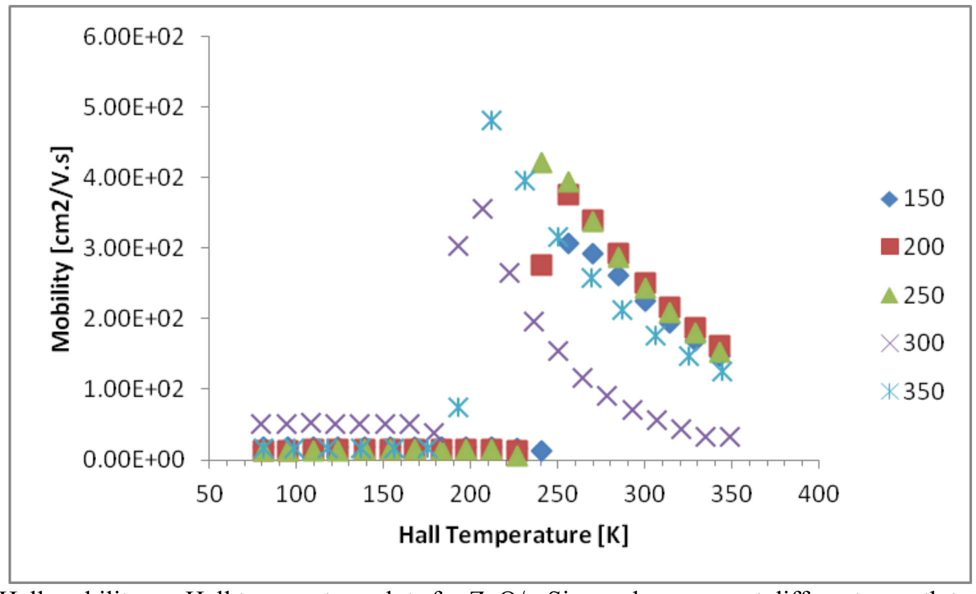

Figure 26. Hall mobility vs. Hall temperature plots for ZnO/p-Si samples grown at different growth temperatures.

The mobility of ZnO/p-Si devices is more interesting, and similar to the conductivity type of these devices, the mobility undergoes a drastic change for varying Hall temperatures from low (70K< T_H< 200K) to high (T_H>200K) Hall temperatures. At low temperatures, the mobility is relatively constant for each device with ionized scattering domination. Increasing the Hall temperature which has significant effects on the concentration of the defects increases lattice vibrations which lead to phonon scattering. Phonon scattering behavior is observed for all ZnO/p-Si devices regardless of the growth conditions. Growth temperature, however, affects the transitional point which is discussed in more details with the conductivity changes of the films.

6.3.1.2 Mobility vs. Hall Effect Temperature Plots; High Oxygen Overpressure Growth

ZnO/n-Si Devices

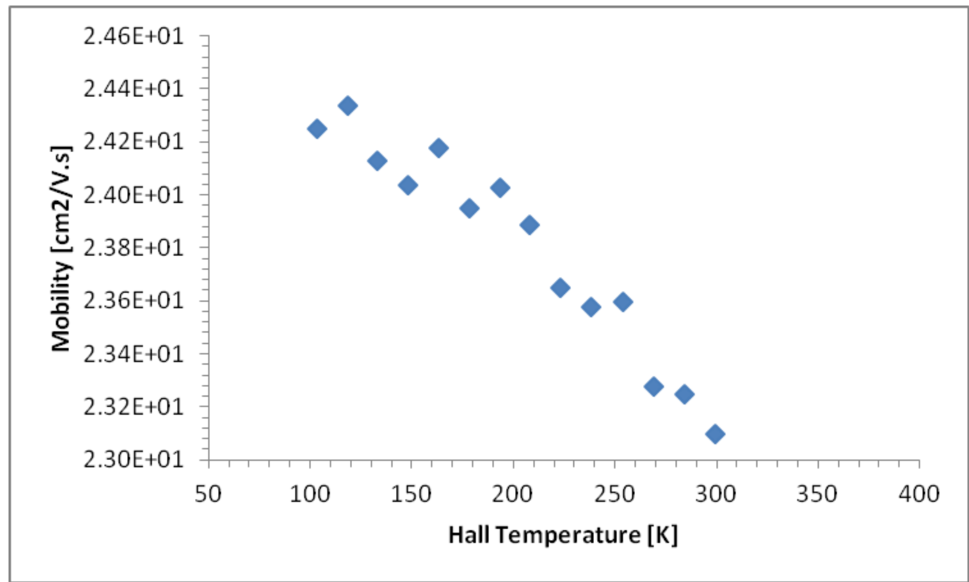

Figure 27. Hall mobility vs. Hall temperature for ZnO/n-Si device grown at 150 °C.

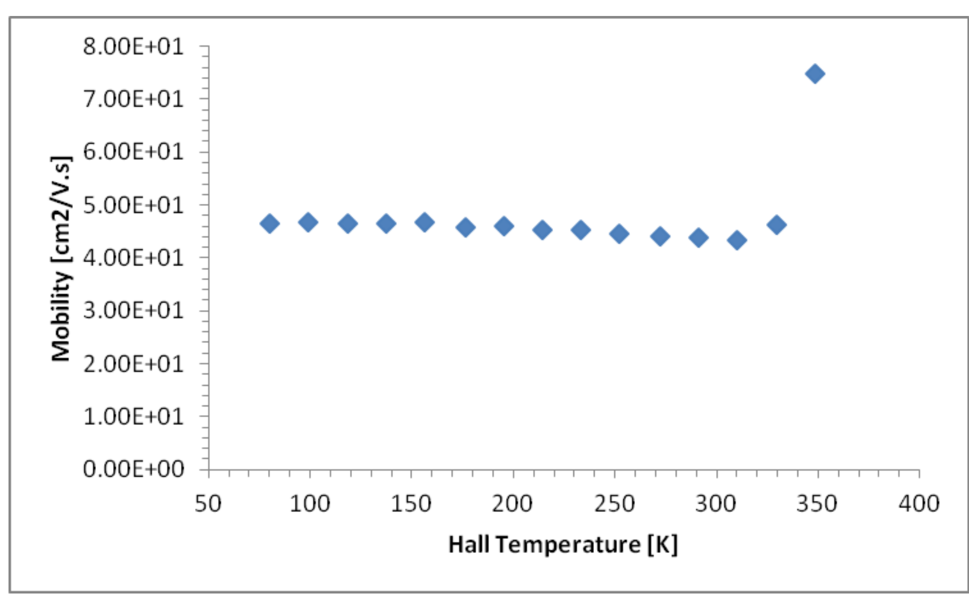

Figure 28. Hall mobility vs. Hall temperature for ZnO/n-Si device grown at 200 ^{o}C.

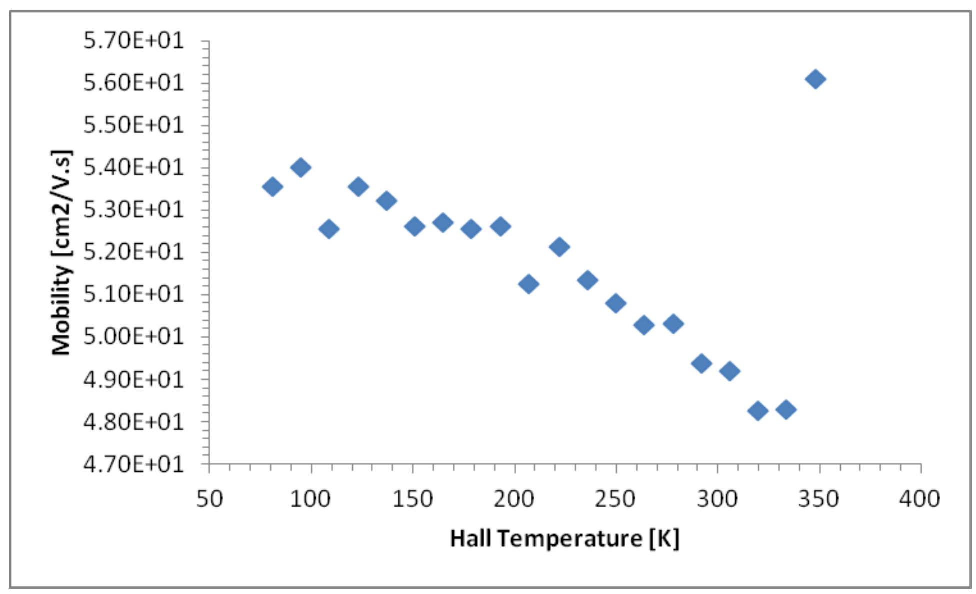

Figure 29. Hall mobility vs. Hall temperature for ZnO/n-Si device grown at 250 ^{o}C.

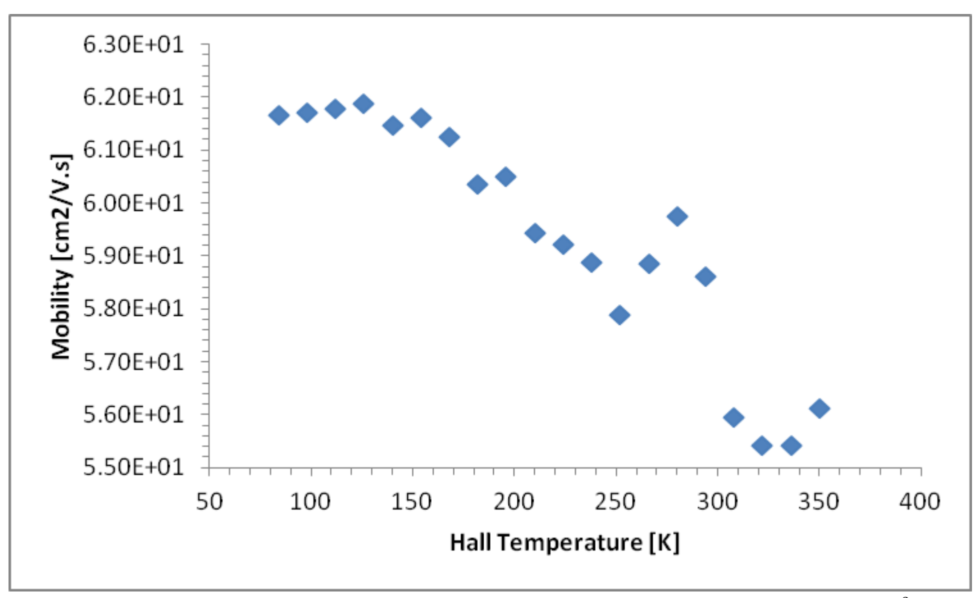

Figure 30. Hall mobility vs. Hall temperature for ZnO/n-Si device grown at 300 ^{o}C.

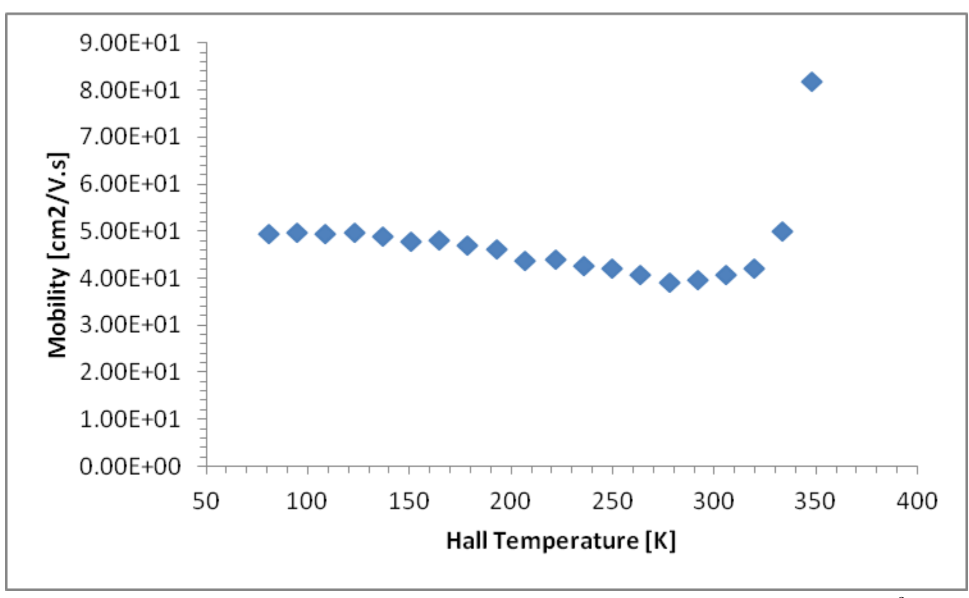

Figure 31. Hall mobility vs. Hall temperature for ZnO/n-Si device grown at 350 ^{o}C.

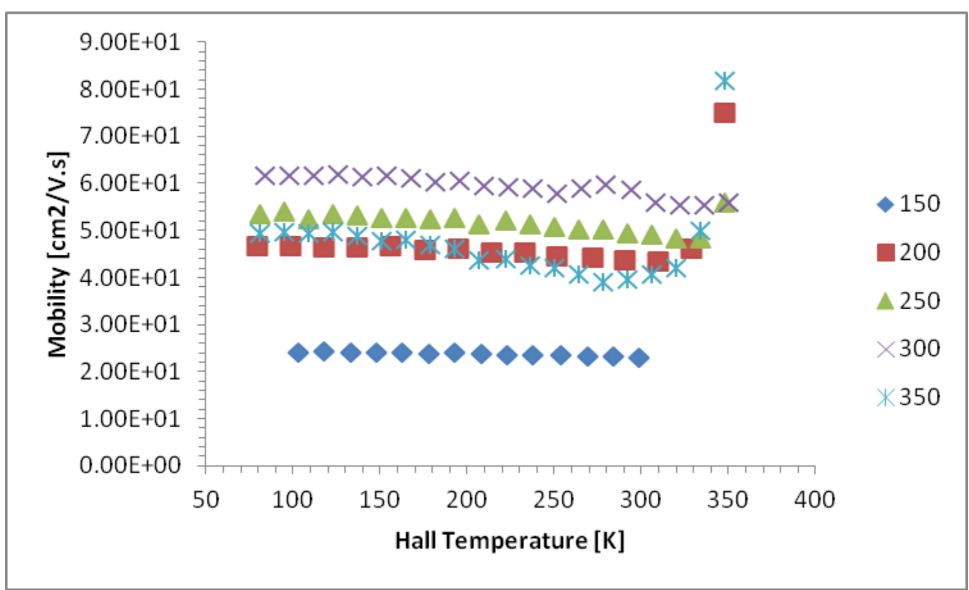

Figure 32. Hall mobility vs. Hall temperature plots for ZnO/n-Si samples grown at different growth temperatures.

Similar to low oxygen overpressure regime, electrons are scattered by ionized impurities scattering centers for ZnO/n-Si devices, and the mobility of the carriers relatively remains constant for each device. Again, different growth conditions affect the mobility of devices due to the changes in defects and impurities concentrations.

Maximum Hall mobility for each growth condition is derived, and the result which is consistent with the carrier concentrations results show that at 300 ^{o}C the scattering centers, i.e. ionized impurities and defects, are at their lowest concentration; hence, the maximum Hall mobility of 61.9 cm^{2}/Vs is achieved.

ZnO/p-Si Devices

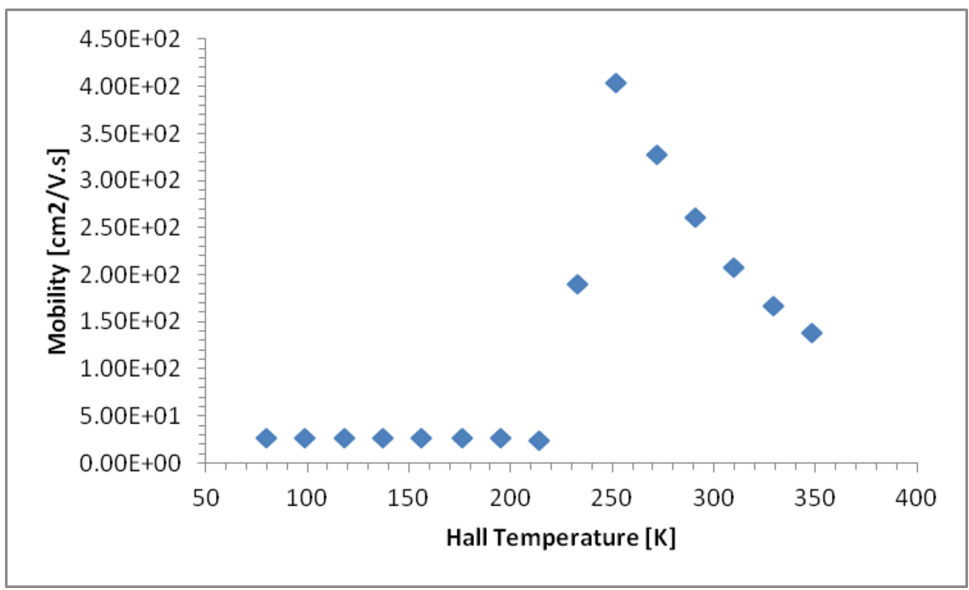

Figure 33. Hall mobility vs. Hall temperature for ZnO/p-Si device grown at 150 ^{o}C.

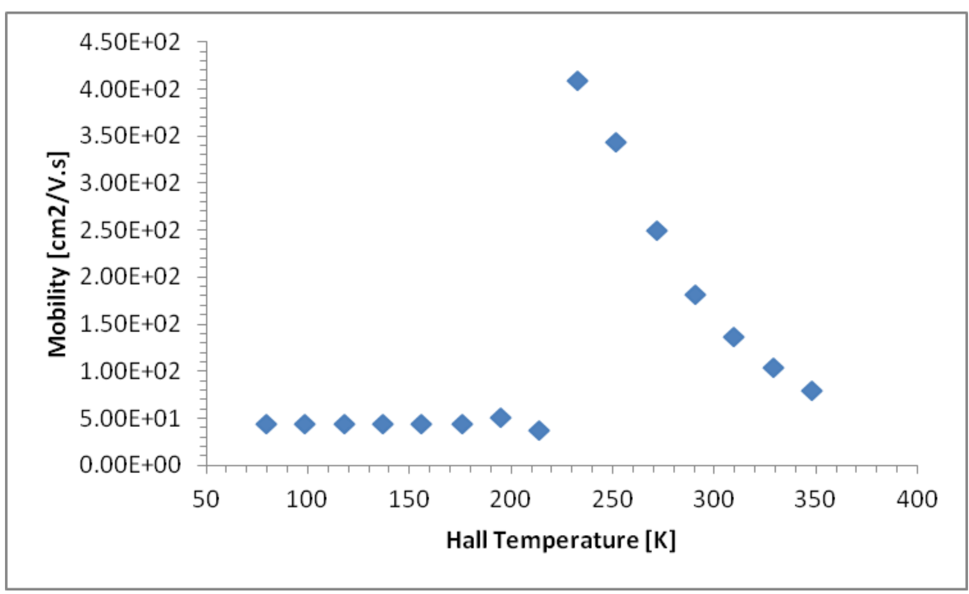

Figure 34. Hall mobility vs. Hall temperature for ZnO/p-Si device grown at 200 ^{o}C.

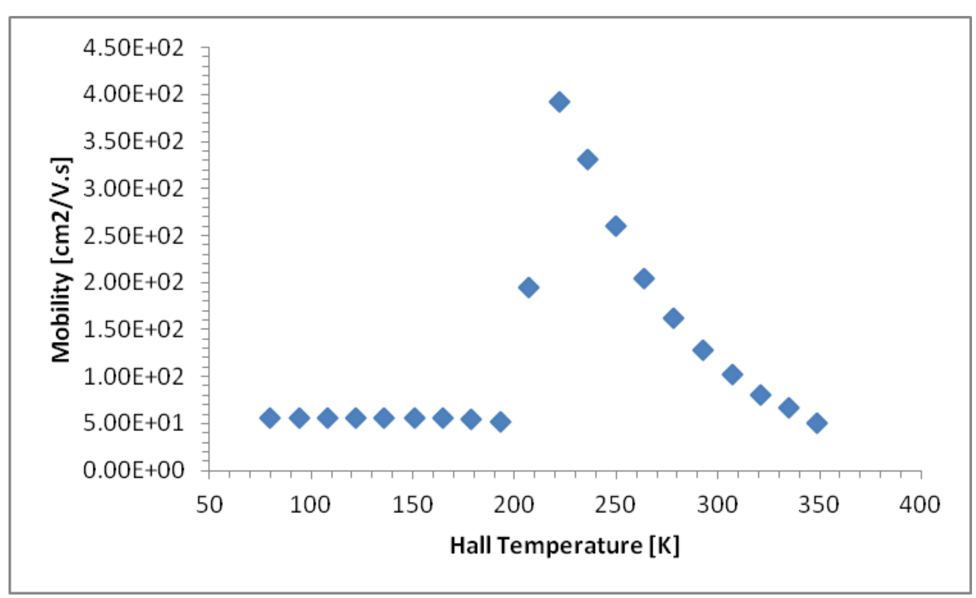

Figure 35. Hall mobility vs. Hall temperature for ZnO/p-Si device grown at 250 ^{o}C.

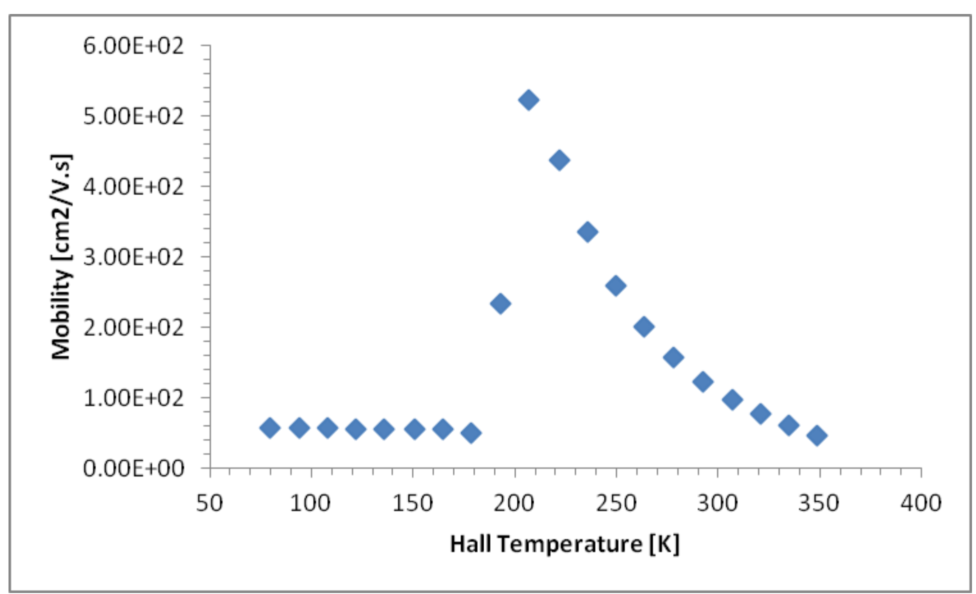

Figure 36. Hall mobility vs. Hall temperature for ZnO/p-Si device grown at 300 ^{o}C.

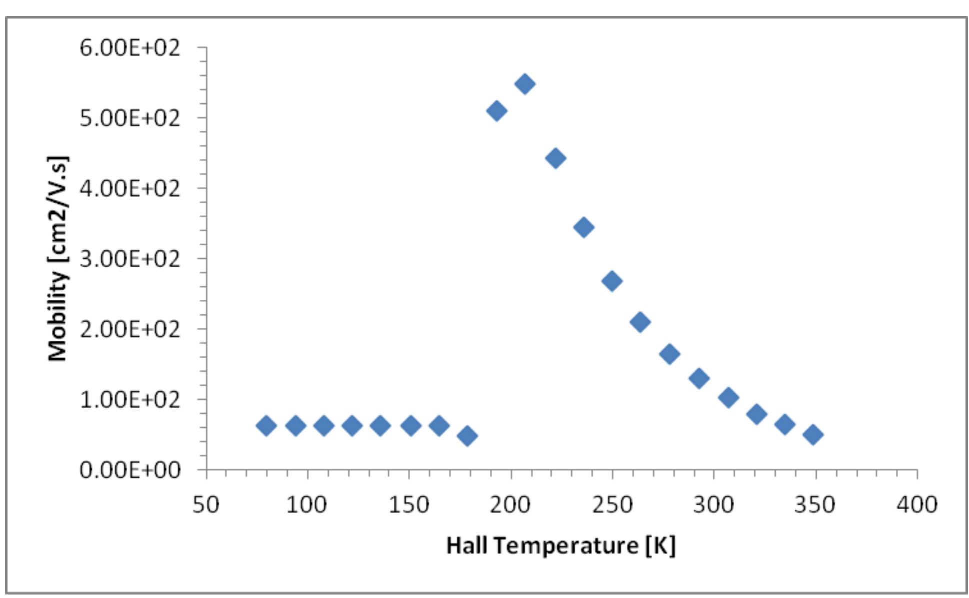

Figure 37. Hall mobility vs. Hall temperature for ZnO/p-Si device grown at 350 ^{o}C.

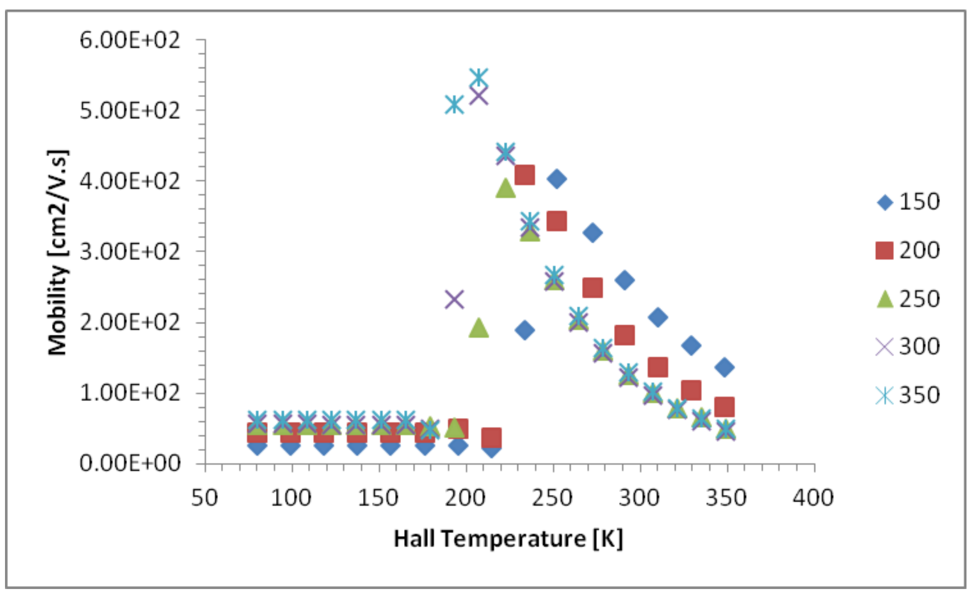

Figure 38. Hall mobility vs. Hall temperature plots for ZnO/p-Si samples grown at different growth temperatures.

The results are consistent with the previous results for low oxygen pressure regime. However, due to the high oxygen pressure the concentration of intrinsic defect, mostly oxygen vacancies, are reduced and therefore the mobility is expected to be higher in this case.

Figure 39 compares the mobility of ZnO/n-Si devices grown at low and high oxygen over pressures. It is evident that high oxygen partial pressure results in higher mobility levels.

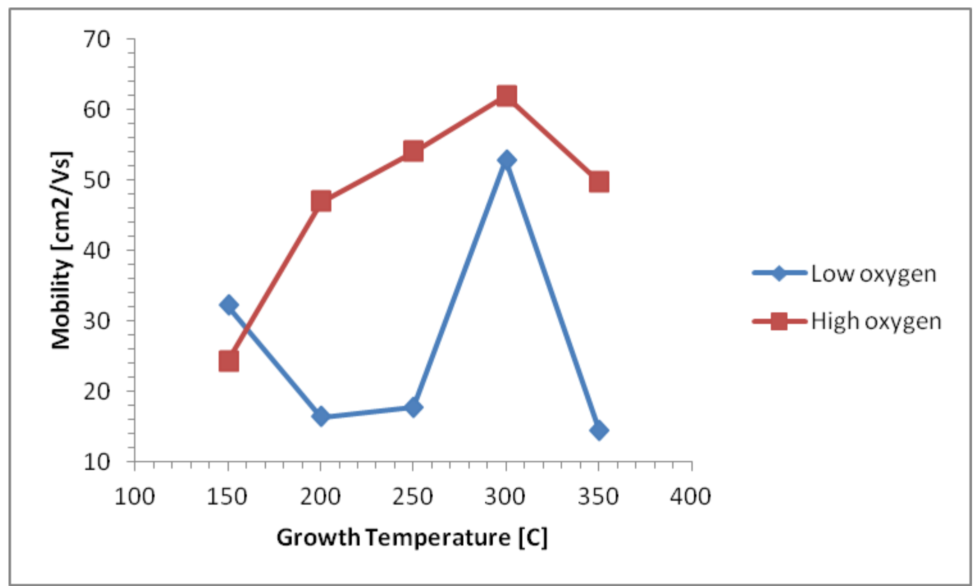

Figure 39. Maximum Hall mobility vs. growth temperature for ZnO/n-Si devices grown at low and high oxygen overpressures. The mobility is maximized at 300 ^{o}C and high oxygen overpressure.

Figure 40 shows the maximum mobility of ZnO/p-Si devices grown at low and high oxygen over pressures. Similar to our n-Si devices, the mobility for high oxygen overpressure is generally higher than the low oxygen pressure growth and the mobility increases with the increase in the growth temperature.

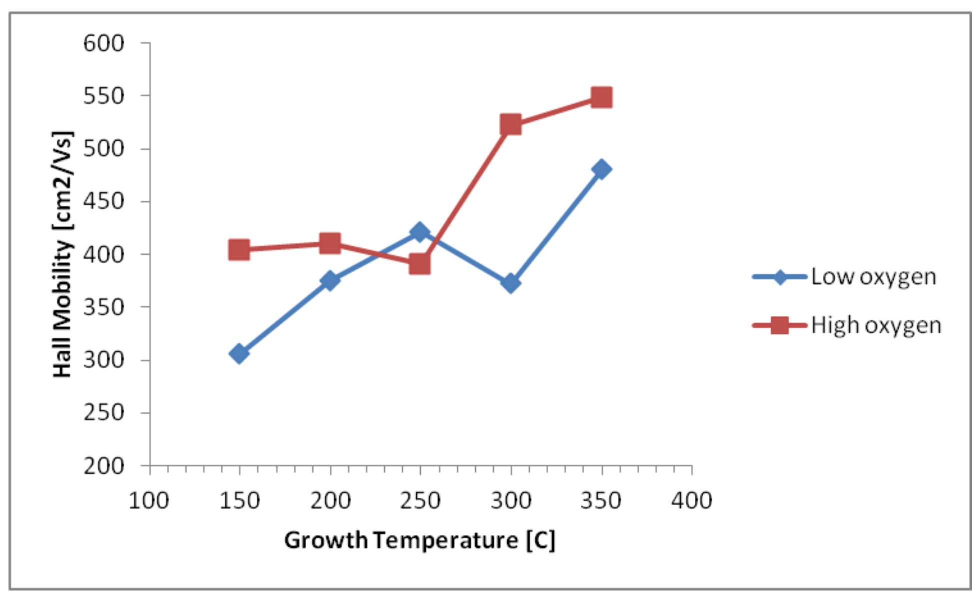

Figure 40. Maximum Hall mobility vs. growth temperature for ZnO/p-Si devices grown at low and high oxygen overpressures. The mobility is higher for samples grown at high oxygen overpressure.

In order to investigate the transport mechanism in ZnO/p-Si devices, the electrical resistivity and conductivities of the films grown on p-Si are studied in more details.

The electrical resistivity of ZnO/p-Si devices grown at different temperatures and the two oxygen overpressures for the wide range of Hall temperatures are shown in figures 47 and 48 respectvely. Three resistivity regions are observed. At low Hall temperatures (80K up to the transition point) a relatively constant resistivity is observed. At temperatures between 180-200K and 200-250K (depending on the growth conditions) a fast reduction of the resistivity is observed, and for high Hall temperatures (250K to 350K) the resistivity increases with the increase in the temperature.

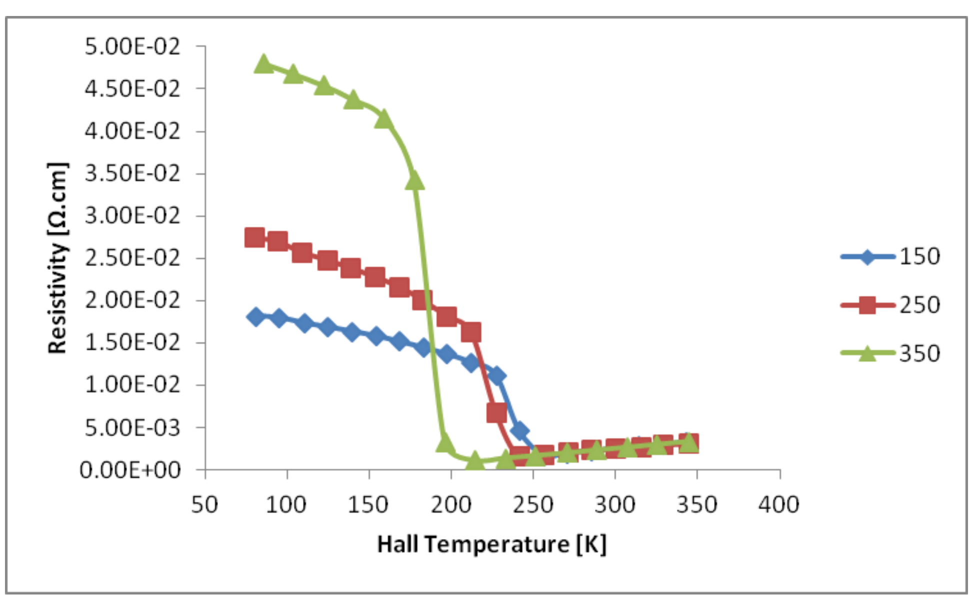

Figure 41. Electrical resistivity vs. Hall temperature for ZnO/p-Si devices grown at different growth temperatures of 150, 250, and 350 °C and low growth pressure. Three regions of resistivity (an almost constant region for low temperatures, a fast-reduction region for middle range temperatures, and an increasing region for high temperatures) are observed.

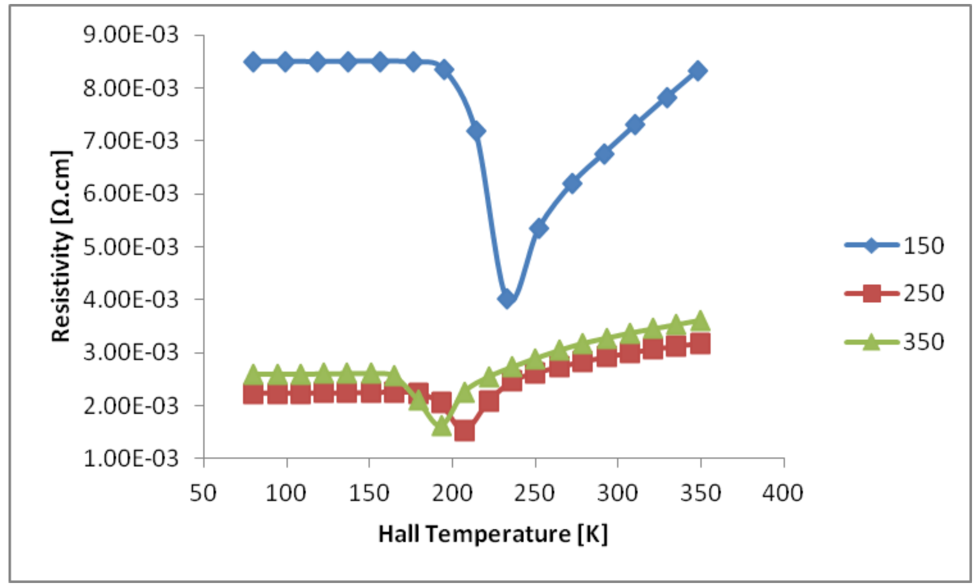

Figure 42. Electrical resistivity vs. Hall temperature for ZnO/p-Si devices grown at different growth temperatures of 150, 250, and 350 °C and high growth pressure. Three regions of resistivity (an almost constant region for low temperatures, a fast-reduction region for middle range temperatures, and an increasing region for high temperatures) are observed.

It is evident that the conduction mechanism changes as the Hall temperature increases. The electrical conductivities of the devices are show in figure 43 and figure 44.

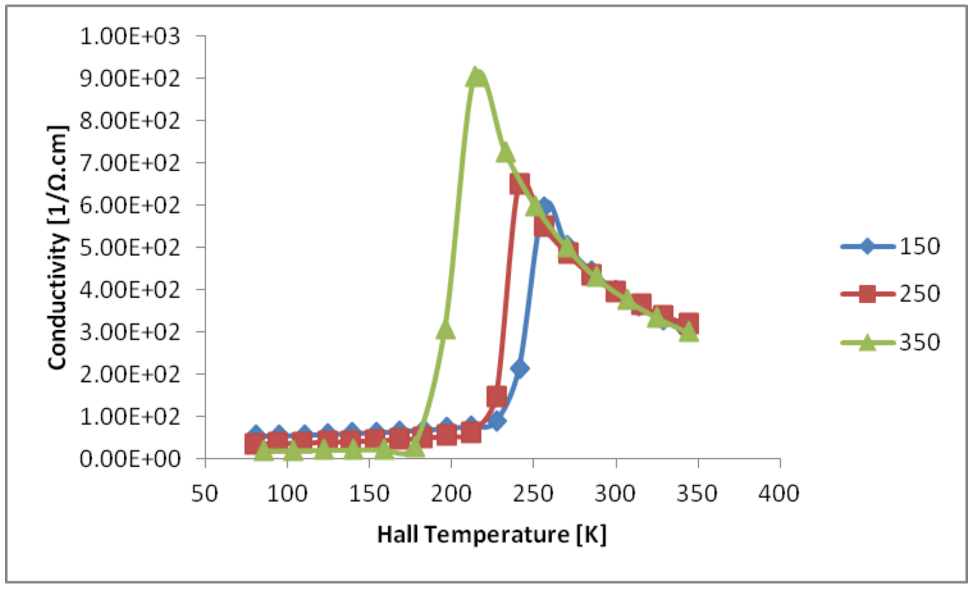

Figure 43. Electrical conductivity vs. Hall temperature for ZnO/p-Si devices grown at different growth temperatures of 150, 250, and 350 °C and low growth pressure.

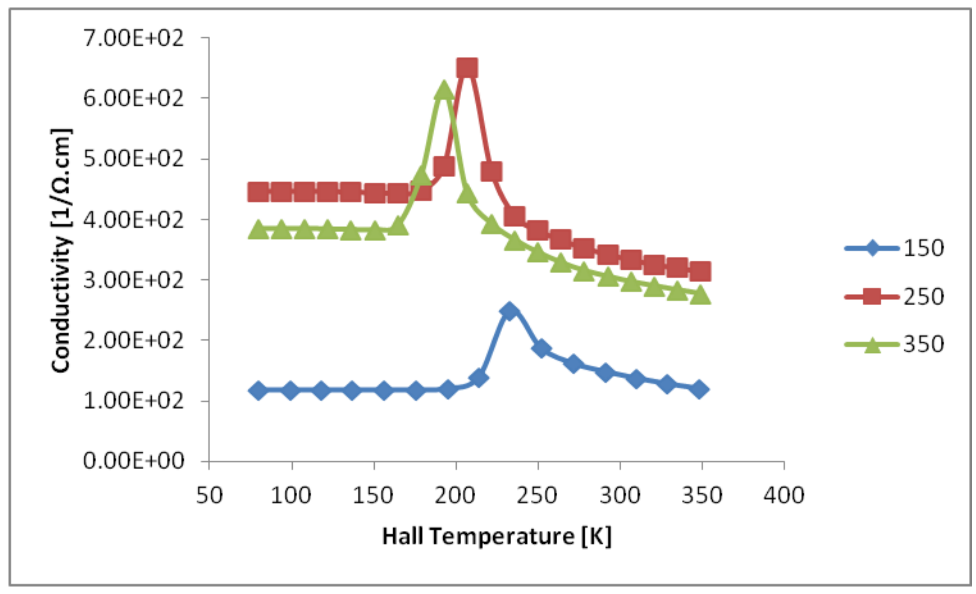

Figure 44. Electrical conductivity vs. Hall temperature for ZnO/p-Si devices grown at different growth temperatures of 150, 250, and 350 °C and high growth pressure.

Our electrical conductivity results show that for low temperatures the conduction mechanism is dominated by hopping in the acceptor bands and for high temperatures the thermally activated behavior is observed. This hopping conduction behavior is reported and explained in details elsewhere(Brilis, et al., 2008).

In a nut shell, this type of conductivity mechanism which is observed for highly doped or compensated semiconductors and disordered materials is explained by the overlapping of the electron wavefunctions and widening of the impurity levels to form a narrow band inside the band-gap. When the impurity bands are not filled, conduction takes place between these impurity bands.

It has been shown that the temperature dependence of the conductivity, and the transport mechanism, is expressed by the variable range hopping conduction mechanism for the low temperatures, the nearest-neighbor hopping conduction mechanism for the medium temperature, and thermal activation of the acceptor band for the high hall temperatures where the p-conductivity is observed. Thus, the Hall mobility for ZnO/p-Si devices can be explained as the following. At low temperatures, hole transport is limited to the narrow impurity (native acceptor-like defects) bands whereas increasing the temperature extends the defects bands to the valance bands and increases the mobility. This is consistent with thermal activation of acceptor bands observed in electrical conductivity of the films. Further increases in the temperature, introduces phonon scatterings (negative slope of the Hall mobility) which is more pronounces for high Hall temperatures.

6.4 Grain Size

In addition to ionized impurities and lattice phonons, scattering by grain boundaries is also important in polycrystalline semiconductors and different theories have been used to express the scattering due to grain boundaries(Ling, 1983). It is shown that grain boundaries are electron traps where electrons are scattering by these scattering centers. In our experiments we observed that growth conditions, namely growth temperature, affect the grain size of the grown ZnO layer. The average grain size of our ZnO samples is calculated by Scherrer formula(Esmaili Sardari, et al., 2010):

$$D = (0.89\lambda)/ (B \cos\theta) \qquad \text{eq. 21}$$

Where

D is the average grain size
λ is the X-ray wavelength of 0.15418 nm
B is FWHM in radians
θ is the diffraction angle

For instance, based on our FWHM values from the XRD spectra, an average grain size of 23, 33, and 22 nm was obtained for samples grown at 200, 250, and 300 ^{o}C. Since films with larger grains have less grain boundaries, then they have less scattering and higher mobility.

Initially, a set of samples on n and p-Si substrates with a 500 nm oxide (SiO_2) layer grown by plasma enhanced chemical vapor deposition (PECVD) were prepared. The samples were grown in low oxygen growth regime (5.0×10^{-6} Torr). The growth temperature was varied between 100 and 350 ^{o}C with 50° step size.

Hall measurements show high carrier concentrations in the order 10^{19}~10^{20} for all samples measured at different Hall temperatures, T_H. There are fluctuations in carrier density and Hall coefficients with respect to reading temperature but they are negligible.

Sample Growth Temperature	Substrate	Bulk Concentration	Average Hall Coefficient
100 ^{o}C	n	-3.1×10^{19} cm^{-3}	-2.0×10^{-1} cm^3/C
100 ^{o}C	p	-3.2×10^{19} cm^{-3}	-1.9×10^{-1} cm^3/C
150 ^{o}C	n	-2.6×10^{19} cm^{-3}	-1.7×10^{-1} cm^3/C
150 ^{o}C	p	-2.4×10^{19} cm^{-3}	-1.5×10^{-1} cm^3/C
200 ^{o}C	n	-2.1×10^{19} cm^{-3}	-2.9×10^{-1} cm^3/C
200 ^{o}C	p	-2.0×10^{19} cm^{-3}	-3.0×10^{-1} cm^3/C
250 ^{o}C	n	-1.8×10^{19} cm^{-3}	-3.3×10^{-1} cm^3/C
250 ^{o}C	p	-1.8×10^{19} cm^{-3}	-3.4×10^{-1} cm^3/C
300 ^{o}C	n	-1.0×10^{20} cm^{-3}	-6.1×10^{-2} cm^3/C
300 ^{o}C	p	-8.5×10^{19} cm^{-3}	-7.3×10^{-2} cm^3/C
350 ^{o}C	n	-1.5×10^{19} cm^{-3}	-4.0×10^{-1} cm^3/C
350 ^{o}C	p	-1.4×10^{19} cm^{-3}	-4.4×10^{-1} cm^3/C

Table 4. Carrier concentration and Hall coefficients for n and ZnO/p-Si devices grown at low oxygen overpressure of ~5.0×10^{-6} Torr and various temperatures. A 500 nm oxide layer is grown by PECVD prior to ZnO growth. All the Hall readings are performed for a wide range of Hall temperatures (80K to 350K) and the average values are reported here.

Another set of samples were then prepared on oxide removed Si substrates at 250 ^{o}C and oxygen pressure of 1.0×10^{-4} Torr. We observed a conductivity change at high Hall temperatures for these samples. Carrier concentrations and Hall coefficients of the samples are reported in table 5.

Sample Growth Temperature	Substrate	Bulk Concentration	Average Hall Coefficient
250 ^{o}C	n	-1.5×10^{19} cm^{-3}	-4.3×10^{-1} cm^3/C
250 ^{o}C	p	80K < T_H< 212K -2.0×10^{14} 212K < T_H 1.3×10^{19} cm^{-3}	80K < T_H< 212K -4.36×10^{-1} to -2.21×10^{-1} 212K< T_H 5.0×10^{-1} cm^3/C

Table 5. Carrier concentration and Hall coefficients for n and ZnO/p-Si devices grown at oxygen overpressure of 1.0×10^{-4} Torr and 250 ^{o}C.

Interesting behavior was observed for the sample grown on p-Si substrate. For this device, low temperature Hall readings showed n-type behavior with significantly lower electron concentrations. On the other hand, p-type characteristic was confirmed for high temperature readings (212K< T_H). To confirm the observed behavior, several samples were fabricated and studied. In the following sections the experimental details along with the results and discussions are presented.

6.5 Electrical Studies of n and ZnO/p-Si Devices

To further investigate the p-type behavior of ZnO films, several samples were fabricated at different growth temperatures and oxygen overpressure. More specifically, two series of samples were prepared at different growth temperatures and two different oxygen overpressure regimes. The oxygen overpressure was kept high at 2.5×10^{-6} Torr for one series of samples, and low at 5.5×10^{-6} Torr for the other. Growth temperatures for both series of ZnO films were 150, 200, 250, 300, and 350 ^{o}C.

6.5.1 Results

6.5.1.1ZnO/n-Si Devices

All the films grown on n-type Si substrates showed almost-constant carrier concentrations for Hall measurement temperature range of 80K to 350K. Carrier concentration of the film grown at low oxygen pressure showed fluctuations with Hall temperature for the device grown at 150 ^{o}C, whereas films grown at high oxygen pressure exhibited no fluctuations in carrier concentrations for all growth temperatures. The lowest carrier concentration was observed for the 300 ^{o}C grown film at low oxygen overpressure regime, while at high oxygen overpressure, lowest concentration was reached for the film grown at 350 ^{o}C. Figure 45 and figure 46 show carrier concentrations versus Hall measuring temperature for films grown on n-Si substrates under growth temperatures of 150, 200, 250, 300, and 350 ^{o}C at high and low oxygen overpressures, respectively. The fluctuations observed in the carrier concentration under low oxygen and low temperature growth (150 ^{o}C) on n-Si substrates, are suppressed at the high oxygen overpressure pressure regime.

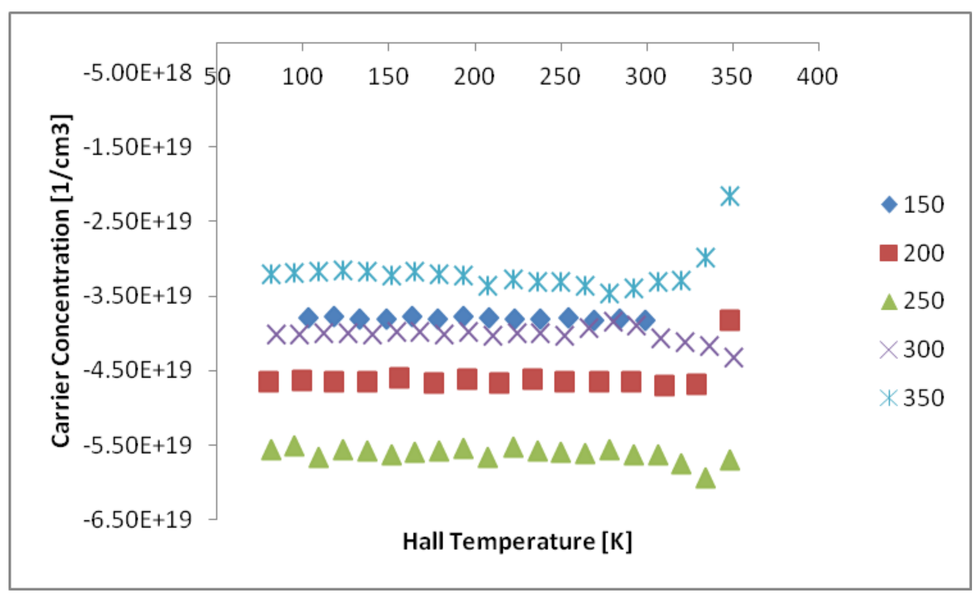

Figure 45. Carrier concentration vs. Hall temperature for samples grown on n-Si substrates under high oxygen overpressure. Different plots are for different growth temperatures.

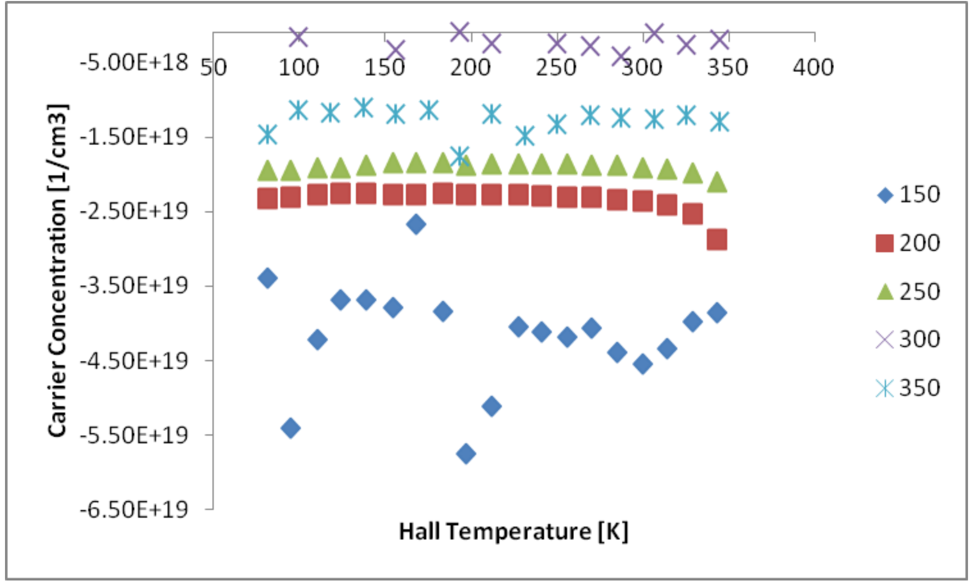

Figure 46. Carrier concentration vs. Hall temperature for samples grown on n-Si substrates under low oxygen overpressure. Different plots are for different growth temperatures.

6.5.1.2 ZnO/p-Si Devices

All films grown on p-Si substrates exhibited different electrical behavior. Regardless of the growth temperature and oxygen overpressure, all ZnO films showed n-type carrier (electron) concentrations for low Hall temperatures while for higher Hall temperatures carrier concentration switched to p-type (hole). For films grown at high oxygen pressure we observed

almost constant concentrations whereas the films grown at low pressure showed small changes with the change in Hall measurement temperatures. For elevated Hall temperatures (between 180 and 250K, depending on growth temperature), all films showed increasing hole concentrations. Figure 47 and figure 48 show both electron and hole concentrations for undoped ZnO films grown on p-Si substrates at different growth temperatures and the two oxygen overpressures.

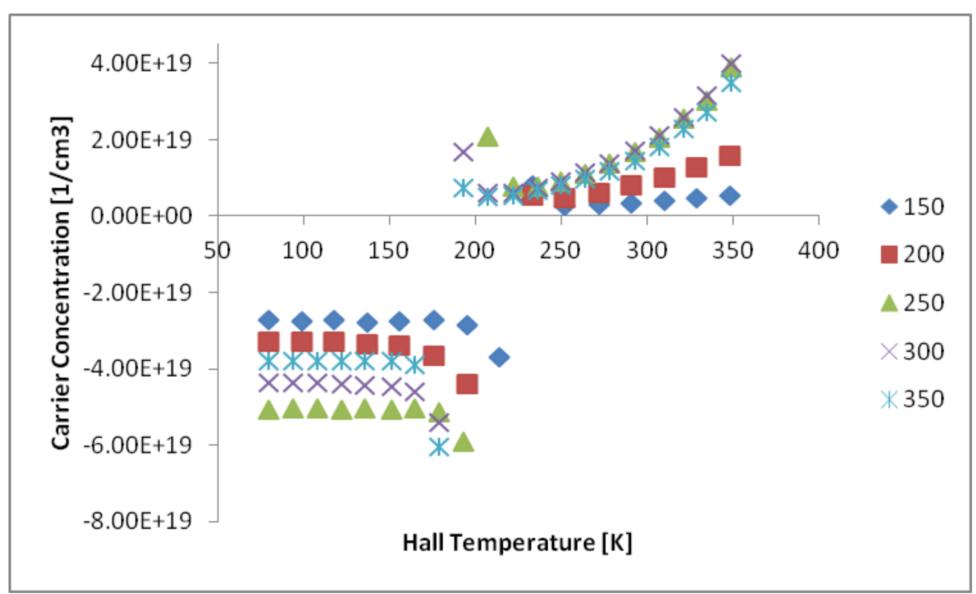

Figure 47. Carrier concentration vs. Hall temperature for samples grown on p-Si substrates and high oxygen overpressure. Different plots are for different growth temperatures.

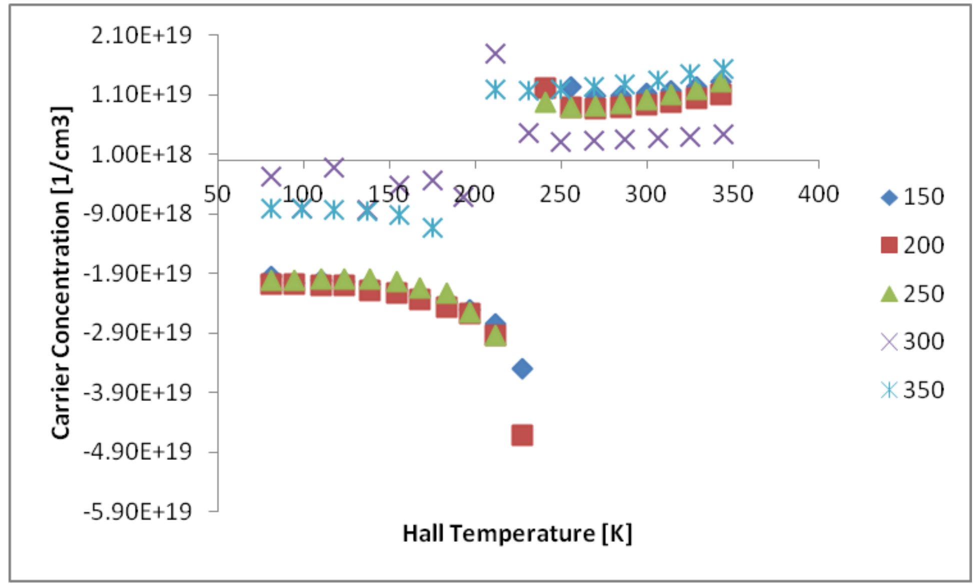

Figure 48. Carrier concentration vs. Hall temperature for samples grown on p-Si substrates and low oxygen overpressure. Different plots are for different growth temperatures.

Our results show that high oxygen overpressure improves the electrical properties of the grown layers and promotes p-type conductivity which is further confirmed by examining the Hall Effect coefficients for films grown on p-Si substrates. Figure 49 and 50 show Hall coefficients versus growth temperatures for films grown on p-Si at high and low oxygen overpressure, respectively. By comparing the two figures, we can see that p-type conductivity at high oxygen overpressure is more dominant due to further reduction in donor-like oxygen vacancy defects. The results also show that films grown at high oxygen overpressure change conductivity to p-type at lower Hall temperatures.

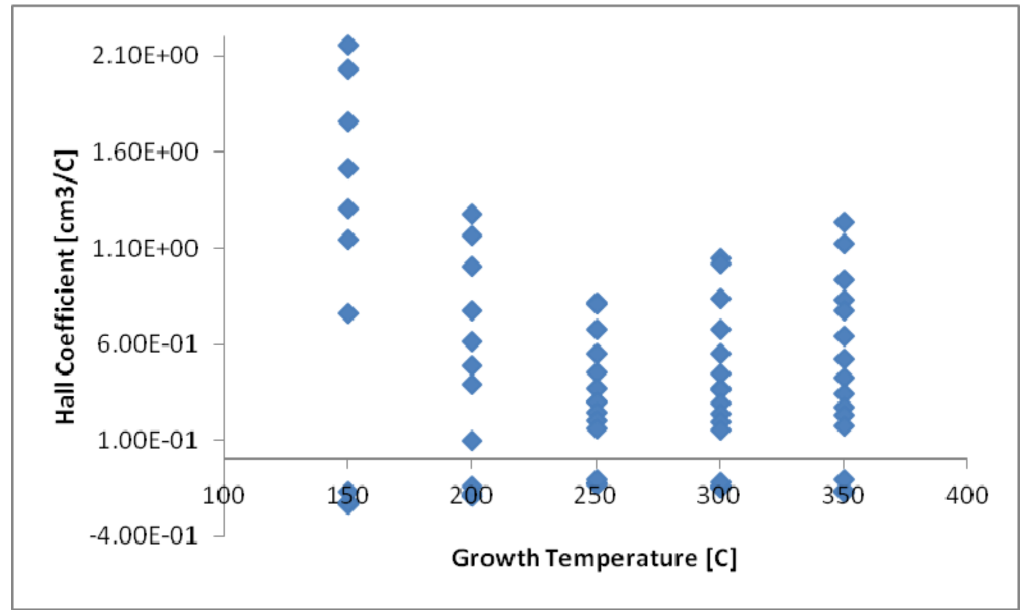

Figure 49. Hall Coefficient vs. growth temperature for films grown on p-type Si (100) substrates at high oxygen overpressure. All samples show n-type behavior at low measuring temperatures while p-type behavior is observed for higher Hall Effect measurement temperatures. As compared with the low oxygen regime p-type conductivity at high oxygen overpressure is more dominant due to the further reduction in donor-like oxygen vacancy defects.

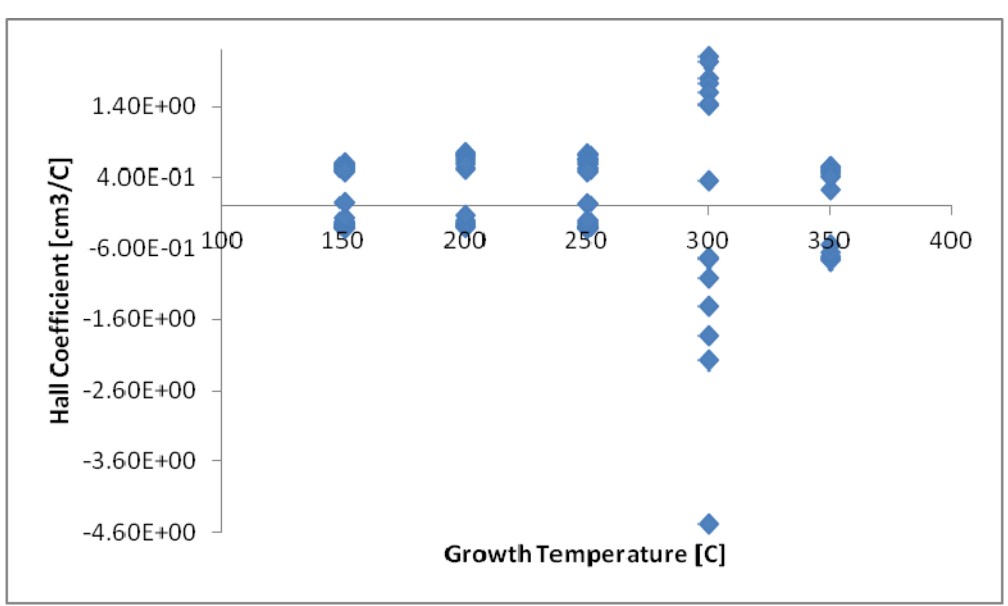

Figure 50. Hall Coefficient vs. growth temperature films grown on p-type Si (100) substrates at low oxygen pressure. All samples show n-type behavior at low measuring temperatures while p-type behavior is observed for higher Hall Effect measurement temperatures.

Conductivity Conversion Temperature

The conductivity conversion was observed at different Hall temperatures, and it correlates with the growth temperature consistently. More specifically, films grown at lower growth temperatures undergo the conversion at higher Hall temperatures, and as the growth temperature increases, the transition-point decreases to lower Hall temperatures. This is attributed to the fact that increasing the growth temperature improves the quality of the films and reduces the intrinsic donor-like native defects including oxygen vacancies and hydrogen complexes. Figure 51 and figure 52 show the Hall coefficient of the ZnO films versus the Hall temperatures.

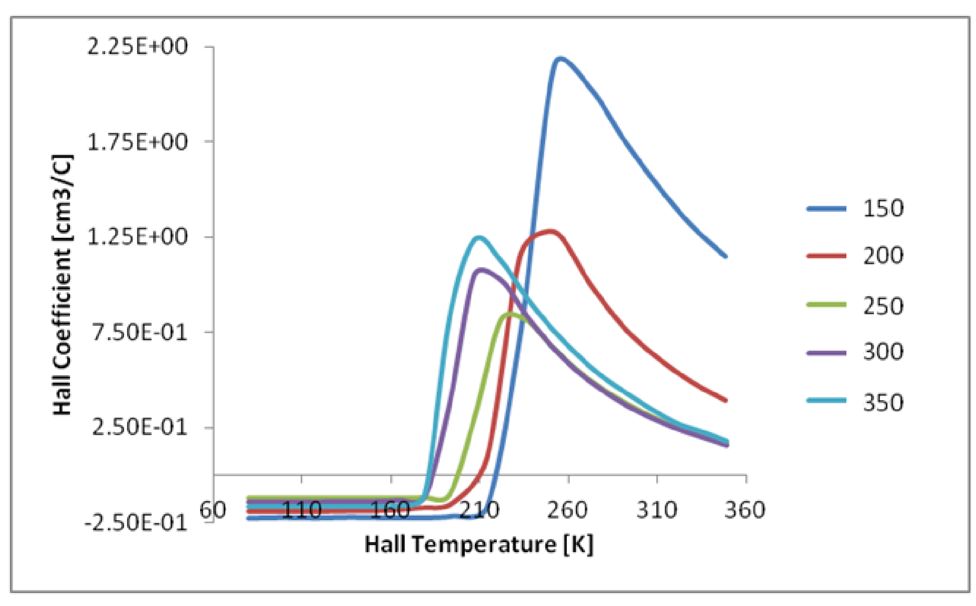

Figure 51. Hall Coefficient vs. Hall measuring temperature for ZnO films grown on p-type Si (100) substrates and high oxygen overpressure. Different plots are for different growth temperatures.

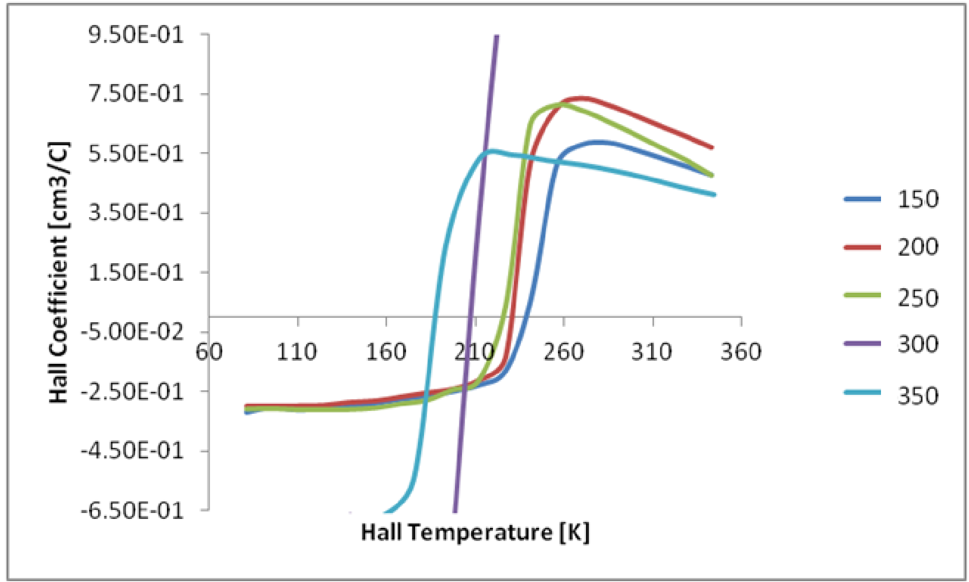

Figure 52. Hall Coefficient vs. Hall measuring temperature for ZnO films grown on p-type Si (100) substrates and low oxygen overpressure. Different plots are for different growth temperatures.

Figure 53 shows the Hall coefficient versus Hall temperature for the film grown at 300 ^{o}C and low oxygen overpressure. This is the extended plot of the sample for 300 ^{o}C shown in figure 52.

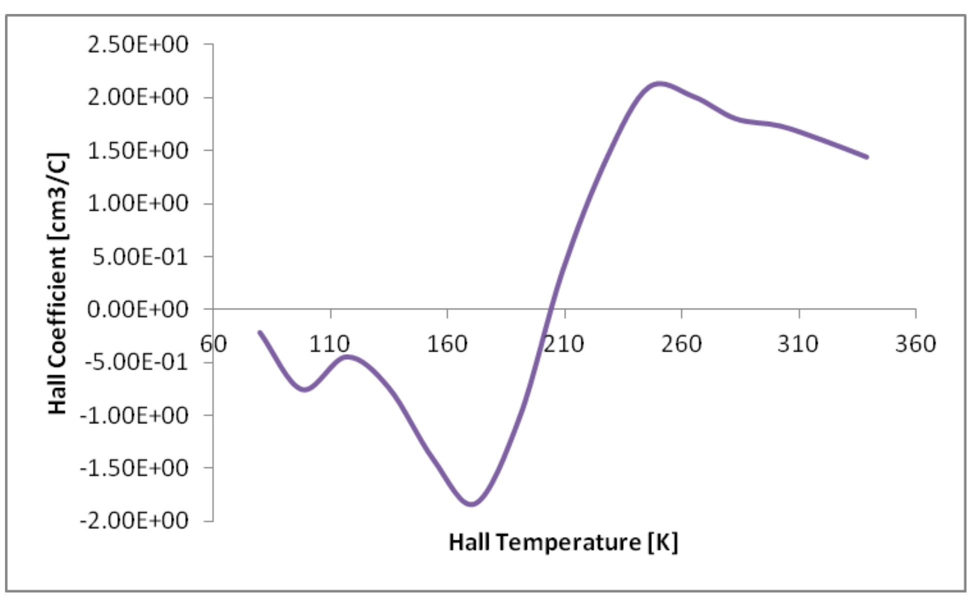

Figure 53. Hall Coefficient vs. Hall measuring temperature for ZnO films grown on p-type Si (100) substrates and low oxygen overpressure and 300 ^{o}C. This is the extended plot of the sample shown in figure 52.

In both cases, the transitions from n to p-type occur at lower Hall temperatures as the growth temperature increases. Figure 53 shows the transition temperature versus the growth temperature for the studied devices.

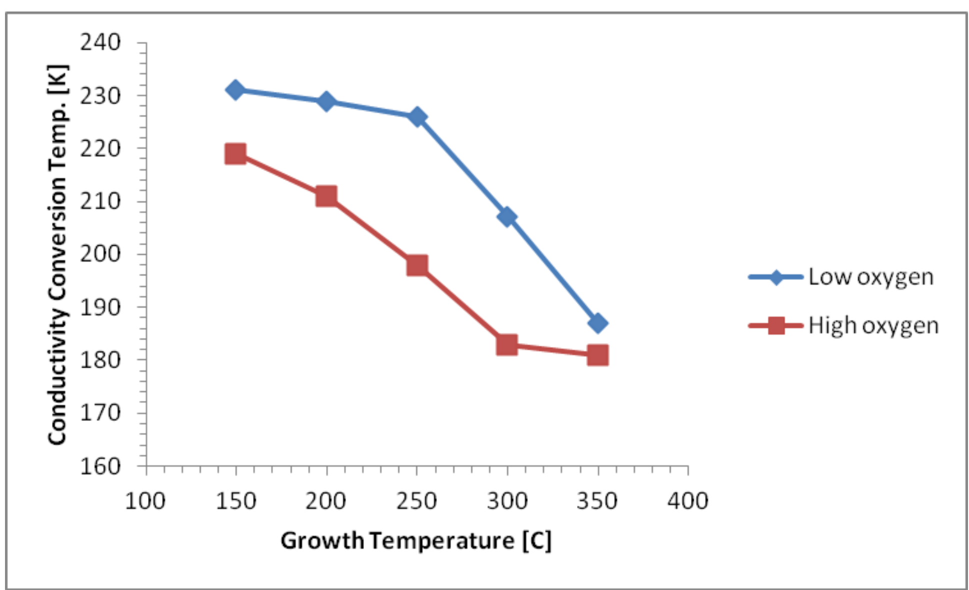

Figure 54. Conductivity conversion temperature vs. growth temperature for the samples grown at low (top plot) and high (bottom plot) oxygen overpressure.

It is evident that the films show p-type behavior at lower temperatures as the growth temperature increases. Moreover, it is worth noting that the transitions occur at lower temperatures for the samples grown at higher oxygen overpressure (for all growth temperatures). Figure 54 compares the transition temperatures between the samples grown at the two pressure regimes. It is observed that for all growth temperatures, films show p-type behavior at lower temperatures when grown at high oxygen overpressure. Specifically, films show p-type conductivity 12, 18, 28, 24, and 6 degrees lower when grown at high pressure and 150, 200, 250, 300, and 350 ^{o}C, respectively.

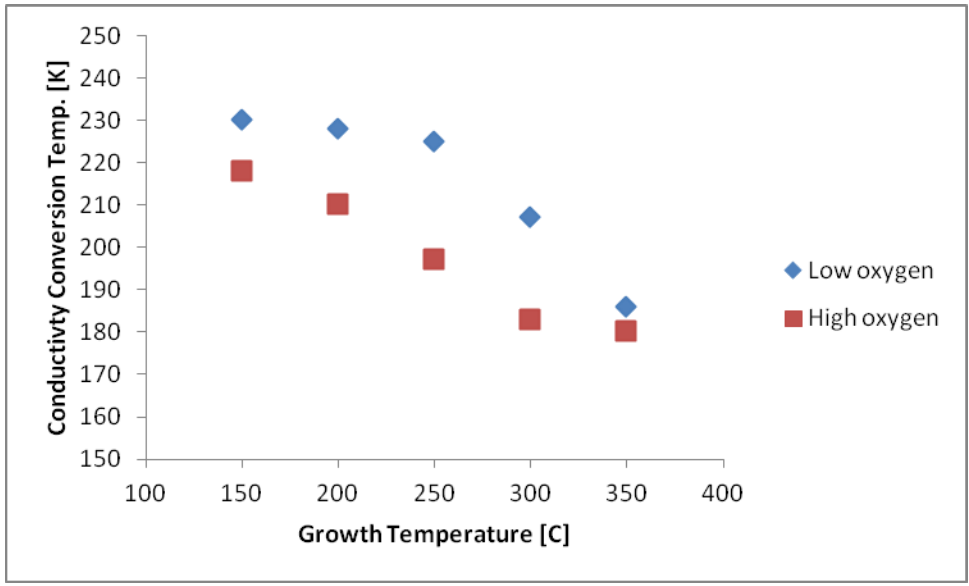

Figure 55. A comparison between the transition points vs. growth temperature for samples grown at high and low oxygen overpressures.

6.6 Discussion

This electrical conductivity conversion can be attributed to the formation of acceptor-like zinc vacancies and oxygen interstitials defects. It has been shown that the formation energies of these acceptor-like compensating defects are higher than the intrinsic donor-like defects such as oxygen vacancies and hydrogen complexes(Esmaili Sardari, et al., 2010)(Lee, et al., 2001). Therefore, at low Hall temperatures intrinsic donor-like defects, mostly oxygen vacancies, are readily formed and the concentration of carriers is an almost-constant value. Increasing Hall Effect measurement temperature provides the necessary thermal energy to activate the acceptor-like defects such as zinc vacancies and oxygen interstitials which compensate the donor-like defects and convert the conductivity of the films. At low measuring temperatures the concentration of carriers is an almost-constant value independent of the temperature, and this can

be attributed to the fact that at low temperatures shallow intrinsic donor-like defects, mostly oxygen vacancies, are readily activated and ionized.

As the reading temperature increases, the concentration of acceptor-like defects goes up and at the conductivity change temperature, we have n=p. For higher Hall temperatures, hole concentration will be even higher and R_H remains positive. It is worth noting that this is not the case for the films grown on n-type substrates where the electron concentration is independent of the measuring temperature. In this case, the increase in the hole concentration is not enough to compensate for the high electron concentration, and the films remain n-type for the whole range of Hall temperatures (80K to 350K).

In addition to the thermal activation of acceptor-like defects and compensation of oxygen vacancies, the observed conductivity change can be attributed to the structural properties and growth dynamics of the films grown on n and p-Si substrates.

6.6.1 Electronic Surface Structure of Si Substrates

Surface differences between n and p-Si substrates affect the properties of the grown films. Boron tends to substitute for sub-surface Si atoms in all reconstructed (100) Si phases while phosphorous has been observed to substitute for surface atoms(Zavodinsky, et al., 1998) where counting statistics has shown that dimers of S—P are the most favorable bounds at (100) Si surface energetically (Zavodinsky, et al., 1998).

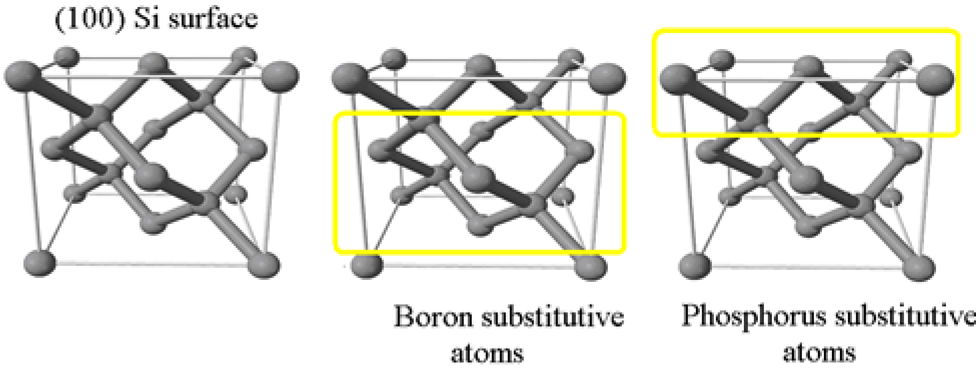

Figure 56. Schematics of silicon crystal. Boron tends to substitute for sub-surface bulk Si atoms whereas phosphorus appear in (100) Si surface. The existence of donor atoms in n-type Si surface and the lack of acceptor atoms in p-type Si surface change the growth dynamics of ZnO and affect the electrical behavior of the thin-film.

On one hand, the presence of phosphorus and the absence of boron at the surface atomic layer change the electronic structure of (100) Si surface between the two. On the other hand, since the ionic structure of ZnO consists of alternating Zn^{2+} and O^{2-} planes stacked along [0001] direction, then at the surface, there exists a macroscopic dipole perpendicular to the ideally truncated bulk

ZnO crystal(Kornherr, et al., 2006)(Overbury, et al., 1998). Therefore, this charge imbalance along with the electronic surface differences between the n and p-Si substrates change the ZnO stacking order which in turn change the terminating plane between the films grown on n and p-Si substrates.

6.6.2 Morphologic Surface Structure of Si Substrates

Atomic scale study of ZnO growth mechanism by molecular dynamic simulations (MDS) shows that ZnO tends to grow on step-and-terrace surfaces rather than smooth surfaces(Kubo, et al., 2000). Once the ejected plume particles arrive at the substrate, single or double bonds form between the particles and the grown layer depending on the surface morphology. It is shown that only the double bonded particles stick to the substrate and the growth proceeds. For smooth surfaces, only single bonds form between the newly ablated arriving particles and the surface which limits the growth. On the other hand, when the surface has step-and-terrace structure, double bonds form which make the particles stick to the surface(Kubo, et al., 2000). Atomic scale schematics of growth mechanism on smooth and rough surfaces for O and Zn-terminated surfaces are shown in the following two figures respectively.

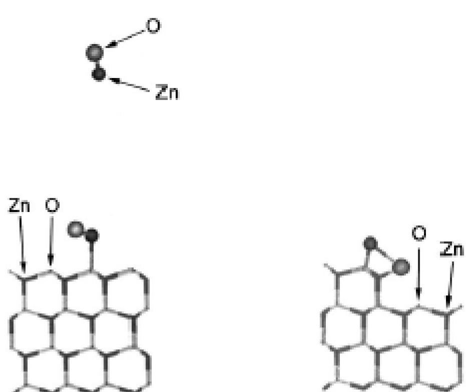

Figure 57. Atomic scale schematics of ZnO growth process on O-terminated surface. The ejected material (top) travels toward the substrate. The arriving ZnO on smooth surface (left) makes a single bond with the substrate which does not stick to the substrate. On the other hand, when the arriving ZnO is at the step of the substrate (right) it connects to the surface with double bonds (Kubo, et al., 2000).

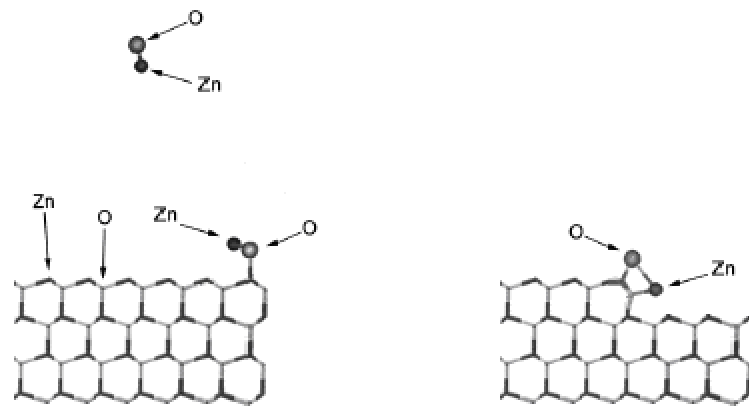

Figure 58. Atomic scale schematics of ZnO growth process on Zn-terminated surface. The ejected material (top) travels toward the substrate. The arriving ZnO on smooth surface (left) makes a single bond with the substrate which does not stick to the substrate. On the other hand, when the arriving ZnO is at the step of the substrate (right) it connects to the surface with double bonds (Kubo, et al., 2000)..

Moreover, it is shown that the surface of HF etched silicon substrates is extremely rough microscopically. For the substrates etched by BHF or BOE the surface is terminated by hydrogen in various forms including mono-hydrides, coupled mono-hydrides, di-hydrides, and tri-hydrides. This hydrogen termination plays an important role on surface morphology of the substrates and makes the substrates very rough with facets and steps(Chabal, et al., 1989).

Again, the presence of phosphorus and the absence of boron at the surface atomic layer of n and p-type (100) Si substrates respectively change the surface morphology between the two and affect the growth dynamics of the ZnO thin films(Zavodinsky, et al., 1998).

To conclude, our results show that electronic and morphologic differences between n and p-(100) Si surfaces affect intrinsic defects and concentrations as well as the ZnO (0001) termination with different electrical, chemical and physical properties(Sumiya, et al., 2000)(Youn, et al., 2004). For instance, O and Zn-terminated films have different surface absorption and chemical activity(Kornherr, et al., 2006)(Wang, et al., 2003) which lead to the adsorption of different surface species and, thus, different electrical behavior.

Chapter Seven: Device Development

High quality ZnO thin films are used in device development. In this chapter, the electrical properties of ZnO/Si vertical transport devices, a reusable Surface Acoustic Wave (SAW) biological sensor along with optoelectronic devices are investigated.

7.1 Vertical Transport Devices

The current-voltage characteristics of ZnO/Si devices grown at 300 ^{o}C were investigated by applying silver contacts to the films and back gating the substrates. By applying a D.C. voltage sweep across the structure vertically, the IV characteristics of ZnO/n-Si and ZnO/p-Si devices grown at low and high oxygen overpressures are studied, and rectifying properties were observed for the films grown at low pressure on both n and p-Si substrates. On the other hand, for the films grown at high pressure, only ZnO/p-Si device showed rectification whereas the ZnO/n-Si device has quadratic IV properties for positive and negative voltages.

7.1.1 ZnO/n-Si Devices

For the ZnO/n-Si device, the low oxygen overpressure creates high defects concentrations, oxygen vacancies specifically, which make the grown film n^{++} with much higher electron concentration (10^{20}) than the n-Si substrate (10^{14}). This makes the substrate "p-type" relative to the ZnO film. Therefore, rectifying properties are expected for this device. The IV characteristics of this device are shown in figure 1. For positive voltages, the device is reverse biased, and for negative applied voltages the device is forward biased.

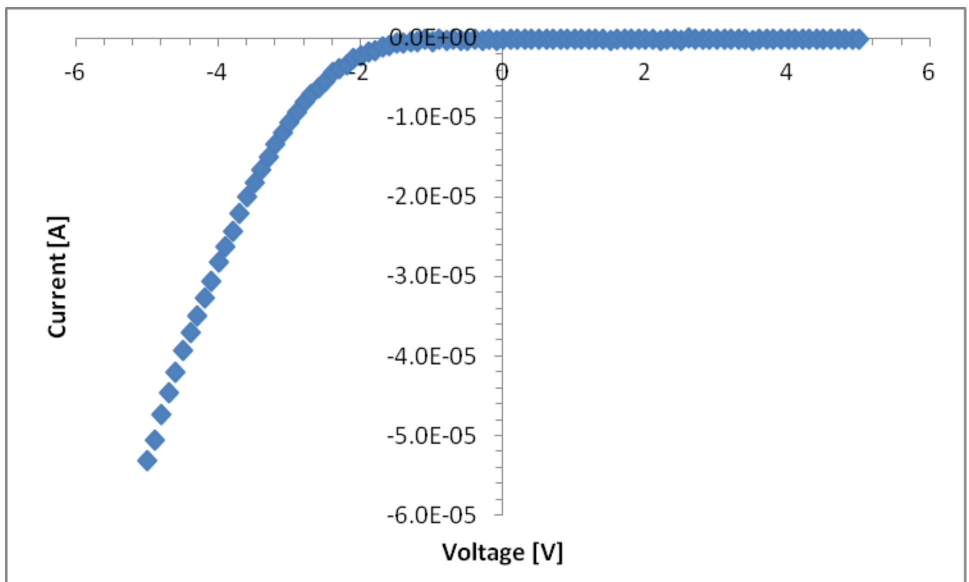

Figure 1. IV characteristics of ZnO/n-Si system for the film grown at 300 ^{o}C and low oxygen pressure. High electron concentration makes the film heavily doped with respect to the lightly doped substrate. The rectification is observed for the "p-n junction" device.

The ZnO/n-Si device grown at high oxygen overpressure, on the other hand, has much lower electron concentration which makes the concentration comparable between the film and the substrate. The IV characteristics of this device are shown in figure 2.

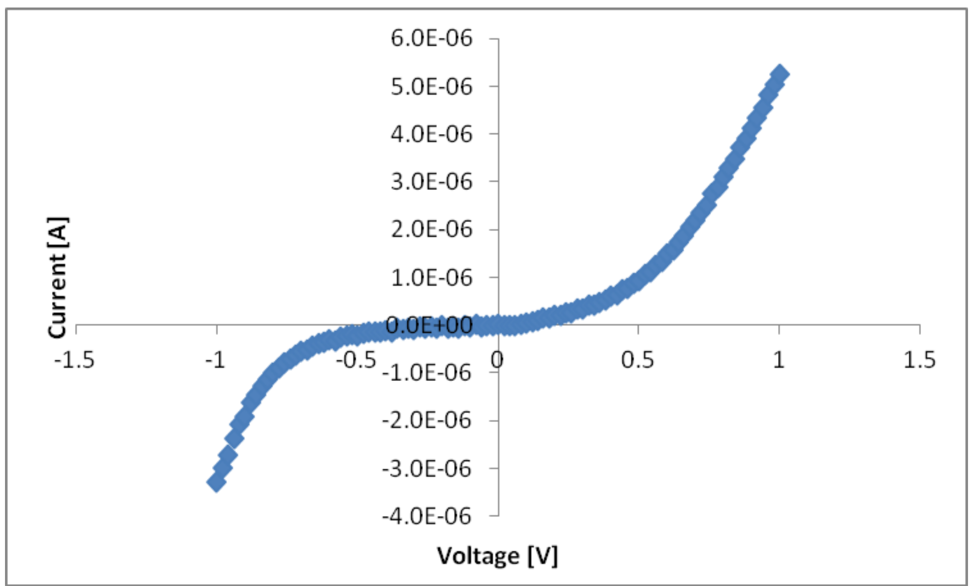

Figure 2. IV characteristics of ZnO/n-Si system for the film grown at 300 ^{o}C and high oxygen pressure. High oxygen overpressure makes the film lightly doped with respect to the substrate. The current is allowed for both polarities.

7.1.2 ZnO/p-Si Devices

The IV characteristics of ZnO/p-Si devices are shown in figure 3 and figure 4. Since the films have p-type conductivity (note that the measurements were performed at room temperature), high oxygen growth which reduces intrinsic donor-like defects improves the p-type behavior and makes the film p^{++} with respect to the substrate. Thus, for the ZnO/p-Si device grown at high pressure rectifying properties are expected. Figure 3 shows forward bias (V>0) and reverse bias (V<0) properties for this device. The small reverse current (even at high reverse voltage of -2 V) is worth noting since this current is significantly increased for the device grown at low oxygen pressure.

Lowering the growth oxygen pressure increases the intrinsic defects counts which in turn increases the electron concentration of the grown ZnO layer. Therefore, the hole concentration of the film is reduced for the device and an increase in the reverse current is observed (figure 4).

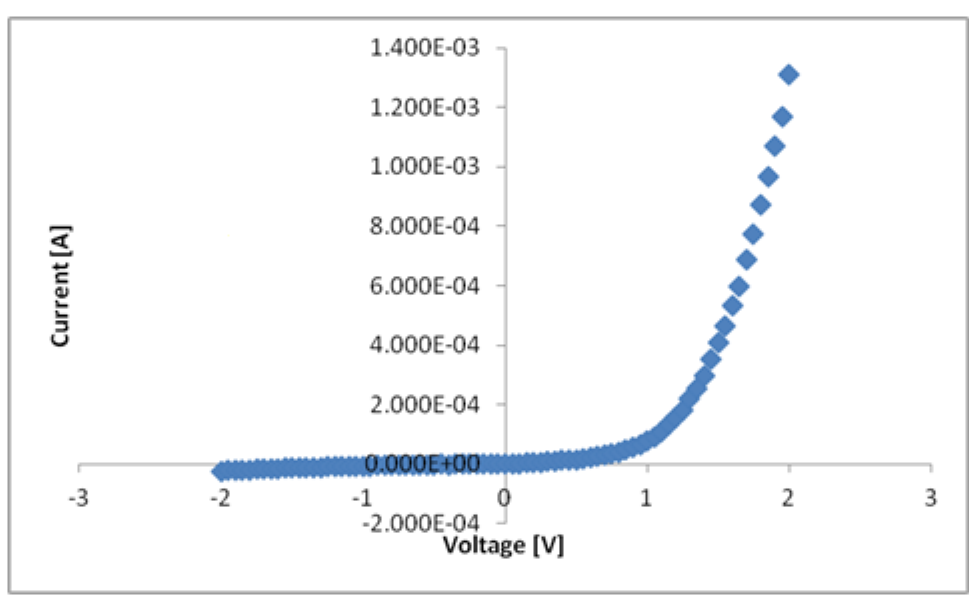

Figure 3. I-V characteristics of ZnO/p-Si system for the film grown at 300 °C and high oxygen pressure. High carrier concentration makes the film heavily doped with respect to the lightly doped substrate. The rectification is observed for the "p-n junction" device.

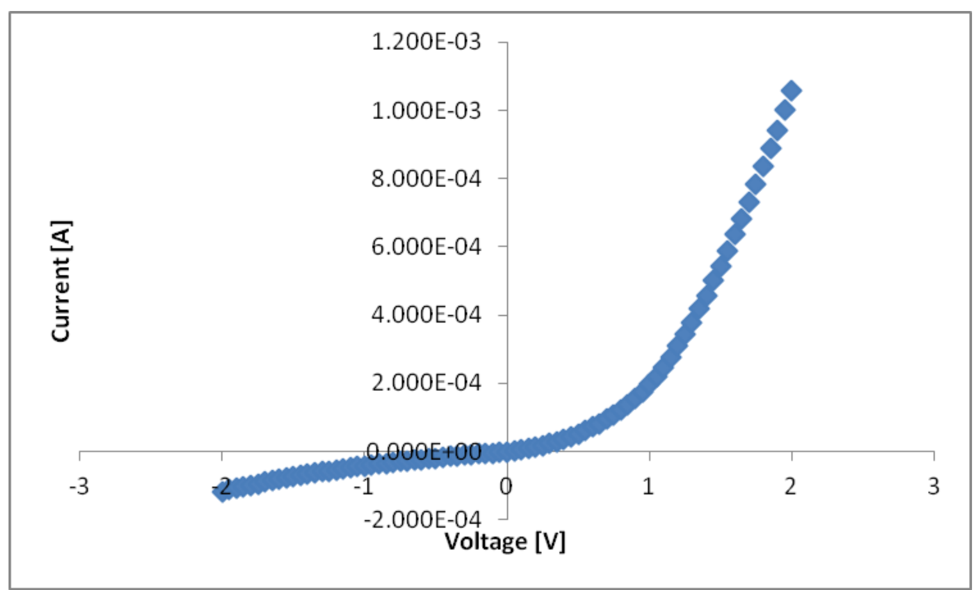

Figure 4. I-V characteristics of ZnO/p-Si system for the film grown at 300 °C and low oxygen pressure. Low oxygen overpressure makes the film lightly doped with respect to the substrate, and the reverse current is significantly increases with respect to fig. 3.

A comparison between figure 2 and figure 4 suggests structural differences between the films grown on n and p-Si substrates. In both cases (figure 2 and figure 4), the rectification is degraded (relative to figure 1 and figure 3, respectively).

Table 1 summarizes the studied structures along with the growth conditions and observed behavior:

Growth Condition	Device Structure	
1. n-Si, low oxygen pressure	+ Ag ZnO n^{++} Si n -	▪ No forward bias current ▪ Reverse bias current is quadratic
2. n-Si, high oxygen pressure	+ Ag ZnO n Si n -	▪ Since the concentrations are comparable, no rectification is observed
3. p-Si, high oxygen pressure	+ Ag ZnO p^{++} Si p -	▪ No reverse bias current ▪ Forward bias current is quadratic
4. p-Si, low oxygen pressure	+ Ag ZnO p Si p -	▪ Since the concentrations are comparable less rectification is observed than 3

Table 1. A summary of the studied devices, growth conditions and IV characteristics results for n and ZnO/p-Si device grown at 300 ^{o}C.

7.1.3 Transport Mechanism

Current-voltage characteristics and the vertical transport mechanism of our ZnO/Si devices are explained by the formation of a space-charge region at the junction between the substrates and the grown ZnO layer. Moreover, there exists the native silicon dioxide layer between the substrate and the ZnO with a wide band gap of ~9 eV and a very low carrier's mobility(Maeng, et al., 2008)(Chen, et al., 2006). The combinations of these properties lead to the space-charge transport that we observe. Grown films have high carrier concentrations, and for degenerate cases where the Fermi level drops below the valance band (for ZnO/p-Si devices) or moves above the conduction band (for ZnO/n-Si) devices, the current is easily injected to the Si substrates and the transport properties are dominated by the substrates. In this case, for low-field biasing conditions where the current density is low, the applied electric field is the dominant field throughout the device and a linear IV characteristic is observed. In this case the transport is bulk-limited since ZnO is an Ohmic contact to the Si substrate. In this case, no band bending occurs in the valence (conduction) band of ZnO which acts metallic, and because the junction is an iso-type junction, the conduction (valance) band bending is not relevant for ZnO/p-Si (ZnO/n-Si) device(Maeng, et al., 2008)(Chen, et al., 2006).

On the other hand, increasing the applied voltage across the device increases the charge transport between the ZnO and Si and affects the space-charge region. The current, however, is limited by the depletion region and it dominates the transport properties. For high fields, we observed a quadratic IV characteristic which is in agreement with space-charge-limited current transport. In this case, the current density J can be calculated as the following have:

$$\mathbf{J} = ne\mathbf{v} \qquad \text{eq. 1}$$

Where

n is the electron concentration
e is the unit charge for an electron
$\boldsymbol{v}$ is the drift velocity of electrons

Let's assume the following coordinates before we proceed:

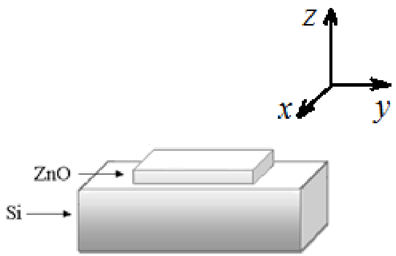

Figure 5. Coordinates used for the discussion.

We can substitute for the drift velocity using $\mathbf{v} = \mu\mathbf{E}$ where μ the electron mobility and $\boldsymbol{E}$ is the electric field. On the other hand from the Poisson's equation we have:

$$\partial\mathbf{E}/\partial\mathbf{z} = ne/\varepsilon \qquad \text{eq. 2}$$

$$ne = \varepsilon\, \partial\mathbf{E}/\partial\mathbf{z} \qquad \text{eq. 3}$$

Substituting in the transport equation above, we have:

$$\mathbf{J} = \mu\varepsilon\, \mathbf{E}\partial\mathbf{E}/\partial\mathbf{z} \qquad \text{eq. 4}$$

Note that the current cannot be a function of the position, i.e. z, since the charge is not accumulated or depleted throughout the device, thus, we have:

$$\mathbf{J}\partial z = \mu\varepsilon\, \mathbf{E}\partial\mathbf{E} \qquad \text{eq. 5}$$

Taking the integral of both sides of equation above, we have:

$$J_z = \frac{1}{2}\,\mu\varepsilon\,(E_o^2 - E^2) \qquad \text{eq. 6}$$

As mentioned before, high carrier concentration of the grown ZnO layer makes an Ohmic contact where force the electric field to vanish at E_o. Therefore, we have:

$$J_z = \frac{1}{2}\,\mu\varepsilon\,E_z^2 \qquad \text{eq. 7}$$

This gives us the space-charge-limited current transport mechanism with the quadratic current-voltage relationship. Such quadratic relationship between current and voltage has been observed by Maeng et al for ZnO nanowall(Maeng, et al., 2008).

7.1.4 Ideality factor

The ideality factor or a p-n junction describes the junction's deviation from an ideal diode situation. More specifically, in the ideal case, the thermionic emission current is due to the band-to-band electron-hole pairs (EHPs) recombination. The EHPs recombination take place in the neutral region of the junction, i.e. outside of the depletion region; hence, the total diode current is a diffusion current with the ideality factor of η =1(Sōga, 2006).

On the other hand, if all EHPs recombine inside the depletion region, facilitated by recombination centers such as defects, then the total current is due to the recombination inside the depletion region. If we apply Shockley theorem to calculate the diffusion current, an ideality factor of η = 2 will be derived for this recombination current.

Since the total diode current is the summation of the diffusion and the recombination currents, the current can be written as:

$$I = I_s \times \left(\exp\left(\frac{qV}{\eta KT}\right)-1\right) \qquad \text{eq. 8}$$

Where η is the dimensionless ideality factor which shows the deviation of the junction's transport properties from the ideal case of η=1 where there is no recombination inside the depletion region. The ideality factor ranges from 1 (for an ideal diode with no recombination inside the depletion region and immediate surroundings) to 2 (for the case where the current is merely due to the EHPs recombination inside the depletion region). It is worth noting that values greater than 2 are also observed and reported which are explained by field-enhanced recombination, trap-assisted tunneling, contact-recombination site, series resistance, and recombination along the extended defects(Sōga, 2006)(Breitenstein, et al., 2006).

In the following sections the two situations discussed above are examined in more details. The calculations of a junction's ideality factor can be started from the diode's current equation. Total current is a combination of Shockley diffusion current and the space charge recombination current.

7.1.4.1 Derivation of ideality factor: Shockley Diffusion Current

In the Shockley model were the diffusion is the rate limiting process, we are particularly interested in the current outside the space charge region or at the edges of the boundary, and we do not consider the effects of EHPs recombination inside the depletion region. Based on this model in a forward biased p-n junction, the current is expressed by the Shockley equation below(Kasap, 2006):

$$I = [(qD_h / L_h N_d) + (qD_e / L_e N_a)]\, n_i^2 \times (\exp(\frac{qV}{KT}) - 1) \qquad \text{eq. 9}$$

Where

q is unit charge
D_h is the diffusivity of holes (or the diffusion constant for holes)
L_h is the diffusion length (for holes)
N_d is the donor concentration
D_e is the diffusivity of electrons (or the diffusion constant for electrons)
L_e is the diffusion length (for electrons)
N_a is the acceptor concentration

Let

$$I_S = [(qD_h / L_h N_d) + (qD_e / L_e N_a)] n_i^2 \qquad \text{eq. 10}$$

Then:

$$I = I_S \times (\exp(\frac{qV}{kT}) - 1) \qquad \text{eq. 11}$$

For high voltages, $V > 3\frac{kT}{q}$, the forward bias Shockley current equation can be written as the following:

$$I = I_S \times \exp(\frac{qV}{kT}) \qquad \text{eq. 12}$$

For this case (from eq. 11) the ideality factor of 1 is derived. However, Shockley model neglects the current due to the recombination in the space charge region(Sōga, 2006)(Kasap, 2006).

7.1.4.2 Derivation of ideality factor: Space charge region Recombination Current

If we just focus on the current due to the recombination inside the depletion region, and note that the concentration of electrons and holes are equal inside the depletion region which is proportional to the deviation of the non-equilibrium Fermi levels, i.e. IMERFs, from the midgap

position (this deviation is equal to the half of the applied voltage at the junction) we find that the recombination current can be calculated by the following equation:

$$I_{rec} = nU \qquad \text{eq. 13}$$

Where

n is the carriers concentration, electrons or holes
U is the recombination rate

Substituting for the concentration, we have the following:

$$I_{rec} = qUV \times \exp(\frac{qV}{2kT}) \qquad \text{eq. 14}$$

Where
V is the recombination region volume, i.e. the volume of the space charge region

The recombination rate, U, can be calculated using the simplified Shockley-Hall-Read recombination rate equation:

$$U = (np - n_i^2) / \tau(n+p+2n_i \cosh[(E_T - E_i)/kT]) \qquad \text{eq. 15}$$

Where

τ is the recombination lifetime
E_T is the recombination-center trap energy level

Maximum recombination happens when the trap energy level, E_T, is located midway between the conduction band and the valance band, i.e. $E_T = E_i$. If we assume that the concentration of electrons and holes inside the depletion region is much higher than the intrinsic concentration, i.e. $n=p >> n_i$, we can further simplify the Shockley-Hall-Read recombination rate as the following:

$$U = np / \tau(n+p) \qquad \text{eq. 16}$$

Where $n=p$ inside the recombination volume, $V=W_{dep} A$ where W_{dep} and A are the width and the effective cross section of the depletion region. Therefore the recombination current can be written as the following:

$$I_{rec} =(1/2\tau)\, qn\, W_{dep}\, A \times \exp(\frac{qV}{2kT}) \qquad \text{eq. 17}$$

Let $I_S = (1/2\tau)\, qn\, W_{dep}\, A$ then:

$$I_{rec} = I_S \times \exp(\frac{qV}{2kT}) \qquad \text{eq. 18}$$

Since for forward bias conditions $\exp(\frac{qV}{2kT}) >> 1$, we can rewrite the recombination current in the form of Shockley current as the following:

$$I_{rec} = I_S \times (\exp(\frac{qV}{2KT}) - 1) \qquad \text{eq. 19}$$

7.1.4.3 Calculation of the Ideality Factor

Once the IV characteristics of the junction are derived the ideality factor can be calculated using IV plots. The the ideality factor can be calculated as the following:

$$\frac{qV}{\eta KT} = \ln(I/I_S) \qquad \text{eq. 20}$$

$$\eta = \frac{qV}{kT} \ln^{-1}(I/I_S) \qquad \text{eq. 21}$$

We can evaluate I_s as the following(von Wenckstern, et al., 2006):

$$I_S = A_{eff} A^* T^2 \times \exp(-q\varphi_b/kT) \qquad \text{eq. 22}$$

Where

A_{eff} is the effective area of the diode (80 mm^2)
$A^* = 32\ cm^{-2} K^{-2} A$ is the Richardson constant
φ_b is the Schottky barrier height

The effective area of the diode depends on the geometry of the device, and it is equal to the contact area of our devices. In the followings, Schottky barrier heights and ideality factors of our devices are calculated using our experimental results.

7.1.5 Derivation of Junction Parameters

Semi-logarithmic IV characteristic plots of the devices (for forward and reverse bias conditions) show the typical behavior of Ohmic and rectifying contacts. As discussed earlier, oxygen overpressure during the growth process changes the defects concentration. Figure 6 and figure 7 show the IV characteristics for ZnO/n-Si (figure 6) and ZnO/p-Si (figure 7) devices grown at low and high oxygen pressure. It is evident that the rectification properties are observed for n-Si and p-Si devices grown at low and high pressures, respectively, which are in good agreement with our previous theoretical discussions (see table 1). On the other hand, high pressure n-Si and low pressure p-Si devices show poor rectification which is explained by the Ohmic MS junction.

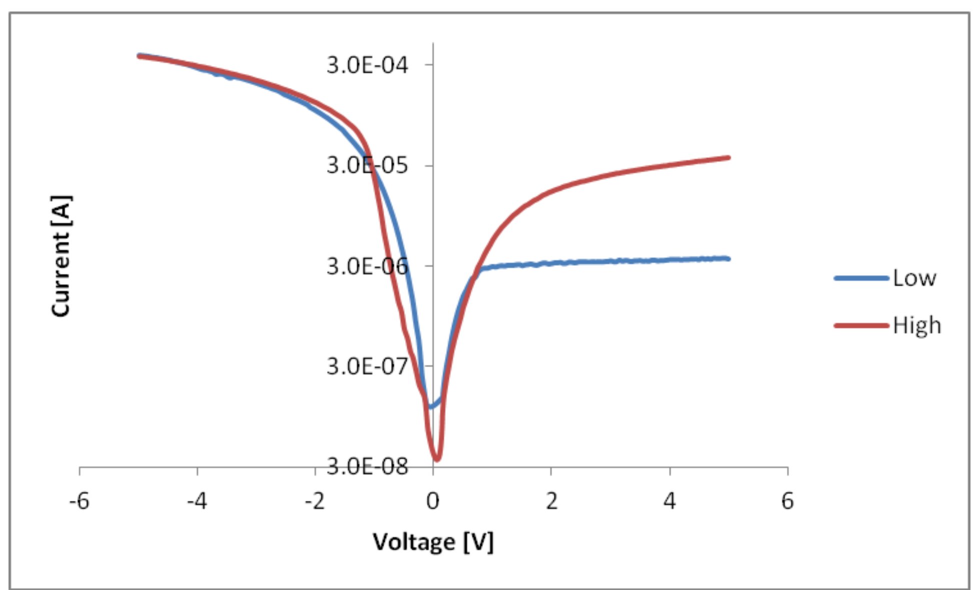

Figure 6. The IV characteristics for $n^{++}ZnO$/n-Si devices grown at low (blue) and high (red) oxygen overpressure and 300 ^{o}C. We observed a reverse saturation current of 3.0×10^{-6} A for the sample grown at low pressure and 5.5×10^{-6} A for the sample grown at high oxygen overpressure at +1 V.

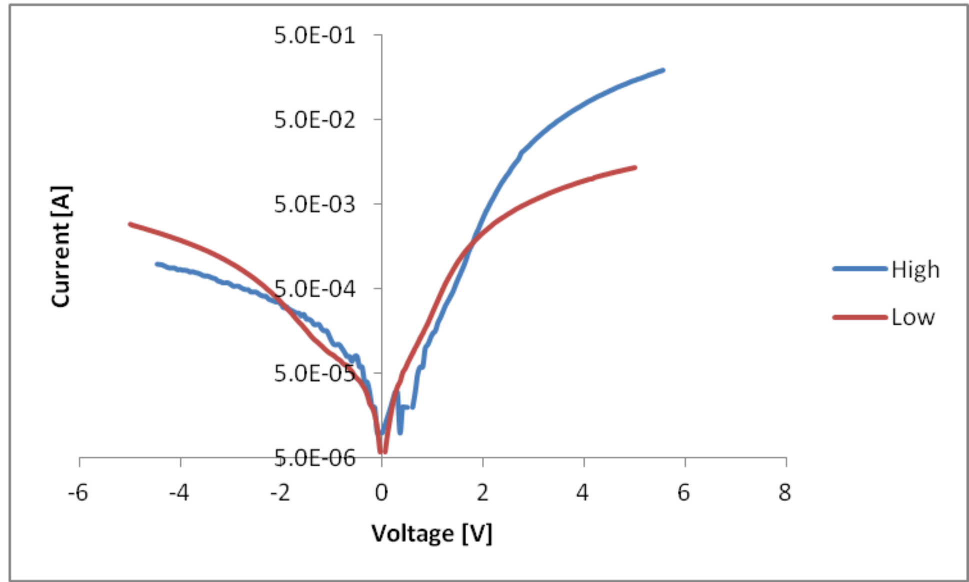

Figure 7. The IV characteristics for $p^{++}ZnO$/p-Si devices grown at low (red) and high (blue) oxygen overpressure and 300 ^{o}C. We observed a reverse saturation current of 8.5×10^{-5} A for the sample grown at low pressure and 6.0×10^{-6} A for the sample grown at high oxygen overpressure at -1 V.

The barrier heights of these structures can be calculated using eq. 22. The calculated Schottky barrier heights are 0.70 and 0.69 eV for ZnO/n-Si samples grown at low and high pressures

respectively. For the ZnO/p-Si devices, the Schottky barrier heights are 0.68 and 0.62 eV for high and low pressures respectively.

The ideality factors of the structures are calculated using eq. 21 and semi-logarithmic plots of I/I_s for small forward biases where the effects of structures' series resistance are negligible. For ZnO/n-Si devices, ideality factors of 1.91 and 2.84 were calculated for the devices grown at high and low oxygen overpressures respectively. For ZnO/p-Si devices ideality factors of 2.79 and 4.8 were derived for high and low pressure respectively. The large values of the ideality factors are explained by defect-assisted tunneling and recombination along the extended defects. Moreover, the deviations of the IV characteristics from the exponential model can also contribute to the large ideality factor values. Table 2 summarizes the electrical properties of our devices.

Growth Condition	Barrier Height	Voltage range [V], Ideality Factor
1. n-Si, low oxygen pressure	0.70 eV	[-0.05, -0.25] , $\eta = 2.84$ [-0.25, -0.60] , $\eta = 5.36$
2. n-Si, high oxygen pressure	0.69 eV	[-0.05, -0.15] , $\eta = 1.91$ [-0.15, -1.00] , $\eta = 6.27$
3. p-Si, high oxygen pressure	0.68 eV	[0.05, 0.15] , $\eta = 2.79$ [0.35, 1.50] , $\eta = 11.9$
4. p-Si, low oxygen pressure	0.62 eV	[0.05, 0.20] , $\eta = 4.8$ [0.50, 1.25] , $\eta = 13.8$

Table 2. A summary of the studied devices, growth conditions and calculated barrier heights and ideality factors for the given linear intervals.

7.2 Bacterial Biofilm Growth Monitoring SAW Sensor

Because of the high quality of our PLD grown films, they can be used as SAW sensors. In that respect our collaboration resulted in a bacterial biofilm growth monitoring SAW Sensor. Bacteria can attach to surfaces and form microcolonies. The colonies start to synthesis and create an extracellular matrix which includes complex polymers and toxic molecules, and they eventually form a bacterial biofilm. Because of the complexity of the bacterial composition, biofilms are extremely resistant to chemically diverse antibiotic treatments in clinical fields and bacteriophages in industry; for instance, bacterial biofilm formation results in bacterial corrosion of metals. Thus, the early detection of biofilm growth is essential for effective management of biofilm associated problems including contaminations, severe infections, and corrosive problems(Kim, et al., 2012). On the other hand, low power consumption, high sensitivity, and extremely low detection limit (on the order of atto-grams) of SAW sensors are employed in the fabrication of a highly sensitive bactrerial biofilm growth monitoring sensor(Krishnamoorthy, et al., 2008).

7.3 Photoresistors and Schottky Diodes

Thin film ZnO based UV photoresistors and Schottky diodes on (100) Si substrates grown by PLD are presented. The devices are selected based on the properties of ZnO and its potentials in optoelectronics. Design optimization process following a theoretical study of band structures is performed to select optimum device materials. The electrical properties of the devices are examined, and the photo responses of the devices under dark and UV illumination conditions are studied.

7.3.1 Device Structures

The principle of the operation relies on the modulation of the active layer's (ZnO) conductivity due to UV illumination(Soleimanpour, et al., 2011)(Fan, et al., 2009). Excess carriers generated by UV illumination affect the film's conductivity which in turn affects the output characteristics of our devices which include the resistance or the slope of the IV characteristics for photoresistors and rectification properties for Schottky diodes.

Photodetectors are fabricated by deposition of Ohmic contacts on ZnO films. In this case we are interested in the effects of UV illumination on the electrical properties of ZnO; therefore, both contacts on ZnO layer are Ohmic to eliminate contact junction effects. As mentioned before, following a theoretical study of band structures, we have selected potential material for the contacts. The material was then deposited on the samples and electrical measurements of the fabricated devices were performed.

Schottky diodes, on the other hand, use the rectification properties of the metal-semiconductor junction; thus, a Schottky contact was used for one of the two contacts deposited on ZnO films. Similar optimization process has been employed to select the better candidate for Schottky material.

All of our devices are fabricated on oxide etched n and p-type (100) Si substrates. Even though the cleaned samples were attached to the substrate holder inside the growth chamber and the pressure was brought down almost immediately, the inevitable native oxide layer of almost 10 Å forms almost immediately on our samples(Morita, et al., 1990). We are ignoring the effects of this oxide layer because the contacts are both on ZnO layer and we use transverse electric transport in ZnO thin films.

7.3.2 Contact Material Optimization and Metallization Process

Following theoretical studies discussed earlier in this work (see Hall chapter) and the electrical properties of our device structures, Al and Ag were selected as Ohmic candidates to ZnO/n-Si devices (and Schottky to ZnO/p-Si). Moreover, since Al has smaller work function, Al was

chosen. On the other hand, among the candidates for Schottky contacts to ZnO/n-Si (and Ohmic to ZnO/p-Si), namely Au and Pt, Au has been selected for device fabrication.

The studies predict that:

- Al has Ohmic properties on ZnO/n-Si and Schottky behavior on ZnO/p-Si devices
- Au has Ohmic properties on ZnO/p-Si and Schottky behavior on ZnO/n-Si devices

In order to confirm the theoretical predictions, contacts have been deposited on ZnO/Si devices by electron beam evaporation (EB) technique. Prior to EB deposition of the contacts, samples have been etched and contact openings have been created by lithography. After EB deposition, excess metal is removed by lift-off.

7.3.2.1 Ohmic Contacts

Figure 8 shows the device fabrication process comprehensively. The process can be summarized as the followings:

A. Silicon wafer is cleaved, and a Si substrate is cleaned for growth
B. ZnO thin film is grown on the substrate
C. The sample is coated with photoresist
D. The photoresist is removed from the periphery of the sample using the clover leaf mask
E. Exposed ZnO is etched
F. Photoresist is removed from the sample
G. The sample is coated with photoresist
H. The photoresist is removed from the corners of the ZnO layer to open contact windows
I. Metal contacts are deposited using EB evaporation technique
J. Excess metal is removed by lift-off

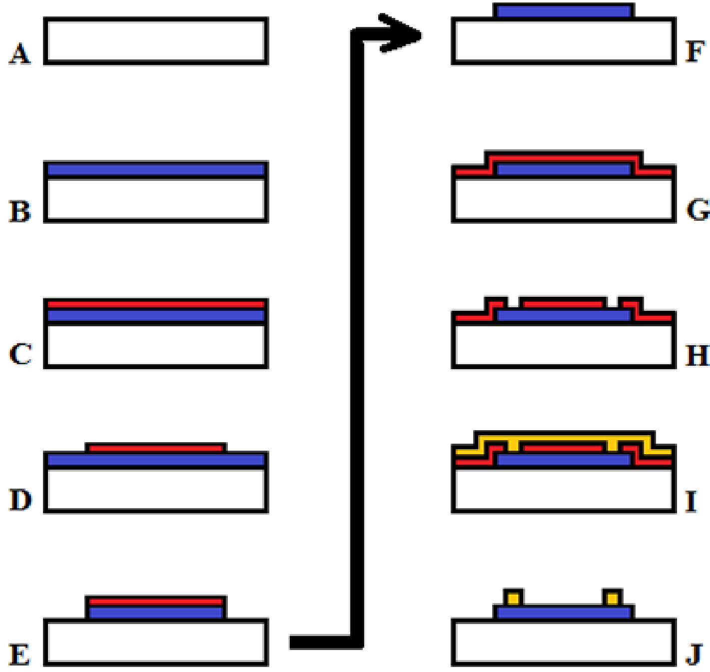

Figure 8. Device fabrication process. The process can be summarized as the followings: A: Silicon substrate is cleaned for growth, B: ZnO thin film is grown, C: Sample is coated with photoresist, D: Photoresist is removed from the periphery of the sample using the clover leaf mask, E: Exposed ZnO is etched, F. Photoresist is removed from the sample, G: Sample is coated with photoresist, H: Photoresist is removed from the corners of the ZnO layer to open contact windows, I: Metal contacts are deposited, J: Lift-off.

7.3.2.2Schottky Contacts

Au on ZnO/n-Si and Al on ZnO/p-Si are deposited and the output characteristics are studied. Since an Ohmic contact is also deposited, the fabrication process for Schottky contacts is more involved than the previous process, i.e. Ohmic contacts deposition studied in figure 8. In this process, one Ohmic contact is deposited first, and then the Schottky material is deposited. Figure 9 shows the fabrication process for deposition of one Ohmic and one Schottky contact on ZnO/Si devices.

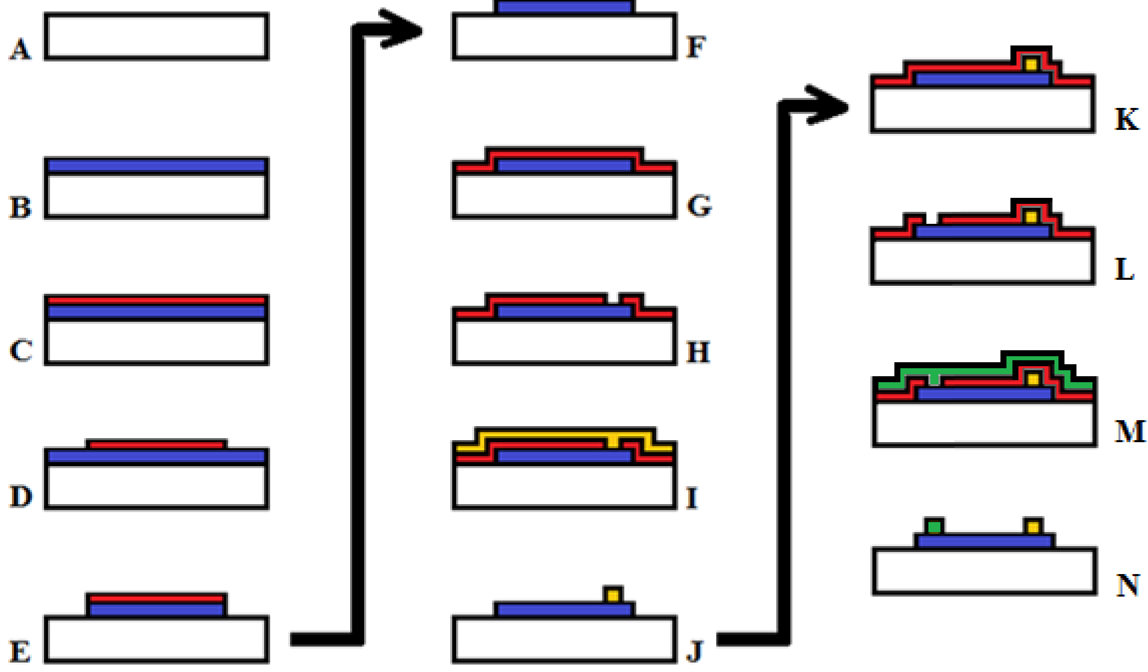

Figure 9. Device fabrication process. Both Ohmic and Schottky contacts are deposited on the sample.

The process (figure 9) can be summarized as the followings:

A. Silicon wafer is cleaved, and a Si substrate is cleaned for growth
B. ZnO thin film is grown on the substrate
C. The sample is coated with photoresist
D. The photoresist is removed from the periphery of the sample using the clover leaf mask
E. Exposed ZnO is etched
F. Photoresist is removed from the sample
G. The sample is coated with photoresist
H. The photoresist is removed to open one contact window
I. Ohmic metal contact is deposited using EB evaporation technique
J. Excess metal is removed by lift-off
K. The sample is coated with photoresist
L. The photoresist is removed to open one contact window
M. Schottky metal contact is deposited using EB evaporation technique
N. Excess metal is removed by lift-off

7.3.3 Results

7.3.3.1 Ohmic Contacts

As mentioned before, Al on n-ZnO/n-Si and Au on p-ZnO/p-Si are deposited and the output characteristics are studied. Figure 10 shows the IV characteristics of 200 nm thick circular Al contacts on an n-ZnO/n-Si system. The linear (Ohmic) behavior of the contacts is verified. The contact resistance is found to be between 277 Ω and 322 Ω for Al Ohmic contacts.

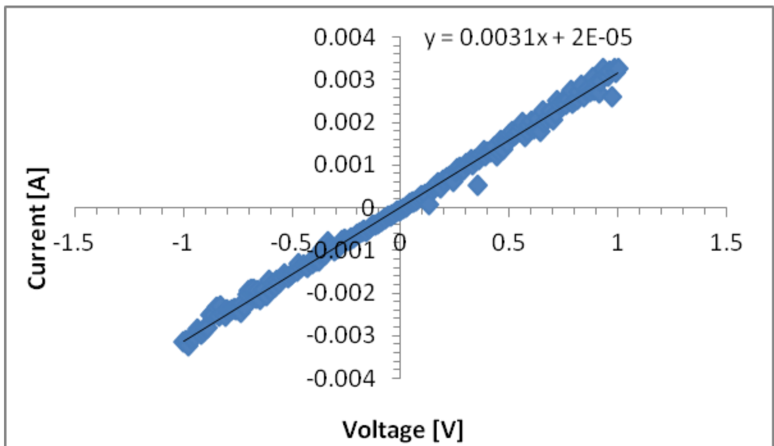

Figure 10. The IV characteristics of 200 nm circular Al contacts on n-ZnO/n-Si. The linear characteristics confirm the Ohmic properties of the contacts.

Figure 11 shows the IV characteristics of 200 nm thick circular Au contacts on a p-ZnO/p-Si system. Similarly, the linear (Ohmic) behavior of the contacts is verified. The contact resistance is found to be between 60 Ω and 69 Ω for Au Ohmic contacts.

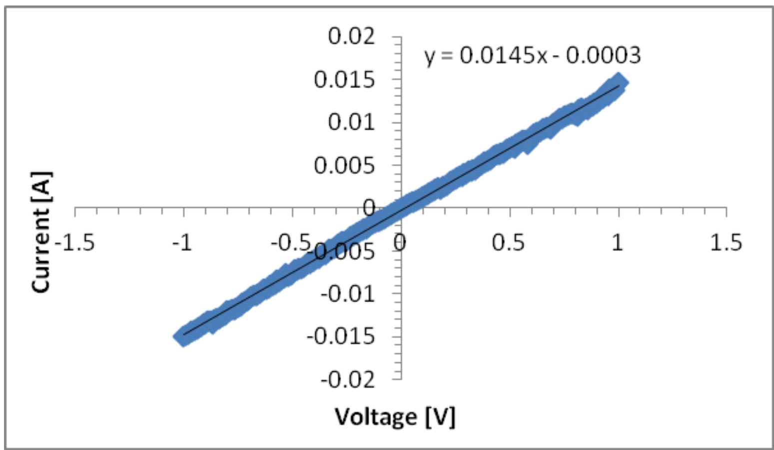

Figure 11. The IV characteristics of 200 nm circular Au contacts on p-ZnO/p-Si. The linear characteristics confirm the Ohmic properties of the contacts.

7.3.3.2Schottky Contacts

Even though theoretical calculations suggested that Al and Au have Schottky behavior on p and n-ZnO, respectively. Based on our results, however, only one set of our devices showed strong rectification properties for both n-Si and ZnO/p-Si devices. The IV characteristics of our Schottky devices are presented in the followings.

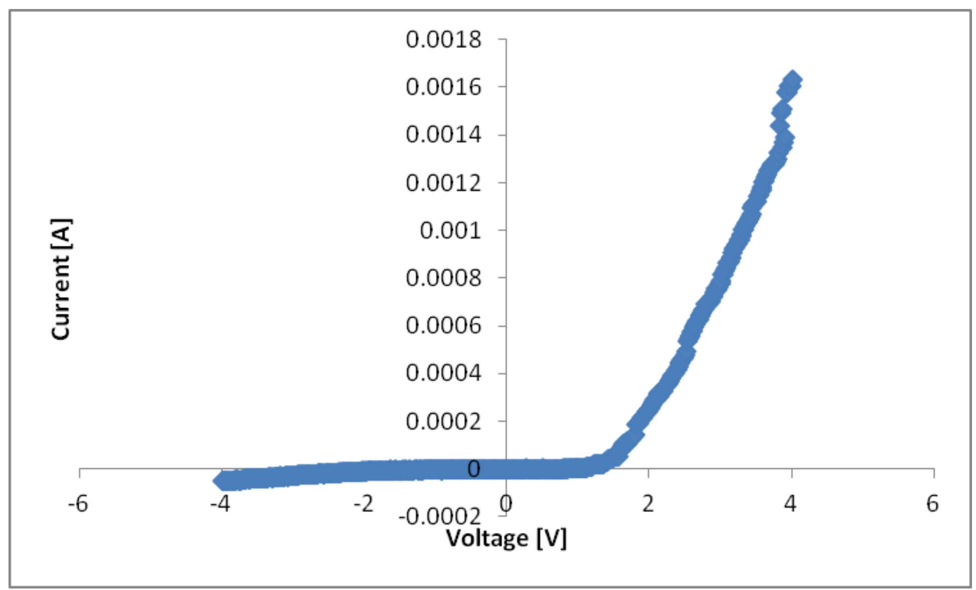

Figure 12. The IV characteristics of Al/p-ZnO/p-Si Schottky diode.

Based on semi logarithmic plot of the IV characteristics of this device (Fig. 13), a barrier height of 3.5 eV is calculated for this device.

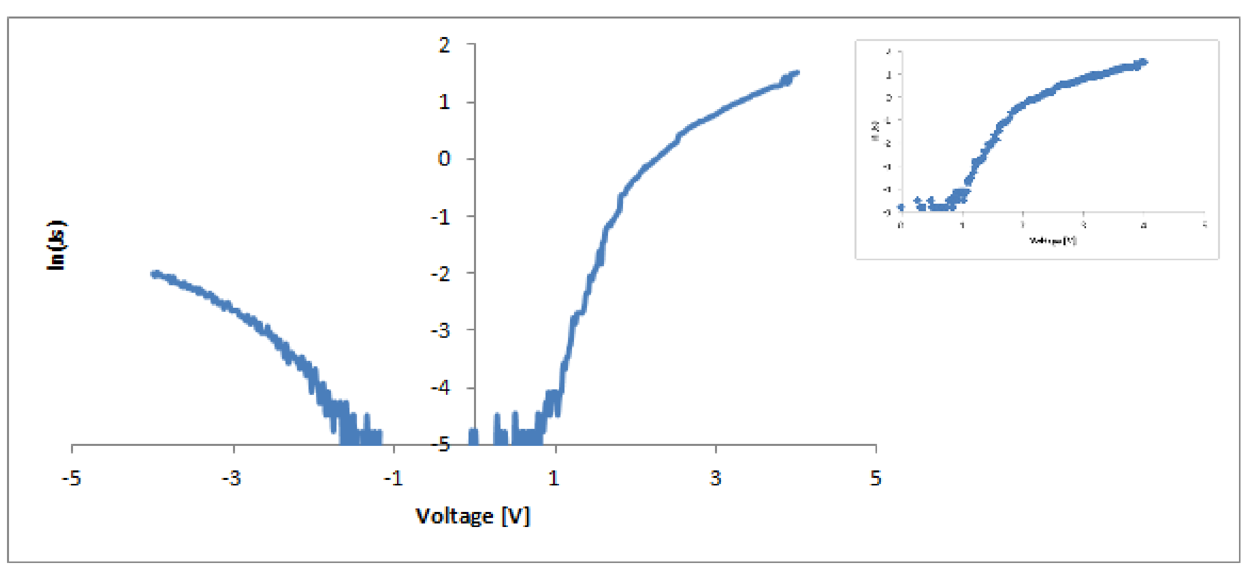

Figure 13. Semi logarithmic plot of the IV characteristics of Al/p-ZnO/p-Si Schottky diode. The inset shows the linear region between 1 and 2 volts.

The IV characteristics of our Au/n-ZnO/n-Si Schottky device is show in figure 14.

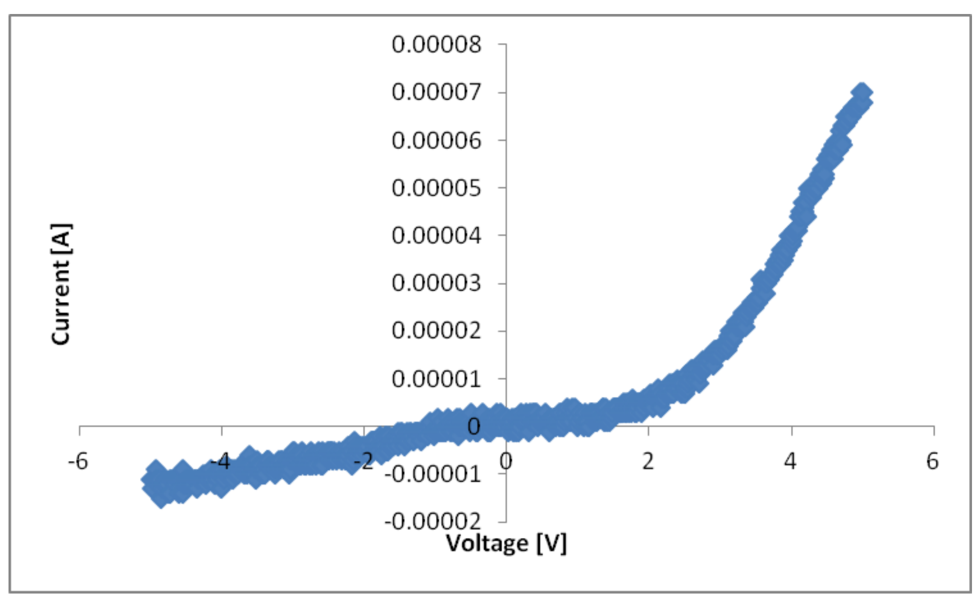

Figure 14. The IV characteristics of Au/n-ZnO/n-Si Schottky diode.

Based on semi logarithmic plot of the IV characteristics of this device (Fig. 15), a barrier height of 0.88 eV is calculated for this device.

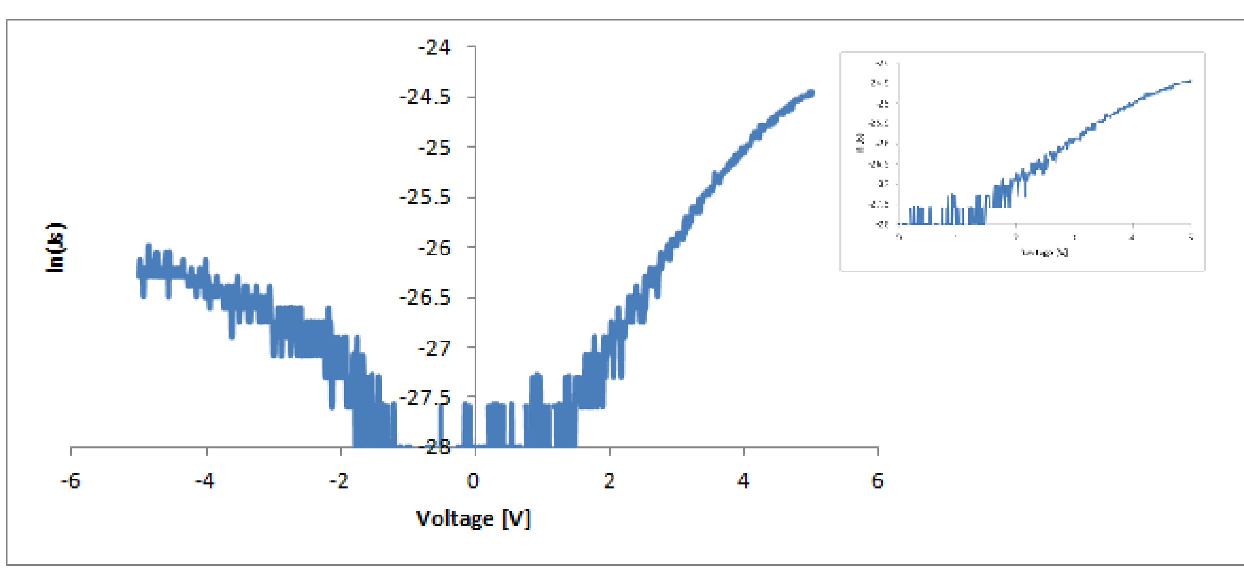

Figure 15. Semi logarithmic plot of the IV characteristics of Au/n-ZnO/n-Si Schottky diode. The inset shows the linear region between 1 and 4 volts.

As discussed before, theoretical calculations of the barrier heights using band-diagrams suggest a barrier height of $\Phi_M - \chi_e = (5.31\sim5.47) - 4.5 = 0.81 \sim 0.97$ eV for Au-n-ZnO/n-Si Schottky and $\frac{EG}{q} - \Phi_M + \chi_e = 7.8 - (4.06\sim4.26) = 3.54 \sim 3.74$ eV for Al/p-ZnO/p-Si Schottky device which are in perfect agreement with our experimental results.

7.3.3.3 Photoresponse of Devices

The optical responses of our devices were studied by comparing the IV characteristics of the devices in dark and UV illuminated situations. A UV light source with controllable variable wavelength was applied to illuminate the devices. The source delivers 0.815, 0.056, and 0.035 $\mu W.mm^{-2}$ UV illumination power densities for 365, 345, and 325 nm emissions respectively. The power density is measured with a calibrated photometer of 2.5 mm head radius. Assuming uniform illumination across the effective area of the devices, 61.96, 4.26, and 2.71 μW is delivered to devices at 365, 345, and 325 nm emissions respectively.

As mentioned before, almost all of our devices showed Ohmic properties except the two samples grown at high oxygen pressure of 2.5×10^{-4} Torr. The optical responses on the other hand, were observed for two devices. This can be explained by contact quality differences between the devices, quality of the films, and measurements errors.

Figure 16 shows the IV characteristics of our ZnO/n-Si photoresistor grown at low oxygen overpressure. The differences between dark and light (λ=365 nm) responses of the device are

evident. Based on our results, the device shows a dark resistance of R_D = 263 Ω and an illuminated resistance of R_L = 357 Ω.

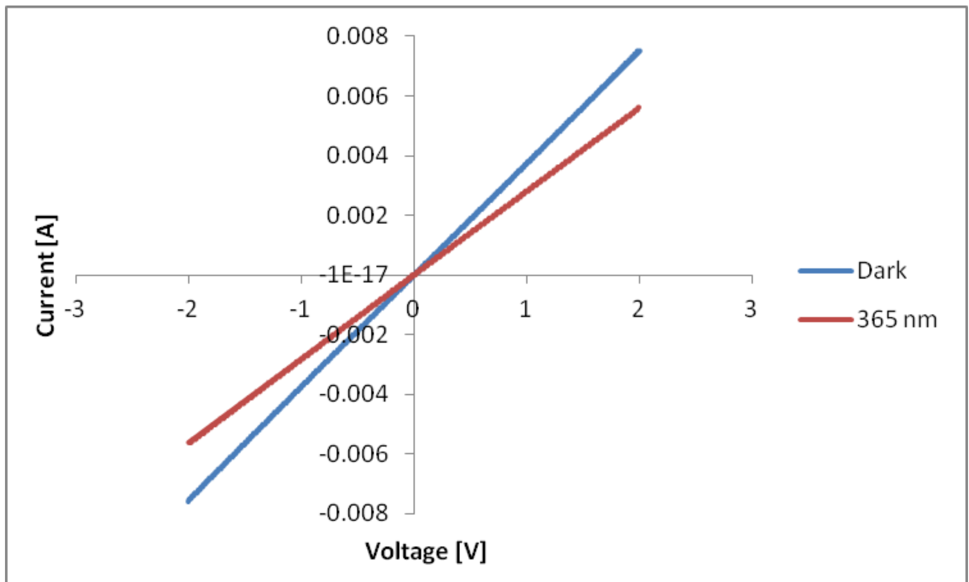

Figure 16. The IV characteristics of Al/n-ZnO/n-Si photoresistor grown at low oxygen overpressure and 300 °C. The response of the device is derived at 365 nm.

Based on the resistivity change of our photoresistor and the illumination power, we can define the sensitivity as the following:

$$S = \Delta R/P \qquad \text{eq. 23}$$

Where

ΔR is the resistance change
P is the excitation power

For our device a sensitivity of S = 1.51 Ω.µW is achieved.

The sensing mechanism of our device is explained by the electron-hole pair generation due to UV illumination. As we discussed before (see section 2.2.1), the formation energy of electron-trap defects, i.e. acceptor-like defects, in an n material is substantially reduced, and excess electrons created by UV illumination are trapped by the defects. The remaining holes recombine with the conduction band electrons; thus, they lower the conductivity of n-ZnO thin film. The process can be described as the followings:

$$h\gamma \rightarrow e^- + h^+ \qquad \text{(EHP generation)} \qquad \text{eq. 24}$$

$$A^o + e^- \rightarrow A^- \qquad \text{(acceptor-like defects activation)} \qquad \text{eq. 25}$$

Equation 24 and 25 can be summarized as the following equation:

$$h\gamma + A^o \rightarrow A^- + h^+ \qquad \text{eq. 26}$$

Thus, the UV illumination creates excess holes which reduce the conductivity in n-ZnO films. For p-ZnO/p-Si devices, on the other hand, the conductivity increases with the UV illumination which is confirmed by our p-ZnO/p-Si Schottky diode.

The process is schematically shown in the following where UV illumination of 365 nm (3.39 eV) generates electron-hole pairs. Electrons are trapped by acceptor-like defects traps which are located in the conduction band (Oba, et al, 2011)(Eun-Cheol Lee); therefore, excess holes reduce the concentration of majority carriers, i.e. electrons.

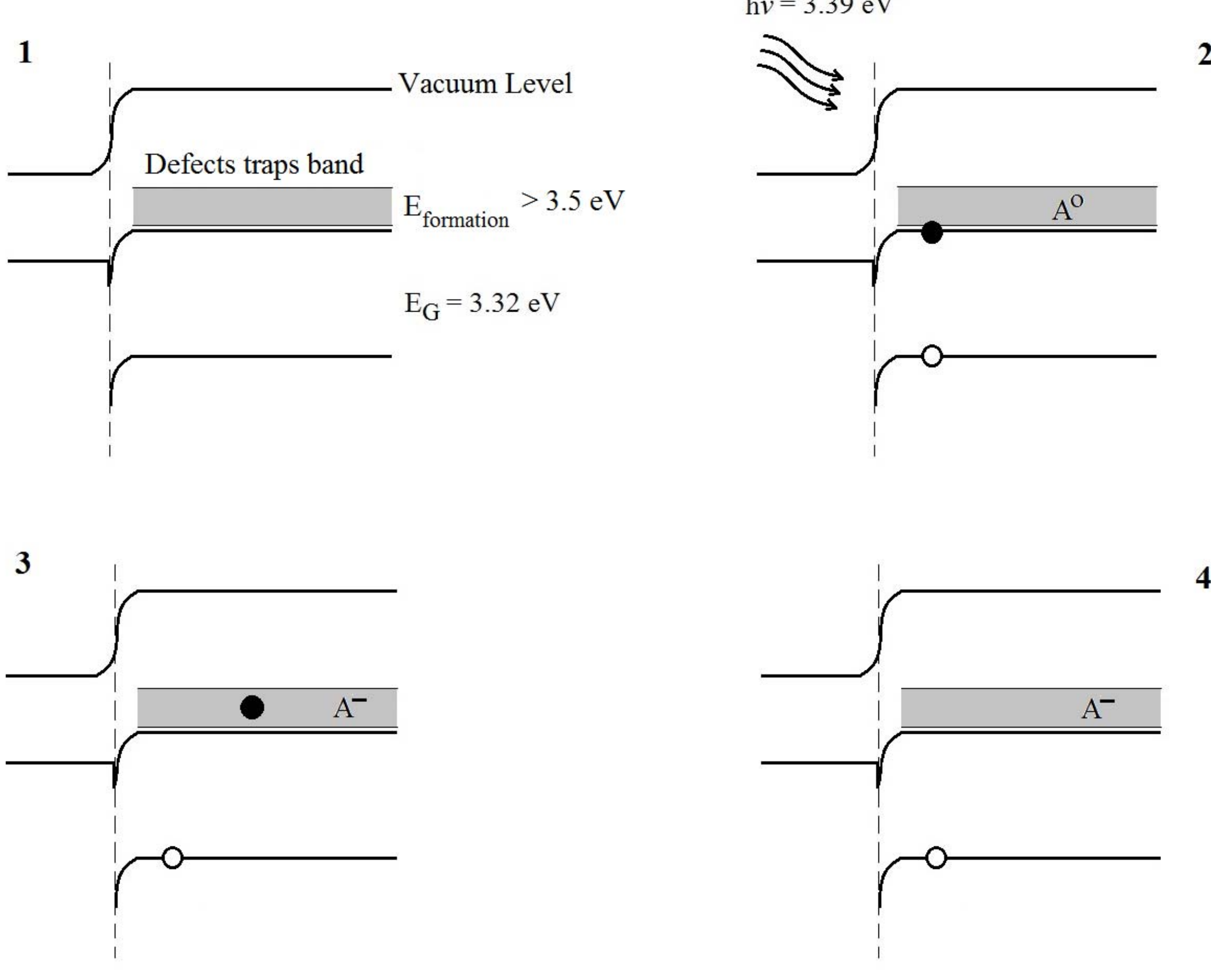

Figure 17. UV sensitivity mechanism for our Al-n-ZnO/n-Si photoconductor. Top left (1) shows the film's band-gap along with the defects traps band. When UV is illuminated (top right) electon-hole pairs are generated and electrons are trapped by defects traps activating defects (shown in 3). Excess holes then reduce the majority carrier concentration, i.e. electrons. Thus, UV illumination activates acceptor-like defects and generates holes in the valance band (shown in 4).

Figure 18 shows the IV characteristics of our Al/p-ZnO/p-Si Schottky diode grown at high oxygen overpressure. The differences between dark and light (λ=320, 345, and 365 nm) responses of this device are evident. As discussed above, an increase in the conductivity of the device is observed.

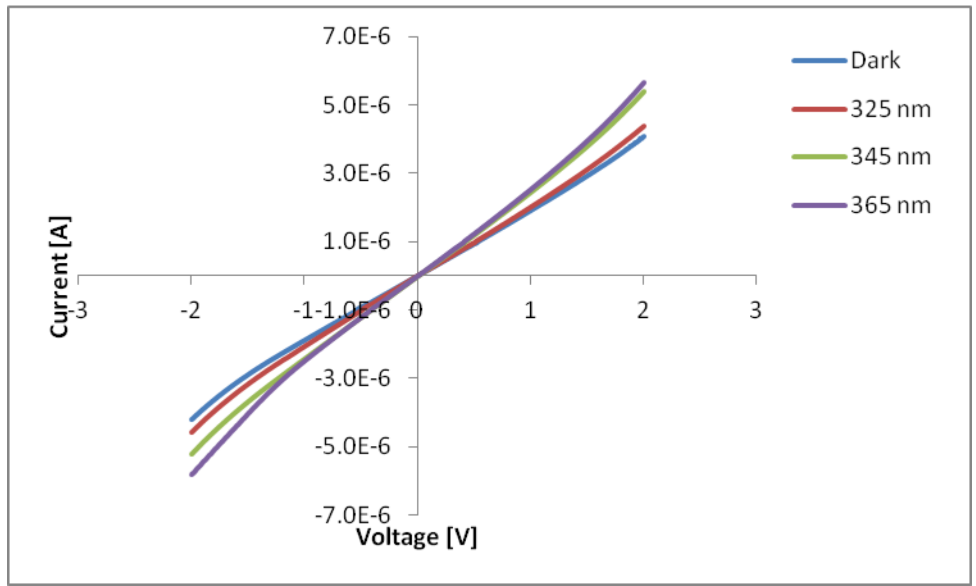

Figure 18. The IV characteristics of our Al/p-ZnO/p-Si Schottky diode grown at high oxygen overpressure. The differences between dark and light (λ=320, 345, and 365 nm) responses of this device are evident.

The sensitivity of the diode can be defined as the ratio of the curvature to the slope of the fitting polynomial for the experimental data (Cho, et al., 2010). We observed the maximum sensitivity for 365 nm excitation. Figure 19 shows the sensitivity of our Schottky diode at 365 nm.

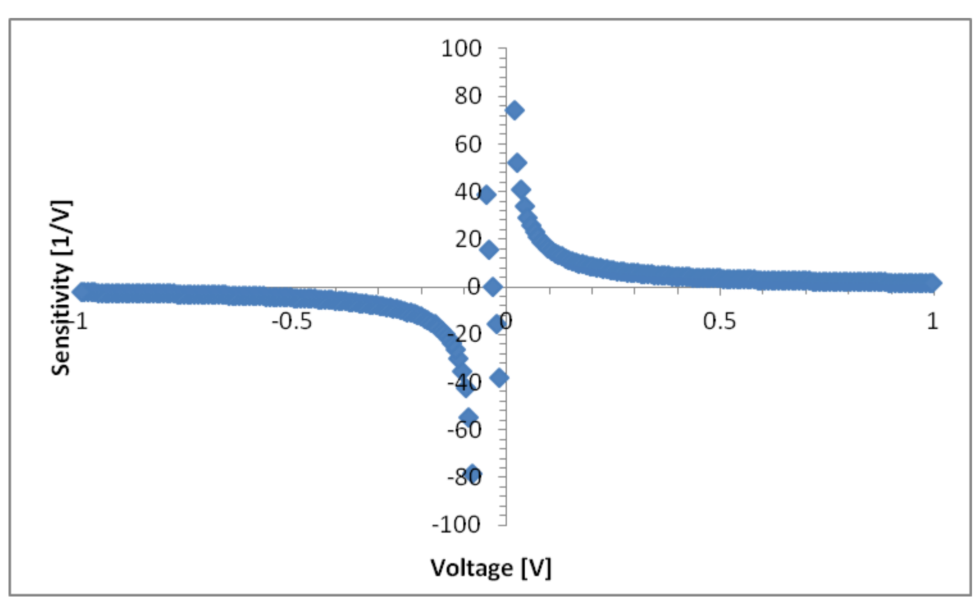

Figure 19. Sensitivity of Al/p-ZnO/p-Si Schottky diode is calculated by I"/I' using polynomial fit.

The IV characteristics of the device show asymmetric properties due to the asymmetry of the contacts positions and alignments; we observed a maximum sensitivity of 74 V^{-1} at 16 mV and 78 V^{-1} at -81 mV.

The optical responses of our devices are consistent with our earlier results. More specifically, as discussed in chapter 6, low oxygen overpressure growth results in high electron concentrations for n-ZnO films. This shifts the Fermi level toward the CBM and reduces the formation energy of the acceptor-like defects significantly. The excess carriers generated by UV illumination then easily activate the defects and excess holes change the intrinsic concentration of the film. Therefore, photo responsivity was only observed for Al/n-ZnO/n-Si photoresistor grown at low oxygen overpressure, and the IV characteristic of the device grown at high pressure did not show UV sensitivity. We also did not observe UV sensitivity for p-ZnO/p-Si photoresistores. This is attributed to the challenges of Ohmic contacts to p-ZnO as well as low sensitivity for the applied UV light.

Optical modulation of rectification properties, on the other hand, was only observed for Al/p-ZnO/p-Si device which is grown at high oxygen overpressure. High oxygen reduces the concentration of oxygen vacancies and moves the Fermi level toward the VBM, and this improves the rectification of Al on p-ZnO. Low oxygen growth regime, on the other hand, reduces the barrier height and effectively makes it an Ohmic contact where we did not observe any UV sensitivity.

Chapter Eight: Conclusions and Future Work

To conclude, n and p-type ZnO thin films are grown on (100) Si substrates with low counts of native defects by optimization of growth conditions using PLD. In this work, an exhaustive investigation of growth parameters is presented and optical, structural, and electrical properties of the films are systematically studied. It is shown that the optimization of the growth dynamics along with the growth conditions leads to a fine control over the formation/activation of native defects which enables us to control the electrical behavior of the grown films.

It is concluded that, in addition to growth conditions, special treatments of the surface of the substrates allow for a control over the growth dynamics of ZnO films. In other words, it is possible to engineer the stacking order of ZnO polar planes along the growth axis to obtain O or Zn-terminated films with significantly different properties by manipulation of surface morphology and its electrical structure. Based on our results, preparation recipes and surface functionalization of the substrates can be employed to promote desired defects and suppress compensating centers. HF treatment of the substrates in the form of BOE or diluted HF is standard in silicon technology; however, the effects of hydrogen in ZnO are all but standard. As we discussed it earlier in this work, hydrogen and its complexes act as shallow donors in ZnO, but it has amphoteric behavior for other semiconductors; it acts as a donor for p-type and as an acceptor for n-type semiconductors. Thus, sample preparations and surface treatments prior to growth process are important.

Because of its high energy particles and deviations from equilibrium, PLD proved to be an effective growth method for fabrication of high quality (low defects) ZnO thin films at relatively low growth temperatures. The ability of low-temperature growth is particularly important for application of various substrates. For instance, this technique can be optimized for

the growth on flexible polymer substrates with potentials in optoelectronics and sensor applications. Even though the details of PLD in terms of its dynamics are not fully understood, it is a simple method with controls over growth parameters along with a relatively high growth rate.

Our crystallographic results confirmed textured structure of wurtzite ZnO films grown along the *c*-axis with high in-plane alignment of crystalline domains. The information also confirms that there is not a significant oxide layer at Si-ZnO junction, and the films are grown epitaxially on the substrates; however, the large lattice mismatch between Si and ZnO introduces extended defects at the interface. This also creates stress in the film, and the bandgap is affected which is confirmed by our XRD and PL results.

Based on our room temperature PL results, we managed to suppress the defect-related emission peak (broad emission band at 450-550 nm) significantly. This suppression shows the low count of native defects (mostly oxygen vacancies) which is further confirmed by Hall Effect measurements. We did not observe any differences in the PL results of the films grown on n and p-Si substrates, but the effects of growth temperature and oxygen overpressure were investigated, and it is concluded that at low growth temperatures (below 100-150 ^{o}C) the arriving plume particles do not have enough energy to form high quality ZnO films and high concentration of native defects are observed. At high growth temperatures (above 300-350 ^{o}C) the particles are too energetic to stick to their lattice sites, and again low quality films are expected. Thus, an optimum temperature window of 200-300 ^{o}C for high quality growth of ZnO films is found empirically. The effect of oxygen overpressure is similar to that of the growth temperature. In other words, too low and too high pressures degrade the quality of the grown species while a relatively moderate pressure window of 10^{-5}—10^{-4} Torr is found to be the optimum. This is due

to the fact that even though oxygen is necessary for the growth, high pressures increase the scatterings of the plume particles as well as laser-gas interactions which affect the growth adversely.

Electrical studies of our thin films show that a conductivity conversion from n to p-type occurs for the films grown on p-Si substrates as the Hall temperature is increased. This is attributed to the thermal formation and activation of acceptor-like defects with higher formation energies (than donor-like defects), out diffusion of interstitial hydrogen, and surface properties of Si substrates. Atomic scale study of ZnO growth on one hand, and electrical and morphological differences between n and p-type (100) Si surfaces on the other, we believe that the stacking order of O^{-2} and Zn^{+2} polar planes, and thus, the termination of the films grown on n and p-type substrates are different with different electrical properties. In addition to the conductivity type of the films, the scattering and transport mechanisms undergo a conversion for high temperatures. It is worth noting that the conductivity conversion of the films occurs at different temperatures based on the growth conditions. More specifically, we expect lower defects and thus lower transition points for films grown at higher temperatures. In fact, our results confirm the inverse relation of the growth temperature with respect to the transition points.

In this work we also presented the application of our high quality ZnO films in ZnO/Si heterojunctions and optoelectronic devices successfully. High rectification properties were observed for devices grown on n and p-Si substrates at low and high oxygen pressures respectively, and the results are consistent with our previous findings. For the optoelectronic devices, excess carriers generated by UV illumination affect the film's conductivity which in turn affects the output characteristics of our devices which include the resistance or the slope of the IV characteristics for photoresistors and rectification properties for Schottky diodes. The

photorespons of an Al/n-ZnO/n-Si photoresistor and an Al/p- ZnO/p-Si Schottky diode in dark and UV light are presented and discussed.

Even though ZnO device are still limited to heterojunctions and some research-scale projects, the author believes that with the current pace of the work on this subject and incremental contributions of each study, including this one, all-ZnO based LEDs, sensors, and ultimately transistors with far superior properties are due to appear soon. Having seen the effects of various growth parameters and growth dynamics on the electrical properties and the conductivity type of ZnO thin films, fabrication of all-ZnO junctions and thin film transistors is the next step to fully integrate this highly sought after material in device applications.

Bibliography

Ali Hasina Afroz and Iliadis, Agis A. Development of self-assembled ZnO nanostructures in diblock copolymers on large area Si wafers and gas sensor applications // Dissertation. - May 2007.

Arnaudov B. [et al.] Multilayer model for Hall effect data analysis of semiconductor structures with step-changed conductivity [Article] // Physical Review B. - 2003. - 045314 : Vol. 67.

Arturas Zukauskas Michael S. Shur, Remis Gaska Introduction to Solid-State Lighting [Book]. - New York : John Wiley & Sons, Inc. , 2002. - 0471215740.

Arturas Zukauskas Michael S. Shur, Remis Gaska Introduction to Solid-State Lighting [Book]. - New York : John Wiley & Sons Inc. , 2002. - 0471215740.

Atsushi Kudo Hiroshi Yanagi, Kazushige Ueda, Hideo Hosono, and Hiroshi Kawazoe, Yoshihiko Yano Fabrication of transparent p –n heterojunction thin film diodesbased entirely on oxide semiconductors [Article] // APPLIED PHYSICS LETTERS. - 1 NOVEMBER 1999. - Vols. 75, NUMBER 18.

B. Joseph P. K. Manoj, V. K. Vaidyan Studies on structural, electrical, and optical properties of Al-doped ZnO thin films prepared by chemical spray deposition [Article] // Ceram Intern. . - 2006. - 32. - pp. 487-493.

B.P.J. de Lacy Costello R.J. Ewen, N.M. Ratcliffe, and M. Richards Highly sensitive room temperature sensors based on the UV-LED activation of zinc oxide nanoparticles [Article] // Sensors and Actuators B: Chemical. - 2008. - 134. - pp. 945-952.

Breitenstein O. [et al.] The origin of ideality factors n > 2 of shunts and surfaces in the dark I-V curves of Si solar cells [Article] // Proceedings of the 21st European Photovoltaic Solar Energy Conference, Munich. - Munich : [s.n.], 2006.

Brilis N. [et al.] Electrical conduction effects at low temperatures in undoped ZnO thin films grown by Pulsed Laser Deposition on Si substrates [Article] // Thin Solid Films . - 2008. - Vol. 516. - pp. 4226–4231.

C. H. Park S. B. Zhang, and Su-Huai Wei Origin of p-type doping difficulty in ZnO: The impurity perspective [Article] // PHYSICAL REVIEW B 66, 073202 (2002).

Ch. Pandis N. Brilis, E. Bourithis, D. Tsamakis, H. Ali, Soumya Krishnamoorthy, Agis A. Iliadis Low–Temperature Hydrogen Sensors Based on Au Nanoclusters and Schottky Contacts on ZnO Films Deposited by Pulsed Laser Deposition on Si and SiO2 Substrates [Article] // IEEE SENSORS JOURNAL, VOL. 7, NO. 3, MARCH 2007.

Ch. Pandis N. Brilis, E. Bourithis, D. Tsamakis, H. Ali, Soumya Krishnamoorthy,Agis A. Iliadis Low-Temperature Hydrogen Sensors Based on Au Nanoclusters and Schottky Contacts on ZnO Films Deposited by Pulsed Laser Deposition on Si and SiO2 Substrates [Article] // IEEE Sensors Journal. - March 2007. - 3 : Vol. 7.

Chabal Y. J. [et al.] Infrared spectroscopy of Si(111) and Si(100) surfaces after HF treatment: Hydrogen termination and surface morphology [Article] // Journal of Vacuum Science & Technology A: Vacuum, Surfaces, and Films. - May 1989. - 3 : Vol. 7. - pp. 2104-2109.

Chen Huibo [et al.] Hydrothermally grown ZnO micro/nano tubes arrays and their properties [Article] // Nanoscale Research Letter. - 2010. - 3 : Vol. 5.

Chen X. D. [et al.] Current Transport Studies of ZnO/p-Si Heterostructures Grown by Plasma Immersion Ion Implantation and Deposition [Article] // Applied Physics Letters. - 2006. - 13 : Vol. 88. - p. 132104.

Cho Kwangsik [et al.] New Process Development for Planar-Type CIC Tunneling Diodes [Article] // IEEE Electron Device Letters. - August 2010. - 8 : Vol. 31. - pp. 809-811.

Choopun S. [et al.] Oxygen pressure-tuned epitaxy and optoelectronic properties of laser-deposited ZnO films on sapphire [Article] // Applied Physics Letters. - December 20, 1999. - 25 : Vol. 75. - p. 3947.

CHUA LEON 0. Memristor-The Missing Circuit Element [Article] // ,EEE TRANSACTIONS ON CIRCUIT THEORY, VOL. CT-18, NO. 5, SEPTEMBER 1971.

Chwang Ronald, Smith B. J. and Crowell C. R. Contact size effects on van der Pauw method for resistivity and Hall coefficient measurement [Article] // Solid-state Electronics. - December 1974. - 12 : Vol. 17. - pp. 1217-1227.

D. B. ROGERS R. D. SHANKON, C. T. PREWITT, AND J. L. GILLSON Chemistry of Noble Metal Oxides. III. Electrical Transport Properties and Crystal Chemistry of ABO2, Compounds with the Delafossite Structure [Article] // Inorganic Chemistry. - 1971. - 4 : Vol. 10.

D. Zhang C. Li, S. Han, X. Liu, T. Tang, W. Jin, C. Zhou Ultraviolet photodetection properties of indium oxide nanowires [Article] // Applied Physics, A 77 . - 2003. - pp. 163-166.

Dae-Kue Hwang Min-Suk Oh, Jae-Hong Lim and Seong-Ju Park ZnO thin films and light-emitting diodes [Article] // J. Phys. D: Appl. Phys. 40 (2007) R387–R412.

Dae-Kue Hwang Soon-Hyung Kang, Jae-Hong Lim, Eun-Jeong Yang, Jin-Yong Oh,Jin-Ho Yang, and Seong-Ju Parka p-ZnO/n-GaN heterostructure ZnO light-emitting diodes [Journal]. - [s.l.] : APPLIED PHYSICS LETTERS, 2005. - 222101 : Vol. 86.

Desnica U. V. DOPING LIMITS IN II-Vl COMPOUNDS - CHALLENGES, PROBLEMS AND SOLUTIONS [Article] // Prog. Crystal Growth and Charact. Vol. 36, No. 4. pp. 291-357, 1998.

Desnica U. V. DOPING LIMITS IN II-Vl COMPOUNDS - CHALLENGES,PROBLEMS AND SOLUTIONS [Article] // Progress in Crystal Growth and Characterization of Materials. - Great Britain : Elsevier Ltd., 1998 Published by Elsevier Ltd. - 4 : Vol. 36.

Dmitri B. Strukov Gregory S. Snider, Duncan R. Stewart & R. Stanley Williams The missing memristor found [Article] // Nature. - 1 May 2008. - Vol. 453.

Esmaili Sardari Saeed [et al.] Crystal quality and conductivity type of (0 0 2) ZnO films on (1 0 0) Si substrates for device applications [Article] // Soid State Electronics. - 2010. - 10 : Vol. 54. - pp. 1150-1154.

Esmaili Sardari Saeed [et al.] Crystal quality and conductivity type of (002) ZnO films on (100) Si substrates for device applications [Article] // Solid-State Electronics. - October 2010. - 10 : Vol. 54. - pp. 1150-1154.

Esmaili Sardari Saeed [et al.] Crystal Quality and Conductivity Type of (002) ZnO on (100) Si Substrates for Device Applications [Article] // Solid-State Electronics. - October 2010. - 10 : Vol. 54. - pp. 1150–1154.

Esmaili Sardari Saeed, Berkovich Andrew and Iliadis Agis Observation of conductivity type conversion in undoped ZnO films grown by pulsed laser deposition on silicon (100) substrates [Article] // Applied Physic Letters. - 2012. - Vol. 100.

Eun Sub Shim Hong Seong Kang, Jeong Seok Kang, Jong Hoon Kim, Sang Yeol Lee Effect of the variation of film thickness on the structural and optical properties of ZnO thin films deposited on sapphire substrate using PLD [Article] // Applied Surface Science. - 2002. - 186. - pp. 474-476.

Eun-Cheol Lee Y.-S. Kim, Y.-G. Jin, and K. J. Chang Compensation mechanism for N acceptors in ZnO [Article] // PHYSICAL REVIEW B, VOLUME 64, 085120. 2001 .

F. Hellegouarc'h F. Arefi-Khonsari, R. Planade, J. Amouroux PECVD prepared SnO2 thin films for ethanol sensors [Article] // Sensors and Actuators B: Chemical. - 2001. - 73. - pp. 27-34.

F. V. Farmakis Th. Speliotis, K. P. Alexandrou, C. Tsamis, M. Kompitsas, I. Fasaki, P. Jedrasik, G. Petersson, B. Nilsson Field-effect transistors with thin ZnO as active layer for gas sensor applications [Article] // Microelectronic Engineering. - 2008. - 85. - pp. 1035-1038.

Fan Shan-Wei, Srivastava A. K. and Dravid V. P. UV-activated room-temperature gas sensing mechanism of polycrystalline ZnO [Article] // Applied Physics Letters. - October 5, 2009. - 14 : Vol. 95.

Fan X. M. [et al.] Effect of the oxygen pressure on the photoluminescence properties of ZnO thin films by PLD [Article] // Journal of Materials Science. - 2007. - Vol. 42. - pp. 2678–2683.

Forsen E, Abadal G and Ghatnekar-Nilsson S, et al. Ultrasensitive mass sensor fully integrated with complementary metal-oxide-semiconductor circuitry [Article] // APPLIED PHYSICS LETTERS . - JUL 25 2005. - 4 : Vol. 87.

G. Eranna B. C. Joshi, D. P. Runthala, and R. P. Gupta Oxide Materials for Development of Integrated Gas Sensors—A Comprehensive Review [Article] // Critical Reviews in Solid State and Materials Sciences. - 2004. - 29. - pp. 111–188.

G.Eranna B. C. Joshi, D. P. Runthala, and R. P. Gupta. "Oxide Materials for Development of Integrated Gas Sensors—A Comprehensive Review." Critical Reviews in Solid States and Materials Sciences, 29:111-188, 2004 [Article].

Gang Xiong John Wilkinson, Brian Mischuck, S. Tu¨zemen, K. B. Ucer, and R. T. Williams Control of p- and n-type conductivity in sputter deposition of undoped ZnO [Article] // APPLIED PHYSICS LETTERS. VOLUME 80, NUMBER 7. 18 FEBRUARY 2002.

Ghosh R., Basak D. and Fujihara S. Effect of substrate-induced strain on the structural, electrical, and optical properties of polycrystalline ZnO thin films [Article] // Journal of Applied Physics. - September 1, 2004. - 5 : Vol. 96.

Gyu-Chul Yi Chunrui Wang and Won ll Park ZnO nanorods: synthesis, characterization and applications [Article] // Semicond. Sci. Technol.. - April 2005. - 20 No. 4.

Hiroshi Kawazoe Masahiro Yasukawa, Hiroyuki Hyodo,Masaaki Kurita, Hiroshi Yanagi & Hideo Hosono P-type electrical conduction in transparent thin films of CuAlO2 [Article] // NATURE. - 1997. - 30 OCTOBER : Vol. 389.

Hiroshi Yanagi Kazushige Ueda, Hiromichi Ohta, Masahiro Orita, Masahiro Hirano, Hideo Hosono Fabrication of all oxide transparent p-n homojunction using bipolar CuInO2 semiconducting oxide with delafossite structure [Article] // Solid State Communications. - 2002. - Vol. 121.

Hiroshi Yanagi Kazushige Ueda, Hiromichi Ohta, Masahiro Orita, Masahiro Hirano, Hideo Hosono Fabrication of all oxide transparent p-n homojunction using bipolar CuInO2 semiconducting oxide with delafossite structure [Article] // Solid State Communications. - 2002. - 121. - pp. 15-18.

Hiroshi Yanagi Tomomi Hase, Shuntaro Ibuki, Kazushige Ueda, and Hideo Hosono Bipolarity in electrical conduction of transparent oxide semiconductor CuInO2 with delafossite structure [Article] // APPLIED PHYSICS LETTERS. - 12 MARCH 2001. - 11 : Vol. 78.

Hussain Sajjad Investigation of Structural and Optical Properties of Nanocrystalline ZnO. - LiTH-IFM-A-EX-08/1928-SE, Linköpings Universitet INSTITUTE OF TECHNOLOGY , The Department of Physics, Chemistry and Biology , Linköpings University , SE-58183 Linköping, Sweden.

Isolde Simon Nicolae BaÃrsan, Michael Bauer, Udo Weimar Micromachined metal oxide gas sensors:opportunities to improve sensor performance [Article] // Sensors and Actuators B 73 (2001) 1-26.

J. A. Van Vechten T. K. Bergstresser Electronic Structures of Semiconductor Alloys [Article] // PHYSICAL REVIEW B. - APRIL 15, 1970. - Vols. 1, NUMBER 8. - pp. 3351-3358.

J. C. Sun J. Z. Zhao, H. W. Liang, J. M. Bian, L. Z. Hu, H. Q. Zhang, X. P. Liang, W. F. Liu, and G. T. Du Realization of ultraviolet electroluminescence from ZnO homojunction with n-ZnO/p-ZnO:As/GaAs structure [Article] // APPLIED PHYSICS LETTERS. 90, 121128 (2007).

Jagadish Chennupati and Pearton S. J. Zinc Oxide Bulk, Thin Films And Nanostructures: Processing, Properties And Applications [Book]. - [s.l.] : Elsevier, 2006. - 0080447228, 9780080447223 .

Janotti Anderson and Van de Walle Chris Fundamentals of zinc oxide as a semiconductor [Article] // Reports on Progress in hysics. - 2009. - Vol. 72. - p. 126501.

Janotti Anderson and Van de Walle Chris G Fundamentals of zinc oxide as a semiconductor [Article] // Reports on Progress in Physics. - 2009. - Vol. 72. - p. 126501.

Jin Chunming [et al.] Growth of epitaxial ZnO films on Si (111) [Article] // Material Research Society Symposium Proceedings. - 2002. - Vol. 722.

Johnson P. D. Phys. Rev. [Article]. - 94, 845 (1954).

Junya Suehiro Nobutaka Nakagawa, Shin-ichiro Hidaka, Makoto Ueda, Kiminobu Imasaka,Mitsuhiro Higashihata, Tatsuo Okada andMasanori Hara Dielectrophoretic fabrication and characterization of a ZnO nanowire-based UV photosensor [Article] // Nanotechnology 17 (2006) 2567–2573.

Karamat S. [et al.] Structural, compositional and magnetic characterization of bulk V2O5 [Article] // Applied Surface Science. - 2010. - Vol. 256. - pp. 2309-2314.

Kasap S. O. Principles of Electronic Materials and Devices, Third Edition [Book]. - [s.l.] : McGraw-Hill, 2006. - 139780073104645.

Kim Young Wook [et al.] A Bacterial Biofilm Surface Acoustic Wave Sensor For Real Time Biofilm Growth Monitoring // The 9th Annual IEEE Conference on Sensors, IEEE Sensors 2010 Conference. - November 2-4, 2010.

Kim Young Wook [et al.] An ALD aluminum oxide passivated Surface Acoustic Wave sensor for early biofilm detection [Article] // Sensors and Actuators B: Chemical. - 2012. - 163. - pp. 136-145.

Kim Young Wook [et al.] An ALD aluminum oxide passivated Surface Acoustic Wave sensor for early biofilm detection [Article] // Sensors and Actuators B: Chemical. - 2012. - Vol. 163. - pp. 136– 145.

Kim Young Wook [et al.] Atomic Layer Deposition of Aluminum Oxide for Effective Surface Passivation of a MEMS Biosensor // The 11th International Conference on Atomic Layer Deposition. - Cambridge, Massachusetts : [s.n.], June 26-29, 2011.

Kittel Charles Introduction to Solid State Physics [Book]. - [s.l.] : John Wiley & Sons, Inc., 8th ed. 2005. - 0-471-41526-X.

Klingshirn C. ZnO: From basics toward applications [Article] // Phys, stat. sol. (b) 244, No. 9. - 2007. - pp. 3027-3073.

Klingshirn C. ZnO: Material, Physics and Applications [Article] // ChemPhysChem. - 2007. - 8. - pp. 782 – 803. - REVIEWS. - DOI: 10.1002/cphc.200700002.

Koffyberg R. P. [Article] // Phys. Rev. B . - 1976. - Vols. 13, 4470 .

Kornherr Andreas [et al.] Adsorption of Organosilanes at a Zn Terminated ZnO (0001) Surface: Molecular Dynamics Study [Article] // Langmuir. - Sep 12, 2006. - Vol. 22. - pp. 8036-8042.

KOVNERISTYI YK LAZAREVA IY, LAZAREV EM, KOROTKOV NA, PANKRATEVA LN, MOROZOV VA CRYSTALLOCHEMICAL INTERACTIONS IN METAL-OXIDE SYSTEM UNDER MICROWAVE ELECTROMAGNETIC IRRADIATION [Article] // RUSSIAN METALLURGY. - 1993. - 4. - pp. 163-169.

Krishnamoorthy S, Iliadis AA and Bei T, et al. An interleukin-6 ZnO/SiO2/Si surface acoustic wave biosensor [Article] // BIOSENSORS & BIOELECTRONICS. - 2008. - 2 : Vol. 24. - pp. 313-318.

Krishnamoorthy S. and Iliadis A.A. Development of high frequency ZnO/SiO2/Si Love mode surface acoustic wave devices // Solid-State Electronics. - 2006. - Vol. 50. - pp. 1113–1118.

Krishnamoorthy Soumya and Iliadis Agis A. Properties of high sensitivity ZnO surface acoustic wave sensors on SiO2/(100) Si substrates [Article] // Solid-State Electronics. - 2008. - Vol. 52. - pp. 1710-1716.

Kubo Momoji [et al.] Homoepitaxial growth mechanism of ZnO (0001): Molecular-dynamics simulations [Article] // Physical Review B. - June 15, 2000. - 23 : Vol. 61.

Lee E. [et al.] [Article] // Physical Review B. - 2001. - Vol. 64. - p. 085120.

Lee Yueh-Chien [et al.] Rapid thermal annealing effects on the structural and optical properties of ZnO films deposited on Si substrates [Article] // Journal of Luminescence. - 2009. - 129. - pp. 148-152.

Lide David R. and Haynes W. M. CRC Handbook of Chemistry and Physics [Book]. - 2010. - 90th edition.

Lillie JJ, Thomas MA and Jokerst NM, et al. Multimode interferometric sensors on silicon optimized for fully integrated complementary-metal-oxide-semiconductor chemical-biological sensor systems [Article] // JOURNAL OF THE OPTICAL SOCIETY OF AMERICA B-OPTICAL PHYSICS. - APR 2006. - 4 : Vol. 23. - pp. 642-651.

Ling C. H. The Effective Carrier Mobility In a Polycrystalline Layer [Article] // Journal of Applied Physics D. - 1983. - Vol. 16. - pp. L239-L242.

Lojek Bo History of Semiconductor Engineering [Book]. - Berlin : Springer-Verlag Berlin Heidelberg, 2007. - 978-3-540-34257-1.

Look David C. Electrical Characterization of GaAs Materials And Devices [Book]. - [s.l.] : John Wiley & Sons Ltd., 1989. - 0471917028.

M. Rusop K. Uma, T. Soga, T. Jimbo Post-growth annealing of zinc oxide thin films pulsed laser deposited underenhanced oxygen pressure on quartz and silicon substrates [Article] // Materials Science and Engineering B 127 (2006) 150–153.

M. Suchea S. Christoulakis, M. Katharakis, G. Kiriakidis, N. Katsarakis, and E. Koudoumas Substrate temperature influence on the properties of nanostructured ZnO transparent ultrathin films grown by PLD [Article] // Applied Surface Science. - 2007. - 253. - pp. 8141-8145.

M.F. Al-Kuhaili S.M.A. Durrani, I.A. Bakhtiari Carbon monoxide gas-sensing properties of CeO2–ZnO thin films [Article] // Applied Surface Science. - 2008. - 255. - pp. 3033–3039.

Maeng Jongsun [et al.] Transient Reverse Current Phenomenon in a P-n Heterojunction Comprised of Poly(3,4-ethylene-dioxythiophene):poly(styrene-sulfonate) and ZnO Nanowall [Article] // Applied Physics Letters. - 2008. - 12 : Vol. 93. - p. 123109.

Marion E. Franke Tobias J. Koplin, and Ulrich Simon Metal and Metal Oxide Nanoparticles in Chemiresistors: Does the Nanoscale Matter? [Article] // small 2006, 2, No. 1, 36 – 50. - www.small-journal.com.

Matthias Batzill Ulrike Diebold The surface and materials science of tin oxide [Article] // Progress in Surface Science 79 (2005) 47–154.

McMurdie H., Morris, M., Evans, E., Paretzkin, B., Wong-Ng, W., Ettlinger, L., Hubbard, C. Powder Diffraction. - 1986. - Vol. 1. - p. 76.

Meyer B. and Marx Dominik Density-functional study of the structure and stability of ZnO surfaces [Article] // Physical Review B. - 2003. - Vol. 67. - p. 035403.

Min-Suk Oh Sang-Ho Kim, and Tae-Yeon Seong Growth of nominally undoped p-type ZnO on Si by pulsed-laser deposition [Journal] // APPLIED PHYSICS LETTERS 87, 122103 (2005).

Min-Suk Oh Sang-Ho Kim, Seong-Ju Park, Tae-Yeon Seong Type conversion of intentionally undoped ZnO layers grown by pulsed laser deposition [Article] // Superlattices and Microstructures 39 (2006) 130–137.

Monod Jacques The Growth of Bacterial Cultures [Article] // Annual Review of Microbiology. - March 1949. - pp. 371-394.

Morita M. [et al.] Growth of native oxide on a silicon surface [Article] // Journal of Applied Physics. - 1990. - Vol. 68.

Morkoç Hadis and Özgür Ümit Zinc Oxide: Fundamentals, Materials and Device Technology [Book]. - Federal Republic of Germany : WILEY-VCH, 2009.

Morkoç Hadis and Özgür Ümit Zinc Oxide: Fundamentals, Materials and Device Technology [Book]. - Federal Republic of Germany : WILEY-VCH, 2009. - 978-3-527-40813-9.

N. Brilis P. Romesis, D. Tsamakis, M. Kompitsas Influence of pulsed laser deposition (PLD) parameters on the H2 sensing properties of zinc oxide thin films [Article] // Superlattices and Microstructures . - 2005. - 38. - pp. 283-290.

N. Izyumskaya V. Avrutin, Ü. Özgür, Y. I. Alivov, and H. Morkoç Preparation and properties of ZnO and devices [Article] // phys. stat. sol. (b). - 2007. - Vols. 244, No. 5. - pp. 1439–1450 .

Nalwa Hari Singh Handbook of Thin Film Materials: Deposition and processing of thin films [Book]. - [s.l.] : Academic Press, 2002. - Vol. 5. - 0125129084, 9780125129084 .

Naoko Tanda Masaki Iwakura, Kyoko Ikawa, Junpei Washio, Ayumi Kusano b, Kengo Suzuki, Takeyoshi Koseki Development of a portable bad-breath monitor and application to field study of halitosis [Article] // International Congress Series 1284 (2005) 201– 202.

Oba F. [et al.] [Article] // Science and Technology of Advanced Materials. - 2011. - Vol. 12. - p. 034302.

Oba Fumiyasu [et al.] Point defects in ZnO: an approach from first principles [Article] // Science and Technology of Adanced Materials . - 2011. - Vol. 12.

Overbury S. H. [et al.] Ion scattering study of the Zn and oxygen-terminated basal plane surfaces of ZnO [Article] // Surface Science. - 1998. - Vol. 410. - pp. 106-122.

P. P. Sahay S. Tewari, S. Jha, M. Shamsuddin sprayed ZnO thin films for ethanol sensors [Article] // Journal of Material Science. - 2005. - 40. - pp. 4791-4793.

P.P. Sahay and R.K. Nath Al-doped ZnO thin films as methanol sensors [Article] // Sensors and Actuators B: Chemical. - 2008. - 134. - pp. 654-659.

Pal U. [et al.] Synthesis and optical properties of ZnO nanostructures with different morphologies [Article] // Optical Materials. - 2006. - Vol. 29. - pp. 65-69.

Park Chan Jun [et al.] The Effects of Rapid Thermal Annealing on the Performance of ZnO Thin-Film Transistors [Article] // Journal of the Korean Physical Society. - November 2009. - 5 : Vol. 55. - pp. 1925-1930.

Pecharsky Vitalij K. and Zavalij Peter Y. Fundamentals of Powder Diffraction and Structural Characterization of Materials [Book]. - New York : Springer, 2009. - Second Edition. - 978-0-387-09578-3, 978-0-387-09579-0.

Pecharsky Vitalij K. and Zavalij Peter Y. Fundamentals of Powder Diffraction and Structural Characterization of Materials [Book]. - [s.l.] : Springer, 2009. - Second. - 978-0-387-09578-3 e-ISBN: 978-0-387-09579-0.

Predo Prachi Patel Beyond Blue [Article] // IEEE Spectrum. - March 2007.

R. Ghosh and D. Basak S. Fujihara Effect of substrate-induced strain on the structural, electrical, and optical properties of polycrystalline ZnO thin films [Article] // JOURNAL OF APPLIED PHYSICS. - 1 SEPTEMBER 2004. - Vols. VOLUME 96, NUMBER 5.

R. Krause-Rehberg H.S. Leipner, T. Abgarjan, A. Polity Review of defect investigations by means of positron annihilation in II−VI compound semiconductors [Journal] // Applied Physics A 66, Materials, Science & Processing. - 1998. - pp. 599–614.

R. Triboulet Jacques Perrie`re Epitaxial growth of ZnO films [Article] // Progress in Crystal Growth and Characterization of Materials. - 47 (2003) 65-138.

R. Triboulet Jacques Perrie`re Epitaxial growth of ZnO films [Article] // Progress in Crystal Growth and Characterization of Materials. 47 (2003) 65-138.

R. Triboulet Jacques Perrie`re Epitaxial growth of ZnO films [Article] // Progress in Crystal Growth and Characterization of Materials. - 2003. - Vol. 47. - pp. 65-138.

Rhoderick E. H. The Hall effect – an important diagnostic tool [Article] // III-Vs Review. - 2000. - 3 : Vol. 13.

Rhoderick E. H. The Hall effect – an important diagnostic tool [Article] // III-Vs Review. - May 2000. - 3 : Vol. 13. - pp. 46-51.

S. Christoulakis M. Suchea, E. Koudoumas, M. Katharakis, N. Katsarakisa, and G. Kiriakidisa Thickness influence on surface morphology and ozone sensing properties of nanostructures ZnO transparent thin films grown by PLD [Article] // Applied Surface Science . - 2006. - 252. - pp. 5351-5354.

S. Mishra C. Ghanshyam, N. Ram, R. P. Bajpai, R. K. Bedi Detection mechanism of metal oxide gas sensor under UV radiation [Article] // Sensors and Actuators B: Chemical. - 2004. - 97. - pp. 387-390.

Sands Donald E. "Crystal Systems and Geometry". Introduction to Crystallography [Book]. - Mineola, New York : Dover Publications, Inc., 1993. - 0-486-67839-3.

Saravanakumar K. [et al.] XPS and Raman Studies on (002) Oriented Nanocrystalline ZnO Films Showing Temperature Dependent Optical Red Shift [Article] // Advanced Studies in Theoretical Physics. - 2011. - 4 : Vol. 5. - pp. 155-170.

Sato N, Morimura H and Shigematsu S, et al. Force-sensing scheme for small mechanical signals in complementary metal oxide semiconductor microelectromechanical system fingerprint sensor [Article] // JAPANESE JOURNAL OF APPLIED PHYSICS PART 1-REGULAR PAPERS BRIEF COMMUNICATIONS & REVIEW PAPERS. - SEP 2005. - 9A : Vol. 44. - pp. Pages: 6481-6489 Part: 1.

Shan Fang [et al.] Imaging Plume Dynamics with Ultrafast Hard X-rays [Article] // Chemical Physics. - 2007. - Vol. 88. - pp. 728-730. - Part XIII.

Sharawi Mohammad S. Optical-electrical printed circuit boards- Part II [Article] // IEEE Potentials. - MARCH/APRIL 2009. - 2 : Vol. 28.

Shubra Singh P Thiyagarajan, K Mohan Kant, D Anita, S Thirupathiah, N Rama, Brajesh Tiwari, M Kottaisamy and M S Ramachandra Rao Structure, microstructure and physical properties of ZnO based materials in various forms: bulk, thin film and nano [Article] // JOURNAL OF PHYSICS D: APPLIED PHYSICS. - J. Phys. D: Appl. Phys. 40 (2007) 6312–6327.

Singh Rajiv K. and Narayan J. Pulsed-laser evaporation technique for deposition of thin films: Physics and theoretical model [Article] // Physical Review B. - May 1, 1990. - 1 : Vol. 41. - p. 88433.

Sōga Tetsuo Nanostructured Materials for Solar Energy Conversion [Book]. - [s.l.] : Elsevier, 2006. - 9780444528445.

Soleimanpour A. M., Hou Y. and Jayatissa A. H. The effect of UV irradiation on nanocrysatlline zinc oxide thin films related to gas sensing characteristics [Article] // Applied Surface Science. - April 1, 2011. - 12 : Vol. 257. - pp. 5398-5402.

Song Kyung [et al.] Application of theta-scan precession electron diffraction to structure analysis of hydroxyapatite nanopowder [Article] // Journal of Electron Microscopy. - 2012. - 1 : Vol. 61. - pp. 9-15.

Staff Mayo Clinic Seasonal affective disorder (SAD) - MayoClinic.com [Online] // Mayo Clinic Web site. - Mayo Foundation for Medical Education and Research, September 24, 2007. - August 26, 2008. - http://www.mayoclinic.com/health/seasonal-affective-disorder/DS00195.

Stokes Jon Intel shows off Tukwila, first 2 billion transistor CPU [Online] // ars technica, the art of technology. - Ars Technica , February 07, 2008 . - May 18, 2008. - http://arstechnica.com/news.ars/post/20080207-intel-shows-off-tukwila-first-2-billion-transistor-cpu.html.

Sumiya M. [et al.] Dependence of impurity incorporation on the polar direction of GaN film growth [Article] // Applied Physics Letters. - 2000. - Vol. 76. - p. 2098.

Sze S. M. and Ng Kwok K. Physics of semiconductor devices [Book]. - [s.l.] : John Wiley & Sons Inc., 2007. - Third edition. - 978-0-471-14323-9, 0-471-14323-5.

Tamargo Maria C. II-VI Semiconductor Materials And Their Applications / Optoelectronic Properties of Semiconductos and Superlattices, Volume 12 [Book]. - Ann Arbor, MI : Taylor & Francis, 2002. - 1-56032-914-9.

The Future of DVD Storage - Blu-ray and HD-DVD [Article] // ASI Tech Newsletter. - October 2006. - 5 : Vol. 5.

Thomas Pearsall Laurent Fulbert The MONA roadmap for photonic and nanotechnologies [Article] // NANO-M. - Dec. 2008. - pp. 6-12.

Ü. Özgür Ya. I. Alivov, C. Liu, A. Teke, M. A. Reshchikov, S. Doğan, V. Avrutin,S.-J. Cho, and H. Morkoç A comprehensive review of ZnO materials and devices [Article] // JOURNAL OF APPLIED PHYSICS. - 2005. - 98, 041301.

V.R. Shinde T.P. Gujar, C.D. Lokhande LPG sensing properties of ZnO films prepared by spray pyrolysis method: Effect of molarity of precursor solution [Article] // Sensors and Actuators B 120 (2007) 551–559.

Vaezi M. R. SnO2/ZnO double-layer thin films: A novel economical preparation and investigation of sensitivity and stability of double-layer gas sensors [Article] // Materials Chemistry and Physics. - 2008. - 110. - pp. 89-94.

Vainshtein Boris K. Modern Crystallography 1: Fundamentals of Crystals. Symmetry, and Methods of Structural Crystallography [Book]. - New York : Springer, 1994. - 3-540-56558-2.

Van de Walle Chris G. Hydrogen as a Cause of Doping in Zinc Oxide [Article] // PHYSICAL REVIEW LETTERS. VOLUME 85, NUMBER 5. 31 JULY 2000.

Vanheusden K. [et al.] Mechanisms behind green photoluminescence in ZnO phosphor powders [Article] // Journal of Applied Physics. - May 15, 1996. - 10 : Vol. 79. - pp. 7983-7990.

von Wenckstern Holger [et al.] Mean barrier height of Pd Schottky contacts on ZnO thin films [Article] // Applied Physics Letters. - 2006. - Vol. 88. - p. 092102.

Walker D. M. Roessler and W. C. [Article] // Phys. Rev.. - 1967. - Vols. 159, 733 .

Walle Chris G. Van de Hydrogen as a Cause of Doping in Zinc Oxide [Article] // PHYSICAL REVIEW LETTERS. VOLUME 85, NUMBER 5. 31 JULY 2000.

Wang Mingsong, Cheng Xiaonong and Yang Juan Controlled visible photoluminescence of ZnO thin films prepared by RF magnetron sputtering [Article] // Applied Physics Letters A: Materials Science and Processing. - 2009. - Vol. 96. - pp. 783–787.

Wang Z. L., Kong X.Y. and Zuo J. M. Induced Growth of Asymmetric Nanocantilever Arrays on Polar Surfaces [Article] // Physical Review Letters. - Oct 31, 2003. - 18 : Vol. 91.

Wang Zhong Lin and Song Jinhui Piezoelectric Nanogenerators Based [Article] // Science. - April 14, 2006. - Vol. 312.

Wang Zhong Lin Nanostructures of zinc oxide [Article] // Materialstoday. - June 2004. - pp. 24-33. - ISSN:1369 7021.

Wei X. Q. [et al.] Comparative study on structural and optical properties of ZnO thin films prepared by PLD using ZnO powder target and ceramic target [Article] // Optics and laser technology. - 2009. - 5 : Vol. 41. - pp. 530-534.

Wen Sy-Bor [et al.] Laser Ablation Induced Vapor Plume Expansion into a Background Gas. II. Experimental Analysis [Article] // Journal of Applied Physics. - 2007. - 2 : Vol. 101.

West Anthony R. Basic Solid State Chemistry, 2nd Edition [Book]. - Chichester : John Wiley & Sons, 1999. - 978-0-471-98756-7.

X. Cheng H. Zhao , L. Huo , S. Gao , J. Zhao ZnO nanoparticulate thin film: preparation, characterization and gas-sensing property [Article] // Sensors and Actuators B: Chemical , Volume 102 , Issue 2 , Pages 248 - 252.

Youn C. J. [et al.] Optical properties of Zn-terminated ZnO bulk [Article] // Journal of Crystal Growth. - 2004. - Vol. 261. - pp. 526-532.

Yu Weidong, Li Xiaomin and Gao Xiangdong Catalytic Synthesis and Structural Characteristics of High-Quality Tetrapod-Like ZnO Nanocrystals by a Modified Vapor Transport Process [Article] // Crystal Growth & Design. - 2005. - 1 : Vol. 5. - pp. 151-155.

Yunbo Wang Mehmet C. Vuran, Steve Goddard Cyber-physical Systems in Industrial Process Control [Article] // ACM SIGBED Review archive. - January 2008. - 1 : Vol. 5. - Special issue on the RTSS forum on deeply embedded real-time computing Article No 12.

Zavodinsky V. G., Kuyanov I. A. and Chukurov E. N. Computer study of boron and phosphorus at the Si(100)−2×1 surface [Article] // The European Physical Journal B. - 1998. - pp. 273-276.

Zhang Yongzhe [et al.] Effect of annealing atmosphere on the photoluminescence of ZnO nanospheres [Article] // Applied Surface Science. - 2009. - Vol. 255. - pp. 4801–4805.

Zhang Zhaoyan, Han Zhen-Xue and Dulikravich George S. Numerical Simulation of Laser Induced Plasma During Pulsed Laser Deposition [Article] // Journal of Applied Physics. - December 15, 2001. - 12 : Vol. 90.

Zhao Jie [et al.] Growth and photoluminescence of ZnO thin films on Si(111) by PLD in oxygen adequate ambient [Article] // Vacuum. - 2007. - Vol. 81. - pp. 1035–1039.

Zheng Jiao Shengyue Wang, Lifeng Bian and Jinhuai Liu Stability of SnO2/Fe2O3 multilayer thin film gas sensor [Article] // Materials Research Bulletin. - 2000.